

Kent Academic Repository

Full text document (pdf)

Citation for published version

Whittlesea, Philip (2019) Unconventional superconductivity: A theoretical study of equal-spin triplet-pairing in LaNiGa₂ and the potential application of topological transitions to quench prevention. Doctor of Philosophy (PhD) thesis, University of Kent,.

DOI

Link to record in KAR

<https://kar.kent.ac.uk/76180/>

Document Version

UNSPECIFIED

Copyright & reuse

Content in the Kent Academic Repository is made available for research purposes. Unless otherwise stated all content is protected by copyright and in the absence of an open licence (eg Creative Commons), permissions for further reuse of content should be sought from the publisher, author or other copyright holder.

Versions of research

The version in the Kent Academic Repository may differ from the final published version.

Users are advised to check <http://kar.kent.ac.uk> for the status of the paper. **Users should always cite the published version of record.**

Enquiries

For any further enquiries regarding the licence status of this document, please contact:

researchsupport@kent.ac.uk

If you believe this document infringes copyright then please contact the KAR admin team with the take-down information provided at <http://kar.kent.ac.uk/contact.html>

Unconventional superconductivity:

A theoretical study of equal-spin triplet-pairing in LaNiGa_2 and the potential application of topological transitions to quench prevention

A thesis submitted for the degree of
Doctor of Philosophy

Author:
Philip Whittlesea

Supervisor:
Dr. Jorge Quintanilla

University of
Kent

University of Kent
School of Physical Sciences
United Kingdom

July 2019

Word count = 50020

Dedication

In memory of my grandfather, Cyril Mercer.

Acknowledgements

I would like to thank my supervisor, Jorge Quintanilla, for first suggesting I would be capable of doing a PhD, as well as taking me on as a PhD student. Without his endless support and guidance both before and during my PhD, I would certainly not have made it this far. I would also like to thank Sudeep Ghosh who, although joining our group towards the end of my PhD, instantly became an invaluable colleague. He was always happy to offer his time to discuss any problems, offer advice and was always empathetic to the frustrations one can often experience during a PhD.

Author's declaration

I declare that this thesis titled: 'Unconventional superconductivity: A theoretical study of equal-spin triplet-pairing in LaNiGa_2 and the potential application of topological transitions to quench prevention' and the work presented within is, unless otherwise stated, my own. I confirm that this work was done wholly or mainly while in candidature for a research degree at the University of Kent. No part of this thesis has previously been submitted for any other academic award, at this institution or otherwise. I declare that when consulting and referring to the works of others, I have always clearly attributed said works by specific reference. Where this thesis is based on work done by myself in collaboration with others, I have made clear below my contribution.

Philip Whittlesea

Signed: _____

Published work

A more concise account of the work presented in chapter 7 has already been published in IEEE Transactions on Applied Superconductivity and resulted from the collaboration of P. Whittlesea (author of this thesis), J. Quintanilla (Supervisor of this author), J. F. Annett, A. D. Hillier and C. Hooley. See reference [1]. P. Whittlesea wrote the simulation code, performed all the simulations, data analysis, obtained the results and conclusions and was author of the article. J. Quintanilla came up with the initial idea and all authors were involved in critical discussions that helped shape the project, data analysis and conclusions.

Contents

Dedication	i
Acknowledgements	ii
Author's declaration	iii
Contents	iv
List of Figures	vii
List of Tables	ix
Notes on units and numerics	x
Units	x
Numerics	x
1 Introduction	1
2 Background	7
2.1 Introduction to BCS theory	7
2.2 Pairing potential	10
2.3 Broken symmetry	11
2.4 Topology in superconductors	13
2.5 Noncentrosymmetric superconductors	14
2.6 Experimental probes	15
2.6.1 Gap structure	16
2.6.2 Broken time reversal symmetry	17
2.7 Summary	21
3 Broken time reversal symmetry in Ni-based LaNiX_2 ($\text{X} = \text{C}, \text{Ga}$)	22
3.1 LaNiC_2	22
3.2 LaNiGa_2	27
3.3 Magnetisation from non-unitary triplet-pairing	28
3.4 Summary	29
4 Variational mean-field theory for singlet pairing	31
4.1 Non-interacting Hamiltonian	32
4.2 Interaction	36
4.3 Mean-field theory	37

4.3.1	Mean-field Hamiltonian	39
4.3.2	Self consistency equations	40
4.4	Diagonalising the mean-field Hamiltonian	41
4.4.1	Solving the eigenvector equations	43
4.5	Deriving the self-consistency equations	44
4.5.1	Gap equation	44
4.5.2	Hartree self-consistency equation	45
4.6	Self-consistency equations - numerical results	46
4.6.1	Solving the self-consistent gap equation via the contour method	46
4.6.2	Solving self-consistency equations iteratively	49
4.7	Free Energy	52
4.7.1	Zero temperature case	52
4.7.2	General case	53
4.7.3	Free energy - numerics	55
4.8	Summary	59
5	Variational mean-field theory of two-band equal-spin-pairing	63
5.1	Non-interacting Hamiltonian	64
5.1.1	Anisotropic nearest-neighbour hopping	66
5.1.2	Anisotropic nearest-neighbour intraband hopping with next-nearest-neighbour interband hopping	67
5.1.3	Isotropic nearest-neighbour hopping	69
5.2	Equal-spin triplet-pairing interaction	72
5.2.1	Mean-field Hamiltonian	72
5.2.2	Diagonalising the mean-field Hamiltonian	73
5.3	Self-consistency equations	76
5.3.1	Self-consistency equations - numerical results	77
5.3.2	Solving the self-consistent gap equation via the contour method	77
5.3.3	Solving the self-consistency equations iteratively	81
5.4	Free energy	85
5.5	Phase diagram	86
5.6	Quasi-particle spectrum	92
5.7	Spin imbalance	93
5.8	Summary	93
6	Magnetism in the equal-spin triplet-pairing theory	97
6.1	Normal state theory of the equal-spin attraction	97
6.2	Stoner theory	101
6.3	Hubbard extension	107
6.4	Summary	109
7	Using topological transitions to engineer quench-resilient wires	114
7.1	Introduction	114
7.2	The simplest quench model	116
7.3	Temperature dependent specific heat	117
7.4	Numerical method	119

7.5	Long term behaviour	121
7.6	Minimum quench model	122
7.7	Results	122
7.8	Conclusion	126
8	Summary	127
A	Diagonalising a Hamiltonian	133
A.1	Diagonalising a matrix	133
A.2	Obtaining the eigenvalues	134
A.3	Unitary Transformation Matrix	134
A.4	The diagonalised Hamiltonian	136
B	Non-unitary triplet-pairing diagonalisation transition matrix	137
C	Dimensionless equations	140
D	Forward in time centred in space algorithm	141
D.1	Technical details of the forward in time centred in space algorithm	141
D.2	Stability of the forward in time centred in space algorithm	142
	Bibliography	143

Todo list

List of Figures

1.1	Schematic of a common phase diagram for unconventional superconductors. . . .	4
2.1	Ginzburg-Landau free energy as a function of the complex order parameter Ψ . .	12
2.2	Tuning of the superconducting gap.	15
2.3	Different nodal structures and their specific heat temperature dependence exponents.	18
2.4	Schematics of the two main μ SR geometries.	19
2.5	Typical example of the spontaneous increase in relaxation rate due to broken TRS in μ SR experiments.	21
3.1	Evolution of LaNiC ₂ pairing states as SOC is adiabatically turned on.	24
3.2	Pressure-temperature phase diagram of LaNiC ₂	26
4.1	Definition of the hopping vector \mathbf{R}_{Δ_j}	33
4.2	Schematic of nearest neighbour hopping for deriving square lattice dispersion. . .	35
4.3	Non-interacting electron dispersion of a 2D square lattice with nearest neighbour hopping.	36
4.4	Fermi-Dirac distribution at different temperatures.	37
4.5	Solution to the BCS self-consistent gap equation.	48
4.6	Evolution of the mean-fields during the iterative process of solving all self-consistency equations.	49
4.7	Solutions of the self-consistency equations obtained by solving iteratively.	51
4.8	Free energy minimisation using the hill descent algorithm.	56
4.9	Comparison of self-consistent solutions obtained by the self-consistency equations and direct free energy minimisation.	58
4.10	Line of constant free energy at zero temperature.	59
4.11	The quasi-particle energy spectrum cut along along $k_x = k_y$	60
4.12	Temperature effect on the line of constant free energy.	60
5.1	Schematics of the allowed electron hopping for a given site.	67

5.2	Non-interacting electron dispersion for a two-dimensional square lattice with nearest neighbour hopping and anisotropic orbitals.	68
5.3	Non-interacting electron dispersion for a two-dimensional square lattice and anisotropic orbitals with nearest-neighbour intraband hopping and next-nearest-neighbour interband hopping.	70
5.4	Comparison between the nearest-neighbour 2D square lattice hopping model and the LaNiGa ₂ Fermi surface.	72
5.5	Solutions to the equal-spin triplet-pairing self-consistent gap equation.	79
5.6	Phase diagram obtained from the solutions of the self-consistent gap-equation only.	80
5.7	Examples of stationary points of the free energy.	82
5.8	Solutions to the self-consistency equations when solved iteratively.	84
5.9	Phase diagram obtained from solving the self-consistent solutions iteratively.	85
5.10	Comparison between the free energy minima obtained by direct hill descent minimisation and iteratively solving the self-consistency equations at finite bare splitting.	87
5.11	Stationary points and their corresponding free energies.	89
5.12	Minima of the free energy obtained by direct minimisation using the hill descent algorithm.	91
5.13	Phase diagram obtained by direct minimisation of the free energy using the hill descent algorithm.	92
5.14	Energy spectrum of the Bogoliubov quasi-particles.	94
6.1	Comparison between the normal state free energy interaction term with and without fixed total particle number.	99
6.2	Normal state free energy.	100
6.3	Normal state zero-temperature phase diagram.	101
6.4	Comparison between the Stoner theory free energy interaction term with and without fixed total particle number.	104
6.5	Stoner theory ground state free energy.	105
6.6	Stoner theory ground state phase diagram.	106
6.7	Normal state zero temperature particle density phase diagram of the equal-spin triplet-pairing theory with additional Hubbard repulsion term.	109
6.8	Normal state zero temperature magnetisation phase diagram of the equal-spin triplet-pairing theory with additional Hubbard repulsion term.	110
6.9	Normal state zero temperature phase diagram of the equal-spin triplet-pairing theory with additional Hubbard repulsion term.	111
7.1	Schematic of a superconductor quench.	115
7.2	Schematic of a general CICC and the simplified CICC model.	116
7.3	Specific heat of the superconductor. The green dotted line shows the linear Sommerfeld specific heat for normal metals. Our model for the nodal superconductors' specific heat is given by the blue dashed line (linear line nodes or shallow point nodes, exponent 2.0) and the red dot-dashed line (shallow line node, exponent 1.5). The specific heat is linear above T_c and a power law below. At low temperatures, a lower exponent gives a higher the specific heat. The jump in specific heat at T_c is fixed.	118

7.4	Comparison between the time evolution of the superconductor's temperature for different exponents.	120
7.5	Convergence test of the quench-fronts position with time for different lengths. . .	120
7.6	Time evolution of a quench.	123
7.7	Time evolution of the quench-front.	124
7.8	Convergence of the quench front with varying wire length.	125
7.9	Quench parameter space phase-diagram	125

List of Tables

2.1	The restrictions to pairing from spin orbit coupling and centre of inversion symmetry close to T_c	14
-----	--	----

Notes on units and numerics

Although this thesis is concerned with the topic of Physics, many of the results were obtained by computational/numerical methods. In order to maintain the focus on physics throughout the thesis, and not on technical details relating the numerics, a short discussion on the different software packages and unit conventions used throughout is presented here.

Units

It is not uncommon when performing numerical calculations of physical systems/equations to use rescaled or non-SI units. Doing so can lead to an improvement in numerical precision and a simplification of the equations. This of course does not affect the resulting general physics (for example whether or not magnetism or quenches occur) but will become important if one wants to compare the results to other areas of the literature.

In chapter 7 where we discuss quench prevention, different rescaled quench models are presented. In this case the details of the rescaled units are given in the chapter and additional detail can be found in appendix C.

In chapters 4 to 6 where we discuss variational mean-field theory and non-unitary triplet-pairing theory, the equations are presented in a standard way, however they are rescaled for all of the numerical calculations and all of the results obey the following convention: All energies are in units of the electron hopping energy, t . This of course includes the chemical potential, the interactions and the mean-fields. In addition, the free energy is also calculated per site. The temperature, T , is in units of t/k_B .

Numerics

A lot of the work carried out for this thesis made use of various computational techniques, programming languages and software packages. It is beyond the scope of this thesis to mention, or discuss in detail, exactly what language or package was used to code a particular algorithm or produce a particular figure. However, here I wish to acknowledge and cite the various programming languages and software packages that were used in one way or another to produce the work presented in this thesis.

- Python [2, 3] — Used for everything from coding quench simulations to solving equations, data processing and plotting.
- Fortran 90, specifically compiled via the GNU Fortran compiler (gfortran) [4] — Used for coding quench simulations and Monte Carlo integration routine.
- NumPy [5] — A fundamental package for scientific computing with python.

- SciPy Library [6] — A collection of Python packages/modules useful for scientific computing.
- Pandas [7] — A useful package for data storage and organisation.
- IPython [8] — An interactive Python command line.
- Jupyter notebook [9] — An extremely useful tool for incorporating and organising reproducible numerical results directly into a set of notes.
- F2PY: Fortran to Python interface generator [10] — Allowed the computationally intensive part of the quench simulation to be written in Fortran and called from within the Python simulation.
- Matplotlib [11] — A 2D plotting python library. Used to produce almost all 2D plots.
- Gnuplot [12] — A plotting/graphing program. Used for '3D' surface plots.

Chapter 1

Introduction

We will begin our introduction with a very brief historical overview of superconductivity, highlighting the most important advances in the field including those that are immediately relevant to this thesis.

Superconductivity [13, 14] was discovered in 1911 when Kamerlingh-Onnes discovered the resistivity of liquid mercury dropped suddenly to zero as it was cooled [15], making the superconductor a perfect conductor. A perfect conductor allows current to flow without any resistance or energy dissipation and will continue to flow endlessly. Such currents are known as *persistent currents*. Indeed, persistent currents set up in superconducting rings have been observed to remain constant over periods of years without any signs of dissipation with lower bounds on their duration set at over 100,000 years [16].

In 1933 superconductivity was revealed as a new phase of matter when Meissner and Ochsenfeld discovered that the magnetic flux from an externally applied magnetic field would be expelled from within a material in the superconducting state [17], an effect now called the Meissner (or Meissner-Ochsenfeld) effect. The Meissner effect identifies superconductivity as a state of matter because it is a thermal equilibrium property — it doesn't matter if the external field is applied in the normal state then cooled or if it is applied in the superconducting state, in either case the final state is the same with the magnetic field being expelled from the material.

In order to expel the magnetic field the superconductor must produce its own internal magnetic field to exactly cancel the externally applied magnetic field. Materials which generate their own magnetic fields to oppose externally applied fields are called diamagnets and those that oppose exactly the applied field are known as *perfect diamagnets* and have magnetic susceptibility $\chi = -1$. The Meissner effect requires superconductors be perfect diamagnets and does not arise from zero resistivity. Both effects therefore are used to identify a superconductor.

The first theory that made significant advances in describing superconductivity was the 1935 London theory by F. London and H. London [18]. The theory describes the superconductor as a mixture of normal electrons and superfluid electrons, similar to the two-fluid hydrodynamic description of superfluid ^4He , where the normal electrons have resistance and the superfluid electrons do not. Their theory predicts a number of correct results including the London equation (relating the current density inside a superconductor to the magnetic vector potential, later derived from the full Bardeen-Cooper-Schrieffer theory), the penetration depth (how far an external magnetic field can penetrate the superconductor) and the

Meissner effect.

Ginzburg and Landau introduced a phenomenological theory of superconductivity in 1950 which was able to predict and agree well with many experimental results, despite making no assumptions about the underlying microscopic details. Using Ginzburg-Landau theory, Abrikosov was able to show that depending on the size of the Ginzburg-Landau parameter κ , a superconductor would belong to one of two classes: type-I or type-II [19, 20].

In type-I superconductors the superconductivity can be destroyed by increasing an externally applied magnetic field beyond a critical value H_{c1} where the superconductor will undergo a first order transition into the normal state. In type-II superconductors there are two critical fields: $0 < H_{c1} < H_{c2}$. At fields below the lower critical field, H_{c1} , the superconductor fully expels magnetic field from the bulk of the entire sample. At stronger fields, $H_{c1} < H < H_{c2}$, the type-II superconductor will enter the mixed state, allowing some magnetic flux to penetrate while remaining superconducting. The amount of flux penetrating increases with the applied field. For applied fields larger than the upper critical field, H_{c2} , there is no diamagnetic response, superconductivity is fully suppressed and the system is in the normal state.

Abrikosov explained that the magnetic flux is able to penetrate the superconductor in the mixed state due to the creation of vortices — regions of small circulating supercurrent surrounding a normal state core which the applied flux can penetrate. The circulating supercurrent serves to screen the rest of the superconductor from the penetrating flux. Abrikosov also showed that many of these vortices would form into a periodic lattice throughout the superconductor, called the Abrikosov flux lattice, the density of which increases with applied field.

Also in 1950 came the discovery of the isotope effect, where the critical temperature of a superconductor was found to depend on its atomic mass: $T_c \propto M^{-\alpha}$ [21, 22, 23]. Early results indicated that $\alpha = 1/2$ [24] with some small variation, especially for lead Pb [25]. Nevertheless this was a key experimental result indicating that phonons play an important role in the phenomenon of superconductivity and helped develop the microscopic theory.

In 1957 Bardeen, Cooper, and Schrieffer [27, 26] (BCS) published their microscopic theory of superconductivity. They suggested that in superconductors there existed an effective attractive interaction between electrons due to the exchange of virtual phonons, and that under the effect of this attraction electrons would form bound state pairs. They argued that the superconducting state would be made up of a macroscopic number of electron pairs in a coherent state, that is the wave function of the system has a well defined phase but an ill-defined, yet macroscopic, number of particles. This was soon realised to be correct as it successfully explained many experimental phenomena, the two most significant being the prediction of the isotope effect exponent $\alpha = 1/2$ and the existence of the fixed ratio between the energy gap at zero temperature and the critical temperature: $\Delta_0 = 1.76k_B T_c$. These two quantities are independent of material specific properties like the band structure and result from the fundamental aspects of the theory: weak coupling of electrons via phonons and the instability of the Fermi surface to attractive interactions. The fact that nearly all of the superconductors at the time agreed very well with these quantities showed that BCS theory was fundamentally correct.

Soon after the publication of BCS theory, both Bogoliubov [28] and Valatin [29] independently showed that a canonical transformation method could be used to formulate BCS theory

in terms of quasi-particle excitations, greatly simplifying the calculations compared to the original BCS wave function method [30]. Further advances came when Gor'kov reformulated BCS theory in the language of quantum field theory and Green's functions, which allowed the description of superconductors beyond the weak coupling limit assumed in BCS [20, 31] and further confirmation of BCS theory came when Gor'kov was able to derive Ginzburg-Landau theory from the microscopic BCS theory [32].

In 1952 Matthias discovered the first “new class” of superconductors in CoSi_2 [33, 34], the first superconductor to be made of two non-superconducting elements: ferromagnetic Co and semiconductor Si. Shortly afterwards Hardy and Hulm [35] discovered the “A15” family of superconductors, who have the A_3B structure where A is a transition metal. This family managed to push the critical temperature up to a record breaking 22.3 K in Nb_3Ge [36] in 1973. Even more significantly, they had high critical currents even in the presence of strong external magnetic fields [37], making them particularly useful for practical applications.

In 1979 Steglich *et al.* [38] discovered superconductivity in CeCu_2Si_2 , the first in the class of “heavy fermion” superconductors and the first “unconventional” superconductor (i.e. that could not be explained by BCS theory). Superconductors in this class have a magnetic (often antiferromagnetic) ground state and significant many-body interactions leading to the renormalisation, and great enhancement, of the electron mass. In 2001 the Ce-based heavy fermion with the highest T_c , CeCoIn_5 , was found [39] and in 2004 the first noncentrosymmetric heavy fermion superconductor, CePt_3Si , was discovered [40].

Although CeCu_2Si_2 and other heavy fermions are superconducting at ambient pressure, there exists those that are non-superconducting antiferromagnets at ambient pressure which become superconducting as pressure is increased and antiferromagnetism is suppressed. CeRhIn_5 exhibits a first order transition from an antiferromagnetic to superconducting state as pressure is increased [41] while CePd_2Si_2 and CeIn_3 show the antiferromagnetism being suppressed to a quantum critical point as pressure is increased with a superconducting dome appearing around it [42]. Indeed it appears that a superconducting dome surrounding a quantum critical point has become a typical feature of the phase diagrams of the heavy fermions as can be seen in e.g. CePd_2Si_2 , CeIn_3 , $\text{CeCu}_2(\text{Si}_{1-x}\text{Ge}_x)$, $\text{Ce}(\text{Rh,Ir,Co})\text{In}_5$ and UGe_2 , see section IV C of [43] and references therein. Figure 1.1 shows a schematic of a common phase diagram seen in unconventional superconductors.

In 1986 Bednorz and Müller [44] discovered superconductivity in the ceramic compound $\text{Ba}_x\text{La}_{5-x}\text{Cu}_5\text{O}_{5(3-y)}$, the first in the class of “cuprate” superconductors. This was fascinating not only because ceramics were usually insulators and were therefore, by definition, terrible conductors let alone superconductors, but also because this superconductor had a T_c of 30 K, the highest of any superconductor at the time. Shortly afterwards, Wu *et al.* [45] discovered superconductivity in $\text{YBa}_2\text{Cu}_3\text{O}_{7-\delta}$ with $T_c = 93$ K, a significant milestone as this was the first superconductor with a critical temperature higher than the boiling point of liquid Nitrogen $T_c > 77$ K which was much more readily available than the liquid Helium required previously. Since then there has been intense research into achieving ever higher T_c 's in this class of materials in search of the holy grail of room temperature superconductivity, with the highest critical temperature achieved so far being $T_c = 135$ K at ambient pressure [46] and $T_c = 164$ K at 31 GPa [47] in a Hg-Ba-Ca-Cu-O compound.

The cuprates, like the heavy fermions, have some common features that suggest they belong to their own separate class of unconventional superconductivity. Like the heavy fermions

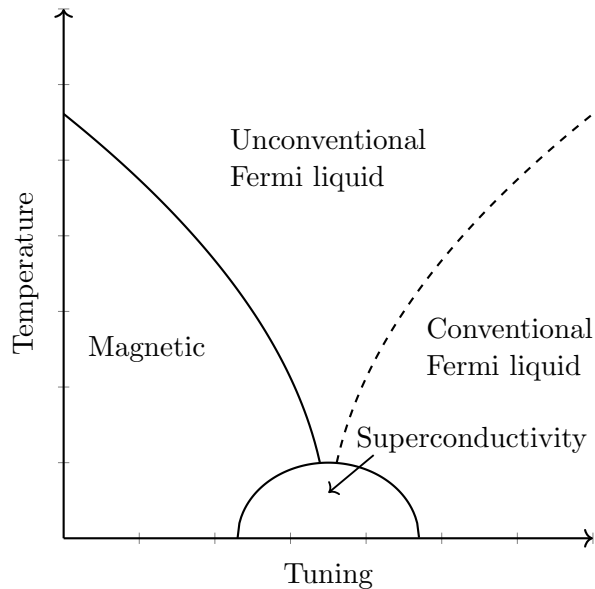


Figure 1.1: Schematic of a common phase diagram for unconventional superconductors. There is a magnetic state which is suppressed by tuning (example by pressure or doping) towards a quantum critical point. A dome of superconductivity emerges around the quantum critical point. Outside of the magnetic and superconducting regions exists the normal state, further separated by a crossover into an unconventional and conventional Fermi liquid state. Adapted from Ref. [42]

the phase diagram as a function of both electron and hole doping contains a dome of superconductivity surrounding what looks like a quantum critical point. While in these systems the superconducting dome appears near to, or coincides with, an antiferromagnetic phase, the quantum critical point corresponds to a pseudogap phase rather than the antiferromagnetic phase, see [48, 49]. Additional signs of unconventional superconductivity come from ARPES [50] and other techniques which heavily suggest that the nature of the pairing state is d-wave, as well as from the isotope effect (or lack thereof) suggesting that electron-phonon mediated pairing is not critical in these compounds (although it may be present and could enhance the superconductivity), see [48] and references therein.

Another significant milestone of direct relevance to this thesis is the detection of spontaneously broken time reversal symmetry (TRS) in the superconducting state, most notably discovered in UPt_3 [51] and Sr_2RuO_4 [52] by muon spin rotation/relaxation (μSR) experiments, later confirmed in both materials by measurements of the Kerr effect [53, 54]. Both techniques are sensitive to very small local magnetic moments and unambiguously determine whether time reversal symmetry is broken or not; something which is useful in determining the possible symmetry-allowed pairing states. Indeed μSR was used to determine broken time reversal symmetry in two compounds LaNiC_2 [55] and LaNiGa_2 [56] from which symmetry analysis concludes the pairing must be unconventional. Beforehand these compounds had appeared to be normal BCS superconductors. We will discuss these two compounds in detail in chapter 3.

In 2008 Kamihara *et al.* [57] discovered superconductivity at $T_c = 26$ K in $\text{LaFeAsO}_{1-x}\text{F}_x$, the first in a new class of iron-based superconductors. The iron-based superconductors (often called ‘iron pnictides’ or just ‘pnictides’) contain superconducting layers of iron and a pnictide and, crucially, the superconductivity in the iron based superconductors specifically involves the iron 3d electrons; simply having iron in a superconducting compound does not make an

iron based superconductor [48]. Like the cuprates the iron based superconductors are strongly dependent on doping, with a similar phase diagram showing antiferromagnetic suppression with electron or hole doping leading to a superconducting dome [58]. The pairing state is much less certain than in the cuprates but it is definitely *not* standard BCS s-wave pairing and is unconventional [48].

Recently the mathematical subject of topology has attracted significant interest in the condensed matter physics community since the theoretical discovery of the Z_2 topological quantum spin Hall insulator [59, 60, 61]. It offers an alternative view of phase transitions rather than the usual Ginzburg-Landau symmetry-based point of view and has been used to explain phenomena such as topological insulators [61], Lifshitz transitions [62] and Majorana fermions [63] (of particular interest recently due to potential application to quantum computing [64]). We will focus more on the topic of topological transitions in superconductors in chapter 2 and their potential applications in chapter 7.

To finish our historical overview of superconductivity it is interesting to note the recent discovery of record breaking superconductivity in hydrogen sulphide with $T_c = 203$ K, despite being a conventional BCS superconductor (albeit at extreme pressures of around 150 GPa) [65]. The fact that even the conventional ‘solved’ problem of BCS superconductivity is still exciting the community, let alone the numerous unconventional systems we have discussed (and many more we haven’t) is a testament to how fascinating and important the phenomenon of superconductivity is.

As was mentioned above, superconductivity can be divided into two categories: conventional and unconventional. Conventional superconductors are generally well explained by BCS theory, or its extension Eliashberg theory [66] (where the retarded nature of the phonon interaction is properly taken into account), where it is accepted that the electron pairing is mediated by phonon exchange, the Cooper pairs form singlet states [67] and experiments agree well with theory. Many elemental superconductors, alloys and simple compounds fall into this category [67, 68]. Unconventional superconductivity on the other hand can not be understood with BCS theory, possibly because the pairing is not mediated by electron-phonon interactions or because symmetries other than $U(1)$ gauge symmetry are broken upon entering the superconducting state. Some common examples of unconventional superconductors include the heavy fermions, the high- T_c cuprates, the Iron based superconductors and Sr_2RuO_4 [48]. In this thesis, we will focus on unconventional superconductivity in TRS breaking $LaNiC_2$ and $LaNiGa_2$ (chapters 3 and 5) as well as tuneable topological superconductors, or more specifically, a potential application of such superconductors (chapter 7).

Finally, let us describe the organisation of the rest of this thesis. Chapter 2 introduces some basic concepts of BCS theory including electron pairing, the concept of the pairing potential and the types of pairing that can occur in conventional and unconventional superconductors. Then the topic of broken symmetry will be discussed and we shall see that unconventional superconductivity can result in the breaking of extra symmetries, specifically broken time reversal symmetry (TRS) and centre of inversion symmetry. The concept of group-theory/symmetry-analysis in the context of superconductors will be introduced. Topology in condensed matter will then be discussed with particular emphasis on the topology associated with different gap structures and the topological transition. Returning to the topic of symmetry, we will see how noncentrosymmetric superconductors can give rise to a pairing potential which is an admixture of singlet and triplet pairing. Finally we shall discuss

some of the experimental techniques involved in determining the gap structure and detecting the breaking of TRS.

In chapter 3 we shall focus on two particularly interesting Ni-based unconventional superconductors that break TRS, namely noncentrosymmetric LaNiC_2 and its centrosymmetric cousin LaNiGa_2 . We will start by reviewing the literature available for both materials and see that there are largely two conflicting viewpoints, with some works finding evidence of unconventional superconductivity while others find evidence of conventional. We shall see that on balance these materials are unconventional and shall discuss a new equal-spin triplet-pairing theory that has been proposed to unify the conflicting results of LaNiGa_2 . We shall investigate this theory further in chapter 5.

Chapter 4 is a more technical chapter with a primarily pedagogical purpose. In it we will demonstrate the application of variational mean-field theory to the well known case of conventional s-wave pairing. In doing so we will learn the necessary techniques and obtain some of the classic results from BCS theory before investigating the equal-spin triplet-pairing theory. Moreover, we will be able to confirm the BCS-like limit of the equal-spin pairing theory with the results obtained in this chapter.

We will then, in chapter 5, apply the variational mean-field method to the equal-spin triplet-pairing theory. We shall derive and solve both the self-consistency equations and the free energy and see that the self-consistency equations can not always be relied upon to find the minimum points in the free energy. By minimising the free energy we will show that this *triplet*-pairing theory gives rise to gapless superconductivity, re-entrant superconductivity and two *nodeless* gaps. However, as we shall see, these gaps are of equal magnitude (making the theory *unitary*) and, furthermore, this theory has no magnetic state. Therefore this theory cannot describe LaNiGa_2 .

In chapter 6 we investigate further the absence of magnetisation in the equal-spin triplet-pairing theory. We investigate the normal state limit of the theory and find that, unexpectedly, it too displays no magnetisation. Comparing with the Stoner theory of ferromagnetism (which was thought to have a similar mechanism for magnetism) we identify the crucial difference that gives rise to magnetism. We suggest an additional Hubbard repulsive interaction to the equal-spin triplet-pairing theory and find that with this addition, magnetisation manifests in the normal state zero temperature phase diagram. We predict that the addition of the repulsive Hubbard interaction will allow for a superconducting state with spontaneous net magnetisation and two *different* sized gaps, making the pairing *non-unitary* and, therefore, could explain the results of LaNiGa_2 .

Finally, in chapter 7, we consider again the topic of topological transitions in noncentrosymmetric superconductors. In particular, we ask whether the enhancement of specific heat associated with such topological transitions could have potential application to the engineering problem of superconductor quench prevention. We shall attempt to answer this question by performing numerical studies of a superconductor quench and show that the enhanced specific heat of the topological transition state can increase the quench resilience of a superconductor, although the effect is small.

Chapter 2

Background

This chapter focuses on the fundamental microscopic aspects of superconductivity; first describing the pairing of electrons and the types of electron pairing that can occur, then discussing the concept of the pairing potential. The possibility of breaking multiple additional symmetries will be discussed, the concept of group theory will be introduced and its application to superconductivity will be discussed. There will be a focus on noncentrosymmetric superconductors and how this particular lack of symmetry can lead to superconductivity with mixed pairing and topological transitions. Finally there will be some discussion of the experimental probes used to investigate superconductivity.

2.1 Introduction to BCS theory

Superconductivity is a phase of matter that is identified by two key phenomena: zero resistivity and the Meissner-Ochsenfeld effect. Zero resistivity or, equivalently, perfect conductance leads to the phenomenon of flux trapping and persistent currents while the Meissner-Ochsenfeld effect is where magnetic fields from the interior of the superconductor are expelled. Together these two effects signify a superconducting phase.

In 1957 Bardeen, Cooper, and Schrieffer [26] (BCS) published their microscopic theory of superconductivity. It described how an effective attraction between electrons, arising from the exchange of virtual phonons, can lead to pairs of electrons forming bound states (now called “Cooper” pairs). The wave function of the system is then written as a *coherent state* of these Cooper pairs, where there is a well defined global phase angle but an ill-defined total number of pairs [13]. The system contains a macroscopic number of these pairs with the same phase and total momentum, like a Bose-Einstein condensate (BEC) but formed from different combinations of available \mathbf{k} -states, rather than with all electrons being in the same state.

The first problem is how electrons can be attracted to each other, since such an attraction would have to overcome the Coulomb repulsion. While this is true for bare electrons, electrons in a metal are screened due to their interaction with each other, for example the Thomas Fermi screening model gives the Coulomb interaction as

$$V(\mathbf{r} - \mathbf{r}') = \frac{e^2}{4\pi\epsilon_0|\mathbf{r} - \mathbf{r}'|} e^{-|\mathbf{r}-\mathbf{r}'|/r_0}$$

where r_0 is the Thomas Fermi screening length [13]. This additional exponential factor makes the interaction much shorter range than original bare electron Coulomb repulsion.

Works by Fröhlich [69] and Bardeen and Pines [70] had suggested that the attractive interaction responsible for the pairing of electrons was due to phonons; an idea which was supported by the experimental observation of the “isotope effect” [22, 21] whereby a superconductors’ critical temperature depends on its atomic mass, $T_c \propto M^\alpha$.

BCS used a simplified form of the effective electron-electron interaction caused by phonon exchange [13]

$$V(\mathbf{q}, \omega) = |g_{\text{eff}}|^2 \frac{1}{\omega^2 - \omega_D^2}, \quad (2.1)$$

where the scattering amplitude is assumed constant, g_{eff} , making the effective interaction independent of the phonon momentum \mathbf{q} . The effective interaction is attractive for phonon frequencies below the Debye frequency, ω_D . Realising the repulsive part isn’t important for superconductivity, BCS further assumed that pairing only happens between electrons with energies $\pm k_B T$ of the Fermi energy, such that their energies are well below $\hbar\omega_D$ and within the attractive regime of the effective interaction. They further assumed that within this attractive regime, all electrons experience the same constant value of attraction, V . The final form of the BCS interaction then becomes

$$V(\mathbf{q}, \omega) = \begin{cases} -V & |\omega| < \omega_D \\ 0 & \text{otherwise} \end{cases}. \quad (2.2)$$

Using the BCS effective interaction, equation (2.2), Cooper [71] was able to show that two electrons outside a *filled* Fermi sea would form a bound state, thereby lowering the energy of the system by an amount Δ (the binding energy of the pair), even for arbitrarily weak attraction. This is surprising as an attractive interaction between two free electrons does not lead to a bound state [13]. The filled Fermi sea and the Pauli exclusion principle forces the pairing electrons to exist on the edge of the Fermi sea, near the Fermi surface where they can experience the attractive interaction and hence is necessary for the formation of Cooper pairs.

The concept of the electron/Cooper pair is critical to superconductivity as they allow the Boson-like behaviour of electrons, allowing a macroscopic number of pairs to occupy the same quantum state, even though their constituent particles are Fermions. The pair wave function takes the form [13]

$$\Psi(\mathbf{r}_1, \sigma_1, \mathbf{r}_2, \sigma_2) = e^{i\mathbf{k}_{\text{cm}} \cdot \mathbf{R}_{\text{cm}}} \varphi(\mathbf{r}_1 - \mathbf{r}_2) \phi_{\sigma_1, \sigma_2}, \quad (2.3)$$

where $\mathbf{R}_{\text{cm}} = (\mathbf{r}_1 + \mathbf{r}_2)/2$ is the centre of mass and $\mathbf{k}_{\text{cm}} = \mathbf{k}_1 + \mathbf{k}_2$ is the total momentum of the pair. The pair wave function is decomposed into the product of two separate wave functions; one for the spin, $\phi_{\sigma_1, \sigma_2}$, and one for position, $\varphi(\mathbf{r}_1 - \mathbf{r}_2)$. Fermion antisymmetry means the wave function of the pair must change sign under the exchange of two particles i.e. $\Psi(\mathbf{r}_1, \sigma_1, \mathbf{r}_2, \sigma_2) = -\Psi(\mathbf{r}_2, \sigma_2, \mathbf{r}_1, \sigma_1)$.

The spin wave function may take the following forms

$$\phi_{\sigma_1, \sigma_2} = \begin{cases} \frac{1}{\sqrt{2}}(|\uparrow\downarrow\rangle - |\downarrow\uparrow\rangle) & \text{singlet} \\ \frac{1}{\sqrt{2}}(|\uparrow\downarrow\rangle + |\downarrow\uparrow\rangle) & \text{triplet} \\ |\uparrow\uparrow\rangle & \text{triplet} \\ |\downarrow\downarrow\rangle & \text{triplet} \end{cases}, \quad (2.4)$$

where the singlet state is odd under the exchange of particles and the triplet state even, requiring that the spatial wave function be even and odd respectively in order to maintain Fermion antisymmetry. Cooper [71] found that the binding energy of the pair was largest if the pair formed a singlet state with total momentum $\mathbf{k}_{\text{cm}} = 0$ and so in BCS theory it is assumed that the electrons form singlet pairs between time reversed electron states $\mathbf{k} \uparrow$ and $-\mathbf{k} \downarrow$.

BCS realised that with an attractive interaction all of the electrons near the Fermi surface would form these Cooper pairs. It was therefore necessary to write down a many-body wave function composed of these pairs. Schrieffer [26] did this by writing down a coherent state of Cooper pairs that satisfied the Pauli exclusion principle, which led to the final BCS state

$$|\Psi_{\text{BCS}}\rangle = \prod_{\mathbf{k}} \left(u_{\mathbf{k}}^* + v_{\mathbf{k}}^* \hat{P}_{\mathbf{k}}^\dagger \right) |0\rangle. \quad (2.5)$$

Here the pair operator, $\hat{P}_{\mathbf{k}}^\dagger = \hat{c}_{\mathbf{k}\uparrow}^\dagger \hat{c}_{-\mathbf{k}\downarrow}^\dagger$, creates a pair of electrons with time reversed electron states (a Cooper pair). The amplitudes $u_{\mathbf{k}}^*$ and $v_{\mathbf{k}}^*$ are given by

$$u_{\mathbf{k}}^* = \frac{1}{(1 + |\alpha_{\mathbf{k}}|^2)^{\frac{1}{2}}} \quad (2.6)$$

$$v_{\mathbf{k}}^* = \frac{1}{(1 - |\alpha_{\mathbf{k}}|^2)^{\frac{1}{2}}} \quad (2.7)$$

and depend on the complex parameter $\alpha_{\mathbf{k}}$, which are the arbitrary complex numbers introduced by forming the coherent state that can be adjusted to minimise the total energy [13]. This wave function adds pairs of electrons to the vacuum, $|0\rangle$, and hence is not number conserving, instead the wave function adopts a well defined phase θ for the complex parameters $\alpha = |\alpha|e^{i\theta}$ and hence the BCS wave function is a coherent state. The free energy is invariant under the choice of phase and so when the system adopts a phase angle θ it is said to have broken gauge-symmetry [13].

BCS were able to use the system wave function of cooper pairs to calculate the thermodynamic, electro-dynamic, transport and non-equilibrium properties of the model [30, 26]. Perhaps the two most significant results are the predictions of the isotope effect's exponent $T_c \propto M^{-1/2}$ and the fixed ratio of the low temperature energy gap Δ_0 to the critical temperature T_c : $\Delta_0 = 1.76k_B T_c$. Each of these arise from fundamental aspects of BCS theory, namely: that the attraction between electrons is due to lattice vibrations (phonons) and that the Fermi surface is unstable to the attractive interaction between electrons.

The isotope effect is predicted by a result of BCS theory in which the relation for T_c is given by: $k_B T_c = -1.14\hbar\omega_D \exp(-1/N(0)V)$ [14]. Here the Debye frequency is $\omega_D \propto M^{-1/2}$. The Debye frequency appears in the theory as a direct consequence of including the electron-phonon interaction equation (2.1). The fact that the Fermi surface is unstable to arbitrarily small attractive interaction is what gives rise to the energy gap. The electrons form bound states in the presence of said attraction and require an energy of 2Δ to break a pair apart and create an excitation. The larger the energy gap the greater the energy required to break the pair and kill superconductivity, so it follows that higher energy gap would give rise to a higher T_c . The fact that both of these predictions fit experimental results with good agreement shows that the underlying physics being described by the theory is correct i.e. weak electron-phonon interaction giving rise to an attractive interaction to which the Fermi surface is unstable, resulting in the formation of electron pair bound states.

2.2 Pairing potential

In a mean-field treatment of a BCS-like theory a mean-field, $\Delta_{\sigma_1, \sigma_2}(\mathbf{k})$, is introduced which couples to the expectation value of creating a pair, $\langle \hat{c}_{\mathbf{k}\sigma_1}^\dagger \hat{c}_{\mathbf{k}\sigma_2}^\dagger \rangle$, and is often referred to as the pairing potential [72]. Roughly speaking this term quantifies “how much” or “how strong” the pairing between electrons, and therefore the superconductivity, is. This term acts as the order parameter for the superconducting state and is zero above T_c when there is no pairing or superconductivity and finite below. In the BCS case, where pairing occurs between time-reversed states due to the simple BCS effective interaction equation (2.2), the pairing potential is finite below T_c and isotropic in momentum space. In this case the energy gap that arises in the quasi-particle excitation spectrum is given by the mean-field/pairing potential Δ , hence Δ is also usually referred to as the gap¹.

The pairing potentials enter the Hamiltonian in the form of a gap matrix [72]

$$\hat{\Delta}(\mathbf{k}) = \begin{pmatrix} \Delta_{\uparrow\uparrow}(\mathbf{k}) & \Delta_{\uparrow\downarrow}(\mathbf{k}) \\ \Delta_{\downarrow\uparrow}(\mathbf{k}) & \Delta_{\downarrow\downarrow}(\mathbf{k}) \end{pmatrix}, \quad (2.8)$$

whose components correspond to pairing potentials between different combinations of spins. The matrix $\hat{\Delta}(\mathbf{k})$ must have the same symmetry as the pairing wave function in momentum space [72] and so requires $\hat{\Delta}(\mathbf{k}) = -\hat{\Delta}^T(-\mathbf{k})$ to maintain Fermion antisymmetry.

In the case of a spin singlet state (antisymmetric) the pair wave function must be symmetric in momentum space and in the case of spin triplet (symmetric) the pair wave function must be antisymmetric. The gap matrix must then also be symmetric and antisymmetric for spin singlet and spin triplet states respectively. A common form of these gap matrices is given by

$$\hat{\Delta}(\mathbf{k})^{\text{singlet}} = i\hat{\sigma}_y \Delta_0(\mathbf{k}) = \begin{pmatrix} 0 & \Delta_0(\mathbf{k}) \\ \Delta_0(\mathbf{k}) & 0 \end{pmatrix} \quad (2.9)$$

$$\hat{\Delta}(\mathbf{k})^{\text{triplet}} = i(\mathbf{d}(\mathbf{k}) \cdot \hat{\boldsymbol{\sigma}})\hat{\sigma}_y = \begin{pmatrix} -d_x(\mathbf{k}) + id_y(\mathbf{k}) & d_z(\mathbf{k}) \\ d_z(\mathbf{k}) & d_x(\mathbf{k}) + id_y(\mathbf{k}) \end{pmatrix} \quad (2.10)$$

where $\Delta_0(\mathbf{k})$ and $\mathbf{d}(\mathbf{k})$ are symmetric and antisymmetric (vectorial) functions of \mathbf{k} respectively [72] and $\hat{\boldsymbol{\sigma}}$ is a vector whose components are the Pauli matrices $\hat{\sigma}_x$, $\hat{\sigma}_y$ and $\hat{\sigma}_z$. This notation is especially useful when carrying out group-theoretical analysis as the \mathbf{d} -vector transforms like a 3D vector under rotation when carrying out spin rotation operations.

The triplet gap matrix can be further classified as *unitary* if $\hat{\Delta}(\mathbf{k})\hat{\Delta}(\mathbf{k})^\dagger \propto \mathbf{I}$ (where \mathbf{I} is the identity matrix) or *non-unitary* otherwise². The triplet pairing gap matrix gives [72]

$$\hat{\Delta}(\mathbf{k})\hat{\Delta}(\mathbf{k})^\dagger = |\mathbf{d}|^2 \mathbf{I} + \mathbf{q}(\mathbf{k}) \cdot \hat{\boldsymbol{\sigma}} \quad (2.11)$$

where $\mathbf{q}(\mathbf{k}) = i(\mathbf{d}(\mathbf{k}) \times \mathbf{d}^*(\mathbf{k}))$. The \mathbf{q} -vector is only non zero (hence the gap matrix is only non-unitary) when $\mathbf{d}(\mathbf{k}) \neq \mathbf{d}^*(\mathbf{k})$. The physical meaning of a finite \mathbf{q} -vector is that the structure of the pairing is different for \uparrow - and \downarrow -spins which occurs only when time reversal symmetry is broken [72]. We shall now discuss the concept of symmetry in superconductors.

¹In general the mean-field Δ may not give the energy gap, e.g. in gapless superconductors where the mean-field order parameter Δ is finite but the quasi-particle energy spectrum is ungapped.

²It is trivial to show that the singlet gap matrix is always unitary by performing the matrix multiplication $\hat{\Delta}(\mathbf{k})^{\text{singlet}} \hat{\Delta}(\mathbf{k})^{\text{singlet}\dagger}$

2.3 Broken symmetry

Another highly successful theory which explains superconductivity phenomenologically is that of Ginzburg and Landau [73]. Being a phenomenological theory it is not concerned with microscopic details such as the formation of electron pairs or what mechanism might lead to such a pairing. Instead it focuses on the phase transition from a thermodynamic point of view, using Landau's theory of second order phase transitions [74] to describe superconductivity.

Landau observed that second order phase transitions typically involve some change in the symmetry of the system and capture this change in symmetry with an appropriate physical quantity called the order parameter. The superconducting phase transition is characterised by a complex order parameter Ψ which is zero in the normal state above T_c and finite below in the superconducting state. In the case of a magnet transitioning through the Curie temperature the magnetisation \mathbf{M} is an appropriate order parameter to describe the phase transition, while in the case of a superconductor Δ plays the role of the order parameter (up to some constant numerical factors) [13]. At the time of course, being some 7 years before the publication of BCS theory, Ginzburg and Landau didn't know that their order parameter Ψ corresponded to the pairing potential Δ , they simply assumed that there must exist some physical quantity which classified the state of the system. It was later that Gor'kov was able to show that Ginzburg-Landau theory could be derived from BCS theory [32].

The free energy of the superconductor is expanded in powers of Ψ :

$$f_s(T) = f_n(T) + a(T)|\Psi|^2 + b(T)|\Psi|^4 + \dots \quad (2.12)$$

where $f_s(T)$ and $f_n(T)$ are the free energy of the superconducting and normal state respectively. $a(T)$ and $b(T)$ are phenomenological parameters of the Ginzburg-Landau theory that vary smoothly with temperature [13]. The expansion is valid for small values of the order parameter and hence Ginzburg-Landau is valid close to T_c (where the order parameter has only just become finite). In the normal state both $a(T)$ and $b(T)$ are positive and the free energy is minimised at $\Psi = 0$. At the transition $a(T)$ goes from positive to negative such that the free energy is minimised by finite Ψ .

Ψ is in general complex but the free energy is real; the minimum of the free energy is a circle with an infinite number of solutions, each with a different phase. Upon entering the superconducting state the order parameter selects a single point with a random phase from the possible minima of the free energy. By selecting a phase the system breaks gauge symmetry, see figure 2.1. Indeed, superconductivity is described by a coherent wave function of Cooper pairs, meaning that all Cooper pairs have the same well defined phase but ill-defined (although macroscopic) number of particles. When the pair potential Δ becomes finite the superconducting pairs are created and adopt a fixed global phase, breaking gauge symmetry as in Ginzburg-Landau theory.

In the case of a ferromagnetic transition, the breaking of the rotational symmetry of the system by all the spins aligning in a common direction is intuitively understood by the experimental observation of a net magnetic field. The breaking of gauge symmetry on the other hand is not so intuitive, however, there is a measurable physical consequence: the Josephson effect [75]. Cooper pairs are able to tunnel between two superconductors in close proximity, giving rise to a supercurrent density $J = J_1 \sin(\phi_1 - \phi_2)$, where J_1 is a constant and ϕ_1 and ϕ_2 are the global phases of the two superconductors [76]. The fact that the superconductor breaks gauge symmetry by selecting a global phase allows for a measurable

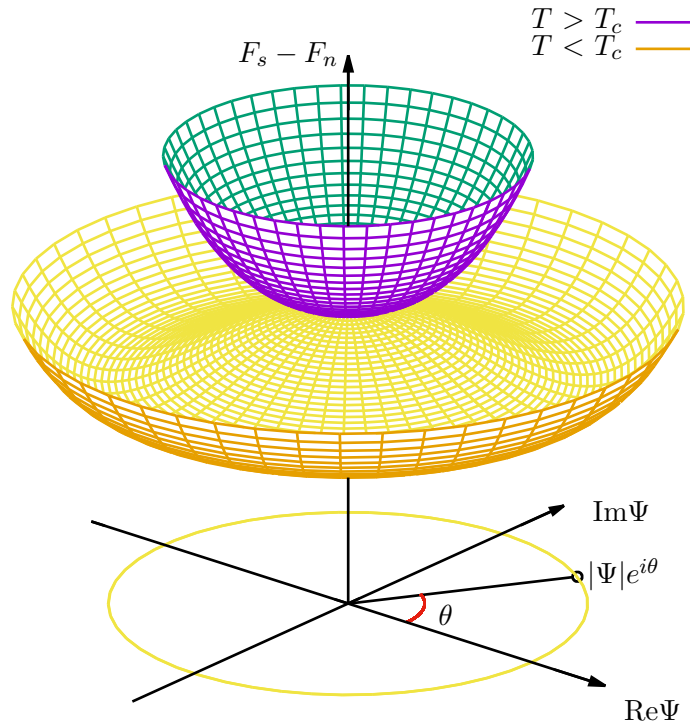


Figure 2.1: Ginzburg-Landau free energy as a function of the complex order parameter Ψ . In the normal state above T_c the free energy is minimised at $|\Psi| = 0$. In the superconducting state below T_c the free energy minimum is given by a circle of infinite solutions, all with the same $|\Psi|$ but with different phase θ . The superconductor spontaneously selects a single point on this circle and hence has a well defined phase θ .

effect that is well understood theoretically and has been experimentally verified [77]. Indeed, the Josephson effect is used in the definition of the standard volt [78] and one of the most accurate magnetometers: SQUID (Superconducting QUantum Interference Device).

The usual general symmetry group of the normal state of superconductors is given by [79]:

$$G = \text{SO}(3) \times G_c \times \text{U}(1) \times \text{T} \quad (2.13)$$

where $\text{SO}(3)$ is the group of rotations in spin space, G_c is the group of symmetry operations of the crystal, $\text{U}(1)$ is gauge symmetry and T is time reversal symmetry. As we have just discussed, upon entering the superconducting state, the system will spontaneously choose a global phase and break gauge symmetry. It is in principle also possible for superconductors to break additional symmetries upon entering the superconducting phase, such superconductors are classed as *unconventional*³ superconductors. For instance, one might imagine a superconducting transition which occurs at a structural transition, or with some exotic ordering, that could break some crystal or point group symmetries; or there could be some spontaneous magnetisation which would break TRS.

A powerful result from very general group-theoretical arguments is that *all* the possible order parameters of a second-order superconducting transition, and their dimensionalities, can be classified by considering the different irreducible representations (irreps) of the

³The breaking of additional symmetries is not a requirement for a superconductor to be classed as unconventional; any superconductor that cannot be well explained by BCS theory or its extensions e.g. Eliashberg theory would also be classified as such.

symmetry group [79]. The irreps are properties of the symmetry group and represent all the possible ways that functions can evolve under the symmetries of the group. By finding the gap functions corresponding to each irrep one obtains the possible symmetry-allowed order parameters of the system. Such a procedure is largely independent of microscopic details, and as such can be used to investigate superconductivity that differs from a conventional BCS description where microscopic details, such as the pairing mechanism, may be unknown.

Of particular relevance to us is the absence of time reversal symmetry and/or centre of inversion symmetry. Magnetic ordering breaks TRS and is often a sign of unconventional superconductivity, see for example the heavy fermion UPt₃ [51], Sr₂RuO₄ [52] and LaNiC₂ and LaNiGa₂ which we shall discuss in chapter 3. The lack of a centre of inversion in a superconductor can also lead to unconventional superconductivity and the interesting phenomenon of topological transitions. Before we discuss noncentrosymmetric superconductors further let us first visit the concept of topology.

2.4 Topology in superconductors

In addition to the Ginzburg-Landau view of phase transitions there is also the topological view point, where the focus is on changes in topology rather than changes of symmetry. From this view point a host of phenomena can be described, from topological insulators to Lifshitz transitions to Majorana fermions [61, 62, 80], none of which can be understood purely from a symmetry point of view.

Two Hamiltonians which can be continuously adiabatically transformed into each other are topologically equivalent. This means there is some well defined quantity, called a topological invariant (or topological charge/number), which remains constant throughout the adiabatic transformation. These topological quantities can be used to define different states of a system, with different states having different values of the topological invariant. Furthermore these topological invariants may offer topological protection — a kind of robustness to perturbations which prevents small perturbations changing the state of the system if it would also require changing the value of the topological invariant.

A *topological transition* is when a system changes between two states with different topological charge values. In the case of topological protection such transitions usually require closing of the energy gap which causes the topological quantity to become ill-defined thus losing topological protection, or the cancelling of topological charges which leaves a topologically trivial unprotected state [62]. These transitions need not be accompanied by a change in the systems symmetry group and therefore are not considered typical phase transitions in the Landau sense.

Topological phases can occur in superconductors where different quantum ground states are identified with different topological invariants [81]. We will focus our discussion on the topological node-reconstruction transition [82, 83], where nodal lines on the Fermi surface form, cross or reconstruct as some tuning parameter (e.g. platinum doping in the Li₂Pd_{3-x}Pt_xB compounds [84, 85, 86, 87]) is changed, changing the associated topological number [82, 88, 89]. In this case the associated topological number is the number of nodal lines on the Fermi surface which can only change by multiples of two [88]. When the topological number changes it does so by going through a nodal-reconstruction transition where the nodal lines cross simultaneously such that the topological number becomes ill-defined.

	Weak SOC	Strong SOC
CS	singlet or triplet	singlet or triplet
NCS	singlet or triplet	admixture - singlet and triplet

Table 2.1: The restrictions to pairing from spin orbit coupling and centre of inversion symmetry close to T_c . The strong spin orbit coupling (SOC) leads to a mixed pairing state in noncentrosymmetric (NCS) superconductors due to the reduction of the symmetry group. In centrosymmetric (CS) superconductors the pairing can never be mixed.

It is possible to tune the topology in the $\text{Li}_2\text{Pd}_{3-x}\text{Pt}_x\text{B}$ compounds because they are *noncentrosymmetric*. We will now discuss noncentrosymmetric superconductors and see how this topological tuning is possible.

2.5 Noncentrosymmetric superconductors

Superconductors that lack inversion symmetry in their point group are known as noncentrosymmetric superconductors. Such superconductors are interesting as they have the possibility of having a pairing state which is an admixture of singlet and triplet pairing, i.e. both types of pairing can occur simultaneously where the gap matrix is given by

$$\hat{\Delta}(\mathbf{k}) = \hat{\Delta}(\mathbf{k})^{\text{singlet}} + \hat{\Delta}(\mathbf{k})^{\text{triplet}}. \quad (2.14)$$

Such a mixed pairing state can only arise when SOC is non-negligible, as it results in a symmetry reduction where the spin transformations and point-group transformations can no longer be treated separately [72]. Instead the group of rotations in spin space and the group of rotations of the crystal are absorbed into one singular group such that the symmetry group becomes:

$$\text{G} = \text{G}_c^{(J)} \times \text{U}(1) \times \text{T} \quad (2.15)$$

where $\text{G}_c^{(J)}$ is the usual space group, G_c , except that each symmetry involving rotation is applied not just to the spatial coordinates but also to the spin coordinates of the order parameter as well [79]. A consequence of this reduced symmetry is that the gap matrix is no longer able to be decomposed into the product of a spin and spatial part. If there is inversion symmetry in the crystal group then the gap matrix must be either even or odd under such symmetry however, without such symmetry there is no such restriction and the gap matrix can be a mixture of both singlet and triplet pairing, see table 2.1. We note however that this analysis is valid strictly near to T_c , where the expansion of the free energy in terms of the order parameter is valid.

An interesting consequence of the mixed state in noncentrosymmetric superconductors with non-negligible spin orbit coupling is the potential presence of nodal transitions. This can arise due to changes in the two pairing components $\hat{\Delta}(\mathbf{k})^{\text{singlet}}$ and $\hat{\Delta}(\mathbf{k})^{\text{triplet}}$ caused by tuning. For example, in the compounds $\text{Li}_2\text{Pd}_{3-x}\text{Pt}_x\text{B}$ Platinum doping is thought to increase spin orbit coupling which increases the triplet component [82, 84, 85, 86, 87]. By tuning the pairing composition in this way it is possible to tune the nodal structure of the energy gap.

Nodes arise when the order parameter changes sign and the energy gap goes to zero. There are two main types of node: point- and line-nodes [90, 79, 72, 91], which can be

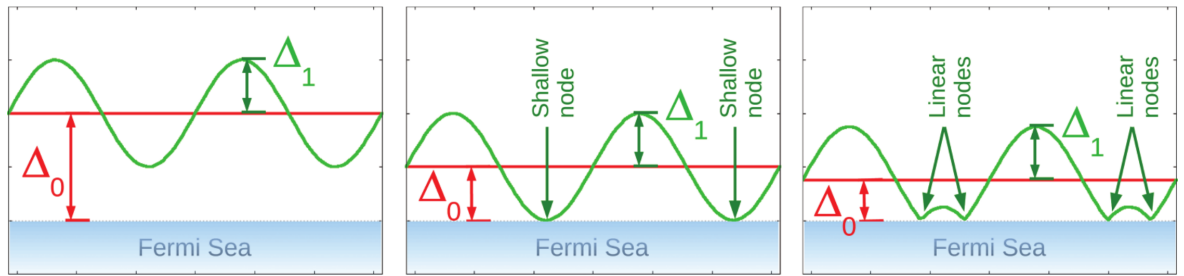


Figure 2.2: Tuning of the superconducting gap. As the ratio of the two gap components change from figure-left to figure-right different types of node emerge. Here Δ_0 and Δ_1 correspond to our $\hat{\Delta}(\mathbf{k})^{\text{singlet}}$ and $\hat{\Delta}(\mathbf{k})^{\text{triplet}}$ respectively. At first the isotropic singlet component dominates and a full gap exists. In the middle panel the singlet component has been reduced and the triplet component just touches the Fermi surface creating a shallow node. In the right panel the triplet component dominates and linear nodes are formed. Adapted from Ref. [82]

further classified into either linear or shallow nodes, where the excitation spectrum varies either linearly or non-linearly (e.g. quadratically) away from the node [82], see figure 2.2. The structure of nodes on the Fermi surface is a topological property (where the number of nodal lines on the Fermi surface is the topological number and can only change in steps of two) and so by tuning the nodal structure one changes the topology of the system.

Nodes allow for arbitrarily low energy excitations which affects the density of states. Different topological states have different nodal structures which gives rise to different density of states for each state. A consequence of this is that thermodynamic properties have identifiable signatures of different nodal structures. For example the specific heat in a nodeless state has an exponential temperature dependence at low temperatures while point- and line-nodes have power laws $C \propto T^3$ and $C \propto T^2$ respectively. We shall review this further in the next section when we discuss experimental probes of the gap structure, section 2.6.1 and revisit it again in chapter 7 when we investigate a potential application of the topological transition state to the prevention of superconducting quenches.

2.6 Experimental probes

We have so far mainly discussed theoretical aspects of superconductivity and some of the differences between conventional and unconventional superconductivity. In this section we are going to take a brief look at a few experimental probes of superconductivity and, specifically, see how it is possible to experimentally detect whether the superconducting gap has a nodal structure and whether or not a superconductor breaks time reversal symmetry.

There are a number of different experimental signatures used to determine whether a superconductor is unconventional or not. Stewart [48] discusses a number of experimental signs of unconventional superconductivity including, for example, superconductivity arising near the quantum critical point of a magnetically ordered phase; the characteristic energy scales not following the BCS convention: $T_c < \Theta_D < T_F$ (as can be determined by, amongst other things, the normal state specific heat or low temperature resistivity) or the lack of an isotope effect. Here we will focus on two signs especially relevant in this thesis: the nodal structure of the superconducting gap and the breaking of TRS. For more details of other experimental signatures see e.g. [48] and references therein.

2.6.1 Gap structure

The gap structure can typically be inferred from measurements of various thermodynamic properties, such as the specific heat, the magnetic penetration depth and nuclear magnetic resonance relaxation rate [48]. Generally speaking the gap structure, or at least the types of node present, is determined by the temperature dependence of these thermodynamic properties *at low temperatures*. The low temperature aspect is crucial because the theoretical models for each node are determined by taking the low temperature limit $T \rightarrow 0$.

Thermodynamic properties are determined by the density of states and as such are sensitive to different gap structures. Measurements of different properties e.g. specific heat, magnetic penetration depth and nuclear magnetic resonance relaxation rate demonstrate different temperature dependencies based on the structure of the gap. Generally speaking an exponential dependence corresponds to a full gap while a nodal gap structure will give rise to some power law e.g. in BCS theory the specific heat has an exponential dependence [26] while for nodal superconductors it has a power law dependence [79, 90, 82]. It should be noted that such temperature dependencies are only valid at very low temperatures $T \ll T_c$ and very deep minima in the gap structure can give such signatures if the temperature is not low enough [48].

The usual types of node in the gap structure are line- and point-nodes. Point nodes can be found, for example, in the ^3He A phase which has a triplet order parameter with nodal points at the poles of a spherical Fermi surface [92, 82]. Line nodes have also been determined in the cuprate d -wave superconductors, for example, $\text{YBa}_2\text{Cu}_3\text{O}_7$ would have four line nodes running the length of an assumed cylindrical Fermi surface [93, 82]. In both cases the form of the gap function is such that the quasiparticle energy spectra vary linearly away from the nodes.

In general the symmetry-allowed gap functions need not vary linearly away from these nodal points; Mazidian *et al.* [82] show that these types of nodes can be generalised from the linear nodes to ‘shallow’ nodes, where the quasiparticle energy spectrum varies quadratically near to the nodes. Furthermore these nodal lines can cross, for example in a d -wave superconductor with a spherical Fermi surface, and in general there exists the possibility of having crossings of both linear and shallow line-nodes [82].

Each of the different types of linear/shallow point/line/crossing nodal structures has a unique expression for the density of states which gives rise to different thermodynamic signatures depending on the gap structure. We will consider for example the case of the specific heat.

The specific heat is given by [90]

$$\begin{aligned} C_v &\equiv T \left(\frac{dS}{dT} \right) \\ &= \sum_{\mathbf{k}} \frac{1}{2} k_B \beta^2 \left[E_{\mathbf{k}} + \beta \left(\frac{dE_{\mathbf{k}}}{d\beta} \right) E_{\mathbf{k}} \operatorname{sech}^2 \left(\frac{\beta E_{\mathbf{k}}}{2} \right) \right] \end{aligned} \quad (2.16)$$

where $\beta = 1/k_B T$, k_B is Boltzmann’s constant and $E_{\mathbf{k}}$ is the energy of the quasiparticles of the system. At low temperatures this is equivalent to the energy integral

$$C_v = \frac{1}{2} k_B \beta^2 \int_0^\infty dE g(E) \operatorname{sech}^2 \left(\frac{\beta E}{2} \right) \quad (2.17)$$

where the density of states is given by $g(E) = \int \int \int \delta(E_{\mathbf{k}} - E) dk_x dk_y dk_z$. For each different nodal structure a unique expression for the density of states is obtained, which in turn gives rise to specific temperature dependencies of the specific heat at low temperatures [82].

In figure 2.3, reproduced from [82], we can see how each nodal structure arises from different symmetry-allowed choices of the gap $|\Delta_{\mathbf{k}}|$, the corresponding density of states expression $g(E)$ and the resulting exponent n of the temperature dependence of the specific heat $C_v \propto T^n$. Such power law temperature dependencies are distinct from each other at low temperatures as well as distinct from the exponential signature one obtains in the case of a full gap with no nodal structure $C_v \propto \exp(-\Delta/k_B T)$ [14] and can therefore be used to determine the gap structure of the superconductor.

Although we have discussed the specific heat above, the key point is the uniqueness of the expression for the density of states for different nodal structures, which is a general result that would apply to any other thermodynamic property. Since the density of states expressions depend solely on the topology of the nodal gap structure [72] other thermodynamic properties such as NMR relaxation rate ($1/T_1$) or magnetic penetration depth, λ will also have power law temperature dependence in the case of nodes and exponential temperature dependence in the case of a full gap. Therefore the exponential or power law dependence of thermodynamic properties can be used to infer the gap structure. Now we shall discuss the experimental detection of broken TRS.

2.6.2 Broken time reversal symmetry

Muon spin rotation/relaxation/resonance (μ SR) is an experimental technique which uses muons, and their sensitivity to static and dynamic microscopic magnetic fields, to investigate structural, magnetic and electronic phenomena in magnets, superconductors, semiconductors and insulators [94]. Of interest to us is the application of muons to the study of magnetic fields in superconductors; specifically the detection of magnetic fields which arise spontaneously upon entering the superconducting state — a definitive sign of broken time reversal symmetry.

With regards to the detection of broken TRS, (μ SR) experiments typically use positive muons, μ^+ , to investigate magnetism within samples. The muons are created by bombarding a graphite or beryllium target with a beam of protons which produces pions; short lived particles which then decay by two-body pion decay into a muon and a muon neutrino:

$$\pi^+ \rightarrow \mu^+ + \nu_{\mu}. \quad (2.18)$$

Due to the maximal violation of parity the muons are produced with their spins ($s=1/2$) anti-parallel to their momentum, thus the muon bunches used in such experiments are fully spin-polarised with a known direction [94, 95].

The muons come to rest *inside* the sample where they can interact with *local* magnetic moments, either caused by magnetic properties of the of the crystal or defects, or because of magnetic flux penetrating a vortex in the mixed state in the presence of an applied field. The muons, which were all initially polarised the same way, will each begin to precess at a rate dependent on their own local magnetic environment.

After some time (half-life $\tau_{\mu} = 2.2 \mu\text{s}$) the muon will decay, emitting a positron who's spin points preferentially in the direction of the muon's spin at disintegration:

$$\mu^+ \rightarrow e^+ + \nu_e + \bar{\nu}_{\mu}. \quad (2.19)$$

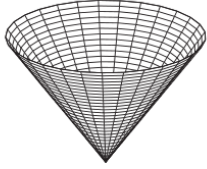
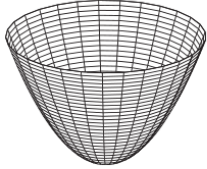
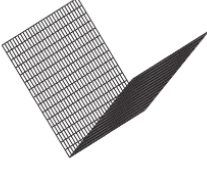
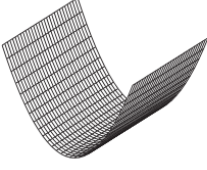
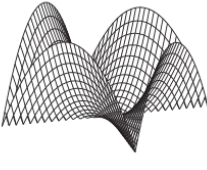
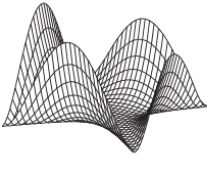
<p>(a) linear point node</p>  $ \Delta_k ^2 = I_1 (k_x^2 + k_y^2)$ $g(E) = \frac{E^2}{2(2\pi)^3 I_1 \sqrt{I_2}}$ $n = 3$	<p>(b) shallow point node</p>  $ \Delta_k ^2 = I_1 (k_x^2 + k_y^2)^2$ $g(E) = \frac{E}{2(2\pi)^3 I_1^{3/4} \sqrt{I_2}}$ $n = 2$
<p>(c) linear line node</p>  $ \Delta_k ^2 = I_1 k_x^2$ $g(E) = \frac{LE}{(2\pi)^3 \sqrt{I_1 I_2}}$ $n = 2$	<p>(d) shallow line node</p>  $ \Delta_k ^2 = I_1 k_x^4$ $g(E) = \frac{L\sqrt{E}}{(2\pi)^3 I_1^{3/4} \sqrt{I_2}}$ $n = 1.5$
<p>(e) crossing of linear line nodes</p>  $ \Delta_k ^2 = I_1 (k_x^2 - k_y^2)^2$ <p>or $I_1 k_x^2 k_y^2$</p> $g(E) = \frac{E(1+2 \ln \frac{L+\sqrt{E}/I_1^{1/4}}{\sqrt{E}/I_1^{1/4}})}{(2\pi)^3 \sqrt{I_1 I_2}}$ $\sim E^{0.8}$ $n = 1.8$	<p>(f) crossing of shallow line nodes</p>  $ \Delta_k ^2 = I_1 (k_x^2 - k_y^2)^4$ <p>or $I_1 k_x^4 k_y^4$</p> $g(E) = \frac{\sqrt{E}(1+2 \ln \frac{L+E^{1/4}/I_1^{1/8}}{E^{1/4}/I_1^{1/8}})}{(2\pi)^3 I_1^{3/4} \sqrt{I_2}}$ $\sim E^{0.4}$ $n = 1.4$

Figure 2.3: Different nodal structures and their specific heat temperature dependence exponents. Each row depicts a different nodal structure: point node, line node and line crossing from top to bottom. The left and right columns show the linear and shallow versions respectively. Shown in each case is the form of the gap, $|\Delta|^2$, giving rise to such a node as well as the associated density of states expression $g(E)$ and specific heat exponent n . Reproduced from Ref. [82]

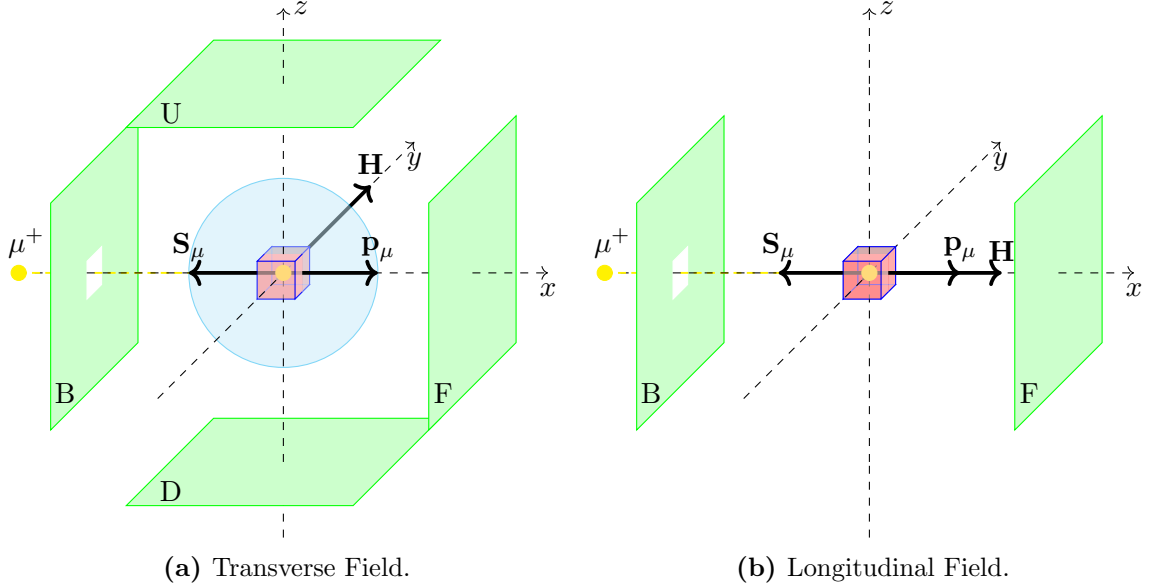


Figure 2.4: Schematics of the two main μ SR geometries. Muon bunches (yellow dots) are injected from the left through the backward (B) detector and implant into the sample (cube) with their momentum \mathbf{p}_μ facing towards the forward (F) detector. In transverse field (TF) geometry (figure 2.4a) an external magnetic field, \mathbf{H} , is applied along the y -axis and the muon spin, \mathbf{S}_μ , precesses around in the xy -plane (blue circle) and the FBUD detectors are used to measure asymmetry. In longitudinal-field (LF) geometry (figure 2.4b) the external magnetic field, \mathbf{H} , is applied parallel to the muon momentum. Zero field (ZF) μ SR is the $\mathbf{H} = 0$ limit of LF- μ SR. In this geometry only the FB detectors are used.

A typical configuration will have 6 detectors aligned with the coordinate axis and labelled according to a ‘beam’s eye view’: forward (F), backward (B), up (U), down (D), left (L), right (R) [94]. By detecting the asymmetry in the direction of emitted positrons, information about the polarisation of the muons and hence the local magnetic structure can be inferred.

There are two common experiments performed when testing a superconductor for broken TRS: transverse-field (TF) and longitudinal-field (LF) or zero-field (ZF). In TF- μ SR experiments a magnetic field is applied perpendicular (transverse) to the initial polarisation of the muons’ spins and 4 detectors in an FBUD configuration are used, see figure 2.4a. The muon spin will precess around the applied magnetic field in the xy -plane due to Larmor precession and the emitted positrons will be detected in the 4 surrounding detectors. In LF- μ SR (of which ZF- μ SR is the special case $\mathbf{B}_{ext} = 0$) the magnetic field is applied parallel to the initial direction of the muons’ spins and hence there will be no Larmor precession. In this case the F and B detectors are used only [94, 95], see figure 2.4b.

The detectors count the number and directions of the positrons being emitted and from this calculate the asymmetry, $A(t)$, in the polarisation of the muons. In the case of a fully polarised set of muons, they all face the same direction and the emitted positrons all hit the same detector; in this case the asymmetry is maximum. If the muons become completely depolarised the positrons will be emitted equally in random directions and there will be zero asymmetry. As the muons each precess individually due to their local environment the polarisation changes and this is reflected in the asymmetry.

The asymmetry (in the LF- μ SR case) is given by

$$A(t) = \frac{N_B(t) - N_F(t)}{N_B(t) + N_F(t)} = A_0 G_z(t) \quad (2.20)$$

and is calculated from the positron counts measured by the detectors. Here $N_D(t)$ is the positron count at the D -detector at time t . The asymmetry can also be determined by the depolarization function, $G_z(t)$, which describes the time evolution of the muons' polarization. A_0 is the initial asymmetry and is known because the muons are all implanted with the same orientation. $G_z(t)$ is unknown and must be fitted, and different theoretical depolarisation models have been derived for different environments [94, 95]. By fitting $G_z(t)$ one can infer information about the environment the muon experiences based on the physical assumptions that went in to the derivation of the depolarisation function.

A common depolarisation function employed is the Kubo-Toyabe function [96] (note below we use the notation of Ref [55])

$$G_z^{\text{KT}}(t) = \frac{1}{3} + \frac{2}{3}(1 - \sigma^2 t^2) \exp\left(-\frac{\sigma^2 t^2}{2}\right), \quad (2.21)$$

where σ is related to the local field distribution width. This function describes the depolarisation of muons due to randomly oriented static nuclear dipole moments in the absence of magnetic ordering [52]. In a muon experiment, the asymmetry, $A(t)$, is measured and the Kubo-Toyabe function (for example) is fitted to the data. In the detection of broken TRS it is common to observe an exponentially damped Kubo-Toyabe function upon entering the superconducting state [52]

$$G_z(t) = A_0 G_z^{\text{KT}}(t) \exp(-\lambda t), \quad (2.22)$$

where $\exp(-\lambda t)$ is the relaxation associated with an additional spontaneous magnetic field and λ is the relaxation rate. The real smoking gun of broken TRS is the observation of the λ or σ increasing at T_c , signalling the onset of a magnetic field in the superconducting state, see figure 2.5. μ SR has successfully been used to detect TRS breaking in, for example, Sr_2RuO_4 [52], UPt_3 [51], LaNiC_2 [55] and Re_6Zr [97] as well as the structure of the vortex lattice e.g. [98].

Another experiment that also detects TRS breaking and complements μ SR is the Kerr effect. In Kerr effect experiments linearly polarised light of an equal superposition of left- and right-circularly polarised light is incident upon a material and the reflected light is compared to the incident light. If the material's complex indices of refraction are different for the left- and right-circularly polarised light then the light reflected by the material will be elliptical and phase shifted from the incident beam [99]; this is the Kerr effect.

The Kerr angle θ_K gives the angle of the major axis of the reflected beam relative to the incident beam, and is given by:

$$\theta_K \approx -\frac{4\pi}{\omega} \Im \left[\frac{\sigma_{xy}}{\bar{n}(\bar{n}^2 - 1)} \right] \quad (2.23)$$

where \bar{n} is the average of the two left- and right-polarised refractive indices and σ_{xy} is non-zero *only* when TRS is broken [99]. Broken TRS is demonstrated by the onset of a non-zero Kerr rotation, $\Delta\theta_K$, when entering the superconducting state from high T . The Kerr effect has been used to investigate TRS breaking in Sr_2RuO_4 and the heavy fermion superconductors CeCoIn_5 , UPt_3 and URu_2Si_2 . In addition to the Kerr effect, the magnetic fields arising from broken TRS can be detected by directly measuring the magnetisation of the sample with a SQUID, as was done recently for LaNiC_2 [100].

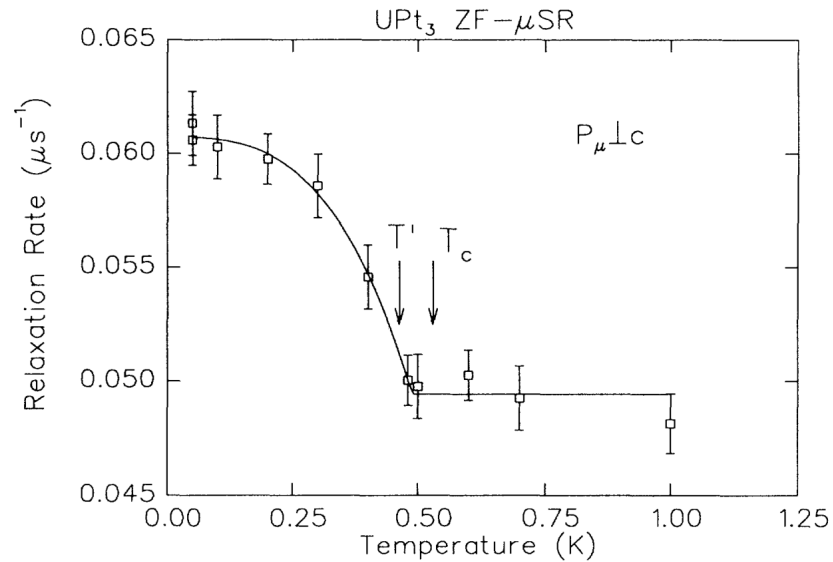


Figure 2.5: Typical example of the spontaneous increase in relaxation rate due to broken TRS in μ SR experiments. Reproduced from Ref. [51]

2.7 Summary

In this chapter we have discussed the basic principles of the BCS theory of superconductivity, seeing how electrons experience an attractive interaction due to exchange of virtual phonons and how this phonon-mediated attraction leads to electrons pairing up and forming bound states. The superconducting state can be described as a coherent state formed of a macroscopic number of these pairs, all with the same global phase θ , and it is from this mechanism that superconductors obtain their fascinating properties.

We have seen how superconductors come in two classes: conventional and unconventional, and that unconventional superconductors can have interesting properties, specifically tunable topological states and the breaking of extra symmetries. Furthermore, we have seen how some of these interesting theoretical concepts can be measured and detected experimentally.

In the next chapter we will see how the experimental detection of broken TRS by μ SR in two Ni-based superconductors, LaNiC_2 and LaNiGa_2 led to an intense research effort to understand what were originally considered conventional superconductors, and ultimately to the proposal of a novel theory of equal spin pairing superconductivity which will be the main focus of this thesis, chapters 5 and 6.

Chapter 3

Broken time reversal symmetry in Ni-based LaNiX_2 ($\text{X} = \text{C}, \text{Ga}$)

In this chapter we will look in detail at two nickel-based superconductors: LaNiC_2 and LaNiGa_2 . Both of these materials break TRS upon entering the superconducting state, demonstrated by the spontaneous appearance of internal magnetic fields — an indicator of unconventional superconductivity. Additionally, both materials have low symmetry, and symmetry analysis for both reveals similar theoretical constraints on the pairing state, despite LaNiC_2 being noncentrosymmetric while LaNiGa_2 is centrosymmetric. Both of these materials display no magnetic ordering in the normal state at ambient pressures. We shall first review the literature for each of these materials and see that the superconductivity in these materials is unconventional. We shall examine a recently proposed novel non-unitary triplet-pairing theory with a view to study it further at a mean field level in chapter 5. Let us start by reviewing the literature of each material.

3.1 LaNiC_2

Superconductivity in noncentrosymmetric LaNiC_2 was discovered in 1996 by Lee *et al.* [101] who measured the resistivity, specific heat and magnetic susceptibility of polycrystalline samples LaNiC_2 and found a superconducting transition between 2.63K and 2.86K. The normal state is paramagnetic. They report that the specific heat data shows unconventional behaviour with the temperature dependence obeying a T^3 power law, rather than the conventional exponential dependence. Given that they detected no signature of any magnetic impurity in the specific heat data they suggest the most likely pairing is p-type triplet-pairing. Lee and Zeng [102] also investigated the effect of thorium doping in $(\text{La}_{1-x}\text{Th}_x)\text{NiC}_2$ and found a superconducting dome in the doping phase diagram, with T_c at first increasing as the material is doped then decreasing again at larger doping. It was also found by Syu *et al.* [103] that nitrifying carbon deficient $\text{LaNiC}_{2-\delta}$ increases T_c compared to the parent LaNiC_2 .

Following the discovery of LaNiC_2 Pecharsky, Miller, and Gschneidner [104] carried out specific heat and magnetism studies on LaNiC_2 and CeNiC_2 and report that the temperature dependence of the specific heat of LaNiC_2 is exponential, implying standard BCS superconductivity. They argue the discrepancy between their results and Lee *et al.* [101] is due to differences in the way the least-squares fitting was performed and show that they can reproduce the result of Lee *et al.* [101] albeit with higher uncertainty than their own method.

Further support that LaNiC_2 was a conventional BCS superconductor came from ^{139}La nuclear quadrupole resonance (NQR) experiments, performed by Iwamoto *et al.* [105], that revealed the relaxation rate $1/T_1$ is enhanced at T_c then decreases exponentially as T is lowered below the superconducting transition. They report that this is strong indication that the superconductivity is of BCS type and suggest that the anomalous T^3 specific heat dependence [101] may be explained by a BCS-type energy gap with anisotropy, as was suggested for lead [106].

At this point it seemed that LaNiC_2 was a conventional superconductor until Hillier, Quintanilla, and Cywinski [55] performed μSR experiments and found spontaneous magnetic fields appeared with the onset of superconductivity, indicating that TRS is broken in the superconducting state. Their symmetry analysis of LaNiC_2 finds 12 possible gap functions, 4 of which break TRS. All 4 of the TRS breaking gap functions are non-unitary triplet states. This includes triplet pairing with the full point group symmetry of the crystal and is a possibility only with noncentrosymmetric superconductors, as the A1 irrep can be even or odd (so the spin part can be singlet or triplet to maintain fermion antisymmetry).

A number of first-principles electronic structure calculations have been performed. Hase and Yanagisawa [107] tried to reproduce the Th-doping phase diagram [102] and found that they could do so for the Th-rich region by an extended rigid band model. Furthermore the Th-doping effect at low doping could not be explained by the isotope effect, leading them to conclude that there is unconventional superconductivity in LaNiC_2 which is made weaker by the Th-disordering, giving rise to conventional superconductivity in the Th-rich region.

Laverock *et al.* [108] and Subedi and Singh [109] also performed first-principles electronic structure calculations and obtained very similar Fermi surfaces for LaNiC_2 . Laverock *et al.* [108] investigated the nesting properties of the Fermi surfaces of a number of members of the $R\text{NiC}_2$ family ($R=\text{La}, \text{Nd}, \text{Sm}$ and Gd). They found that the Fermi surface of LaNiC_2 is topologically different to those of the other members of the $R\text{NiC}_2$ family and has poor nesting properties, accounting for the absence of a charge-density-wave state in LaNiC_2 .

Subedi and Singh [109] calculated the electronic structure and electron-phonon coupling. They report that LaNiC_2 is a conventional electron-phonon superconductor with intermediate coupling based on their value of $T_c \approx 3$ being close to the experimentally observed $T_c = 2.7 \text{ K}$. They suggest that the TRS breaking may arise from a mixed pairing state of mostly singlet with a small amount of triplet pairing (possible thanks to the lack of inversion symmetry). They argue such a state would break TRS while being fully gapped, giving rise to exponential specific heat.

It turns out however, that a mixed singlet triplet pairing state as proposed by Subedi and Singh [109] cannot break TRS. Quintanilla *et al.* [110] demonstrate this by extending the symmetry analysis of [55] to include the relativistic effect of spin orbit coupling. They show that in the presence of strong spin orbit coupling all 4 of the symmetry-allowed pairings are one dimensional and therefore cannot break TRS, compared with the weak spin orbit coupling case of [55] where there are 4 non-unitary states (out of a total of 12 possible states) which do break TRS. Therefore, to be consistent with the experimental observation of broken TRS, spin orbit coupling must be negligible. Nevertheless, there must be some SOC in any crystal, which raises the question of how a system with finite SOC can break TRS. Quintanilla *et al.* [110] answer this by adiabatically turning on the spin orbit coupling and figure 3.1 shows the result. They find that the 8 TRS preserving states smoothly evolve into one of the 4 strong

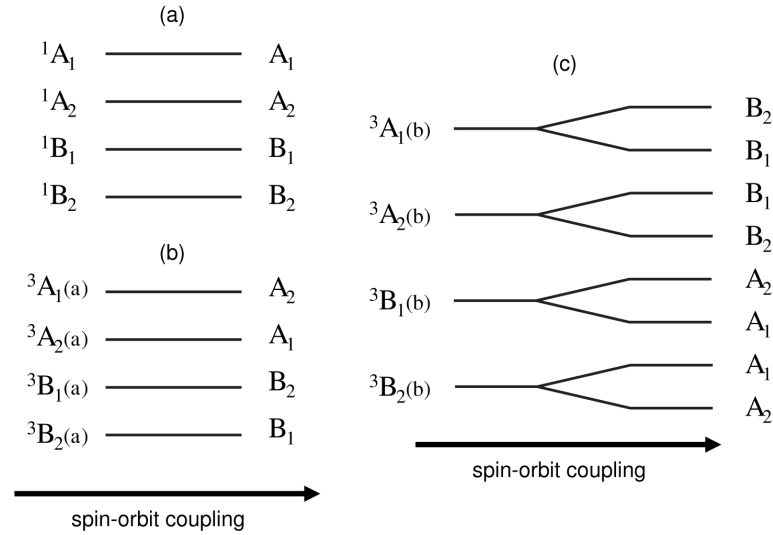


Figure 3.1: Schematic shows how the LaNiC_2 pairing instabilities change from weak to strong SOC. In cases (a) and (b) the pairing instabilities are TRS preserving for both weak and strong SOC. These cannot explain the experimental observation of broken TRS. Case (c) shows how the non-unitary TRS breaking states with weak SOC evolve into the TRS preserving states with strong SOC. The system will undergo two transitions: first into a TRS preserving state with only one of the instabilities present, then into a second TRS breaking state when the second instability arises (it is the presence of both instabilities, and their relative phase, which breaks TRS). Figure from Ref. [110].

spin orbit coupling TRS preserving states (figure 3.1 (a) and (b)). This includes the pairing admixture proposed in [109]. The 4 TRS breaking non-unitary states instead are split by spin orbit coupling into two distinct transitions (figure 3.1 (c)). First the normal state transitions into one of the TRS preserving superconducting states, then a second transition follows where the second pairing state appears. It is the presence of both components, and the relative phase between them, that breaks TRS. With large SOC these two transitions would be well separated however, in the limit of weak SOC they would occur close together and appear experimentally as a single transition into a TRS breaking superconducting state, consistent with the μSR experiments. Mukherjee and Curnoe [111] also find that a non-unitary triplet pairing state is required to break TRS and this state should have line nodes. Since the discovery of spontaneous magnetic fields [55] there have been a number of experimental attempts to ascertain the pairing in LaNiC_2 . Bonalde *et al.* [112] performed penetration depth measurements on different quality samples of LaNiC_2 and found T^2 dependence far below T_c , indicating a nodal gap structure. They argue that previous experiments indicating conventional s-wave behaviour either did not go to low enough temperatures or that the lower-quality samples were affected by magnetic impurities.

Nodal gap pairing was also supported theoretically with a variational Monte Carlo method by Yanagisawa and Hase [113]. They study the Hubbard model on a triangular lattice and show how the energy of the s-wave, p-wave, d-wave and f-wave pairing states vary with Δ and compare to the normal state energy. Their results show that the triplet states are stable and indeed are of lower energy than the s-wave state. They further explain that the triplet state can emerge due to the SOC and the constraints from symmetry analysis and do not require a magnetic phase or a magnetic field.

On the other hand Hirose *et al.* [114] managed to grow the first single crystal of LaNiC_2

(all samples were polycrystalline beforehand) and measured the electrical resistivity, de Hass–van Alphen (dHvA) and specific heat, to determine the Fermi surface and superconducting properties. They find that there exists two Fermi surfaces which are best described by the first-principles calculations of [107] for YNiC_2 although there are some differences. The low-temperature specific heat is exponential implying full gap superconductivity, which they attribute to a standard BCS interpretation. Other than acknowledging the broken TRS reported in [55], there is no mention of whether their single crystal sample breaks TRS or how a BCS interpretation could explain it.

Further support of a full gap comes from Chen *et al.* [115] who measure the penetration depth, specific heat and electronic resistivity of high quality polycrystalline samples of LaNiC_2 and show the results are best described by a two-gap BCS model when compared with single gap BCS and T^2 power law behaviour. They state that the exact nature of the pairing and its mechanism cannot be conclusively determined yet but that two-gap is definite.

Additionally Katano *et al.* [116] investigated the effect of magnetic impurities on the superconductivity of LaNiC_2 by substituting Ce for La. It is found that T_c is reduced and superconductivity eventually destroyed by Ce substitution. They report that this reduction in T_c can be described by Abrikosov-Gor'kov theory for conventional s-wave superconductors with localised magnetic moments, indicating LaNiC_2 is a BCS superconductor with full gaps and that this result would be consistent with the experimental results of [115] which found evidence for two-gap superconductivity.

Further investigation of the spontaneous magnetisation was performed by Sumiyama *et al.* [117] who constructed a specialised SQUID to measure spontaneous magnetic fields in superconductors. Using this they were able to show that the direction of the spontaneous magnetic field along the c -axis is reversed when the sample is reversed [100]. This showed that the spontaneous magnetic field is pinned to the crystal and indicates the importance of the noncentrosymmetric symmetry and is a potential realisation of the spontaneous magnetic field predicted to arise from the non-unitary triplet-pairing state [56]. Furthermore, this result is significant in that it is one of few examples where broken TRS detected by μSR has been confirmed by another experiment that directly addresses TRS.

Recently there has been some experimental effort to investigate the effect of pressure on LaNiC_2 . Katano *et al.* [118] studied LaNiC_2 under high pressure using electronic resistivity measurements. They found superconductivity was enhanced (T_c is increased) as pressure is increased up until 3 GPa, above which the enhancement is suppressed by a new state. The phase diagram of LaNiC_2 with pressure shows a superconducting dome at ambient pressure and a different high-energy scale state at high pressures. This is interesting both because this is opposite to the usual case where the superconductivity arises from pressure (or other tuning parameter) and because the normal state is not as normal as first thought (akin to other unconventional superconductors that all seem to have a non-Fermi liquid). This result indicates that LaNiC_2 is not a normal metal but is highly correlated with strong electron interactions that contribute to the superconductivity.

Wiendlocha *et al.* [119] attempted to explain the experimental results of [118] using ab initio calculations of the electronic structure, phonons and electron-phonon coupling and Eliashberg formalism to determine the thermodynamic properties of the superconducting state. It was assumed the superconductivity is mediated by electron-phonon interaction. They find that T_c is increased with pressure over the full pressure range 0 GPa to 15 GPa which

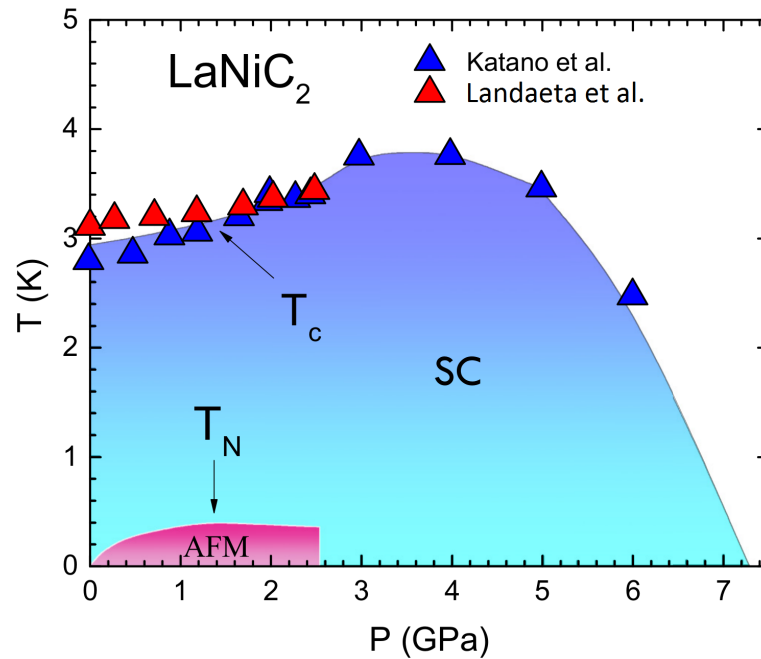


Figure 3.2: Pressure-temperature phase diagram of LaNiC_2 . An antiferromagnetic phase is detected inside the superconducting dome, emerging with pressure. At ambient pressure there is no magnetic ordering. The superconducting dome is detected both by resistivity measurements from Katano *et al.* [118] and penetration-depth and superfluid density measurements by Landaeta *et al.* [120]. Figure adapted from Ref. [120].

fails to capture the experimental result of [118] where increasing pressure above 4 GPa causes a decrease in T_c and eventually full suppression of superconductivity. To obtain this behaviour at high pressures the Eliashberg formalism requires a large Coulomb pseudopotential $\mu^* > 0.2$, supporting the idea of [118] that a new electronic phase is induced by the high pressure.

Further information was added to the LaNiC_2 pressure phase diagram when Landaeta *et al.* [120] reported magnetic penetration-depth measurements of high purity single crystals of LaNiC_2 at different pressures. The results show that penetration depth, re-analysed specific heat data from [114] and superfluid density simulations all indicate point nodes; a clear sign of unconventional superconductivity. Moreover at low temperatures and *finite* pressure the penetration depth shows a sudden upturn followed by a sudden drop as temperature is decreased, indicating pressure induced magnetic order.

The phase diagram for LaNiC_2 then shows the coexistence of superconductivity and magnetism, with an antiferromagnetic phase surrounding a magnetic quantum critical point at low temperatures and ambient pressure, see figure 3.2. This is strong evidence that LaNiC_2 is an unconventional superconductor and makes it more consistent with other unconventional superconductors where the unconventional superconductivity appears near magnetic instabilities. The observation of spontaneous magnetic fields upon entering the superconducting state by both μSR [55] and SQUID measurements [117] are clear evidence of unconventional superconductivity and, although the nature of the unconventional superconductivity is not yet certain (point-nodes, line-nodes, two-gap etc), it seems it cannot be explained by a conventional BCS theory.

3.2 LaNiGa_2

Superconductivity in centrosymmetric LaNiGa_2 was co-discovered by Aoki, Terayama, and Sato [121] and Zeng and Lee [122] in 1995. Specific heat and DC electrical resistivity measurements give the transition temperature as 1.93 K to 2.01 K. The Sommerfeld coefficient was estimated from the jump in the specific heat at T_c and found to be in good agreement with BCS theory and the temperature-dependence at low temperatures was exponential. Both indicate that LaNiGa_2 is a basic BCS-type phonon-mediated superconductor.

Again however, Hillier *et al.* [56] performed zero-field and transverse-field μSR experiments on LaNiGa_2 and found a spontaneous magnetic field appeared at T_c , just like with LaNiC_2 . Such a field indicates the superconducting state breaks time reversal symmetry (TRS), which implies the existence of unconventional pairing. Their symmetry analysis of this low-symmetry material finds that only 4 of the 12 possible gap functions break TRS, all of which are non-unitary triplet-pairing states, again just like LaNiC_2 . The similarity between centrosymmetric LaNiGa_2 and the noncentrosymmetric LaNiC_2 suggests these two compounds may form a new class of superconductors.

First-principles calculations by Singh [123] and Hase and Yanagisawa [124] both find the electronic structure of LaNiGa_2 is more complex (having essentially five Fermi surface sheets) than that of LaNiC_2 . Singh [123] found no evidence of proximity to ferromagnetism but found a moderately high density of states at the Fermi level which, together with the experimentally determined Sommerfeld coefficient [122], is consistent with weak coupling. Furthermore, Singh argues, signs of the triplet pairing as proposed in [55], such as heavy renormalised bands and a repulsive interaction, are not supported by the results of the first-principles calculations.

On the other hand however, Hase and Yanagisawa [124] suggest that because LaNiGa_2 has multiple bands a new gap state: “ $\Delta_1 + i\Delta_2$ ” is possible. They claim that such a state breaks TRS because of the non trivial complex phase and the two order parameters Δ_1 and Δ_2 can take any symmetry allowed by the crystal symmetry. As long as both order parameters are never nodal in the same place, such a state would be fully gapped *and* break TRS - consistent with the exponential specific heat in [122], the observation of broken TRS and the symmetry required triplet pairing [56]. However, Mazidian [125] argues that, within the framework of Ginzburg-Landau theory, such a state cannot be a ground state of the free energy.

More recently Weng *et al.* [126] measured the London penetration depth, specific heat, upper critical field and superfluid density of LaNiGa_2 and found that the results are best explained by two-gap nodeless superconductivity. They propose a new theory with non-unitary triplet-pairing via an on-site attractive interaction acting between electrons with the same spin but in different orbitals. Since the pairing is on-site but between *different* orbitals the Pauli exclusion principle is not violated. The exchange of orbital labels is antisymmetric to ensure overall wave function antisymmetry. They show that from this theory two *full gaps* of potentially different magnitudes emerge — consistent with the experimental results, while the non-unitary nature of the pairing satisfies the symmetry analysis of [56, 55] and would give rise to the magnetisation observed by μSR [56].

3.3 Magnetisation from non-unitary triplet-pairing

As already mentioned, the symmetry analysis for both LaNiC_2 [55] and LaNiGa_2 [56] reveals non-unitary triplet-pairing (a type of pairing introduced in section 2.2) to be the only symmetry-allowed pairing that breaks TRS. The resulting magnetisation that arises from such pairing is especially interesting in these materials because it both opposes the conventional behaviour of BCS superconductivity and arises in materials that are paramagnetic in their normal state. Non-unitary triplet-pairing had been identified in ferromagnetic superconductors and is understood to arise from critical magnetic fluctuations near the ferromagnetic quantum critical point helping to mediate the triplet pairing [127], however, this explanation does not apply in the the case of LaNiC_2 and LaNiGa_2 because they are paramagnetic in the normal state.

Using Ginzburg-Landau arguments, Hillier *et al.* [56] explain how the net magnetisation arises as a sub-dominant order parameter to the superconductivity as follows: The usual form of the free energy for a triplet pairing instability is given by

$$F = a|\boldsymbol{\eta}|^2 + \frac{b}{2}|\boldsymbol{\eta}|^4 + b'|\boldsymbol{\eta} \times \boldsymbol{\eta}^*|^2 \quad (3.1)$$

where $\boldsymbol{\eta}$ is the triplet order parameter that relates to the triplet component of the gap-matrix through the \mathbf{d} -vector (see equation (2.10)) by $\mathbf{d}(\mathbf{k}) = \boldsymbol{\eta}\Gamma(\mathbf{k})$. Here $\Gamma(\mathbf{k})$ are the irreducible representations determined by the symmetry analysis of each material, see e.g. [55, 56, 110]. With this form of the free energy, as discussed in section 2.3, the instability occurs at, and T_c is determined by, $a = 0$ while it varies smoothly from the normal state ($a > 0$) to the superconducting state ($a < 0$). This is independent of whether the pairing is unitary or non-unitary. The term $b'|\boldsymbol{\eta} \times \boldsymbol{\eta}^*|^2$, and more specifically the sign of b' , determines whether the pairing will be unitary or non-unitary. If the pairing is unitary then the cross product of the order parameter is zero, while it is finite if the pairing is non-unitary. The free energy is minimised therefore by unitary pairing if $b' > 0$ and by non-unitary pairing if $b' < 0$.

In the case of LaNiC_2 and LaNiGa_2 however, it is known that they are paramagnetic. As such there must be an additional term in the free energy coupling $\boldsymbol{\eta}$ to the magnetisation of the system, \mathbf{m} . The simplest form of the free energy that contains the relevant terms and obeys the required normal-state symmetries is [56]:

$$F = a|\boldsymbol{\eta}|^2 + \frac{\mathbf{m}^2}{2\chi} + \frac{b}{2}|\boldsymbol{\eta}|^4 + b'|\boldsymbol{\eta} \times \boldsymbol{\eta}^*|^2 + b''\mathbf{m} \cdot (i\boldsymbol{\eta} \times \boldsymbol{\eta}^*) \quad (3.2)$$

where χ is the magnetic susceptibility. The last term in equation (3.2) describes the coupling of the magnetisation \mathbf{m} to the effective magnetic field caused by the triplet pairing: $\mathbf{h}_{\text{eff}} = -b''(i\boldsymbol{\eta} \times \boldsymbol{\eta}^*)$. The magnetisation that results from the effective magnetic field is given by $\mathbf{m} = \mathbf{h}_{\text{eff}}\chi = -b''\chi(i\boldsymbol{\eta} \times \boldsymbol{\eta}^*)$ and if we substitute that into equation (3.2) we get:

$$F = a|\boldsymbol{\eta}|^2 + \frac{b}{2}|\boldsymbol{\eta}|^4 + (b' - \frac{b''^2\chi}{2})|\boldsymbol{\eta} \times \boldsymbol{\eta}^*|^2. \quad (3.3)$$

Equation (3.3) is of the same form as equation (3.2) and so a similar argument applies as to whether the pairing will be unitary or non-unitary. Again this depends on the sign of the term in front of the cross product, making the condition for non-unitary pairing as:

$$b' - b''^2\chi/2 < 0. \quad (3.4)$$

If this condition is satisfied then non-unitary pairing will lower the free energy compared to unitary pairing. Hillier *et al.* [56] reason that because the second term on the LHS of equation (3.4) is always negative for paramagnets, non-unitary triplet-pairing will be favoured, with the strongest effect being realised in proximity to a Stoner instability. They also note that such terms exist in the case of ferromagnetic triplet superconductors, where they act to increase the T_c of the non-unitary transitions relative to the unitary ones, thus stabilising the non-unitary pairing.

What we have seen then is that the non-unitary triplet-pairing in a paramagnetic material will create an effective magnetic field, causing the free energy to be further lowered by aligning more spins with said effective field. By aligning more spins, more pairing between spins of the same orientation can occur, thus allowing more superconducting pairs to form. It is this relationship between the superconducting order parameter and the sub-dominant magnetic order parameter that is self-reinforcing and favours non-unitary triplet-pairing in these materials.

3.4 Summary

Both noncentrosymmetric LaNiC_2 and centrosymmetric LaNiGa_2 are superconductors who break TRS upon entering the superconducting state, as indicated by the spontaneous appearance of a magnetic field detected by μSR experiments [55, 56]. Furthermore, in both materials, the magnetism detected in the superconducting state arises from a system that was initially not magnetically ordered (and from a state that conventionally opposes magnetism) showing that the superconductivity and magnetism are inherently linked.

In both cases the symmetry analysis [55, 56] reveals 12 possible pairings, 4 of which break TRS. All 4 TRS breaking states are non-unitary triplet-pairing states. As discussed previously, chapter 2, the Ginzburg-Landau symmetry-based treatment of the superconducting phase transition is based on a very general theory of second order phase transitions. It neither requires, nor makes any assumption about, the underlying microscopic details of the superconductor such as the pairing mechanism or gap structure. Instead it uses the symmetry of the system — a well known and defined property of the material — to calculate the *possible* gap structures. This, together with the fact broken TRS conveniently reduces the number of possible pairings to *only* those that are non-unitary triplet, provides strong evidence that said pairing must be present in these materials.

Neither experimental efforts [101, 104, 105, 112, 114] or first-principle calculations [107, 109] have been able to conclusively identify the pairing or gap structure of LaNiC_2 . Both find evidence to support conventional (exponential specific heat [104, 114], exponential NQR relaxation [105] and good agreement of first-principles T_c with experimental T_c [109]) and unconventional superconductivity (T^3 specific heat power law [101], T^2 penetration-depth power law [112] and inability to reproduce Th-doping effects with BCS first-principles calculations or isotope effect [107]). Furthermore the suggestion of a mixed singlet-triplet state [109] (only possible in noncentrosymmetric superconductors with strong spin orbit coupling) was shown by relativistic symmetry analysis not to break TRS [110].

Further evidence of triplet pairing in LaNiC_2 came from a theoretical Monte Carlo study of the energies of different pairings, which found the triplet state was stable and of lowest energy [113], and an experimental SQUID investigation that confirmed the existence of the

spontaneous magnetisation arising in the superconducting state as well as finding that the magnetisation was pinned to the c -axis of the crystal. Furthermore the linear increase in magnetisation near to T_c as temperature is decreased could be a realisation of the magnetisation expected to arise from non-unitary triplet-pairing [56].

The unconventional nature of the superconductivity is further supported by the experimental observation of a highly correlated normal state with strong electron interactions when under pressure [118], further supported by ab initio calculations [119]. Further confirmation comes from pressure-dependent magnetic penetration-depth measurements which identify an antiferromagnetic phase emerging with pressure from a magnetic quantum critical point at ambient pressure [120].

Experimentally speaking the situation for LaNiGa_2 is slightly better resolved (although there are far fewer reports available) with measurements of the specific heat [122, 126], London penetration depth and superfluid density [126] all suggesting a full gap, although in [122] conventional superconductivity is suggested while in [126] a two-gap model is proposed. With a more recent report of penetration-depth, specific heat and electronic resistivity measurements of LaNiC_2 also finding two-gap behaviour [115], additionally supported by an investigation into the effect of paramagnetic impurities [116], it seems as if a two-gap model may be a common feature of both LaNiC_2 and LaNiGa_2 .

The current situation seems to be that both LaNiC_2 and LaNiGa_2 are TRS breaking unconventional superconductors. Older thermodynamic measurements that indicate conventional full gap superconductivity may be instead explained by the more recent observation of two-gap behaviour observed in both materials. Although the most recent results find LaNiC_2 is in fact probably nodal [120], no such evidence exists as yet for LaNiGa_2 . In order to marry the seemingly contradictory findings of symmetry required non-unitary triplet-pairing and observations of a nodeless full gap a new theoretical model has been proposed [126]. In this theory pairing occurs between electrons of the same spin (triplet) on the same site but different orbitals. This gives rise to two nodeless full gaps $\Delta_{\uparrow\uparrow}$ and $\Delta_{\downarrow\downarrow}$ which can in principle be different (non-unitary). We have seen how, from a Ginzburg-Landau perspective, this non-unitary triplet-pairing lowers the free energy compared to unitary pairing, despite (and because of) the materials being paramagnetic. This theory has been proposed to explain the superconductivity in LaNiGa_2 and may have potentially been applicable to LaNiC_2 before the most recent observation of nodal signs in a high-quality single crystal [120]. We shall consider this theory in more detail in chapter 5 where we shall perform a variational mean field treatment of the theory. Before that however we shall demonstrate the application of the variational mean field method to conventional BCS-like s-wave pairing.

Chapter 4

Variational mean-field theory for singlet pairing

In this chapter we apply variational mean-field theory, otherwise known as the self-consistent field method [14], to s-wave singlet pairing; the same pairing as used in BCS theory. During this chapter we will use the terms ‘s-wave’ or ‘singlet pairing’ interchangeably with ‘BCS theory’ even though, strictly speaking, what we present here is not the original BCS theory; in the sense that the mathematical techniques being employed are not the same as used in the original work [26]. The results we obtain here are the same as obtained in the original BCS theory.

The purpose of this chapter is primarily pedagogical, showing not only how the variational mean-field theory is applied to a particular well known problem but also detailing the technical steps which someone just starting this subject may be unfamiliar with. Discussing the technical details here allows us to omit such details when discussing the equal-spin triplet-pairing theory of chapter 5 and focus on the novel physics. The secondary purpose is two-fold: firstly we verify our use of the method by obtaining the same well known results for BCS superconductivity, and secondly we can compare these results directly with those of a special case (BCS-like case) of the equal-spin triplet-pairing theory, chapter 5.

A comparison between the two theories is possible because, in a certain limit, there exists a mapping between the equal-spin triplet-pairing theory and BCS theory. The equal-spin triplet-pairing theory considers pairing between *equal* spins on *two different* orbitals of the same site, while in BCS theory, pairing occurs between *opposite* spins on the same site (with only one orbital). In general there is an effective energy splitting between the two orbitals and in the limit where that splitting is zero, the equal-spin pairing theory becomes mathematically similar to BCS theory, with the two orbital labels playing the role of the BCS spin labels. Henceforth, the definition of the BCS-like case of the equal-spin triplet-pairing theory is when the effective orbital splitting is zero, enabling a mapping between the two theories.

Our starting point when using the self-consistent field method is the Hamiltonian.

$$\hat{\mathcal{H}}_{\text{BCS}} = \hat{\mathcal{K}}_{\text{BCS}} - \mu\hat{\mathcal{N}} + \hat{\mathcal{V}}_{\text{BCS}} \quad (4.1)$$

where $\hat{\mathcal{K}}_{\text{BCS}}$ is the total ‘kinetic energy’ of all the particles, μ is the chemical potential and $\hat{\mathcal{N}}$ is the total number of particles. Together these form the non-interacting part of the Hamiltonian, so called because the electrons do not interact with each other. The interacting

part of the Hamiltonian, \hat{V}_{BCS} , describes electron-electron interactions. We will first deal with the non-interacting part of the Hamiltonian.

4.1 Non-interacting Hamiltonian

First we will consider the non-interacting part of the Hamiltonian and see how to derive the non-interacting energy dispersion. In real space the kinetic energy is given by

$$\hat{\mathcal{K}}_{\text{BCS}} = - \sum_{j=1}^{\mathcal{N}} \sum_{j'=1}^{\mathcal{N}} \begin{pmatrix} \hat{c}_{j\uparrow}^\dagger & \hat{c}_{j\downarrow}^\dagger \end{pmatrix} \begin{pmatrix} t_{jj'}^{\uparrow\uparrow} & t_{jj'}^{\uparrow\downarrow} \\ t_{jj'}^{\downarrow\uparrow} & t_{jj'}^{\downarrow\downarrow} \end{pmatrix} \begin{pmatrix} \hat{c}_{j'\uparrow} \\ \hat{c}_{j'\downarrow} \end{pmatrix} \quad (4.2)$$

where each summation runs over all of the sites of a square lattice with a total of \mathcal{N} sites, $\hat{c}_{j\sigma}^\dagger$ ($\hat{c}_{j\sigma}$) is the creation (annihilation) operator that creates (annihilates) an electron with spin σ on site j and $t_{jj'}^{\sigma\sigma'}$ is the energy of a particle with spin σ' , at site j' , hopping to site j , with spin σ .

The Fourier transform of the creation/annihilation operators is given by:

$$\hat{c}_{j\sigma}^\dagger = \frac{1}{\sqrt{\mathcal{N}}} \sum_{\mathbf{k}} e^{-i\mathbf{k}\cdot\mathbf{R}_j} \hat{c}_{\mathbf{k}\sigma}^\dagger \quad \hat{c}_{j\sigma} = \frac{1}{\sqrt{\mathcal{N}}} \sum_{\mathbf{k}} e^{i\mathbf{k}\cdot\mathbf{R}_j} \hat{c}_{\mathbf{k}\sigma} \quad (4.3a)$$

$$\hat{c}_{\mathbf{k}\sigma}^\dagger = \frac{1}{\sqrt{\mathcal{N}}} \sum_j e^{i\mathbf{k}\cdot\mathbf{R}_j} \hat{c}_{j\sigma}^\dagger \quad \hat{c}_{\mathbf{k}\sigma} = \frac{1}{\sqrt{\mathcal{N}}} \sum_j e^{-i\mathbf{k}\cdot\mathbf{R}_j} \hat{c}_{j\sigma} \quad (4.3b)$$

where in two dimensions $\mathcal{N} = \frac{L_x}{a_x} \frac{L_y}{a_y}$ is the total number of sites of the two-dimensional square lattice with sides of length L_x and L_y and lattice spacing a_x and a_y . \mathbf{R}_j is the position vector of the j 'th site. With these Fourier transforms it is possible to rewrite the Kinetic energy in terms of momentum-space rather than real-space. This transformation is performed as follows. We multiply out the matrices in equation (4.2), and write the real space creation/annihilation operators in terms of momentum space ones using the Fourier transformations.

$$\begin{aligned} \hat{\mathcal{K}}_{\text{BCS}} &= - \sum_{j=1}^{\mathcal{N}} \sum_{j'=1}^{\mathcal{N}} \left\{ t_{jj'}^{\uparrow\uparrow} \hat{c}_{j\uparrow}^\dagger \hat{c}_{j'\uparrow} + t_{jj'}^{\uparrow\downarrow} \hat{c}_{j\uparrow}^\dagger \hat{c}_{j'\downarrow} + t_{jj'}^{\downarrow\uparrow} \hat{c}_{j\downarrow}^\dagger \hat{c}_{j'\uparrow} + t_{jj'}^{\downarrow\downarrow} \hat{c}_{j\downarrow}^\dagger \hat{c}_{j'\downarrow} \right\} \\ &= - \frac{1}{\mathcal{N}} \sum_{j=1}^{\mathcal{N}} \sum_{j'=1}^{\mathcal{N}} \left\{ t_{jj'}^{\uparrow\uparrow} \sum_{\mathbf{k}_1} e^{-i\mathbf{k}_1\cdot\mathbf{R}_j} \hat{c}_{\mathbf{k}_1\uparrow}^\dagger \sum_{\mathbf{k}_2} e^{i\mathbf{k}_2\cdot\mathbf{R}_{j'}} \hat{c}_{\mathbf{k}_2\uparrow} + \right. \\ &\quad + t_{jj'}^{\uparrow\downarrow} \sum_{\mathbf{k}_3} e^{-i\mathbf{k}_3\cdot\mathbf{R}_j} \hat{c}_{\mathbf{k}_3\uparrow}^\dagger \sum_{\mathbf{k}_4} e^{i\mathbf{k}_4\cdot\mathbf{R}_{j'}} \hat{c}_{\mathbf{k}_4\downarrow} + \\ &\quad + t_{jj'}^{\downarrow\uparrow} \sum_{\mathbf{k}_5} e^{-i\mathbf{k}_5\cdot\mathbf{R}_j} \hat{c}_{\mathbf{k}_5\downarrow}^\dagger \sum_{\mathbf{k}_6} e^{i\mathbf{k}_6\cdot\mathbf{R}_{j'}} \hat{c}_{\mathbf{k}_6\uparrow} + \\ &\quad \left. + t_{jj'}^{\downarrow\downarrow} \sum_{\mathbf{k}_7} e^{-i\mathbf{k}_7\cdot\mathbf{R}_j} \hat{c}_{\mathbf{k}_7\downarrow}^\dagger \sum_{\mathbf{k}_8} e^{i\mathbf{k}_8\cdot\mathbf{R}_{j'}} \hat{c}_{\mathbf{k}_8\downarrow} \right\} \end{aligned}$$

\mathbf{R}_j and $\mathbf{R}_{j'}$ are the position vectors of the sites j and j' from some arbitrary origin on the 2D square lattice.

For any pair of sites j and j' there exists a hopping vector between them $\mathbf{R}_{\Delta_j} = \mathbf{R}_j - \mathbf{R}_{j'}$ describing the direct path from site j' to site j , see figure 4.1. Rather than summing over all pairs of sites we can equivalently sum over all sites and, for each site, sum over all possible hopping vectors \mathbf{R}_{Δ_j} . Mathematically this is done by writing $\mathbf{R}_{j'} = \mathbf{R}_j - \mathbf{R}_{\Delta_j}$ and replacing

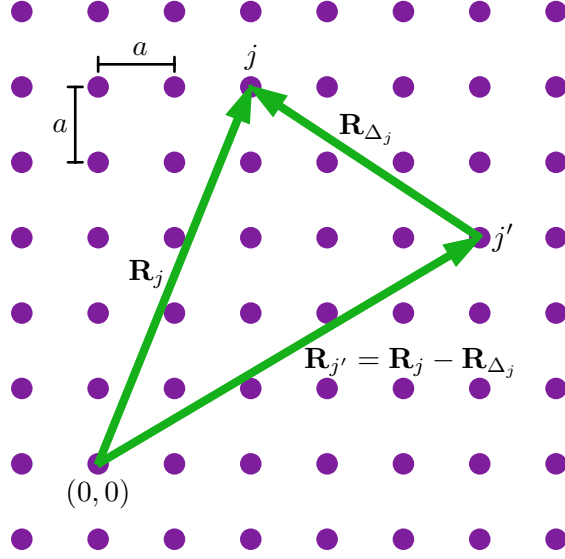


Figure 4.1: Definition of the hopping vector \mathbf{R}_{Δ_j} . The hopping vector \mathbf{R}_{Δ_j} separates two sites, j and j' , which an electron hops to and from respectively. \mathbf{R}_j and $\mathbf{R}_{j'}$ are two vectors that describe the position of the two sites j and j' relative to some arbitrary origin. As shown, $\mathbf{R}_{j'}$ can be written in terms of \mathbf{R}_j and \mathbf{R}_{Δ_j} which turns out to be useful when deriving the non-interacting electron energies.

the sum over j' with a sum over all possible hoppings Δ_j . The exponential terms take the form of, for example, $e^{i(\mathbf{k}_2 - \mathbf{k}_1) \cdot \mathbf{R}_j} e^{-i\mathbf{k}_2 \cdot \mathbf{R}_{\Delta_j}}$. The Fourier transform of the Kronecker delta function

$$\sum_j e^{i(\mathbf{k}_\alpha - \mathbf{k}_\beta) \cdot \mathbf{R}_j} = \mathcal{N} \delta_{\mathbf{k}_\alpha \mathbf{k}_\beta} \quad (4.4)$$

can then be used to remove the sum over all sites j and cancel the factor of $\frac{1}{\mathcal{N}}$ giving:

$$\hat{\mathcal{K}}_{\text{BCS}} = - \sum_{\Delta_j} \left\{ \begin{aligned} & \sum_{\mathbf{k}_1 \mathbf{k}_2} \delta_{\mathbf{k}_1 \mathbf{k}_2} t_{\Delta_j}^{\uparrow\uparrow} e^{-i\mathbf{k}_2 \cdot \mathbf{R}_{\Delta_j}} \hat{c}_{\mathbf{k}_1 \uparrow}^\dagger \hat{c}_{\mathbf{k}_2 \uparrow} + \\ & \sum_{\mathbf{k}_3 \mathbf{k}_4} \delta_{\mathbf{k}_3 \mathbf{k}_4} t_{\Delta_j}^{\uparrow\downarrow} e^{-i\mathbf{k}_4 \cdot \mathbf{R}_{\Delta_j}} \hat{c}_{\mathbf{k}_3 \uparrow}^\dagger \hat{c}_{\mathbf{k}_4 \downarrow} + \\ & \sum_{\mathbf{k}_5 \mathbf{k}_6} \delta_{\mathbf{k}_5 \mathbf{k}_6} t_{\Delta_j}^{\downarrow\uparrow} e^{-i\mathbf{k}_6 \cdot \mathbf{R}_{\Delta_j}} \hat{c}_{\mathbf{k}_5 \downarrow}^\dagger \hat{c}_{\mathbf{k}_6 \uparrow} + \\ & \sum_{\mathbf{k}_7 \mathbf{k}_8} \delta_{\mathbf{k}_7 \mathbf{k}_8} t_{\Delta_j}^{\downarrow\downarrow} e^{-i\mathbf{k}_8 \cdot \mathbf{R}_{\Delta_j}} \hat{c}_{\mathbf{k}_7 \downarrow}^\dagger \hat{c}_{\mathbf{k}_8 \downarrow} \end{aligned} \right\}. \quad (4.5)$$

Mathematically speaking, using the Kronecker delta function is a nice trick to remove one of the sums over all sites, simplifying the calculation, but there is a physical interpretation as well. In the thermodynamic limit, all sites can be considered identical as the effect of sites on or near to the boundary are negligible. As such it is necessary to calculate the hoppings of a single site only, and simply scale by the number of sites.

When performing the double \mathbf{k} -summations, the only terms that are non-zero are when

$\mathbf{k}_\alpha = \mathbf{k}_\beta$, this effectively removes one of the sums leaving:

$$\hat{\mathcal{K}}_{\text{BCS}} = - \sum_{\Delta_j} \left\{ \begin{aligned} & \sum_{\mathbf{k}_2} t_{\Delta_j}^{\uparrow\uparrow} e^{-i\mathbf{k}_2 \cdot \mathbf{R}_{\Delta_j}} \hat{c}_{\mathbf{k}_2\uparrow}^\dagger \hat{c}_{\mathbf{k}_2\uparrow} + \\ & \sum_{\mathbf{k}_4} t_{\Delta_j}^{\uparrow\downarrow} e^{-i\mathbf{k}_4 \cdot \mathbf{R}_{\Delta_j}} \hat{c}_{\mathbf{k}_4\uparrow}^\dagger \hat{c}_{\mathbf{k}_4\downarrow} + \\ & \sum_{\mathbf{k}_6} t_{\Delta_j}^{\downarrow\uparrow} e^{-i\mathbf{k}_6 \cdot \mathbf{R}_{\Delta_j}} \hat{c}_{\mathbf{k}_6\downarrow}^\dagger \hat{c}_{\mathbf{k}_6\uparrow} + \\ & \sum_{\mathbf{k}_8} t_{\Delta_j}^{\downarrow\downarrow} e^{-i\mathbf{k}_8 \cdot \mathbf{R}_{\Delta_j}} \hat{c}_{\mathbf{k}_8\downarrow}^\dagger \hat{c}_{\mathbf{k}_8\downarrow} \end{aligned} \right\}. \quad (4.6)$$

Each sum is performed over the same set of momenta so we can let $\mathbf{k}_2 = \mathbf{k}_4 = \mathbf{k}_6 = \mathbf{k}_8 = \mathbf{k}$ and write in matrix form:

$$\hat{\mathcal{K}}_{\text{BCS}} = \sum_{\mathbf{k}} \begin{pmatrix} \hat{c}_{\mathbf{k}\uparrow}^\dagger & \hat{c}_{\mathbf{k}\downarrow}^\dagger \end{pmatrix} \begin{pmatrix} \varepsilon_{\mathbf{k}}^{\uparrow\uparrow} & \varepsilon_{\mathbf{k}}^{\uparrow\downarrow} \\ \varepsilon_{\mathbf{k}}^{\downarrow\uparrow} & \varepsilon_{\mathbf{k}}^{\downarrow\downarrow} \end{pmatrix} \begin{pmatrix} \hat{c}_{\mathbf{k}\uparrow} \\ \hat{c}_{\mathbf{k}\downarrow} \end{pmatrix} \quad (4.7)$$

where

$$\varepsilon_{\mathbf{k}}^{\sigma\sigma'} = - \sum_{\Delta_j} t_{\Delta_j}^{\sigma\sigma'} e^{-i\mathbf{k} \cdot \mathbf{R}_{\Delta_j}} \quad (4.8)$$

is the kinetic energy of a non-interacting electron of momentum \mathbf{k} hopping between two sites separated by position vector \mathbf{R}_{Δ_j} while flipping its spin ($\sigma \neq \sigma'$) or not ($\sigma = \sigma'$). Note the minus sign originally in front of equation (4.7) has been incorporated into these hopping energies.

Obtaining an expression for the kinetic energies $\varepsilon_{\mathbf{k}}^{\sigma\sigma'}$ requires summing over all possible hopping vectors \mathbf{R}_{Δ_j} . To simplify this (and for consistency with the equal-spin triplet-pairing theory of chapter 5) we focus on the case of a 2d square lattice and permit only nearest neighbour hopping, see figure 4.2, which means there are only four nearest neighbours and hence four hopping vectors, which we will call \mathbf{R}_1 through \mathbf{R}_4 . For each hopping vector there are two hopping amplitudes: $t_{\Delta_j}^{\sigma\sigma} = t$ if the electron hops and maintains its spin or $t_{\Delta_j}^{\sigma\bar{\sigma}} = t'$ if its spin flips. Under such conditions equation (4.8) for both spin up and down becomes:

$$\begin{aligned} \varepsilon_{\mathbf{k}}^{\uparrow\uparrow} = \varepsilon_{\mathbf{k}}^{\downarrow\downarrow} &= -t \left[e^{-i\mathbf{k} \cdot \mathbf{R}_1} + e^{-i\mathbf{k} \cdot \mathbf{R}_2} + e^{-i\mathbf{k} \cdot \mathbf{R}_3} + e^{-i\mathbf{k} \cdot \mathbf{R}_4} \right] \\ &= -t \left[e^{-ik_x a} + e^{ik_x a} + e^{-ik_y a} + e^{ik_y a} \right] \\ &= -2t [\cos(k_x a) + \cos(k_y a)]. \end{aligned} \quad (4.9)$$

We assume that the hybridisation is zero, i.e. $t' = 0 \implies \varepsilon_{\mathbf{k}}^{\sigma\bar{\sigma}} = 0$, so equation (4.7) is diagonal.

Before the energy of the non-interacting Hamiltonian can be obtained the chemical potential part, $\mu \hat{\mathcal{N}}$, also needs to be written in momentum space for consistency with the kinetic energy part, $\hat{\mathcal{K}}_{\text{BCS}}$. In the grand canonical ensemble the chemical potential acts like an external bath which electrons can move into and out of in order to keep the total particle number fixed.

The total number of particles is obtained with the number operator $\hat{\mathcal{N}}$ and is given by

$$\hat{\mathcal{N}} = \sum_{j\sigma} \hat{n}_{j\sigma} = \sum_{j\sigma} \hat{c}_{j\sigma}^\dagger \hat{c}_{j\sigma}$$

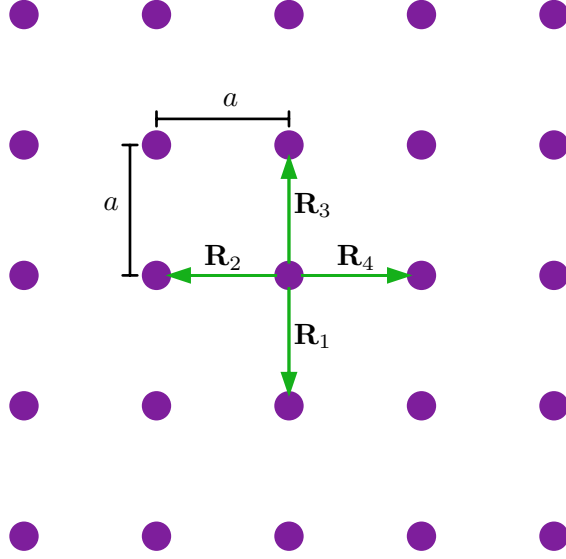


Figure 4.2: Schematic of nearest neighbour hopping for deriving square lattice dispersion. With nearest neighbour hopping, the summation over all possible hopping vectors, $\sum_{\Delta_j} t_{\Delta_j}^{\sigma\sigma'} e^{-i\mathbf{k}\cdot\mathbf{R}_{\Delta_j}}$, contains only the four vectors shown, i.e. $\mathbf{R}_{\Delta_j} = \mathbf{R}_1$ to \mathbf{R}_4 .

where $\sum_{j\sigma}$ sums over all electron states, $\hat{n}_{j\sigma} = \hat{c}_{j\sigma}^\dagger \hat{c}_{j\sigma}$ is the number operator of a given electron state and counts the number of particles in that state. Again by using the Fourier transforms, equation (4.3a), following the same procedure as before, section 4.1, $\hat{\mathcal{N}}$ can be written in momentum space:

$$\hat{\mathcal{N}} = \sum_{\mathbf{k}\sigma} \hat{n}_{\mathbf{k}\sigma} = \sum_{\mathbf{k}\sigma} \hat{c}_{\mathbf{k}\sigma}^\dagger \hat{c}_{\mathbf{k}\sigma}.$$

The non-interacting part of the Hamiltonian is therefore given by

$$\hat{\mathcal{K}}_{\text{BCS}} - \mu \hat{\mathcal{N}} = \sum_{\mathbf{k}} \begin{pmatrix} \hat{c}_{\mathbf{k}\uparrow}^\dagger & \hat{c}_{\mathbf{k}\downarrow}^\dagger \end{pmatrix} \begin{pmatrix} \varepsilon_{\mathbf{k}}^{\uparrow\uparrow} - \mu & 0 \\ 0 & \varepsilon_{\mathbf{k}}^{\downarrow\downarrow} - \mu \end{pmatrix} \begin{pmatrix} \hat{c}_{\mathbf{k}\uparrow} \\ \hat{c}_{\mathbf{k}\downarrow} \end{pmatrix}. \quad (4.10)$$

The diagonal elements of the matrix in equation (4.10) are the eigenvalues of the non-interacting single-particle Hamiltonian. These eigenvalues are the energy that an electron in state \mathbf{k} with spin σ would have without any electron-electron interactions. The collection of these energies for each spin, for all \mathbf{k} , form the electron dispersion - in this case two degenerate bands, one for each spin, see figure 4.3. This non-interacting energy dispersion is naturally bounded between $\pm 4t$, an advantage of which is the integrations can be performed numerically without invoking the Debye cut-off. Therefore the hopping, t , makes a natural choice of units and in all numerical calculation we will be working with the energy in units of t .

At zero temperature the chemical potential plays the role of the Fermi-energy - the highest energy state that can be occupied. The occupation of the electrons obeys the Fermi-Dirac distribution

$$f(E) = \frac{1}{1 + e^{\beta E}}, \quad (4.11)$$

where $f(E)$ is the probability that a fermionic state, with energy E relative to the chemical potential, is occupied or not. This quantity is implicitly dependent on temperature because

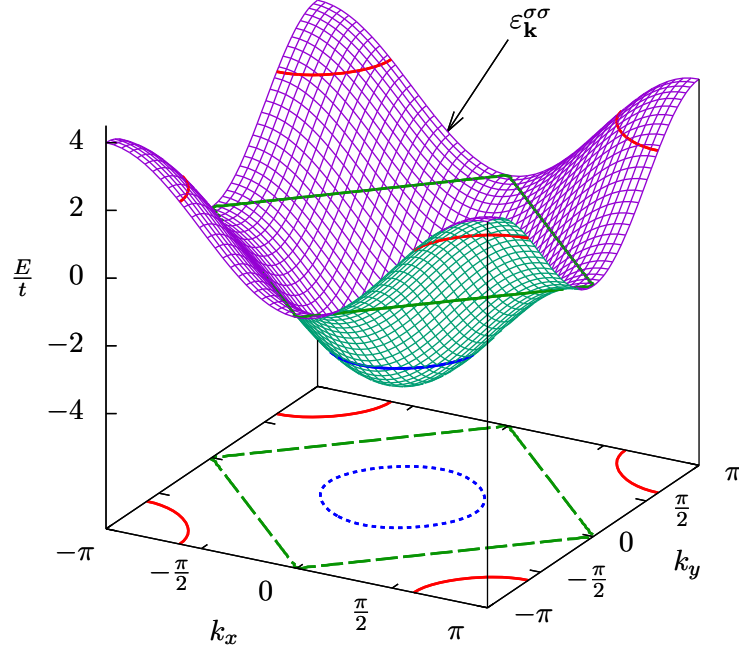


Figure 4.3: Non-interacting electron dispersion of a 2D square lattice with nearest neighbour hopping. The surface (technically two degenerate surfaces, one for each spin) represents the non-interacting dispersion of a 2D square lattice with nearest neighbour hopping and no hybridisation. The contours on the surface and their projection on the $k_x k_y$ -plane correspond to different values of chemical potential μ . The red, green and blue contours correspond to $\mu = 2.5$, $\mu = 0.0$ and $\mu = -2.5$ respectively. The chemical potential controls the number of electrons in the system and at $T = 0$ the chemical potential is equivalent to the Fermi energy. The energy is in units of the particle hopping, t .

$\beta = \frac{1}{k_B T}$. The temperature dependence is not written explicitly for simplicity. As shown by the Fermi-Dirac distribution, figure 4.4, Fermion states with energy above (below) the chemical potential μ are empty (occupied) at $T = 0$; at finite temperature there is a smoothing with states just above (below) the Fermi level having some finite probability of being occupied (empty). We shall now consider the interaction part of the Hamiltonian.

4.2 Interaction

Having obtained the non-interacting dispersion we can now consider the Hamiltonian with the interaction term. The interaction term is given by:

$$\hat{V}_{\text{BCS}} = -U \sum_j \hat{c}_{j\uparrow}^\dagger \hat{c}_{j\downarrow}^\dagger \hat{c}_{j\downarrow} \hat{c}_{j\uparrow}$$

which is an on-site *attractive* interaction between electrons of opposite spins, where U is the amplitude of the on-site interaction and is a positive constant. This term is quartic in creation and annihilation operators and as such cannot be diagonalised in the usual way.

In order to determine how a physical system behaves for a given set of parameters e.g. interaction strength, chemical potential or temperature, one needs to minimise the free energy.

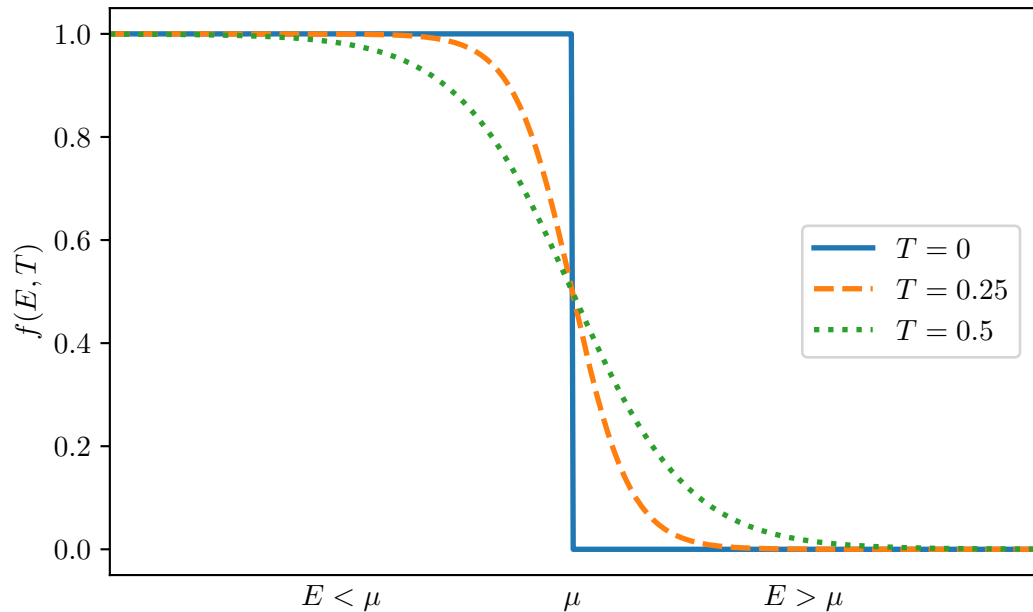


Figure 4.4: Fermi-Dirac distribution at different temperatures. The Fermi-Dirac distribution gives the probability of a fermionic state with energy E being occupied. At zero temperature the Fermi-Dirac distribution is a step function where states below (above) the chemical potential are occupied (empty). At finite temperatures the distribution is smoothed near the chemical potential.

The free energy in general is given by

$$F = -k_B T \ln(Z) = \langle H \rangle - TS \quad (4.12)$$

where k_B is Boltzmann's constant, T is the temperature and S is the entropy. Z is the partition function and $\langle H \rangle$ is the expectation value of the Hamiltonian, both of which depend on the eigenvalues and/or eigenstates of the Hamiltonian. The eigenstates and eigenvectors are obtained by diagonalising the Hamiltonian and since, as noted above, the interaction part cannot be diagonalised in the usual way, we will make use of variational mean-field theory to proceed.

4.3 Mean-field theory

Mean-field theory, in short, works by introducing a new Hamiltonian (the mean-field Hamiltonian), with variable parameters (the mean-fields), which can be solved exactly. It is assumed that the eigenvalues and eigenstates of the mean-field Hamiltonian are a good approximation to those of the original Hamiltonian. In doing so one is able to approximate the free energy of the original Hamiltonian by using the eigenstates of the mean-field Hamiltonian. The values of the mean fields are fixed by the requirement that the free energy gives the best possible approximation to the exact value (i.e. is as low as possible). We shall now go through this in detail.

We define a mean-field Hamiltonian:

$$\hat{\mathcal{H}}_{\text{BCS}}^{\text{MF}} = \hat{\mathcal{K}}_{\text{BCS}} - \mu \hat{\mathcal{N}} + \hat{\mathcal{V}}_{\text{BCS}}^{\text{MF}} \quad (4.13)$$

where the non-interacting part of the Hamiltonian is the same as in the original Hamiltonian and the interacting part $\hat{\mathcal{V}}_{\text{BCS}}^{\text{MF}}$ contains terms which are quadratic in creation/annihilation

operators (exactly solvable) and contains the mean-fields — variational parameters which allow $\hat{\mathcal{H}}_{\text{BCS}}^{\text{MF}}$ to approximate $\hat{\mathcal{H}}_{\text{BCS}}$.

Assuming the eigenstates and eigenvalues of $\hat{\mathcal{H}}_{\text{BCS}}^{\text{MF}}$ are a good approximation to $\hat{\mathcal{H}}_{\text{BCS}}$, the free energy can be written as:

$$F = \langle \hat{\mathcal{H}}_{\text{BCS}} \rangle - TS \approx \langle \hat{\mathcal{H}}_{\text{BCS}} \rangle_{\text{MF}} - TS_{\text{MF}}$$

where

$$\langle \hat{\mathcal{H}}_{\text{BCS}} \rangle = \sum_n e^{-\beta E_n} \langle n | \hat{\mathcal{H}}_{\text{BCS}} | n \rangle \quad (4.14a)$$

$$\langle \hat{\mathcal{H}}_{\text{BCS}} \rangle_{\text{MF}} = \sum_n e^{-\beta E_n^{\text{MF}}} \langle n^{\text{MF}} | \hat{\mathcal{H}}_{\text{BCS}} | n^{\text{MF}} \rangle. \quad (4.14b)$$

Here $\langle \hat{\mathcal{H}}_{\text{BCS}} \rangle$ is the normal expectation value of the Hamiltonian $\hat{\mathcal{H}}_{\text{BCS}}$ using its eigenstates, $|n\rangle$, and eigenvalues, E_n , while $\langle \hat{\mathcal{H}}_{\text{BCS}} \rangle_{\text{MF}}$ is the expectation value of the Hamiltonian using the eigenvalues, E_n^{MF} , and eigenstates, $|n^{\text{MF}}\rangle$, of the mean-field Hamiltonian $\hat{\mathcal{H}}_{\text{BCS}}^{\text{MF}}$. S_{MF} is the entropy of the mean-field system.

The free energy can be written

$$\begin{aligned} F &\approx \langle \hat{\mathcal{H}}_{\text{BCS}} \rangle_{\text{MF}} - \langle \hat{\mathcal{H}}_{\text{BCS}}^{\text{MF}} \rangle_{\text{MF}} + \langle \hat{\mathcal{H}}_{\text{BCS}}^{\text{MF}} \rangle_{\text{MF}} - TS_{\text{MF}} \\ &\approx \langle \hat{\mathcal{H}}_{\text{BCS}} - \hat{\mathcal{H}}_{\text{BCS}}^{\text{MF}} \rangle_{\text{MF}} + F_{\text{MF}} \end{aligned} \quad (4.15)$$

where $F_{\text{MF}} = -k_B T \ln(Z_{\text{MF}})$ is the free energy of the mean-field Hamiltonian and $Z_{\text{MF}} = \sum_n \exp(-\beta E_n^{\text{MF}})$ is the partition function of the mean-field system. All the terms in the free energy require the eigenstates and eigenvalues of the mean-field Hamiltonian which, since $\hat{\mathcal{H}}_{\text{BCS}}^{\text{MF}}$ is diagonalisable, are known. Hence it is now possible to calculate and minimise the free energy of the original Hamiltonian.

The first term in equation (4.15) containing the difference between the two Hamiltonians can be simplified as follows:

$$\begin{aligned} \langle \hat{\mathcal{H}}_{\text{BCS}} - \hat{\mathcal{H}}_{\text{BCS}}^{\text{MF}} \rangle_{\text{MF}} &= \langle \hat{\mathcal{H}}_{\text{BCS}} \rangle_{\text{MF}} - \langle \hat{\mathcal{H}}_{\text{BCS}}^{\text{MF}} \rangle_{\text{MF}} \\ &= \langle \hat{\mathcal{V}}_{\text{BCS}} \rangle_{\text{MF}} - \langle \hat{\mathcal{V}}_{\text{BCS}}^{\text{MF}} \rangle_{\text{MF}}. \end{aligned} \quad (4.16)$$

where the non-interacting parts vanish because they are identical in both Hamiltonians. In order to evaluate $\langle \hat{\mathcal{V}}_{\text{BCS}} \rangle_{\text{MF}}$ we make use of an application of Wick's theorem [14]

$$\begin{aligned} \langle \hat{c}_{j\uparrow}^\dagger \hat{c}_{j\downarrow}^\dagger \hat{c}_{j\downarrow} \hat{c}_{j\uparrow} \rangle_{\text{MF}} &= \langle \hat{c}_{j\uparrow}^\dagger \hat{c}_{j\downarrow}^\dagger \rangle_{\text{MF}} \langle \hat{c}_{j\downarrow} \hat{c}_{j\uparrow} \rangle_{\text{MF}} && \text{GOR'KOV} \\ &- \langle \hat{c}_{j\uparrow}^\dagger \hat{c}_{j\downarrow} \rangle_{\text{MF}} \langle \hat{c}_{j\downarrow}^\dagger \hat{c}_{j\uparrow} \rangle_{\text{MF}} && \text{FOCK} \\ &+ \langle \hat{c}_{j\uparrow}^\dagger \hat{c}_{j\uparrow} \rangle_{\text{MF}} \langle \hat{c}_{j\downarrow}^\dagger \hat{c}_{j\downarrow} \rangle_{\text{MF}} && \text{HARTREE} \end{aligned} \quad (4.17)$$

This is an exact result which simplifies the quartic interaction term, allowing us to write $\langle \hat{\mathcal{V}}_{\text{BCS}} \rangle_{\text{MF}}$ as

$$\begin{aligned} \langle \hat{\mathcal{V}}_{\text{BCS}} \rangle_{\text{MF}} &= -U \sum_j \left\{ \langle \hat{c}_{j\uparrow}^\dagger \hat{c}_{j\downarrow}^\dagger \rangle_{\text{MF}} \langle \hat{c}_{j\downarrow} \hat{c}_{j\uparrow} \rangle_{\text{MF}} \right. \\ &- \langle \hat{c}_{j\uparrow}^\dagger \hat{c}_{j\downarrow} \rangle_{\text{MF}} \langle \hat{c}_{j\downarrow}^\dagger \hat{c}_{j\uparrow} \rangle_{\text{MF}} \\ &\left. + \langle \hat{c}_{j\uparrow}^\dagger \hat{c}_{j\uparrow} \rangle_{\text{MF}} \langle \hat{c}_{j\downarrow}^\dagger \hat{c}_{j\downarrow} \rangle_{\text{MF}} \right\}. \end{aligned} \quad (4.18)$$

In order to calculate the remaining terms required by the free energy we need the eigenvalues and eigenstates of the mean-field Hamiltonian $\hat{\mathcal{H}}_{\text{BCS}}^{\text{MF}}$, hence we now need to introduce the mean-field Hamiltonian explicitly.

4.3.1 Mean-field Hamiltonian

To create the mean-field Hamiltonian, the interaction $\hat{\mathcal{V}}_{\text{BCS}}$ needs to be replaced by some diagonalisable mean-field interaction $\hat{\mathcal{V}}_{\text{BCS}}^{\text{MF}}$. To decide which terms to include in $\hat{\mathcal{V}}_{\text{BCS}}^{\text{MF}}$ one can look at the terms present in the original Hamiltonian. From $\langle \hat{\mathcal{V}}_{\text{BCS}} \rangle_{\text{MF}}$, equation (4.18), there arises Gorkov pairing terms and Fock spin-flipping terms, whilst there are Hartree particle density terms present in both interacting and non-interacting parts of $\hat{\mathcal{H}}_{\text{BCS}}$. These are all of the possible terms one could include in $\hat{\mathcal{V}}_{\text{BCS}}^{\text{MF}}$ as they all arise naturally from the original Hamiltonian. Any other terms we may wish to include will be self-consistently zero.

In general, when constructing the mean-field Hamiltonian, one does not need to include all of the terms present in $\hat{\mathcal{H}}_{\text{BCS}}$, just those that are expected to be relevant to the physics being studied. For example, one can arrive at the Stoner theory of ferromagnetism from Hubbard theory by choosing to include only particle density fields in the mean-field Hamiltonian, which is fine if one is interested only in magnetism¹. As we shall see in section 6.3, one can additionally include the pairing mean-fields, yielding a mean-field theory which gives rise to superconductivity and magnetisation.

For the purposes of BCS theory we expect superconductivity with Cooper pairs, hence the expectation values $\langle \hat{c}^\dagger \hat{c}^\dagger \rangle$ and $\langle \hat{c} \hat{c} \rangle$ (Gor'kov terms) should be non-zero, whence pairing mean-fields, Δ , are required (otherwise those expectations would self-consistently be zero and there would be no superconductivity). The Fock expectations could also lower the free energy if included however, these would add an additional, non-superconducting, spontaneous spin-flipping complication to the model that we are not interested in. Therefore such terms will not be included.

The particle density expectations $\langle \hat{c}^\dagger \hat{c} \rangle$ appear in both interacting and non-interacting parts of the Hamiltonian $\hat{\mathcal{H}}_{\text{BCS}}$ and will be naturally non-zero even without including the mean-fields, they should therefore be included for self-consistency purposes. The particle density mean-fields, ϕ , need not appear with a spin-dependence as there is no mechanism which should lead to an imbalance in spins. We choose to include them here however, in analogy with our equal-spin triplet-pairing theory, chapter 5, and as we shall see, in BCS theory the spin-dependent ϕ -fields are self-consistently equal. We thus define our mean-field interaction as

$$\hat{\mathcal{V}}_{\text{BCS}}^{\text{MF}} = - \sum_{j\sigma} \phi_\sigma \hat{c}_{j\sigma}^\dagger \hat{c}_{j\sigma} - \sum_j \Delta \hat{c}_{j\uparrow}^\dagger \hat{c}_{j\downarrow}^\dagger - \sum_j \Delta^* \hat{c}_{j\downarrow} \hat{c}_{j\uparrow} \quad (4.19)$$

where ϕ_σ is a particle-density mean-field, coupling with the number operator $\hat{n}_{j\sigma}$. The spin-dependence allows for magnetisation which, as discussed above, is not necessary for BCS theory. The pairing potential Δ and its Hermitian conjugate Δ^* couples with terms that create a pair of electrons and holes respectively. It is this term that will lead to superconductivity. Additionally, this term is the same pairing potential term introduced in chapter 2. In this case Δ is isotropic in momentum space but, as discussed, it can in principle take more complex forms.

¹Indeed, we will do just this with Stoner theory in chapter 6 when we investigate the magnetisation of this equal-spin pairing theory.

With an explicit form for $\hat{\mathcal{V}}_{\text{BCS}}^{\text{MF}}$ it is now possible to diagonalise $\hat{\mathcal{H}}_{\text{BCS}}^{\text{MF}}$ to obtain the eigenstates and eigenvalues which are required to calculate the free energy, equation (4.15). We shall do this in section 4.4 but before that we will derive the self-consistency equations.

4.3.2 Self consistency equations

Physically the system will want to minimise the free energy, which is a function of the variational mean-fields. The values of the mean-fields obtained after minimising the free energy describe the state of the system e.g. if $\Delta = 0$ minimises the free energy then the system is not superconducting. Here we will derive the self-consistency equations — a set of equations whose solutions directly give the mean-fields that minimise² the free energy.

To minimise the free energy we vary the eigenstates of $\hat{\mathcal{H}}_{\text{BCS}}^{\text{MF}}$ with respect to the mean-fields and require that the variation in free energy be a stationary point, i.e. $\delta F = 0$. Using our expression for F , equation (4.15), we get:

$$\delta F = 0 = \delta \left\langle \hat{\mathcal{H}}_{\text{BCS}} - \hat{\mathcal{H}}_{\text{BCS}}^{\text{MF}} \right\rangle_{\text{MF}} + \delta F_{\text{MF}}.$$

The quantity $F_{\text{MF}} = \left\langle \hat{\mathcal{H}}_{\text{BCS}}^{\text{MF}} \right\rangle_{\text{MF}} - TS_{\text{MF}}$ is already minimised ($\delta F_{\text{MF}} = 0$) with respect to variations in the mean-fields since the eigenvectors of $\hat{\mathcal{H}}_{\text{BCS}}^{\text{MF}}$ are the exact eigenvectors of the Hamiltonian [14]. Using this and equation (4.16) gives

$$\delta \left\langle \hat{\mathcal{V}}_{\text{BCS}}^{\text{MF}} \right\rangle_{\text{MF}} = \delta \left\langle \hat{\mathcal{V}}_{\text{BCS}} \right\rangle_{\text{MF}}.$$

$\delta \left\langle \hat{\mathcal{V}}_{\text{BCS}}^{\text{MF}} \right\rangle_{\text{MF}}$ is simply given by:

$$\begin{aligned} \delta \left\langle \hat{\mathcal{V}}_{\text{BCS}}^{\text{MF}} \right\rangle_{\text{MF}} = \sum_j \left\{ -\phi_{\uparrow} \delta \left\langle \hat{c}_{j\uparrow}^{\dagger} \hat{c}_{j\uparrow} \right\rangle_{\text{MF}} - \phi_{\downarrow} \delta \left\langle \hat{c}_{j\downarrow}^{\dagger} \hat{c}_{j\downarrow} \right\rangle_{\text{MF}} \right. \\ \left. - \Delta \delta \left\langle \hat{c}_{j\uparrow}^{\dagger} \hat{c}_{j\downarrow}^{\dagger} \right\rangle_{\text{MF}} - \Delta^* \delta \left\langle \hat{c}_{j\downarrow} \hat{c}_{j\uparrow} \right\rangle_{\text{MF}} \right\}. \end{aligned} \quad (4.20)$$

To evaluate $\delta \left\langle \hat{\mathcal{V}}_{\text{BCS}} \right\rangle_{\text{MF}}$ we use the product rule to differentiate each of the Gorkov, Hartree and Fock terms in equation (4.17):

$$\begin{aligned} \delta \left\langle \hat{\mathcal{V}}_{\text{BCS}} \right\rangle_{\text{MF}} = -U \sum_j \left\{ \delta \left\langle \hat{c}_{j\uparrow}^{\dagger} \hat{c}_{j\downarrow}^{\dagger} \right\rangle_{\text{MF}} \left\langle \hat{c}_{j\downarrow} \hat{c}_{j\uparrow} \right\rangle_{\text{MF}} + \left\langle \hat{c}_{j\uparrow}^{\dagger} \hat{c}_{j\downarrow}^{\dagger} \right\rangle_{\text{MF}} \delta \left\langle \hat{c}_{j\downarrow} \hat{c}_{j\uparrow} \right\rangle_{\text{MF}} \right. \\ \left. - \delta \left\langle \hat{c}_{j\uparrow}^{\dagger} \hat{c}_{j\downarrow} \right\rangle_{\text{MF}} \left\langle \hat{c}_{j\downarrow}^{\dagger} \hat{c}_{j\uparrow} \right\rangle_{\text{MF}} - \left\langle \hat{c}_{j\uparrow}^{\dagger} \hat{c}_{j\downarrow} \right\rangle_{\text{MF}} \delta \left\langle \hat{c}_{j\downarrow}^{\dagger} \hat{c}_{j\uparrow} \right\rangle_{\text{MF}} \right. \\ \left. + \delta \left\langle \hat{c}_{j\uparrow}^{\dagger} \hat{c}_{j\uparrow} \right\rangle_{\text{MF}} \left\langle \hat{c}_{j\downarrow}^{\dagger} \hat{c}_{j\downarrow} \right\rangle_{\text{MF}} + \left\langle \hat{c}_{j\uparrow}^{\dagger} \hat{c}_{j\uparrow} \right\rangle_{\text{MF}} \delta \left\langle \hat{c}_{j\downarrow}^{\dagger} \hat{c}_{j\downarrow} \right\rangle_{\text{MF}} \right\}. \end{aligned} \quad (4.21)$$

Comparing equations (4.20) and (4.21) and equating the coefficients of the variations, $\delta \langle \dots \rangle_{\text{MF}}$, which are independent of each other, yields the self-consistency equations

$$\Delta = U \left\langle \hat{c}_{j\downarrow} \hat{c}_{j\uparrow} \right\rangle_{\text{MF}} \quad (4.22a)$$

$$\Delta^* = U \left\langle \hat{c}_{j\uparrow}^{\dagger} \hat{c}_{j\downarrow}^{\dagger} \right\rangle_{\text{MF}} \quad (4.22b)$$

$$\phi_{\uparrow} = U \left\langle \hat{c}_{j\downarrow}^{\dagger} \hat{c}_{j\downarrow} \right\rangle_{\text{MF}} \quad (4.22c)$$

$$\phi_{\downarrow} = U \left\langle \hat{c}_{j\uparrow}^{\dagger} \hat{c}_{j\uparrow} \right\rangle_{\text{MF}}. \quad (4.22d)$$

²Technically they find the stationary points of the free energy with no guarantee that the solution is a minimum.

These equations give the values of the mean-fields which correspond to the stationary points of the free energy. Often these equations offer an easier and quicker way of finding the minima of the free energy compared with directly minimising the free energy itself however, as we shall see in chapter 5, these equations sometimes have multiple solutions, requiring the free energy to be calculated in order to determine which solution corresponds to the minimum. To proceed further requires the eigenvectors and eigenvalues of the mean-field Hamiltonian, which we shall now obtain by diagonalisation.

4.4 Diagonalising the mean-field Hamiltonian

In order to evaluate either the free energy or the self-consistency equations we need to be able to calculate various thermal averages using the mean-field eigenvalues and eigenstates. To obtain these quantities we need to diagonalise the mean-field Hamiltonian which we shall do now. For a detailed discussion of diagonalisation, see appendix A.

Using the Fourier transformation, equation (4.3a), the mean-field Hamiltonian can be written in momentum space. The process is the same as we have seen previously, see section 4.1, except for a slight difference when transforming terms with two creation or two annihilation operators. Let us consider, for example, the second term in equation (4.19). Written in momentum space it is given by

$$\begin{aligned} -\sum_j \Delta \hat{c}_{j\uparrow}^\dagger \hat{c}_{j\downarrow}^\dagger &= -\frac{\Delta}{\mathcal{N}} \sum_j \sum_{\mathbf{k}_1} e^{-i\mathbf{k}_1 \cdot \mathbf{R}_j} \hat{c}_{\mathbf{k}_1\uparrow}^\dagger \sum_{\mathbf{k}_2} e^{-i\mathbf{k}_2 \cdot \mathbf{R}_j} \hat{c}_{\mathbf{k}_2\downarrow}^\dagger \\ &= -\frac{\Delta}{\mathcal{N}} \sum_{\mathbf{k}_1 \mathbf{k}_2} \underbrace{\sum_j e^{-i(\mathbf{k}_1 + \mathbf{k}_2) \cdot \mathbf{R}_j}}_{\mathcal{N} \delta_{-\mathbf{k}_1, \mathbf{k}_2}} \hat{c}_{\mathbf{k}_1\uparrow}^\dagger \hat{c}_{\mathbf{k}_2\downarrow}^\dagger \end{aligned}$$

where, this time, the definition of the Kronecker delta function, equation (4.4), requires $-\mathbf{k}_1 - \mathbf{k}_2 = 0$, making $\mathbf{k}_2 = -\mathbf{k}_1$ in all non-zero terms. The \mathcal{N} 's cancel and performing one of the \mathbf{k} -summations gives

$$-\sum_j \Delta \hat{c}_{j\uparrow}^\dagger \hat{c}_{j\downarrow}^\dagger = -\Delta \sum_{\mathbf{k}_1} \hat{c}_{\mathbf{k}_1\uparrow}^\dagger \hat{c}_{-\mathbf{k}_1\downarrow}^\dagger.$$

It is clear now that the mean field Hamiltonian written in momentum space is

$$\hat{\mathcal{H}}_{\text{BCS}}^{\text{MF}} = \sum_{\mathbf{k}\sigma} \epsilon_{\mathbf{k}\sigma} \hat{c}_{\mathbf{k}\sigma}^\dagger \hat{c}_{\mathbf{k}\sigma} - \sum_{\mathbf{k}} \Delta \hat{c}_{\mathbf{k}\uparrow}^\dagger \hat{c}_{\bar{\mathbf{k}}\downarrow}^\dagger - \sum_{\mathbf{k}} \Delta^* \hat{c}_{\bar{\mathbf{k}}\downarrow} \hat{c}_{\mathbf{k}\uparrow},$$

where $\epsilon_{\mathbf{k}\sigma} = \varepsilon_{\mathbf{k}\sigma}^{\sigma\sigma} - \mu - \phi_\sigma$ is the renormalised dispersion of the σ -channel and we have introduced the notation $\bar{\mathbf{k}} = -\mathbf{k}$. In order to diagonalise $\hat{\mathcal{H}}_{\text{BCS}}^{\text{MF}}$ we first write it in matrix form,

$$\hat{\mathcal{H}}_{\text{BCS}}^{\text{MF}} - \sum_{\mathbf{k}} \epsilon_{\mathbf{k}\downarrow} = \sum_{\mathbf{k}} \begin{pmatrix} \hat{c}_{\mathbf{k}\uparrow}^\dagger & \hat{c}_{\bar{\mathbf{k}}\downarrow}^\dagger \end{pmatrix} \begin{pmatrix} \epsilon_{\mathbf{k}\uparrow} & -\Delta \\ -\Delta^* & -\epsilon_{\mathbf{k}\downarrow} \end{pmatrix} \begin{pmatrix} \hat{c}_{\mathbf{k}\uparrow} \\ \hat{c}_{\bar{\mathbf{k}}\downarrow} \end{pmatrix}. \quad (4.23)$$

and, since the matrix $\mathbf{H}_{\text{BCS}}^{\text{MF}} = \begin{pmatrix} \epsilon_{\mathbf{k}\uparrow} & -\Delta \\ -\Delta^* & -\epsilon_{\mathbf{k}\downarrow} \end{pmatrix}$ is Hermitian, it can be diagonalised via a unitary transformation matrix $\mathbf{U} = \begin{pmatrix} u_{\mathbf{k}} & -v_{\mathbf{k}}^* \\ v_{\mathbf{k}} & u_{\mathbf{k}}^* \end{pmatrix}$ in the usual way: $\mathbf{H}_{\text{BCS}}^{\text{MF}} = \mathbf{U} \mathbf{D} \mathbf{U}^*$.

After diagonalisation, equation (4.23) becomes the Bogoliubov de Gennes Hamiltonian $\hat{\mathcal{H}}_{\text{BdG}}$:

$$\hat{\mathcal{H}}_{\text{BdG}} - \sum_{\mathbf{k}} \epsilon_{\mathbf{k}\downarrow} = \sum_{\mathbf{k}} \begin{pmatrix} \hat{\gamma}_{a\mathbf{k}}^\dagger & \hat{\gamma}_{b\mathbf{k}} \end{pmatrix} \begin{pmatrix} \lambda_{a\mathbf{k}} & 0 \\ 0 & \lambda_{b\mathbf{k}} \end{pmatrix} \begin{pmatrix} \hat{\gamma}_{a\mathbf{k}} \\ \hat{\gamma}_{b\mathbf{k}}^\dagger \end{pmatrix} \quad (4.24)$$

where $\lambda_{a\mathbf{k}}$ and $\lambda_{b\mathbf{k}}$ are the eigenvalues of $\mathbf{H}_{\text{BCS}}^{\text{MF}}$ and the $\hat{\gamma}_{m\mathbf{k}}^\dagger$ ($\hat{\gamma}_{m\mathbf{k}}$)-operators can be interpreted as creation (annihilation) operators of some new fermionic quasi-particles, often called Bogoliubons. These Bogoliubons are composed of a linear superposition of particles and holes, as described by the Bogoliubov transformation (see appendix A.4):

$$\hat{\gamma}_{a\mathbf{k}}^\dagger = v_{\mathbf{k}} \hat{c}_{\mathbf{k}\downarrow}^\dagger + u_{\mathbf{k}} \hat{c}_{\mathbf{k}\uparrow}^\dagger \quad \hat{\gamma}_{a\mathbf{k}} = v_{\mathbf{k}}^* \hat{c}_{\mathbf{k}\downarrow}^\dagger + u_{\mathbf{k}}^* \hat{c}_{\mathbf{k}\uparrow} \quad (4.25a)$$

$$\hat{\gamma}_{b\mathbf{k}}^\dagger = u_{\mathbf{k}}^* \hat{c}_{\mathbf{k}\downarrow}^\dagger - v_{\mathbf{k}} \hat{c}_{\mathbf{k}\uparrow}^\dagger \quad \hat{\gamma}_{b\mathbf{k}} = u_{\mathbf{k}} \hat{c}_{\mathbf{k}\downarrow}^\dagger - v_{\mathbf{k}} \hat{c}_{\mathbf{k}\uparrow}. \quad (4.25b)$$

The inverse transformation gives the electron creation/annihilation operators in terms of the Bogoliubon creation/annihilation operators:

$$\hat{c}_{\mathbf{k}\uparrow}^\dagger = u_{\mathbf{k}}^* \hat{\gamma}_{a\mathbf{k}}^\dagger - v_{\mathbf{k}} \hat{\gamma}_{b\mathbf{k}} \quad \hat{c}_{\mathbf{k}\uparrow} = u_{\mathbf{k}} \hat{\gamma}_{a\mathbf{k}} - v_{\mathbf{k}}^* \hat{\gamma}_{b\mathbf{k}}^\dagger \quad (4.26a)$$

$$\hat{c}_{\mathbf{k}\downarrow}^\dagger = v_{\mathbf{k}}^* \hat{\gamma}_{a\mathbf{k}}^\dagger + u_{\mathbf{k}} \hat{\gamma}_{b\mathbf{k}} \quad \hat{c}_{\mathbf{k}\downarrow} = v_{\mathbf{k}} \hat{\gamma}_{a\mathbf{k}} + u_{\mathbf{k}}^* \hat{\gamma}_{b\mathbf{k}}^\dagger. \quad (4.26b)$$

The eigenvalues of $\mathbf{H}_{\text{BCS}}^{\text{MF}}$ are obtained by solving the characteristic polynomial in the usual way (see appendix A.2) and are given by:

$$\lambda_{a\mathbf{k}} = +\sqrt{\xi_{\mathbf{k}\sigma}^2 + \Delta\Delta^*} + s_{\mathbf{k}}^* \\ \lambda_{b\mathbf{k}} = -\sqrt{\xi_{\mathbf{k}\sigma}^2 + \Delta\Delta^*} + s_{\mathbf{k}}^*,$$

where

$$\xi_{\mathbf{k}\sigma} = \frac{1}{2}(\epsilon_{\mathbf{k}\uparrow} + \epsilon_{\mathbf{k}\downarrow}) = \epsilon_{\mathbf{k}} - \mu - \frac{1}{2}(\phi_\uparrow + \phi_\downarrow) \quad (4.28)$$

is the average energy of the two spin-bands and

$$s_{\mathbf{k}}^* = \frac{1}{2}(\epsilon_{\mathbf{k}\uparrow} - \epsilon_{\mathbf{k}\downarrow}) = \frac{1}{2}(\phi_\downarrow - \phi_\uparrow) \quad (4.29)$$

is the effective splitting between them.

We want to write the Hamiltonian $\hat{\mathcal{H}}_{\text{BdG}}$ in the form $\hat{\mathcal{H}}_{\text{BdG}} = \sum_n E_n \hat{\gamma}_n^\dagger \hat{\gamma}_n + E_g$ where E_n is the positive energy associated with adding a quasi-particle created (annihilated) by $\hat{\gamma}_n^\dagger$ ($\hat{\gamma}_n$) [14]. This energy is in addition to a constant energy level corresponding to all quasi-particle states being unoccupied. Equation (4.24) can be written as

$$\begin{aligned} \hat{\mathcal{H}}_{\text{BdG}} &= \sum_{\mathbf{k}} \left\{ \lambda_{a\mathbf{k}} \hat{\gamma}_{a\mathbf{k}}^\dagger \hat{\gamma}_{a\mathbf{k}} + \lambda_{b\mathbf{k}} \hat{\gamma}_{b\mathbf{k}} \hat{\gamma}_{b\mathbf{k}}^\dagger \right\} + \sum_{\mathbf{k}} \epsilon_{\mathbf{k}\downarrow} \\ &= \sum_{\mathbf{k}} \left\{ \lambda_{a\mathbf{k}} \hat{\gamma}_{a\mathbf{k}}^\dagger \hat{\gamma}_{a\mathbf{k}} - \lambda_{b\mathbf{k}} \hat{\gamma}_{b\mathbf{k}}^\dagger \hat{\gamma}_{b\mathbf{k}} \right\} + \sum_{\mathbf{k}} (\epsilon_{\mathbf{k}\downarrow} + \lambda_{b\mathbf{k}}) \\ &= \sum_{\mathbf{k}} \left\{ E_{a\mathbf{k}} \hat{\gamma}_{a\mathbf{k}}^\dagger \hat{\gamma}_{a\mathbf{k}} + E_{b\mathbf{k}} \hat{\gamma}_{b\mathbf{k}}^\dagger \hat{\gamma}_{b\mathbf{k}} \right\} + E_g \end{aligned}$$

where we have used the anti-commutation relations to express $\hat{\gamma}_{b\mathbf{k}} \hat{\gamma}_{b\mathbf{k}}^\dagger$ in normal order.

The powerful interpretation of this Bogoliubov de Gennes transformation is that the BCS system can be described as a system of non-interacting quasi-particle states, rather than worrying about the underlying electrons. There is a ground state, completely devoid of quasi

particles, with energy $E_g = \sum_{\mathbf{k}} (\epsilon_{\mathbf{k}\downarrow} + \lambda_{b\mathbf{k}})$. The energy of the system increases (decreases) by a well defined amount $E_{m\mathbf{k}}$ when a quasi-particle is added ($\hat{\gamma}_{m\mathbf{k}}^\dagger$ (removed $\hat{\gamma}_{m\mathbf{k}}$). The quasi-particle energies are given by $E_{a\mathbf{k}} = \lambda_{a\mathbf{k}}$ and $E_{b\mathbf{k}} = -\lambda_{b\mathbf{k}}$.

We now have the eigenvalues of the mean-field Hamiltonian but still require expressions for the amplitudes of the eigenvectors before proceeding. We shall derive those now by solving the eigenvector equations.

4.4.1 Solving the eigenvector equations

As is explained in appendix A the columns of the transformation matrix \mathbf{U} are eigenvectors of $\mathbf{H}_{\text{BCS}}^{\text{MF}}$ and form eigenvalue equations with the eigenvalues in \mathbf{D} . These eigenvalue equations are a simple instance of the famous ‘‘Bogoliubov de Gennes equations’’ [14] and are given by:

$$\begin{pmatrix} \epsilon_{\mathbf{k}\uparrow} & -\Delta \\ -\Delta^* & -\epsilon_{\mathbf{k}\downarrow} \end{pmatrix} \begin{pmatrix} u_{\mathbf{k}} \\ v_{\mathbf{k}} \end{pmatrix} = \lambda_{a\mathbf{k}} \begin{pmatrix} u_{\mathbf{k}} \\ v_{\mathbf{k}} \end{pmatrix} \quad \text{and} \quad \begin{pmatrix} \epsilon_{\mathbf{k}\uparrow} & -\Delta \\ -\Delta^* & -\epsilon_{\mathbf{k}\downarrow} \end{pmatrix} \begin{pmatrix} -v_{\mathbf{k}}^* \\ u_{\mathbf{k}}^* \end{pmatrix} = \lambda_{b\mathbf{k}} \begin{pmatrix} -v_{\mathbf{k}}^* \\ u_{\mathbf{k}}^* \end{pmatrix}.$$

This gives us a set of four equations which can be used to work out the expressions for the eigenvector amplitudes

$$\epsilon_{\mathbf{k}\uparrow} u_{\mathbf{k}} - \Delta v_{\mathbf{k}} = \lambda_{a\mathbf{k}} u_{\mathbf{k}} \quad (4.30a)$$

$$-\Delta^* u_{\mathbf{k}} - \epsilon_{\mathbf{k}\downarrow} v_{\mathbf{k}} = \lambda_{a\mathbf{k}} v_{\mathbf{k}} \quad (4.30b)$$

$$-\epsilon_{\mathbf{k}\uparrow} v_{\mathbf{k}}^* - \Delta u_{\mathbf{k}}^* = -\lambda_{b\mathbf{k}} v_{\mathbf{k}}^* \quad (4.30c)$$

$$\Delta^* v_{\mathbf{k}}^* - \epsilon_{\mathbf{k}\downarrow} u_{\mathbf{k}}^* = \lambda_{b\mathbf{k}} u_{\mathbf{k}}^*. \quad (4.30d)$$

Solving 4.30a for Δ and substituting into 4.30c gives

$$(\epsilon_{\mathbf{k}\uparrow} - \lambda_{a\mathbf{k}}) u_{\mathbf{k}} u_{\mathbf{k}}^* = (-\epsilon_{\mathbf{k}\uparrow} + \lambda_{b\mathbf{k}}) v_{\mathbf{k}} v_{\mathbf{k}}^*.$$

Recalling that for a unitary transformation we have $u_{\mathbf{k}} u_{\mathbf{k}}^* + v_{\mathbf{k}} v_{\mathbf{k}}^* = 1$ we can write the expression in terms of just $u_{\mathbf{k}} u_{\mathbf{k}}^*$ or $v_{\mathbf{k}} v_{\mathbf{k}}^*$ giving the familiar expressions of BCS theory [14]:

$$u_{\mathbf{k}} u_{\mathbf{k}}^* = \frac{1}{2} \left(1 + \frac{\xi_{\mathbf{k}\sigma}}{\sqrt{\xi_{\mathbf{k}\sigma}^2 + \Delta \Delta^*}} \right) \quad (4.31a)$$

$$v_{\mathbf{k}} v_{\mathbf{k}}^* = \frac{1}{2} \left(1 - \frac{\xi_{\mathbf{k}\sigma}}{\sqrt{\xi_{\mathbf{k}\sigma}^2 + \Delta \Delta^*}} \right). \quad (4.31b)$$

If we instead solve 4.30a for $\epsilon_{\mathbf{k}\uparrow}$ and substitute into 4.30c we obtain:

$$-\Delta (v_{\mathbf{k}} v_{\mathbf{k}}^* + u_{\mathbf{k}} u_{\mathbf{k}}^*) = (\lambda_{a\mathbf{k}} - \lambda_{b\mathbf{k}}) u_{\mathbf{k}} v_{\mathbf{k}}^*$$

again using the unitary condition gives the well known expression from the BCS gap equation [14]:

$$u_{\mathbf{k}} v_{\mathbf{k}}^* = \frac{-\Delta}{2\sqrt{\xi_{\mathbf{k}\sigma}^2 + \Delta \Delta^*}}. \quad (4.32)$$

Now that we have the eigenvalues and amplitudes we can derive the self consistency equations.

4.5 Deriving the self-consistency equations

In section 4.3.2 the mean-field self-consistency equations (4.22) were derived. This section will demonstrate the steps involved in evaluating those equations. First we consider the self-consistent gap equation, equation (4.22a), which gives the value of Δ that minimises the free energy.

4.5.1 Gap equation

As usual we use the Fourier transforms, equation (4.3a), to write the gap self-consistency equation, equation (4.22a), in momentum space:

$$\Delta = \frac{U}{\mathcal{N}} \sum_{\mathbf{k}_1 \mathbf{k}_2} e^{i(\mathbf{k}_1 + \mathbf{k}_2) \cdot \mathbf{R}_j} \left\langle \hat{c}_{\mathbf{k}_1 \downarrow} \hat{c}_{\mathbf{k}_2 \uparrow} \right\rangle_{\text{MF}}.$$

By introducing a sum over all sites to both sides we can use equation (4.4) to simplify:

$$\begin{aligned} \sum_j \Delta &= \frac{U}{\mathcal{N}} \sum_{\mathbf{k}_1 \mathbf{k}_2} \overbrace{\sum_j e^{i(\mathbf{k}_1 + \mathbf{k}_2) \cdot \mathbf{R}_j}}^{\mathcal{N} \delta_{\mathbf{k}_1 \bar{\mathbf{k}}_2}} \left\langle \hat{c}_{\mathbf{k}_1 \downarrow} \hat{c}_{\mathbf{k}_2 \uparrow} \right\rangle_{\text{MF}} \\ \mathcal{N} \Delta &= U \frac{1}{\mathcal{N}} \sum_{\mathbf{k}_1 \mathbf{k}_2} \mathcal{N} \delta_{\mathbf{k}_1 \bar{\mathbf{k}}_2} \left\langle \hat{c}_{\mathbf{k}_1 \downarrow} \hat{c}_{\mathbf{k}_2 \uparrow} \right\rangle_{\text{MF}}. \end{aligned}$$

\mathcal{N} can be cancelled from both sides and, performing one of the \mathbf{k} -summations, $\delta_{\mathbf{k}_1 \bar{\mathbf{k}}_2}$ ensures only terms with $\mathbf{k}_1 = \bar{\mathbf{k}}_2$ are non-zero. We relabel the dummy variable $\mathbf{k}_2 \rightarrow \mathbf{k}$ which gives the gap equation in momentum space

$$\Delta = \frac{U}{\mathcal{N}} \sum_{\mathbf{k}} \left\langle \hat{c}_{\bar{\mathbf{k}} \downarrow} \hat{c}_{\mathbf{k} \uparrow} \right\rangle_{\text{MF}}. \quad (4.33)$$

Using the Bogoliubov transformation, equation (4.26), the electron annihilation operators can be written in terms of the quasi-particle creation/annihilation operators like so:

$$\begin{aligned} \Delta &= \frac{U}{\mathcal{N}} \sum_{\mathbf{k}} \left\langle \left(v_{\mathbf{k}}^* \hat{\gamma}_{a\mathbf{k}}^\dagger + u_{\mathbf{k}} \hat{\gamma}_{b\mathbf{k}} \right) \left(u_{\mathbf{k}} \hat{\gamma}_{a\mathbf{k}} - v_{\mathbf{k}}^* \hat{\gamma}_{b\mathbf{k}}^\dagger \right) \right\rangle_{\text{MF}} \\ \Delta &= \frac{U}{\mathcal{N}} \sum_{\mathbf{k}} \left\{ v_{\mathbf{k}}^* u_{\mathbf{k}} \left\langle \hat{\gamma}_{a\mathbf{k}}^\dagger \hat{\gamma}_{a\mathbf{k}} \right\rangle_{\text{MF}} - v_{\mathbf{k}}^* v_{\mathbf{k}}^* \left\langle \hat{\gamma}_{a\mathbf{k}}^\dagger \hat{\gamma}_{b\mathbf{k}}^\dagger \right\rangle_{\text{MF}} + u_{\mathbf{k}} u_{\mathbf{k}} \left\langle \hat{\gamma}_{b\mathbf{k}} \hat{\gamma}_{a\mathbf{k}} \right\rangle_{\text{MF}} - u_{\mathbf{k}} v_{\mathbf{k}}^* \left\langle \hat{\gamma}_{b\mathbf{k}} \hat{\gamma}_{b\mathbf{k}}^\dagger \right\rangle_{\text{MF}} \right\}. \end{aligned}$$

The Hamiltonian is diagonal in the quasi-particle basis meaning that eigenstates of the system have well defined quasi-particle number, even though the number of electrons/holes is not well defined. As such the thermal averages have to conserve quasi-particle number and obey the mean value rules [14]:

$$\left\langle \hat{\gamma}_{m\alpha}^\dagger \hat{\gamma}_{m\beta} \right\rangle = \delta_{nm} \delta_{\alpha\beta} f(E_{n\alpha}) \quad (4.34a)$$

$$\left\langle \hat{\gamma}_{m\alpha} \hat{\gamma}_{m\beta} \right\rangle = 0. \quad (4.34b)$$

Here $f(E_{n\alpha})$ is the Fermi-Dirac distribution, equation (4.11).

Writing all terms in normal order and using the mean value rules to identify the non-zero averages gives the gap equation as

$$\begin{aligned} \Delta &= \frac{U}{\mathcal{N}} \sum_{\mathbf{k}} \left\{ v_{\mathbf{k}}^* u_{\mathbf{k}} \left\langle \hat{\gamma}_{a\mathbf{k}}^\dagger \hat{\gamma}_{a\mathbf{k}} \right\rangle_{\text{MF}} - u_{\mathbf{k}} v_{\mathbf{k}}^* \left(1 - \left\langle \hat{\gamma}_{b\mathbf{k}}^\dagger \hat{\gamma}_{b\mathbf{k}} \right\rangle_{\text{MF}} \right) \right\} \\ \Delta &= \frac{U}{\mathcal{N}} \sum_{\mathbf{k}} \left\{ -u_{\mathbf{k}} v_{\mathbf{k}}^* \left(1 - \left\langle \hat{\gamma}_{a\mathbf{k}}^\dagger \hat{\gamma}_{a\mathbf{k}} \right\rangle_{\text{MF}} \right) - \left\langle \hat{\gamma}_{b\mathbf{k}}^\dagger \hat{\gamma}_{b\mathbf{k}} \right\rangle_{\text{MF}} \right\}. \end{aligned}$$

The remaining thermal averages are given by the Fermi-Dirac distribution and $u_{\mathbf{k}}v_{\mathbf{k}}^*$ is known from equation (4.32) making the gap equation

$$\Delta = \frac{U}{\mathcal{N}} \sum_{\mathbf{k}} \left\{ \frac{\Delta}{2\sqrt{\xi_{\mathbf{k}\sigma}^2 + \Delta\Delta^*}} [1 - f(E_{a\mathbf{k}}) - f(E_{b\mathbf{k}})] \right\}. \quad (4.35)$$

Note in this mean-field treatment of s-wave pairing we include ϕ_{σ} -fields that have a σ -dependence and as a result equation (4.35) looks slightly different to the usual BCS gap equation, equation (4.36). The inclusion of such a σ -dependence is in analogy with our equal-spin pairing theory of chapter 5 (which necessarily has this dependence due to the orbital splitting at the non-interacting level) and facilitates the aforementioned mapping between the two theories. We will see that in this case the free energy is indeed minimised by having $\phi_{\uparrow} = \phi_{\downarrow}$ and so is consistent with other treatments which may not have included this freedom. Indeed, when the ϕ_{σ} -fields are equal the two quasi-particle excitation energies are also equal ($E_{a\mathbf{k}} = E_{b\mathbf{k}}$) and the gap equation takes on the familiar form:

$$\Delta = \frac{U}{\mathcal{N}} \sum_{\mathbf{k}} \left\{ \frac{\Delta}{2\sqrt{\epsilon_{\mathbf{k}}^2 + \Delta\Delta^*}} [1 - 2f(E_{a\mathbf{k}})] \right\}. \quad (4.36)$$

4.5.2 Hartree self-consistency equation

We now do the same for the self-consistency equations for the ϕ -fields, equations (4.22c) and (4.22d). First we write them in momentum space:

$$\begin{aligned} \phi_{\uparrow} &= \frac{U}{\mathcal{N}} \sum_{\mathbf{k}} \langle \hat{c}_{\mathbf{k}\downarrow}^{\dagger} \hat{c}_{\mathbf{k}\downarrow} \rangle_{\text{MF}} \\ \phi_{\downarrow} &= \frac{U}{\mathcal{N}} \sum_{\mathbf{k}} \langle \hat{c}_{\mathbf{k}\uparrow}^{\dagger} \hat{c}_{\mathbf{k}\uparrow} \rangle_{\text{MF}} \end{aligned}$$

then using the Bogoliubov transform, equation (4.26), to write in terms of the quasi-particle creation/annihilation operators and using the mean value rules, equation (4.34), to simplify gives

$$\begin{aligned} \phi_{\uparrow} &= \frac{U}{\mathcal{N}} \sum_{\mathbf{k}} \left\{ u_{\mathbf{k}}u_{\mathbf{k}}^* \langle \hat{\gamma}_{b\mathbf{k}}^{\dagger} \hat{\gamma}_{b\mathbf{k}} \rangle_{\text{MF}} + v_{\mathbf{k}}v_{\mathbf{k}}^* \left(1 - \langle \hat{\gamma}_{a\mathbf{k}}^{\dagger} \hat{\gamma}_{a\mathbf{k}} \rangle_{\text{MF}} \right) \right\} \\ \phi_{\downarrow} &= \frac{U}{\mathcal{N}} \sum_{\mathbf{k}} \left\{ u_{\mathbf{k}}u_{\mathbf{k}}^* \langle \hat{\gamma}_{a\mathbf{k}}^{\dagger} \hat{\gamma}_{a\mathbf{k}} \rangle_{\text{MF}} + v_{\mathbf{k}}v_{\mathbf{k}}^* \left(1 - \langle \hat{\gamma}_{b\mathbf{k}}^{\dagger} \hat{\gamma}_{b\mathbf{k}} \rangle_{\text{MF}} \right) \right\}. \end{aligned}$$

Again the thermal averages can be replaced by the Fermi-Dirac distribution and the $u_{\mathbf{k}}u_{\mathbf{k}}^*$ and $v_{\mathbf{k}}v_{\mathbf{k}}^*$ terms are given by equations (4.31a) and (4.31b) respectively, giving the self-consistency equations for the ϕ_{σ} -fields as:

$$\phi_{\uparrow} = \frac{U}{\mathcal{N}} \sum_{\mathbf{k}} \left\{ \frac{1}{2} \left(1 + \frac{\xi_{\mathbf{k}\sigma}}{\sqrt{\xi_{\mathbf{k}\sigma}^2 + \Delta\Delta^*}} \right) f(E_{b\mathbf{k}}) + \frac{1}{2} \left(1 - \frac{\xi_{\mathbf{k}\sigma}}{\sqrt{\xi_{\mathbf{k}\sigma}^2 + \Delta\Delta^*}} \right) [1 - f(E_{a\mathbf{k}})] \right\} \quad (4.37)$$

$$\phi_{\downarrow} = \frac{U}{\mathcal{N}} \sum_{\mathbf{k}} \left\{ \frac{1}{2} \left(1 + \frac{\xi_{\mathbf{k}\sigma}}{\sqrt{\xi_{\mathbf{k}\sigma}^2 + \Delta\Delta^*}} \right) f(E_{a\mathbf{k}}) + \frac{1}{2} \left(1 - \frac{\xi_{\mathbf{k}\sigma}}{\sqrt{\xi_{\mathbf{k}\sigma}^2 + \Delta\Delta^*}} \right) [1 - f(E_{b\mathbf{k}})] \right\}. \quad (4.38)$$

The expectation values forming the self-consistency equations are commonly occurring and appear again in the free energy. For convenience we will write the self-consistency equations in a shortened form and define the expectation values short hand notation as follows:

$$\Delta = \frac{U}{\mathcal{N}} \chi \quad (4.39a)$$

$$\phi_{\uparrow} = \frac{U}{\mathcal{N}} N_{\downarrow} \quad (4.39b)$$

$$\phi_{\downarrow} = \frac{U}{\mathcal{N}} N_{\uparrow}, \quad (4.39c)$$

where

$$\begin{aligned} \chi &= \sum_{\mathbf{k}} \langle \hat{c}_{\mathbf{k}\downarrow} \hat{c}_{\mathbf{k}\uparrow} \rangle_{\text{MF}} \\ &= \sum_{\mathbf{k}} \left\{ -u_{\mathbf{k}} v_{\mathbf{k}}^* \left(1 - \langle \hat{\gamma}_{a\mathbf{k}}^{\dagger} \hat{\gamma}_{a\mathbf{k}} \rangle_{\text{MF}} - \langle \hat{\gamma}_{b\mathbf{k}}^{\dagger} \hat{\gamma}_{b\mathbf{k}} \rangle_{\text{MF}} \right) \right\} \\ &= \sum_{\mathbf{k}} \left\{ \frac{\Delta}{2\sqrt{\xi_{\mathbf{k}\sigma}^2 + \Delta\Delta^*}} [1 - f(E_{a\mathbf{k}}) - f(E_{b\mathbf{k}})] \right\}, \end{aligned} \quad (4.40)$$

$$\begin{aligned} N_{\downarrow} &= \sum_{\mathbf{k}} \langle \hat{c}_{\mathbf{k}\downarrow}^{\dagger} \hat{c}_{\mathbf{k}\downarrow} \rangle_{\text{MF}} = \sum_{\mathbf{k}} \hat{n}_{\mathbf{k}\downarrow} \\ &= \sum_{\mathbf{k}} \left\{ u_{\mathbf{k}} u_{\mathbf{k}}^* \langle \hat{\gamma}_{b\mathbf{k}}^{\dagger} \hat{\gamma}_{b\mathbf{k}} \rangle_{\text{MF}} + v_{\mathbf{k}} v_{\mathbf{k}}^* \left(1 - \langle \hat{\gamma}_{a\mathbf{k}}^{\dagger} \hat{\gamma}_{a\mathbf{k}} \rangle_{\text{MF}} \right) \right\} \end{aligned} \quad (4.41)$$

and

$$\begin{aligned} N_{\uparrow} &= \sum_{\mathbf{k}} \langle \hat{c}_{\mathbf{k}\uparrow}^{\dagger} \hat{c}_{\mathbf{k}\uparrow} \rangle_{\text{MF}} = \sum_{\mathbf{k}} \hat{n}_{\mathbf{k}\uparrow} \\ &= \sum_{\mathbf{k}} \left\{ u_{\mathbf{k}} u_{\mathbf{k}}^* \langle \hat{\gamma}_{a\mathbf{k}}^{\dagger} \hat{\gamma}_{a\mathbf{k}} \rangle_{\text{MF}} + v_{\mathbf{k}} v_{\mathbf{k}}^* \left(1 - \langle \hat{\gamma}_{b\mathbf{k}}^{\dagger} \hat{\gamma}_{b\mathbf{k}} \rangle_{\text{MF}} \right) \right\}. \end{aligned} \quad (4.42)$$

N_{\uparrow} and N_{\downarrow} give the number of spin-up and spin-down electrons respectively. Now we shall set about solving the self-consistency equations.

4.6 Self-consistency equations - numerical results

Solving the self-consistency equations properly requires solving all three (equations (4.35), (4.37) and (4.38)) simultaneously, which is complicated by the fact that each equation depends on all of the mean-fields. Before we discuss how to solve these equations simultaneously we will first consider the gap equation only and examine it from a mathematical perspective by use of a ‘contouring method’. Following that we will solve all three self-consistency equations simultaneously with an iterative solver.

4.6.1 Solving the self-consistent gap equation via the contour method

We will first examine the self-consistent gap equation from a mathematical perspective. By that we mean the equation will be solved but that the solutions will not in general correspond to the minimum of the free energy, i.e. the results will be perfectly mathematically valid but will not in general be physically correct. This is necessarily the case because we are solving the gap equation only. In order to do so the ϕ -fields are assigned some arbitrary values - they

are not self-consistent and hence are unlikely to correspond to the global minima of the free energy. As such the solutions obtained may not be physically exact but often do provide a good first order approximation to the behaviour of Δ .

Recall that in two-dimensions $\mathcal{N} = \mathcal{N} = (L/a)^2$ and $\sum_k \dots = (L/2\pi)^2 \iint \dots dk_x dk_y$. Using this, equation (4.35) is written in integral form

$$\Delta = U \left(\frac{1}{2\pi} \right)^2 \iint \left\{ \frac{\Delta}{2\sqrt{\xi_{\mathbf{k}\sigma}^2 + \Delta\Delta^*}} [1 - f(E_{a\mathbf{k}}) - f(E_{b\mathbf{k}})] \right\} dk_x a dk_y a.$$

The same reasoning can be used to write equations (4.37) and (4.38) in integral form. Cancelling Δ from both sides and taking U to the left hand side, the gap equation becomes

$$\frac{1}{U} = \left(\frac{1}{2\pi} \right)^2 \iint \left\{ \frac{\Delta}{2\sqrt{\xi_{\mathbf{k}\sigma}^2 + \Delta\Delta^*}} [1 - f(E_{a\mathbf{k}}) - f(E_{b\mathbf{k}})] \right\} dk_x a dk_y a. \quad (4.43)$$

The right hand side depends only on Δ and T for a fixed μ , ϕ_\uparrow and ϕ_\downarrow . Using a numerical integration routine (scipy's [6] inbuilt 'nquad' method, own implementation of a Monte Carlo integration [128] routine, or any other suitable routine) to evaluate the integral for multiple Δ and T , one produces a surface where the z -axis $\propto \frac{1}{U}$. Contour lines on this surface then give Δ vs T for a given U . Figure 4.5 shows the solutions of the BCS self-consistent gap equation obtained via this 'contouring method'.

Figure 4.5a shows the usual behaviour expected of BCS theory (see [14]): At some critical temperature, T_c , the order parameter, Δ , suddenly becomes finite, then increases until reaching saturation, Δ_0 , at $T = 0$. Increasing the interaction, U , increases the critical temperature, T_c . The value of T_c agrees well with the value predicted by BCS theory, i.e. $\Delta_0 = 1.76k_B T_c$. At $U = 3.6$ there is a percentage difference of -0.5% between the calculated and predicted value of T_c and is the largest error of all the contours shown. Note that the value of the chemical potential, μ , can make some calculations numerically difficult (i.e. $\mu = 0$ causes the Van Hove singularity in the density of states to become dominant) and can cause a greater difference between the calculated and predicted value of T_c unless the numerical parameters (number of integration points, integration tolerance, pre-calculated values of density of states) are improved. In this case the fields were chosen such that the effective spin-splitting was zero i.e. $\phi_\uparrow = \phi_\downarrow$ which is consistent with the usual treatment of BCS theory, but in general we can choose our fields in such a way that the effective splitting is finite.

Figure 4.5b shows the behaviour of equation (4.43) when the ϕ -fields are chosen to give finite effective splitting. This behaviour is qualitatively quite different from the expected BCS behaviour. For large enough interaction the behaviour remains BCS-like but for smaller interaction at a fixed T there may exist multiple non-trivial solutions to the gap equation. This highlights how the ϕ -fields can affect the solutions to the gap equation and that it is necessary to self-consistently determine all fields and, in the cases where multiple solutions exist, determine the solution that minimises the free energy. In this case, as we shall see, self-consistently determining all mean-fields reveals $\phi_\uparrow = \phi_\downarrow$ and therefore the discussion of finite splitting between the spin bands is not relevant for BCS theory. As such we will delay a discussion of finite splitting until chapter 5, where the splitting (this time between orbitals rather than spins) becomes relevant.

We have seen that, when solved by itself, the self-consistent gap equation gives some insight into the potential behaviour of the system however that behaviour can vary significantly

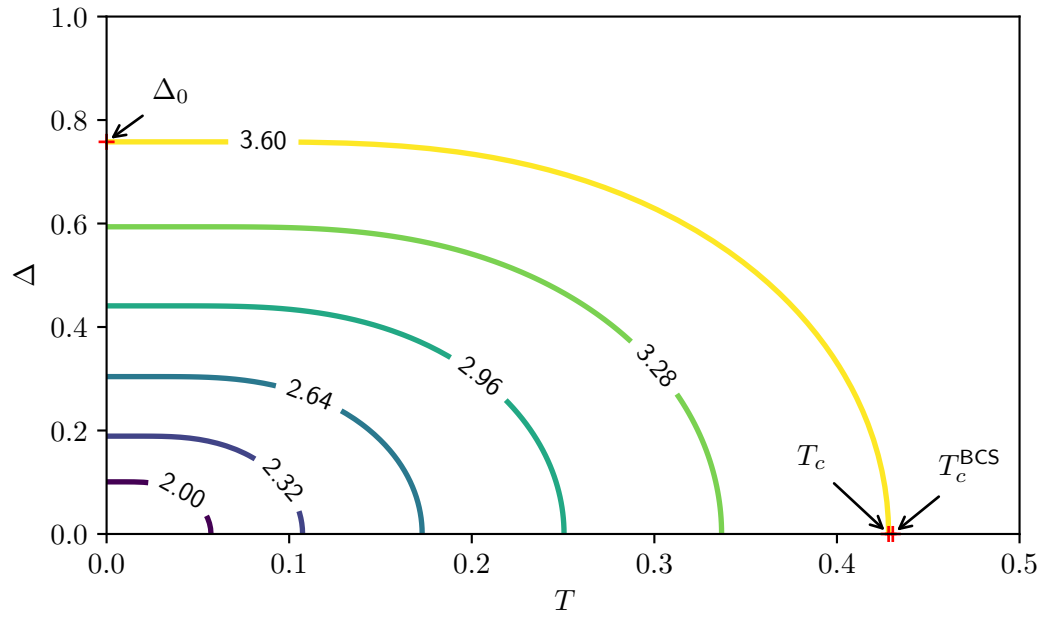
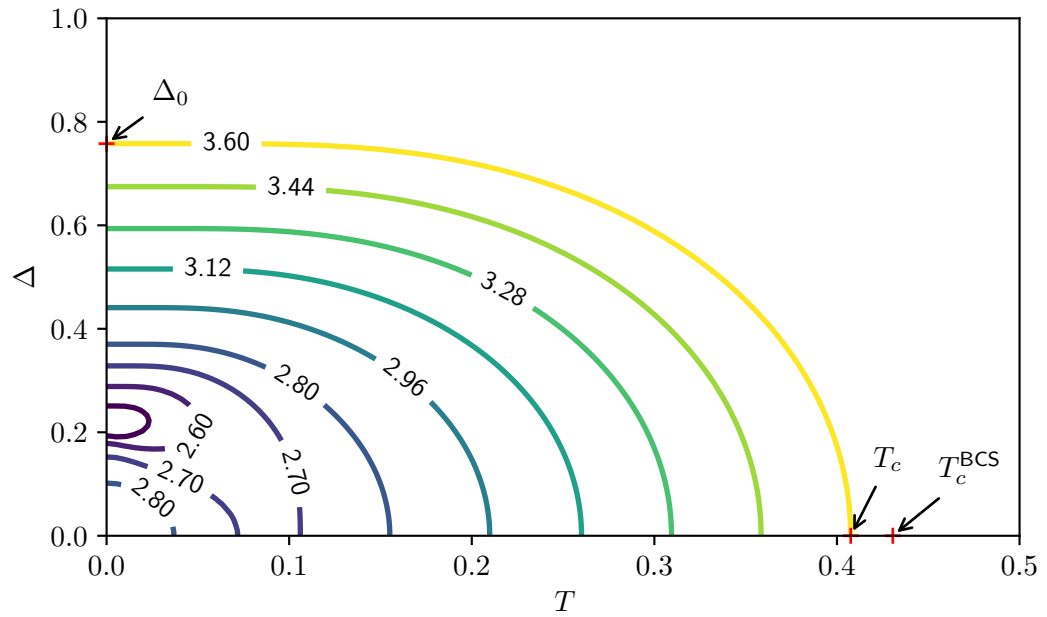
(a) Zero effective splitting: $\phi_{\uparrow} = \phi_{\downarrow} = 0$ (b) Finite effective splitting: $\phi_{\uparrow} = -\phi_{\downarrow} = 0.2$

Figure 4.5: Solution to the BCS self-consistent gap equation. The different lines show Δ vs T for different interaction strengths, U , obtained by solving the self-consistent gap equation for arbitrary values of chemical potential and ϕ -fields. Figures 4.5a and 4.5b correspond to zero and finite effective splitting respectively. In both cases $\mu = -2$.

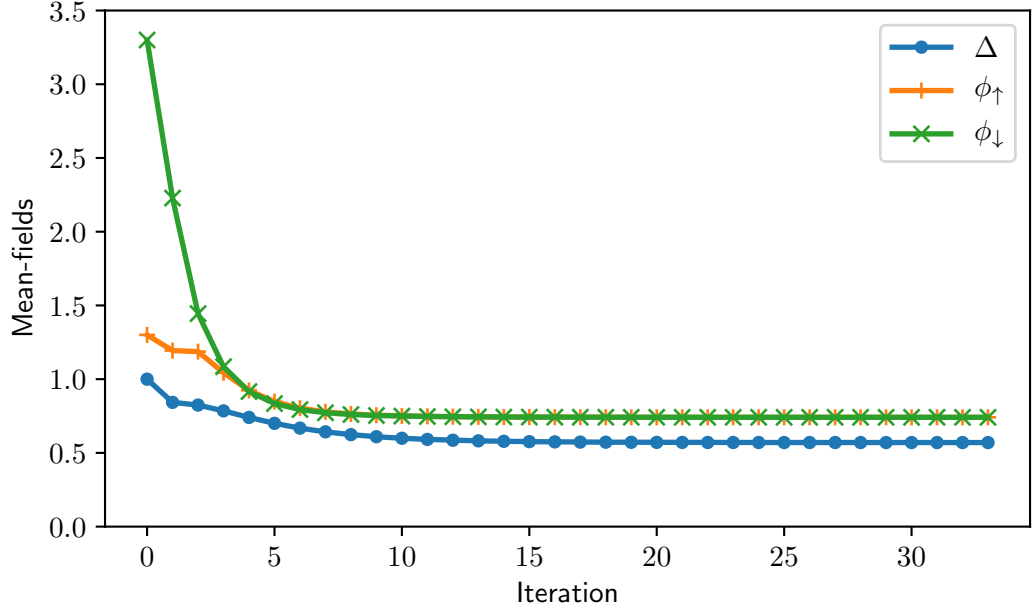


Figure 4.6: Evolution of the mean-fields during the iterative process of solving all self-consistency equations. The self-consistency equations with chemical potential $\mu = -2.3$, interaction $U = 2.8$ and temperature $T = 0.05$ are solved iteratively. The mean-fields vary with each iteration, converging on the self-consistent values until some tolerance is reached.

depending on the values of the other mean-fields. It is necessary therefore to calculate all mean-fields simultaneously in a self-consistent manner. We shall do this now.

4.6.2 Solving self-consistency equations iteratively

Solving the self-consistent equations simultaneously can be done iteratively by a simple algorithm. In its most basic form this iterative solver consists of a single loop which repeatedly solves all three self-consistent equations. To start, an initial guess of the mean-field values is made and used to solve the self-consistency equations. The result of solving all three equations is then used as the input for the next iteration. The loop continues until some convergence condition is met. While this algorithm is fast, it is not guaranteed to converge. Furthermore if it does converge then while the solutions are guaranteed to be stationary points they are not guaranteed to be *minima* of the free energy.

When solving for Δ there is always one trivial solution, $\Delta = 0$. It is important not to start with an initial guess too close to this value as the algorithm may miss any non-trivial solutions. It can also happen that the algorithm may ‘jump’ past a solution, then tend towards the trivial solution. To avoid this we introduce a numerical ‘friction’ term, which uses a small amount of the current solution when forming the new solution, i.e. the value of the gap at the $(i + 1)$ ’th iteration, Δ_{i+1} , would be given by

$$\Delta_{i+1} = (1 - f)U\chi + f\Delta_i.$$

Here f is the friction, a small number which scales how much of the current value of Δ to include in the next guess. When $f = 0$ the next value of the gap Δ_{i+1} is determined entirely by the solution to the self-consistency equation. At each iteration all mean-fields are calculated

in a similar fashion and used as the input on the next iteration. Figure 4.6 shows how the mean-fields vary with each iteration as the self-consistency equations are solved. Starting at the initial guess, the mean-fields change at each iteration, converging on the self-consistent solution.

Solving the self-consistency equations iteratively enables us to obtain information about how Δ changes with temperature T at different interaction strengths U , much in the same way that solving the gap equation with the contour method gave us figures 4.5a and 4.5b. Unlike in those cases however, where we had to solve the self-consistent gap equation for some arbitrary values of ϕ_σ , this time we obtain all three mean-fields self-consistently and ϕ_σ are no longer free parameters. The result is figure 4.7 where the temperature dependence of Δ and the ϕ -fields are shown in the top and bottom panels respectively.

The top panel in figure 4.7 is similar to figure 4.5a, which is as expected for BCS theory, supporting the results obtained by the contour method with zero splitting between spins and implying that the result obtained when the splitting is finite, figure 4.5b, is not self-consistent. We note that T_c is very close to the value predicted by BCS, T_c^{BCS} , with the difference between the two values dependent on how T_c is numerically determined. The slight discrepancy that still exists is due to numerical errors, which are most significant around T_c , where the integrations become numerically difficult, smoothing the transition. The two main sources of error when solving the self-consistency equations iteratively are: firstly, the precision with which integrations are performed and secondly, the number of iterations performed by the algorithm (or equivalently, the requested tolerance). Improving both of these improves the estimation of T_c , at the expense of computation time.

The bottom panel of figure 4.7 shows that $\phi_\uparrow = \phi_\downarrow$ and compared with Δ , the ϕ -fields are relatively temperature-independent. The equivalence of these two mean-fields is expected in BCS theory because, as each field is proportional to the number of particles $\phi_\sigma \propto N_\sigma$, $\phi_\uparrow \neq \phi_\downarrow$ would imply an imbalance in spin populations and hence a net magnetisation - the opposite of what is expected in superconductors. It should be noted that below T_c there is in fact a slight difference between the two ϕ -fields. This difference is small, of the order of 10^{-8} however, it is a well understood numerical artefact and not physical. It can be understood after deriving and solving the free energy, which we shall do now.

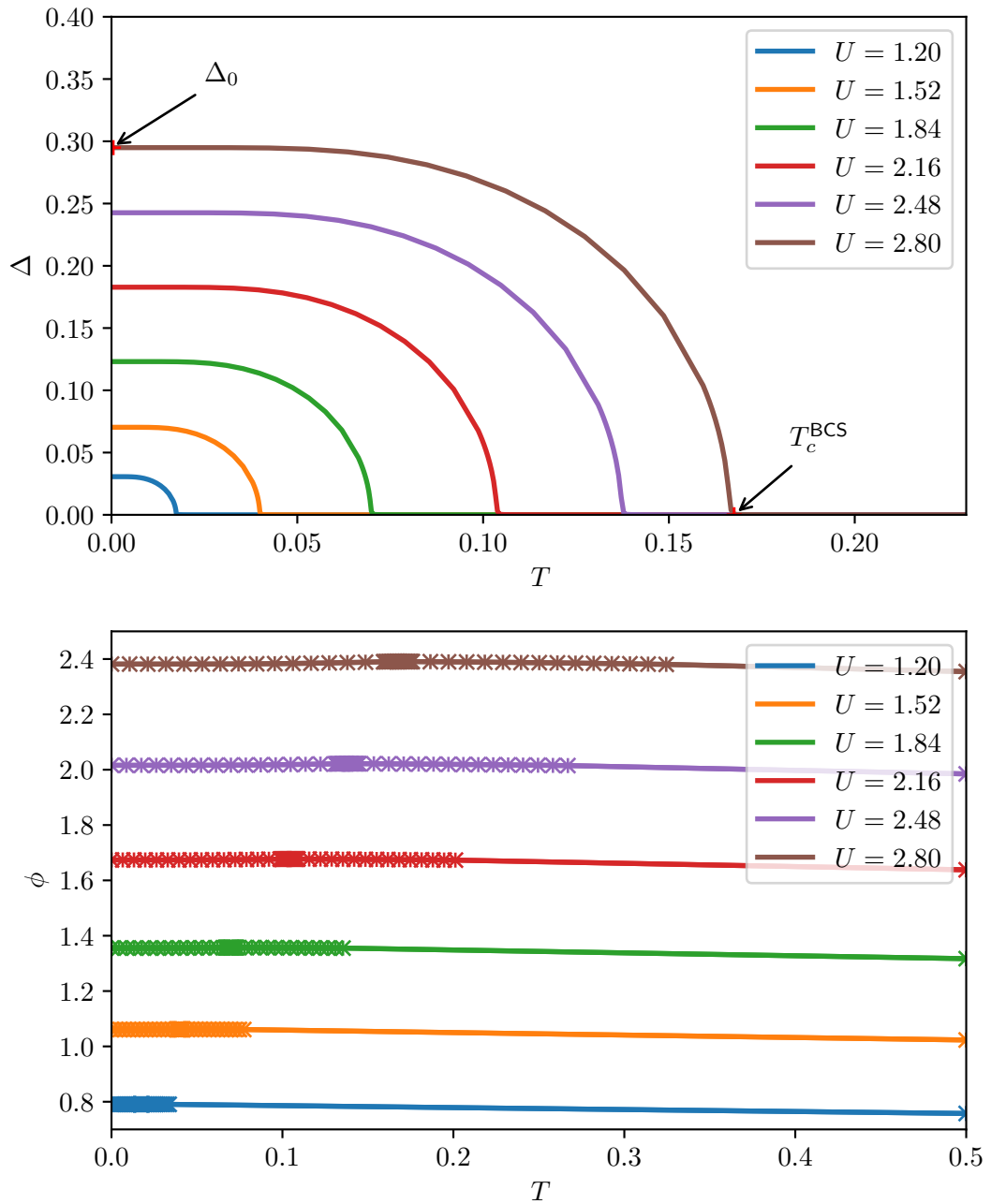


Figure 4.7: Solutions of the self-consistency equations obtained by solving iteratively. In both panels, the different colour lines correspond to different values of interaction U . The top panel shows typical BCS temperature dependence of Δ . The temperature at which Δ becomes finite is in good agreement with the critical temperature predicted by BCS: $T_c^{\text{BCS}} = \Delta_0/1.76$. The lower panel shows the self-consistently determined ϕ_{\uparrow} - and ϕ_{\downarrow} -fields, corresponding to lines with \times and $+$ markers respectively. The ϕ -fields are comparatively less temperature dependent than pairing potential Δ and they are spin independent i.e. $\phi_{\uparrow} = \phi_{\downarrow}$.

4.7 Free Energy

In this section we derive two forms of the free energy: the ground state free energy where $T = 0$ and the general form valid for all T . The free energy is useful as it can be used to verify the solutions to the self-consistent gap equation and, in instances where there is more than one solution, it can reveal which solution is the true minimum, this will become particularly important in chapter 5. Let us start with the zero temperature case.

4.7.1 Zero temperature case

As seen in section 4.3 the free energy is given by equation (4.15) which at zero temperature can be simplified to

$$\begin{aligned} F &\approx \langle \hat{\mathcal{H}}_{\text{BCS}} \rangle_{\text{MF}} \\ &\approx \langle \hat{\mathcal{K}}_{\text{BCS}} \rangle_{\text{MF}} - \mu \langle \hat{\mathcal{N}} \rangle_{\text{MF}} + \langle \hat{\mathcal{V}}_{\text{BCS}} \rangle_{\text{MF}} \\ &\approx \sum_{\mathbf{k}\sigma} (\epsilon_{\mathbf{k}}^{\sigma\sigma} - \mu) \langle \hat{c}_{\mathbf{k}\sigma}^\dagger \hat{c}_{\mathbf{k}\sigma} \rangle_{\text{MF}} - U \sum_j \langle \hat{c}_{j\uparrow}^\dagger \hat{c}_{j\downarrow}^\dagger \hat{c}_{j\downarrow} \hat{c}_{j\uparrow} \rangle_{\text{MF}}. \end{aligned}$$

The non-interacting expectation value is converted from electron creation/annihilation operators to Bogoliubon operators in exactly the same way as was done before for the self-consistency equations, see section 4.5.2. The interaction term is expanded with Wick's theorem

$$-U \sum_j \langle \hat{c}_{j\uparrow}^\dagger \hat{c}_{j\downarrow}^\dagger \hat{c}_{j\downarrow} \hat{c}_{j\uparrow} \rangle_{\text{MF}} = -U \sum_j \langle \hat{c}_{j\uparrow}^\dagger \hat{c}_{j\downarrow}^\dagger \rangle_{\text{MF}} \langle \hat{c}_{j\downarrow} \hat{c}_{j\uparrow} \rangle_{\text{MF}} \quad (4.44a)$$

$$+U \sum_j \langle \hat{c}_{j\uparrow}^\dagger \hat{c}_{j\downarrow} \rangle_{\text{MF}} \langle \hat{c}_{j\downarrow}^\dagger \hat{c}_{j\uparrow} \rangle_{\text{MF}} \quad (4.44b)$$

$$-U \sum_j \langle \hat{c}_{j\uparrow}^\dagger \hat{c}_{j\uparrow} \rangle_{\text{MF}} \langle \hat{c}_{j\downarrow}^\dagger \hat{c}_{j\downarrow} \rangle_{\text{MF}} \quad (4.44c)$$

and each product of expectation values is written in momentum space, then in terms of the Bogoliubon creation/annihilation operators and finally the mean value rules, equation (4.34), are used to determine which thermal averages are non-zero. We will now demonstrate this for the Gor'Kov term, which written in momentum space is

$$\begin{aligned} -U \sum_j \langle \hat{c}_{j\uparrow}^\dagger \hat{c}_{j\downarrow}^\dagger \rangle_{\text{MF}} \langle \hat{c}_{j\downarrow} \hat{c}_{j\uparrow} \rangle_{\text{MF}} &= -\frac{U}{\mathcal{N}^2} \sum_{\substack{\mathbf{k}_1 \mathbf{k}_2 \\ \mathbf{k}_3 \mathbf{k}_4}} \sum_j e^{i(-\mathbf{k}_1 - \mathbf{k}_2 + \mathbf{k}_3 + \mathbf{k}_4) \cdot \mathbf{R}_j} \langle \hat{c}_{\mathbf{k}_1\uparrow}^\dagger \hat{c}_{\mathbf{k}_2\downarrow}^\dagger \rangle_{\text{MF}} \langle \hat{c}_{\mathbf{k}_3\downarrow} \hat{c}_{\mathbf{k}_4\uparrow} \rangle_{\text{MF}} \\ &= -\frac{U}{\mathcal{N}} \sum_{\mathbf{k}_2 \mathbf{k}_3 \mathbf{k}_4} \langle \hat{c}_{\mathbf{k}_1\uparrow}^\dagger \hat{c}_{\mathbf{k}_2\downarrow}^\dagger \rangle_{\text{MF}} \langle \hat{c}_{\mathbf{k}_3\downarrow} \hat{c}_{\mathbf{k}_4\uparrow} \rangle_{\text{MF}}, \end{aligned}$$

where, while performing the sum over \mathbf{k}_1 , the Kronecker delta function, equation (4.4), restricts $\mathbf{k}_1 = \mathbf{k}_3 + \mathbf{k}_4 - \mathbf{k}_2$. The electron operators are replaced by the Bogoliubon operators using the Bogoliubov transformation, equation (4.26), giving:

$$\begin{aligned} -U \sum_j \langle \hat{c}_{j\uparrow}^\dagger \hat{c}_{j\downarrow}^\dagger \rangle_{\text{MF}} \langle \hat{c}_{j\downarrow} \hat{c}_{j\uparrow} \rangle_{\text{MF}} &= -\frac{U}{\mathcal{N}} \sum_{\mathbf{k}_2 \mathbf{k}_3 \mathbf{k}_4} \left\langle \left(u_{\mathbf{k}_1}^* \hat{\gamma}_{a\mathbf{k}_1}^\dagger - v_{\mathbf{k}_1} \hat{\gamma}_{b\mathbf{k}_1} \right) \left(v_{\mathbf{k}_2} \hat{\gamma}_{a\bar{\mathbf{k}}_2} + u_{\mathbf{k}_2}^* \hat{\gamma}_{b\bar{\mathbf{k}}_2}^\dagger \right) \right\rangle_{\text{MF}} \\ &\quad \left\langle \left(v_{\mathbf{k}_3}^* \hat{\gamma}_{a\bar{\mathbf{k}}_3}^\dagger + u_{\mathbf{k}_3} \hat{\gamma}_{b\bar{\mathbf{k}}_3} \right) \left(u_{\mathbf{k}_4} \hat{\gamma}_{a\mathbf{k}_4} - v_{\mathbf{k}_4}^* \hat{\gamma}_{b\mathbf{k}_4}^\dagger \right) \right\rangle_{\text{MF}}. \end{aligned}$$

Multiplying the brackets, writing the expectation values in normal order and using the mean value rules to eliminate those which are always zero gives

$$-U \sum_j \langle \hat{c}_{j\uparrow}^\dagger \hat{c}_{j\downarrow}^\dagger \rangle_{\text{MF}} \langle \hat{c}_{j\downarrow} \hat{c}_{j\uparrow} \rangle_{\text{MF}} = -\frac{U}{\mathcal{N}} \sum_{\mathbf{k}_2 \mathbf{k}_3 \mathbf{k}_4} \left\{ \left[u_{\mathbf{k}_1}^* v_{\bar{\mathbf{k}}_2} \langle \hat{\gamma}_{a\mathbf{k}_1}^\dagger \hat{\gamma}_{a\bar{\mathbf{k}}_2} \rangle_{\text{MF}} - v_{\mathbf{k}_1} u_{\mathbf{k}_2}^* \left(\delta_{\bar{\mathbf{k}}_2 \mathbf{k}_1} - \langle \hat{\gamma}_{b\bar{\mathbf{k}}_2}^\dagger \hat{\gamma}_{b\mathbf{k}_1} \rangle_{\text{MF}} \right) \right] \right. \\ \left. \left[v_{\mathbf{k}_3}^* u_{\mathbf{k}_4} \langle \hat{\gamma}_{a\bar{\mathbf{k}}_3}^\dagger \hat{\gamma}_{a\mathbf{k}_4} \rangle_{\text{MF}} - u_{\bar{\mathbf{k}}_3} v_{\mathbf{k}_4}^* \left(\delta_{\mathbf{k}_4 \bar{\mathbf{k}}_3} - \langle \hat{\gamma}_{b\mathbf{k}_4}^\dagger \hat{\gamma}_{b\bar{\mathbf{k}}_3} \rangle_{\text{MF}} \right) \right] \right\}$$

the terms in the second set of square brackets will only be finite when $\bar{\mathbf{k}}_3 = \mathbf{k}_4$ which, because $\mathbf{k}_1 = \mathbf{k}_3 + \mathbf{k}_4 - \mathbf{k}_2$, means $\mathbf{k}_1 = \bar{\mathbf{k}}_2$. Therefore

$$-U \sum_j \langle \hat{c}_{j\uparrow}^\dagger \hat{c}_{j\downarrow}^\dagger \rangle_{\text{MF}} \langle \hat{c}_{j\downarrow} \hat{c}_{j\uparrow} \rangle_{\text{MF}} = -\frac{U}{\mathcal{N}} \sum_{\mathbf{k}_2 \mathbf{k}_4} \left\{ \left[-u_{\bar{\mathbf{k}}_2}^* v_{\bar{\mathbf{k}}_2} \left(1 - \langle \hat{\gamma}_{a\bar{\mathbf{k}}_2}^\dagger \hat{\gamma}_{a\bar{\mathbf{k}}_2} \rangle_{\text{MF}} - \langle \hat{\gamma}_{b\bar{\mathbf{k}}_2}^\dagger \hat{\gamma}_{b\bar{\mathbf{k}}_2} \rangle_{\text{MF}} \right) \right] \right. \\ \left. \left[-v_{\mathbf{k}_4}^* u_{\mathbf{k}_4} \left(1 - \langle \hat{\gamma}_{a\mathbf{k}_4}^\dagger \hat{\gamma}_{a\mathbf{k}_4} \rangle_{\text{MF}} - \langle \hat{\gamma}_{b\mathbf{k}_4}^\dagger \hat{\gamma}_{b\mathbf{k}_4} \rangle_{\text{MF}} \right) \right] \right\}.$$

Each square bracket depends on only one of the two momentum labels so the double summation can be written as the product of two separate summations. Those two summations take the same form as the self-consistent gap equation, equation (4.40), or it's complex conjugate, meaning we can finally write this term of the free energy as

$$-U \sum_j \langle \hat{c}_{j\uparrow}^\dagger \hat{c}_{j\downarrow}^\dagger \rangle_{\text{MF}} \langle \hat{c}_{j\downarrow} \hat{c}_{j\uparrow} \rangle_{\text{MF}} = -\frac{U}{\mathcal{N}} \chi \chi^*.$$

The same procedure is applied to the other two terms of the interaction, equations (4.44b) and (4.44c). It turns out that all expectation values in equation (4.44b) are zero, which gives the interaction as:

$$-U \sum_j \langle \hat{c}_{j\uparrow}^\dagger \hat{c}_{j\downarrow}^\dagger \hat{c}_{j\downarrow} \hat{c}_{j\uparrow} \rangle_{\text{MF}} = -\frac{U}{\mathcal{N}} (\chi \chi^* + N_\uparrow N_\downarrow). \quad (4.45)$$

where χ and N_σ are the same expressions from the derivation of the self-consistency equations, equations (4.40) to (4.42). With this, the free energy at $T = 0$ is given by:

$$F_0 = -\frac{U}{\mathcal{N}} (\chi \chi^* + N_\uparrow N_\downarrow) + \sum_{\mathbf{k}} \left\{ \left(\varepsilon_{\mathbf{k}}^{\uparrow\uparrow} - \mu \right) \hat{n}_{\mathbf{k}\uparrow} + \left(\varepsilon_{\mathbf{k}}^{\downarrow\downarrow} - \mu \right) \hat{n}_{\mathbf{k}\downarrow} \right\}. \quad (4.46)$$

Let us now consider the general case of the free energy, valid for all temperatures T .

4.7.2 General case

In general the free energy is given by equation (4.15), which can be simplified, by equation (4.16), to

$$F \approx \langle \hat{\mathcal{V}}_{\text{BCS}} \rangle_{\text{MF}} - \langle \hat{\mathcal{V}}_{\text{BCS}}^{\text{MF}} \rangle_{\text{MF}} + F_{\text{MF}}. \quad (4.47)$$

Writing the expectation values of the interaction terms explicitly gives

$$F \approx -U \sum_j \langle \hat{c}_{j\uparrow}^\dagger \hat{c}_{j\downarrow}^\dagger \hat{c}_{j\downarrow} \hat{c}_{j\uparrow} \rangle_{\text{MF}} + \sum_{j\sigma} \phi_\sigma \langle \hat{c}_{j\sigma}^\dagger \hat{c}_{j\sigma} \rangle \\ + \Delta \sum_j \langle \hat{c}_{j\uparrow}^\dagger \hat{c}_{j\downarrow}^\dagger \rangle + \Delta^* \sum_j \langle \hat{c}_{j\downarrow} \hat{c}_{j\uparrow} \rangle + F_{\text{MF}}. \quad (4.48)$$

The mean-field free energy F_{MF} is given by:

$$F_{\text{MF}} = -k_B T \ln(Z_{\text{MF}}) \quad (4.49)$$

where the partition function Z_{MF} is given by

$$Z_{\text{MF}} = \sum_i e^{-\beta E_i}.$$

Here i is the i 'th configuration, or microstate, of the system and E_i is its total energy. The Bogoliubov transformation means a microstate is described by a ground state with energy E_g , and some well defined number of quasi-particles with energy $E_{m\mathbf{k}}$, see section 4.4. The microstate could range from being completely devoid of Bogoliubons to being completely filled, and any number and combination in between. The Bogoliubons are Fermions and as such all quasi-particle states can be singularly occupied or empty. This can be written as

$$Z_{\text{MF}} = \sum_{n_1=0,1} \sum_{n_2=0,1} \dots \sum_{n_n=0,1} e^{-\beta(E_{n_1}n_1 + E_{n_2}n_2 + \dots + E_{n_n}n_n + E_g)}.$$

Each sum and label n_i corresponds to a different quasi-particle state. There are as many summations as there are quasi-particle states. This combination of summations creates all possible microstates; when all $n_i = 0$ all states are empty which corresponds to the ground state, when all $n_i = 1$ all possible quasi-particle states are filled. The partition function can then be written as:

$$\begin{aligned} Z_{\text{MF}} &= \sum_{n_1=0,1} \sum_{n_2=0,1} \dots \sum_{n_n=0,1} e^{-\beta E_{n_1}n_1} e^{-\beta E_{n_2}n_2} \dots e^{-\beta E_{n_n}n_n} e^{-\beta E_g} \\ &= e^{-\beta E_g} \sum_{n_1=0,1} e^{-\beta E_{n_1}n_1} \sum_{n_2=0,1} e^{-\beta E_{n_2}n_2} \dots \sum_{n_n=0,1} e^{-\beta E_{n_n}n_n} \end{aligned}$$

which can be written more concisely as

$$= e^{-\beta E_g} \prod_i \left\{ \sum_{n_i=0,1} e^{-\beta E_{n_i}n_i} \right\}$$

where the product is over all of quasi-particle states i . Performing the sum over state occupation number gives

$$Z_{\text{MF}} = e^{-\beta E_g} \prod_i \left\{ 1 + e^{-\beta E_{n_i}} \right\}. \quad (4.50)$$

Substituting the partition function, equation (4.50), into the free energy, equation (4.49), gives

$$F_{\text{MF}} = -k_B T \ln \left(e^{-\beta E_g} \prod_i \left\{ 1 + e^{-\beta E_{n_i}} \right\} \right),$$

where the product rule of logarithms gives

$$= E_g - k_B T \sum_i \ln \left(1 + e^{-\beta E_{n_i}} \right).$$

Replacing the abstract state-label i with the specific labels m, \mathbf{k} of the quasi-particle states gives

$$= E_g - k_B T \sum_{m\mathbf{k}} \ln \left(1 + e^{-\beta E_{m\mathbf{k}}} \right).$$

The label m takes the values a and b , representing the two ‘flavours’ of quasi-particle. The mean-field free energy becomes:

$$F_{\text{MF}} = E_g - k_B T \sum_{\mathbf{k}} \left\{ \ln \left(1 + e^{-\beta E_{a\mathbf{k}}} \right) + \ln \left(1 + e^{-\beta E_{b\mathbf{k}}} \right) \right\}. \quad (4.51)$$

Having obtained F_{MF} , we now need to deal with the remaining terms of equation (4.48).

As usual the expectation values in equation (4.48) need to be written in momentum space using the Fourier transform, equation (4.3a), transformed into the Bogoliubon basis using the Bogoliubov transform, equation (4.26), and simplified with the mean value rules, equation (4.34). This has already been done in previous sections; for the interaction expectation $-U \sum_j \langle \hat{c}_{j\uparrow}^\dagger \hat{c}_{j\downarrow}^\dagger \hat{c}_{j\downarrow} \hat{c}_{j\uparrow} \rangle_{\text{MF}}$ see section 4.7.1 equation (4.45), and for the other expectation values accompanying the mean-fields see the derivation of the self-consistency equations, section 4.5. The free energy can now be written

$$F \approx - \frac{U}{\mathcal{N}} (\chi \chi^* + N_\uparrow N_\downarrow) + \phi_\uparrow N_\uparrow + \phi_\downarrow N_\downarrow + \Delta \chi^* + \Delta^* \chi + F_{\text{MF}}. \quad (4.52)$$

This form of the free energy is valid at any temperature but will run into numerical problems at very low temperatures (exponential overflow) and at zero temperature (divide by zero). Hence the $T = 0$ case is useful to help confirm the low temperature results obtained by the general case. Now we shall minimise the free energy numerically.

4.7.3 Free energy - numerics

To calculate the free energy numerically we first write it in integral form in the same way we did for the self-consistency equations, section 4.6. When converting each summation in either free energy expression, equation (4.46) or (4.52), into integral form we use the relation $\sum_{\mathbf{k}} \dots = \frac{\mathcal{N}}{4\pi^2} \iint \dots dk_x a dk_y a$. This results in an extra factor of \mathcal{N} for every summation. It turns out that the overall effect of this conversion is that the free energy picks up an extra factor of \mathcal{N} , which is expected as the free energy is an extensive quantity, dependent on the size of the system. All numerical calculations in this section evaluate the free energy per site, an intensive quantity.

The free energy needs to be minimised with respect to the mean-fields, Δ and ϕ_σ , for a given chemical potential μ , interaction U , and temperature T . We use a ‘hill descent algorithm’ which ‘walks’ its way through the 3D parameter space towards the point of lowest free energy. It is a simple algorithm which works by calculating the free energy around a given point and moving in the direction of the lowest free energy i.e. if the algorithm is at point $(\Delta^i, \phi_\uparrow^i, \phi_\downarrow^i)$ then it evaluates the free energy at the surrounding points

$$\begin{array}{ccc} (\Delta^i + \delta\Delta, \phi_\uparrow^i, \phi_\downarrow^i) & (\Delta^i, \phi_\uparrow^i + \delta\phi, \phi_\downarrow^i) & (\Delta^i, \phi_\uparrow^i, \phi_\downarrow^i + \delta\phi) \\ (\Delta^i - \delta\Delta, \phi_\uparrow^i, \phi_\downarrow^i) & (\Delta^i, \phi_\uparrow^i - \delta\phi, \phi_\downarrow^i) & (\Delta^i, \phi_\uparrow^i, \phi_\downarrow^i - \delta\phi) \end{array}$$

and if, for example, the free energy was lowest in the $+\delta\Delta$ direction then the algorithm would move to that point and once again check the free energy of the surrounding points. It repeats this until no improvements are found (to within some tolerance).

Figure 4.8 shows how the mean-fields (top panel) and free energy (bottom panel) vary as the hill descent algorithm progresses. All quantities tend to converge with increasing iteration, with the ϕ -fields equalising as expected and the free energy lowering until some tolerance is

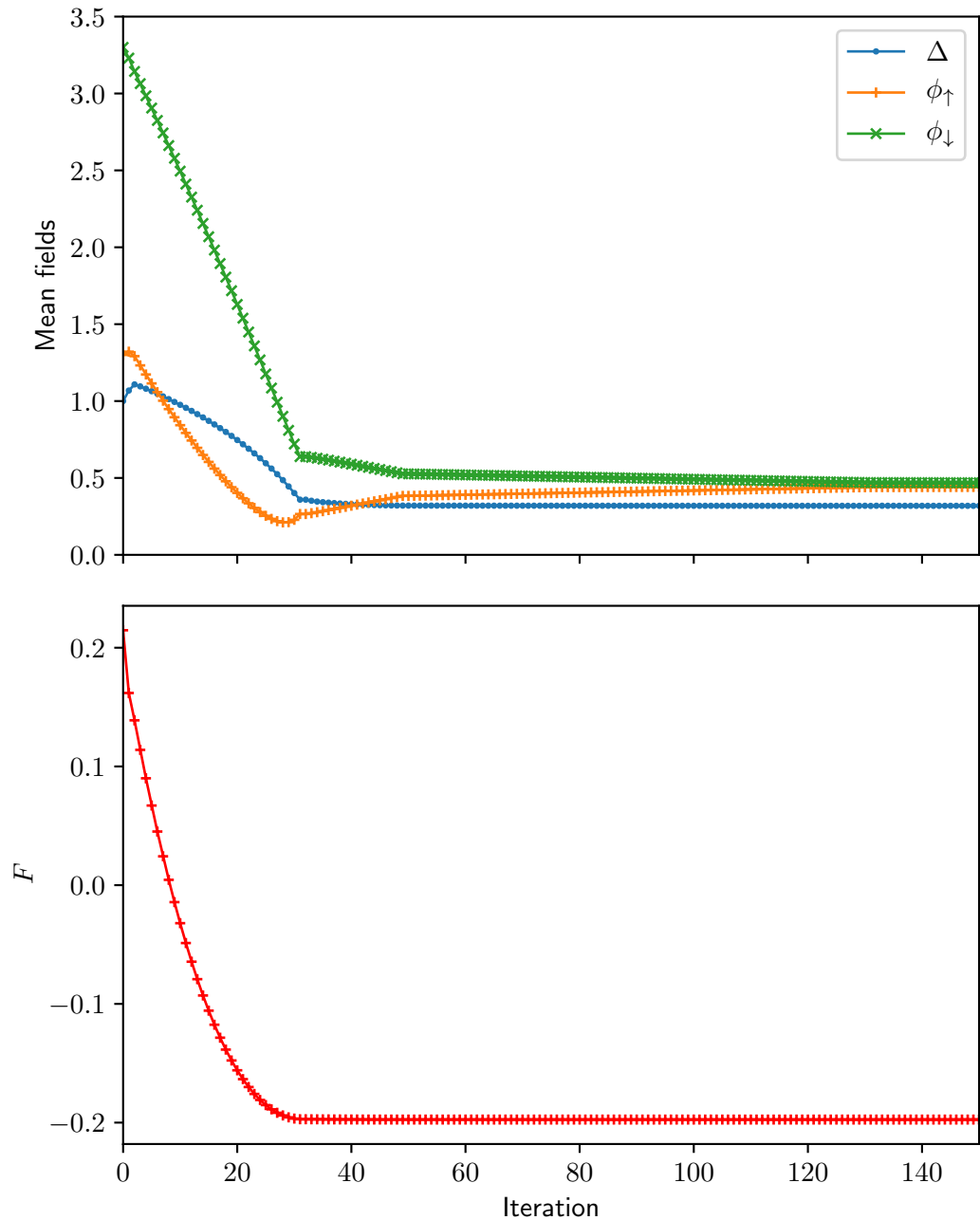


Figure 4.8: Free energy minimisation using the hill descent algorithm. Minimisation of the free energy when chemical potential $\mu = -2.7$, interaction $U = 2.8$ and temperature $T = 0.05$. Both panels show how key quantities vary as the hill descent algorithm proceeds, with the top panel showing how the mean-fields Δ , ϕ_{\uparrow} and ϕ_{\downarrow} vary and the bottom panel showing how the free energy varies. The free energy gets lower as would be expected with a minimisation routine and the ϕ -fields equalise, consistent with the results from the solving the self-consistency equations iteratively and BCS theory.

reached. One advantage of this method over solving the self-consistency equations is that we can actually observe the free energy lowering throughout the process, and if multiple solutions are returned, the one corresponding to the lowest energy is easily determined.

Using the hill descent algorithm the free energy can be minimised for different values of interaction U and temperature T . Doing so we can calculate Δ vs T as was done previously in section 4.6 where the self-consistency equations were solved iteratively. Figure 4.9 shows

the result of this hill descent minimisation alongside the results obtained via the iterative self-consistent solver. The temperature dependence of the Δ - and ϕ -fields is shown in the top and bottom panels of figure 4.9 respectively.

Both methods give the same result: Δ becomes finite at the critical temperature T_c and increases to some saturation value Δ_0 at $T = 0$ while the ϕ -fields equalise; confirming that both the hill descent algorithm and the iterative self-consistent solver are working as expected. The equalisation of the ϕ -fields confirms that the possibility of multiple solutions to the gap equation, as observed in figure 4.5b where the ϕ -fields were chosen to give finite effective splitting, is not physically correct. In the event that multiple solutions do exist, the direct minimisation of the free energy will pick up only the minima while the self-consistency equations make no such distinction. The free energy and its minimisation are useful tools which offer more information than the self-consistency equations but at the cost of computational efficiency.

As mentioned before when discussing the results of the self-consistency equations, there is a small difference between the ϕ -fields below T_c . Even so, the discussion above still holds because, as we shall now see, this difference is a numerical artefact. Running the hill descent algorithm multiple times at $T = 0$ with different initial conditions yields different solutions for the minima, all with the same Δ but with differing values of ϕ_\uparrow and ϕ_\downarrow . Interestingly all these solutions have the same value of $\phi_\uparrow + \phi_\downarrow$, but different $\phi_\downarrow - \phi_\uparrow$. These two quantities are important because every term in the free energy ultimately depends on them through the average energy $\xi_{\mathbf{k}\sigma}$ and the effective splitting $s_{\mathbf{k}}^*$, see equations (4.28) and (4.29).

Figure 4.10 shows the free energy w.r.t. the mean-fields, near the minima, at $T = 0$ for some value of interaction U and chemical potential μ^3 . The line of darkest points at $\Delta \approx 0.3$ all have the same free energy and $\xi_{\mathbf{k}\sigma}$ but different $s_{\mathbf{k}}^*$. In the centre of that line is the solution with $\phi_\uparrow = \phi_\downarrow$ ($s_{\mathbf{k}}^* = 0$), as one traverses that line away from the centre in either direction, $s_{\mathbf{k}}^*$ changes but the free energy remains constant until, at some critical value of $|s_{\mathbf{k}}^*|$ the free energy suddenly increases. This behaviour is observed for different values of Δ and $\xi_{\mathbf{k}\sigma}$, with the line of constant free energy changing in length based on Δ .

At $T = 0$ the line of constant free energy occurs for a range of values of splitting $s_{\mathbf{k}}^*$ because the Fermi-Dirac distribution is insensitive to changes in the splitting. This is depicted in figure 4.11 where at zero-splitting the two energy dispersions of the Bogoliubons are degenerate and *positive* but at $|s_{\mathbf{k}}^*| > \Delta$ the two energy bands separate and part of one crosses the zero-level and becomes *negative* (the sign of $s_{\mathbf{k}}^*$ determines which band will cross). For all $s_{\mathbf{k}}^* < \Delta$ (the light-green region) the energy bands are all positive. Since the Fermi-Dirac distribution at $T = 0$ is a step-function it is only sensitive to the sign of the quasi-particle energy. As such, the contribution to the free energy from the Fermi-Dirac distribution will be the same for all dispersions within the light-green region. Additionally all points along the line of constant free energy have constant $\xi_{\mathbf{k}\sigma}$ and Δ , hence constant free energy.

As soon as the temperature becomes non-zero the Fermi-Dirac distribution is no longer exactly a step function, see figure 4.4. The occupation of energies far away from the chemical potential is almost unchanged but near to it there is a difference. This difference means that the free energy can no longer be constant in the green-region of figure 4.11. As such the line of constant free energy should disappear. Indeed, this can be seen in figure 4.12, which shows the free energy as a function of $s_{\mathbf{k}}^*$, at different temperatures, for a fixed value

³In this example $U = 2.8$ and $\mu = 0$ but the general idea holds as long as Δ is finite

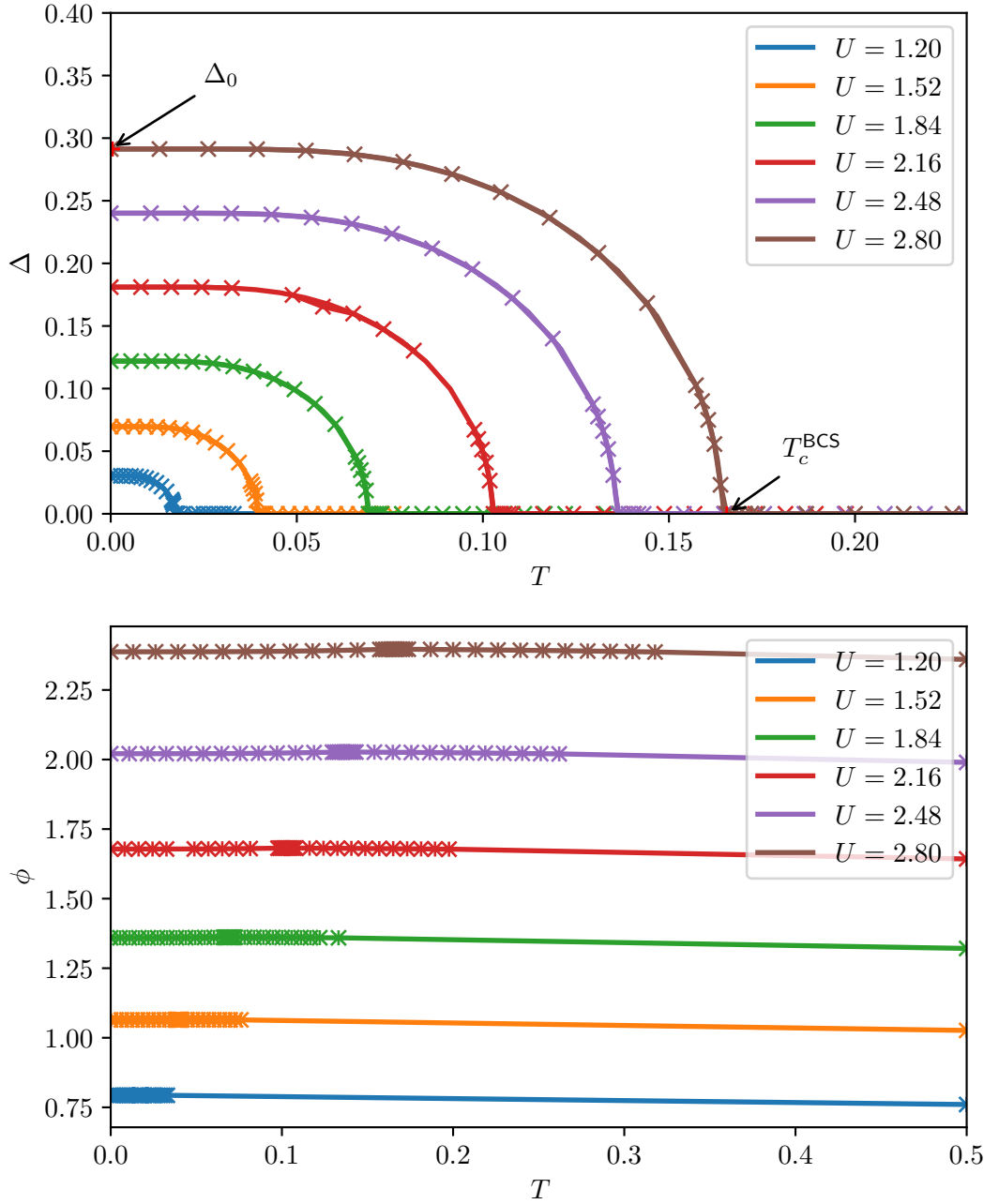


Figure 4.9: Comparison of self-consistent solutions obtained by the self-consistency equations and direct free energy minimisation. Both the hill climb minimisation and solving the self-consistency equations iteratively give the same results. In both panels the different colours correspond to different values of interaction U . The solid lines in both panels were obtained by solving the self-consistency equations iteratively. In the top panel \times -markers were obtained by the Hill climb method. In the bottom panel both the \times - and $+$ -markers were obtained by the hill descent method and correspond to ϕ_{\uparrow} and ϕ_{\downarrow} respectively. The critical temperature as predicted by BCS theory, $T_c^{\text{BCS}} = \Delta_0/1.76$, is labelled for the interaction $U = 2.8$ and is in good agreement with the observed T_c .

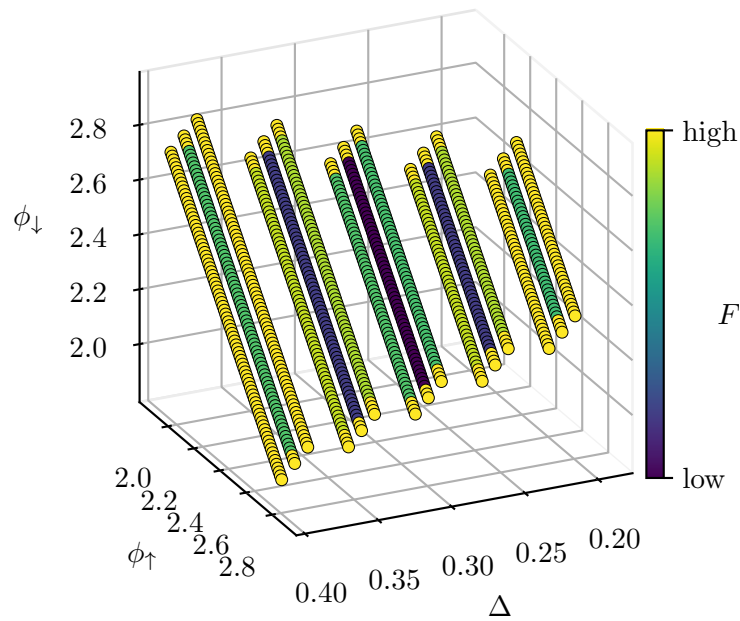


Figure 4.10: Line of constant free energy at zero temperature. The free energy at $T = 0$ is constant along lines of finite length in parameter space where $\phi_\uparrow + \phi_\downarrow = \text{constant}$. The darkest line corresponds to the minimum of the free energy. Changing Δ or $\phi_\uparrow + \phi_\downarrow$ increases the free energy as expected. Unexpectedly however there exists more lines of constant free energy and, moreover, they end abruptly with a sudden increase in free energy when the effective splitting $s_{\mathbf{k}}^* > \Delta$. Note the colour scale has been adjusted to highlight the lines of solutions and their abrupt termination.

of Δ , U and μ . At $T = 0$ the free energy really is constant for $|s_{\mathbf{k}}^*| < \Delta$, whereas for $T > 0$ there exists a minimum at $\phi_\uparrow = \phi_\downarrow$. At small temperatures it is hard to see this minimum because of the scales involved. At such scales neither the relative precision of the integration routine, or the numerical precision of the computer would be enough to capture it, and the free energy would appear constant. It is because of this numerical effect that there appears very slight splitting in the ϕ -fields when Δ is finite and large, as we observed in section 4.6.2. Furthermore, this selection of a particular combination of ϕ_\uparrow and ϕ_\downarrow at $T = 0^+$, out of the many degenerate possibilities at $T = 0$, is an example of ‘order by disorder’ and the same happens, for example, with the Pomeranchuk instability [129].

4.8 Summary

In this chapter we have demonstrated the application of the variational mean-field method to s-wave pairing, otherwise referred to as singlet or BCS pairing. Pairing takes place between electrons of opposite spin and opposite momentum on the same site of a two-dimensional square lattice, due to an attractive interaction. Such an interaction is simply assumed and we do not concern ourselves with its origin⁴.

⁴Of course BCS theory [26] tells us that the origin of such an attraction is down to phonons but since the non-interacting dispersion is naturally bounded between $\pm 4t$ the integrations can be performed numerically without needing to invoke the Debye cut-off.

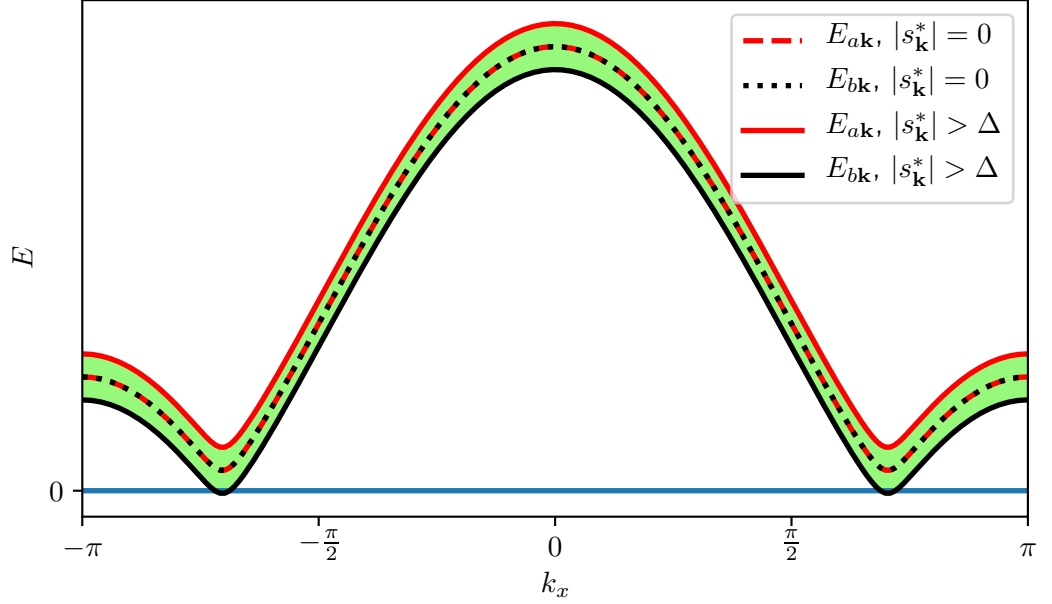


Figure 4.11: The quasi-particle energy spectrum cut along along $k_x = k_y$. When the effective splitting $s_{\mathbf{k}}^*$ is zero the two quasi-particle energy bands (red dashed and black dotted lines) are degenerate and positive. With finite splitting, $s_{\mathbf{k}}^* < \Delta$, the spectrum separate but both remain positive. At large enough splitting, $s_{\mathbf{k}}^* > \Delta$, the separation in the energy bands is large enough that part of one of the bands becomes negative. The sign of $s_{\mathbf{k}}^*$ determines which band becomes negative.

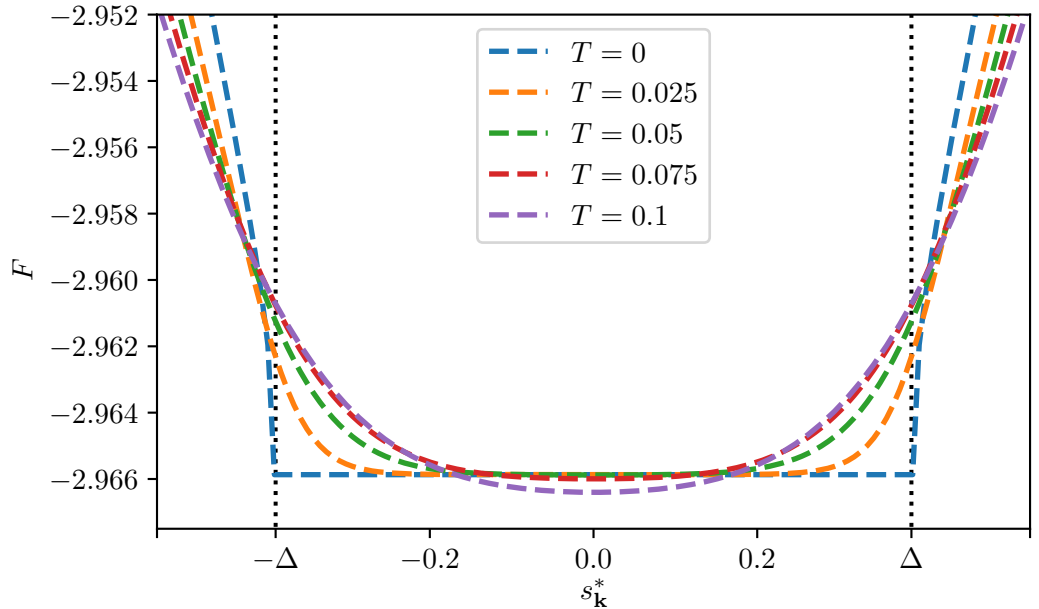


Figure 4.12: Temperature effect on the line of constant free energy. The free energy is calculated near to its minimum with fixed Δ and varying $s_{\mathbf{k}}^*$. At $T = 0$ the free energy is constant when $|s_{\mathbf{k}}^*| < \Delta$. The Fermi-Dirac distribution at this temperature is a step function and is insensitive to changes in $s_{\mathbf{k}}^*$ as long as the quasi-particle energy spectrum remains above the chemical potential μ . At $T > 0$ the Fermi-Dirac function is no longer an exact step function and becomes sensitive to changes in $s_{\mathbf{k}}^*$, with the sensitivity increasing with temperature. This sensitivity causes the free energy to vary with $s_{\mathbf{k}}^*$.

We started in section 4.1 by considering the non-interacting part of the Hamiltonian and derived the non-interacting electron dispersion for the 2D square lattice, where electron hopping was restricted to nearest neighbour sites only, both for simplicity and consistency with our treatment of the equal-spin triplet-pairing theory to come, chapter 5. In doing so we demonstrated how to use the Fourier transform to transform an equation from a real space to a momentum space representation, as well as how the possible hopping available to the electron are included in the non-interacting electron dispersion.

In section 4.2 we introduced the explicit form of the attractive interaction responsible for the electron pairing and, ultimately, superconductivity. As the interaction was quartic in creation/annihilation operators it was not possible to simply diagonalise it as we did for the non-interacting part, hence we turned to variational mean-field theory to proceed, section 4.3. We saw that by introducing a new, variable, exactly solvable Hamiltonian, called the variational mean-field Hamiltonian, $\hat{\mathcal{H}}_{\text{BCS}}^{\text{MF}}$, we could approximate the free energy of, and therefore solve, the original Hamiltonian, $\hat{\mathcal{H}}_{\text{BCS}}$.

Along with the mean-field Hamiltonian we introduced the mean-fields ϕ_{\uparrow} , ϕ_{\downarrow} and Δ — variable parameters which allow $\hat{\mathcal{H}}_{\text{BCS}}^{\text{MF}}$ to approximate $\hat{\mathcal{H}}_{\text{BCS}}$. Δ is the all important pairing potential and is the superconducting order parameter. ϕ_{\uparrow} and ϕ_{\downarrow} couple to the particle densities for up- and down-spins respectively and allow imbalancing of the spin-populations.

We diagonalised the mean-field Hamiltonian by a Bogoliubov de Gennes transformation and saw that we could describe the system in terms of non-interacting quasi-particle excitations (Bogoliubons) on top of a vacuum state devoid of any such quasi-particles, section 4.4. We obtained the energy spectrum for these quasi-particles and obtained the usual expressions for the eigenvector amplitudes $u_{\mathbf{k}}u_{\mathbf{k}}^*$, $v_{\mathbf{k}}v_{\mathbf{k}}^*$ and $u_{\mathbf{k}}v_{\mathbf{k}}^*$. Using these we were able to derive the mean-field self-consistency equations — a set of equations whose solutions correspond to the stationary points of the free energy, sections 4.3.2 and 4.5. As expected, the derived self-consistency equations were consistent with the well known examples from BCS theory.

In section 4.6 we solved the self-consistency equations numerically. We first treated the ϕ -fields as free parameters and solved the self-consistent gap equation for the mean-field Δ . We found that when there was zero effective splitting between the spin flavours, $s_{\mathbf{k}}^* = 0$, the gap equation revealed Δ had the usual temperature dependence of BCS theory, however when the effective splitting was finite, $s_{\mathbf{k}}^* \neq 0$, we found unusual behaviour where the gap equation had more than one non-trivial solution for a given temperature, see figure 4.5. As expected, it turned out that this potentially interesting situation was not realised in BCS theory and as such we shall postpone further discussion until chapter 5, where it becomes relevant to the theory of inter-orbital pairing which, in a certain limit, can be mapped to the pairing between opposite spins in BCS theory.

By solving the self-consistency equations iteratively, section 4.6.2, we could simultaneously determine all mean-fields self-consistently. By doing so we obtained the standard result $\phi_{\uparrow} = \phi_{\downarrow}$ (apart from a very small random splitting at low temperatures, $T \ll T_c$) as expected in BCS theory, i.e. the effective splitting was always zero and hence the unusual behaviour obtained by just solving the gap function with finite splitting imposed was not physically relevant. By solving all self-consistency equations simultaneously we obtained the usual temperature dependence of the order parameter, Δ , which displayed a critical temperature, T_c , with very good agreement to the critical temperature predicted by BCS theory, T_c^{BCS} .

The free energy was then derived for two cases: the general case, section 4.7.1 and the zero

temperature case, section 4.7.2. The general case was valid for all temperatures but would run into numerical problems as $T \rightarrow 0$, while the zero temperature expression was only valid at $T = 0$. Using these expressions the free energy was minimised using a ‘hill descent algorithm’, section 4.7.3. It was found that the results from the free energy minimisation agreed well with the results from solving the self-consistency equations iteratively, a sign that both methods were working as intended. Furthermore, by studying the behaviour of the free energy near to its minimum point we were able to identify that the random, small splitting between the ϕ_{\uparrow} and ϕ_{\downarrow} fields at low temperatures was caused by numerical limitations. Namely, changes in the Fermi-Dirac distribution at very low temperatures, due to varying the effective splitting $s_{\mathbf{k}}^*$, are numerically imperceptible and so there exists a line in parameter space with $|s_{\mathbf{k}}^*| < \Delta$ where the free energy is constant (and minimum). In reality the splitting is exactly zero for all $T > 0$.

In conclusion we have demonstrated the application of variational mean-field theory to the well known case of BCS s-wave pairing. We have introduced the concept of the mean-field Hamiltonian, its mean-fields and the Bogoliubov transformation. Using the Bogoliubov transformation we have seen how a system of interacting electrons can be described by a more simple system of particle-like excitations — Bogoliubons.

The self-consistency equations and free energy have been derived and simple algorithms for solving both numerically have been presented. Using these algorithms we have reproduced the familiar Δ vs T phase diagram of BCS theory and shown that the free energy is minimised when the mean-fields coupling to the two spin-resolved components of the particle density are equivalent, $\phi_{\uparrow} = \phi_{\downarrow}$.

We have shown that the variational mean-field theory can be used to describe a superconducting system by applying it to the well known case of BCS s-wave pairing and by obtaining the same well known expressions for the self-consistency equations and free energy, as well as obtaining the same Δ vs T phase diagram of BCS theory. The main purpose of this chapter was to act as a pedagogical introduction to variational mean field theory and superconductivity, although the results are fairly standard, the technical details included in the derivations and calculations are not often found. Having covered such details here we will be able to focus more on the physics, rather than the technical steps, in what is to come. In the next chapter we shall apply the same variational mean-field method to a novel two-orbital equal-spin triplet-pairing model.

Chapter 5

Variational mean-field theory of two-band equal-spin-pairing

In this chapter we will apply variational mean-field theory to the novel two-band equal-spin triplet-pairing model (ESP) proposed by Weng *et al.* [126] to explain the conflicting experimental results of LaNiGa₂, previously discussed in chapter 3. In this model the attractive interaction acts between electrons with the same spin, on the same site but in two different orbitals to maintain fermion antisymmetry. As discussed by Weng *et al.* [126] the pairing potential has the form $\Delta_{\sigma_1, \sigma_2}^{A, B}(\mathbf{k})$, where A and B are the two orbitals and σ_1 and σ_2 are the two spins. Since pairing between equal spins is a form of triplet-pairing, the pairing potential will be symmetric under the exchange of the spin labels $\Delta_{\sigma_1, \sigma_2}^{A, B}(\mathbf{k}) = \Delta_{\sigma_2, \sigma_1}^{A, B}(\mathbf{k})$. Ordinarily, in the case of a single orbital, this forces the momentum part of the wave function to be antisymmetric, however in this instance it is assumed that the momentum part is symmetric and isotropic in momentum space. Therefore to maintain fermion antisymmetry a new orbital-dependent part of the pairing potential is introduced which is antisymmetric under the exchange of orbital labels $\Delta_{\sigma_1, \sigma_2}^{A, B} = -\Delta_{\sigma_1, \sigma_2}^{B, A}$.

The equal-spin triplet-pairing theory is a theory with two full (nodeless) gaps, one for each spin species $\Delta_{\uparrow\uparrow}$ and $\Delta_{\downarrow\downarrow}$. Two nodeless gaps would be consistent with the recent experimental observation [126] as discussed in chapter 3. In principle these gaps may take different values, which would make this non-unitary triplet-pairing, as discussed in section 2.2. Such a theory, therefore, would be consistent with the symmetry analysis of LaNiC₂ [55] and LaNiGa₂ [56] which found only non-unitary triplet-pairing states could explain the observation of broken TRS in these superconductors, see chapter 3. Furthermore, it was thought that this theory would generate a magnetisation in the superconducting state [56, 130], consistent with the spontaneous magnetic field observed in experiments, due to the imbalance between spin-populations caused by the different pairing potentials for each spin-species.

Mean-field theory was used in [126] to study the proposed equal-spin triplet-pairing model but was not done at a self-consistent level. In this chapter we will continue the mean-field analysis of this model by solving the self-consistency equations and by directly minimising the free energy. Interestingly we shall see that our mean-field treatment, and direct minimisation of the free energy, of the equal-spin-pairing theory finds no imbalance between the two gaps, nor does it display any magnetisation. Consequently, the main result of this chapter is that the theory as proposed is not a non-unitary triplet-pairing theory (which requires $\Delta_{\uparrow\uparrow} \neq \Delta_{\downarrow\downarrow}$) but rather a unitary triplet-pairing theory. Despite this, we find that the theory does display

interesting physics, including the emergence of full gap superconductivity from triplet-pairing as well as gapless and re-entrant superconductivity. We shall discuss the lack of magnetisation and how our results can be reconciled with Hillier *et al.* [56] and Miyake [130] further in chapter 6.

In this chapter we will use the same mathematical techniques as described in detail for BCS singlet-pairing in chapter 4. We will first consider the non-interacting terms of the Hamiltonian and consider different tight-binding models, including a simple toy-model with a small amount of band splitting whose Fermi surface shares some key features with that of first principle calculations for LaNiGa₂ [123]. We will then include an attractive interaction between electrons of the same spin, on the same site, on different orbitals and derive the self-consistency equations for such a theory. We will see how the self-consistency equations predict multiple non-trivial solutions to the gap-equation, indicating potentially interesting unconventional behaviour. The free energy will be derived and minimised in order to elucidate which of the potential solutions leads to its minimisation. With this theory we will see that equal-spin triplet-pairing can lead to a full gap, rather than the a nodal gap structure commonly associated with triplet-pairing. However we shall also see that this theory gives rise to only a single gap and does not lead to spontaneous magnetisation, both of which are predicted to occur [126].

The equal-spin triplet-pairing Hamiltonian is given by:

$$\hat{\mathbb{H}} = \hat{\mathbb{K}} - \mu\hat{\mathbb{N}} + \hat{\mathbb{V}} \quad (5.1)$$

where $\hat{\mathbb{K}}$ is the total kinetic energy operator, μ is the chemical potential, $\hat{\mathbb{N}}$ is the total particle number operator and $\hat{\mathbb{V}}$ is the interaction between electrons. We start by considering the non-interacting part of the Hamiltonian.

5.1 Non-interacting Hamiltonian

In this section we attempt to obtain a non-interacting electron dispersion that at least qualitatively looks like the Fermi surface of LaNiGa₂, see figure 5.4b. Figure 5.4b shows (highlighted by yellow lines) Fermi surfaces which are slightly separated and run parallel to each other. In the corners of the Brillouin zone are what look like two cylindrical Fermi surfaces while the other set of Fermi surfaces run parallel until nearing the Brillouin zone edges where they diverge. Although being able to reproduce the shape of the Fermi surface would be ideal, the most important aspect we wish to capture is the *splitting* between regions of similar, parallel Fermi surfaces. Doing so will allow us to investigate the effect that the splitting has on the *interband* pairing, central to this model.

It was thought that a good approximation to the Fermi surface of LaNiGa₂ may be reproduced by hybridisation between two 1D Fermi sheets. We consider a two-dimensional square lattice with anisotropic orbitals (for example, but not necessarily, p-wave orbitals) which allow hopping between one type of the orbitals in the x -direction and between the other type in the y -direction, see figure 5.1. We shall see that such hopping gives rise to 1D Fermi surfaces as expected, but does not hybridise in a way that resembles the LaNiGa₂ Fermi surface.

The Hamiltonian that describes the total Kinetic energy of all the particles is:

$$\hat{\mathbb{K}} = - \sum_{\sigma=\uparrow,\downarrow} \sum_{j=1}^{\mathcal{N}} \sum_{j'=1}^{\mathcal{N}} \begin{pmatrix} \hat{c}_{Aj\sigma}^\dagger & \hat{c}_{Bj\sigma}^\dagger \end{pmatrix} \begin{pmatrix} t_{jj'}^{AA} & t_{jj'}^{AB} \\ t_{jj'}^{BA} & t_{jj'}^{BB} \end{pmatrix} \begin{pmatrix} \hat{c}_{Aj'\sigma} \\ \hat{c}_{Bj'\sigma} \end{pmatrix}. \quad (5.2)$$

As in the BCS case (equation (4.2)) there are two summations which run over all of the sites of a square lattice with \mathcal{N} sites but this time there is an additional sum over all spins. $\hat{c}_{mj\sigma}^\dagger$ ($\hat{c}_{mj\sigma}$) is the creation (annihilation) operator that creates (annihilates) an electron in orbital m with spin σ on site j . $t_{jj'}^{mm'}$ is the hopping energy of a particle at site j' with orbital m' , hopping to site j with orbital m . Each site has two orbitals labelled A and B .

The Fourier transformations of the creation/annihilation operators are given by:

$$\hat{c}_{A\mathbf{k}\sigma}^\dagger = \frac{1}{\sqrt{\mathcal{N}}} \sum_{j=1}^{\mathcal{N}} e^{i\mathbf{k}\cdot\mathbf{R}_j} \hat{c}_{Aj\sigma}^\dagger \quad \hat{c}_{Aj\sigma}^\dagger = \frac{1}{\sqrt{\mathcal{N}}} \sum_{\mathbf{k}} e^{-i\mathbf{k}\cdot\mathbf{R}_j} \hat{c}_{A\mathbf{k}\sigma}^\dagger \quad (5.3a)$$

$$\hat{c}_{A\mathbf{k}\sigma} = \frac{1}{\sqrt{\mathcal{N}}} \sum_{j=1}^{\mathcal{N}} e^{-i\mathbf{k}\cdot\mathbf{R}_j} \hat{c}_{Aj\sigma} \quad \hat{c}_{Aj\sigma} = \frac{1}{\sqrt{\mathcal{N}}} \sum_{\mathbf{k}} e^{i\mathbf{k}\cdot\mathbf{R}_j} \hat{c}_{A\mathbf{k}\sigma} \quad (5.3b)$$

where $\mathcal{N} = \mathcal{N}_x \mathcal{N}_y = \frac{L_x}{a} \frac{L_y}{a}$ and \mathcal{N} is the total number of sites, L is the length and a is the lattice spacing. Using these relations the kinetic energy equation (5.2) can be written in momentum space:

$$\hat{\mathbb{K}} = \sum_{\sigma=\uparrow,\downarrow} \sum_{\mathbf{k}} \begin{pmatrix} \hat{c}_{A\mathbf{k}\sigma}^\dagger & \hat{c}_{B\mathbf{k}\sigma}^\dagger \end{pmatrix} \begin{pmatrix} \varepsilon_{\mathbf{k}\sigma}^{AA} & \varepsilon_{\mathbf{k}\sigma}^{AB} \\ \varepsilon_{\mathbf{k}\sigma}^{BA} & \varepsilon_{\mathbf{k}\sigma}^{BB} \end{pmatrix} \begin{pmatrix} \hat{c}_{A\mathbf{k}\sigma} \\ \hat{c}_{B\mathbf{k}\sigma} \end{pmatrix} \quad (5.4)$$

where

$$\varepsilon_{\mathbf{k}\sigma}^{mm'} = - \sum_{\Delta_j} e^{i\mathbf{k}\cdot\mathbf{R}_{\Delta_j}} t_{\Delta_j}^{mm'} \quad (5.5)$$

is the hopping energy in momentum space representation and Δ_j is the label of the hopping vector \mathbf{R}_{Δ_j} . The negative sign in the front of equation (5.2) has been incorporated in the definition of the hopping energies, equation (5.5). Additionally, the Fourier transformation is also used to write the total particle number operator, $\hat{\mathbb{N}}$, in a momentum space representation:

$$\begin{aligned} \hat{\mathbb{N}} &= \sum_{\mathbf{k}\sigma} \left(\hat{c}_{A\mathbf{k}\sigma}^\dagger \hat{c}_{A\mathbf{k}\sigma} + \hat{c}_{B\mathbf{k}\sigma}^\dagger \hat{c}_{B\mathbf{k}\sigma} \right) \\ &= \sum_{\mathbf{k}\sigma} \left(\hat{n}_{A\mathbf{k}\sigma} + \hat{n}_{B\mathbf{k}\sigma} \right). \end{aligned}$$

See section 4.1 for a detailed description of the transformation from real space to momentum space for both terms of the non-interacting Hamiltonian.

In the event that hybridisation is zero ($t_{\Delta_j}^{AB} = t_{\Delta_j}^{BA} = 0$) then the hopping Hamiltonian is already diagonal in the orbital index:

$$\hat{\mathbb{K}} = \sum_{\sigma=\uparrow,\downarrow} \sum_{\mathbf{k}} \begin{pmatrix} \hat{c}_{A\mathbf{k}\sigma}^\dagger & \hat{c}_{B\mathbf{k}\sigma}^\dagger \end{pmatrix} \begin{pmatrix} \varepsilon_{\mathbf{k}\sigma}^{AA} & 0 \\ 0 & \varepsilon_{\mathbf{k}\sigma}^{BB} \end{pmatrix} \begin{pmatrix} \hat{c}_{A\mathbf{k}\sigma} \\ \hat{c}_{B\mathbf{k}\sigma} \end{pmatrix} \quad (5.6)$$

and $\varepsilon_{\mathbf{k}\sigma}^{AA}$ ($\varepsilon_{\mathbf{k}\sigma}^{BB}$) is the band dispersion for the A -orbital (B -orbital). In general however there will be hybridisation ($t_{\Delta_j}^{AB} = t_{\Delta_j}^{BA} \neq 0$), in which case diagonalising¹ the hopping Hamiltonian gives:

$$\hat{\mathbb{K}} = \sum_{\sigma=\uparrow,\downarrow} \sum_{\mathbf{k}} \begin{pmatrix} \hat{c}_{1\mathbf{k}\sigma}^\dagger & \hat{c}_{2\mathbf{k}\sigma}^\dagger \end{pmatrix} \begin{pmatrix} \varepsilon_{1\mathbf{k}} & 0 \\ 0 & \varepsilon_{2\mathbf{k}} \end{pmatrix} \begin{pmatrix} \hat{c}_{1\mathbf{k}\sigma} \\ \hat{c}_{2\mathbf{k}\sigma} \end{pmatrix} \quad (5.7)$$

¹See appendix A for more details on diagonalisation.

where the new creation/annihilation operators are some linear superposition of the original electron creation/annihilation operators and $\varepsilon_{n\mathbf{k}}$ is a band dispersion with a band index $n = 1, 2$. The band dispersions are given by:

$$\varepsilon_{1\mathbf{k}} = \frac{\varepsilon_{\mathbf{k}\sigma}^{AA} + \varepsilon_{\mathbf{k}\sigma}^{BB}}{2} + \sqrt{\left(\frac{\varepsilon_{\mathbf{k}\sigma}^{AA} - \varepsilon_{\mathbf{k}\sigma}^{BB}}{2}\right)^2 + \varepsilon_{\mathbf{k}\sigma}^{AB} \varepsilon_{\mathbf{k}\sigma}^{BA}} \quad (5.8)$$

$$\varepsilon_{2\mathbf{k}} = \frac{\varepsilon_{\mathbf{k}\sigma}^{AA} + \varepsilon_{\mathbf{k}\sigma}^{BB}}{2} - \sqrt{\left(\frac{\varepsilon_{\mathbf{k}\sigma}^{AA} - \varepsilon_{\mathbf{k}\sigma}^{BB}}{2}\right)^2 + \varepsilon_{\mathbf{k}\sigma}^{AB} \varepsilon_{\mathbf{k}\sigma}^{BA}}. \quad (5.9)$$

and the creation/annihilation operators of the new quasi-particles are given by:

$$\hat{c}_{1\mathbf{k}\sigma}^\dagger = u_{\mathbf{k}} \hat{c}_{A\mathbf{k}\sigma}^\dagger + v_{\mathbf{k}} \hat{c}_{B\mathbf{k}\sigma} \quad \hat{c}_{1\mathbf{k}\sigma} = u_{\mathbf{k}}^* \hat{c}_{A\mathbf{k}\sigma} + v_{\mathbf{k}}^* \hat{c}_{B\mathbf{k}\sigma}^\dagger \quad (5.10a)$$

$$\hat{c}_{2\mathbf{k}\sigma} = -v_{\mathbf{k}}^* \hat{c}_{A\mathbf{k}\sigma}^\dagger + u_{\mathbf{k}}^* \hat{c}_{B\mathbf{k}\sigma} \quad \hat{c}_{2\mathbf{k}\sigma}^\dagger = -v_{\mathbf{k}} \hat{c}_{A\mathbf{k}\sigma} + u_{\mathbf{k}} \hat{c}_{B\mathbf{k}\sigma}. \quad (5.10b)$$

where the u 's and v 's are the amplitudes of the eigenvectors of the Hamiltonian. They can be obtained by solving the eigenvector equation as we did previously, section 4.4.1, although we will not do so here.

Now we need to calculate the hopping energies. This requires summing over all possible hopping vectors, \mathbf{R}_{Δ_j} . The larger the hopping distance $|\mathbf{R}_{\Delta_j}|$ between two sites, the less likely it is for an electron to hop between them. Imposing an upper limit on the distance an electron can hop simplifies equation (5.5) by reducing the number of hopping vectors in the summation. This allows manageable expressions for the electron hopping energies to be obtained. Two different cases will be considered: nearest-neighbour hopping and next-nearest-neighbour hopping.

5.1.1 Anisotropic nearest-neighbour hopping

Under the nearest-neighbour hopping restriction electrons can only hop as far as their nearest neighbours, see figure 5.1a. On a 2D square lattice there are 4 nearest-neighbour sites. We have assumed some directional orbital e.g. p -orbital, so that the A -orbitals will be close together in the a -direction and the B -orbital will be close in the b -direction. The allowed hopping vectors have the following hopping energies:

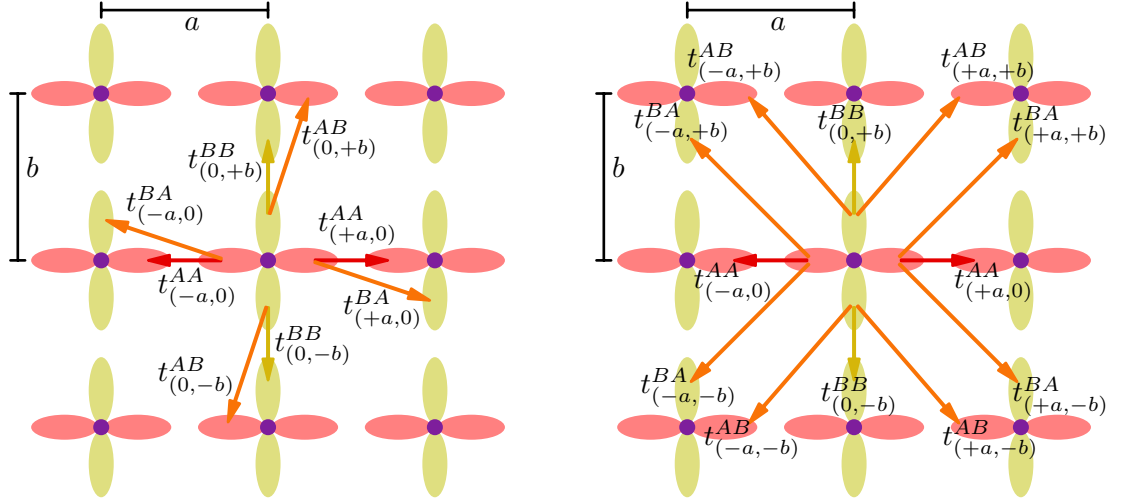
$$\text{if } \mathbf{R}_{\Delta_j} = \begin{pmatrix} \pm a \\ 0 \end{pmatrix} \text{ then: } t_{\Delta_j}^{AA} = t, t_{\Delta_j}^{AB} = t_{\Delta_j}^{BA} = t' \text{ and } t_{\Delta_j}^{BB} = 0$$

$$\text{if } \mathbf{R}_{\Delta_j} = \begin{pmatrix} 0 \\ \pm b \end{pmatrix} \text{ then: } t_{\Delta_j}^{AA} = 0, t_{\Delta_j}^{AB} = t_{\Delta_j}^{BA} = t' \text{ and } t_{\Delta_j}^{BB} = t$$

$$\text{for all other } \mathbf{R}_{\Delta_j}, t_{\Delta_j}^{AA} = t_{\Delta_j}^{BB} = t_{\Delta_j}^{AB} = t_{\Delta_j}^{BA} = 0.$$

The intra-band hopping is restricted to the directions in which the orbitals are closest while the inter-band hopping is allowed for all nearest neighbours. Expanding the summation of equation (5.5) using all the allowed hopping vectors for the $\varepsilon_{\mathbf{k}\sigma}^{AB}$ case, for example, gives:

$$\begin{aligned} \varepsilon_{\mathbf{k}\sigma}^{AB} &= -t' \left\{ e^{ik_x a} + e^{ik_x (-a)} + e^{ik_y b} + e^{ik_y (-b)} \right\} \\ &= -2t' \{ \cos(k_x a) + \cos(k_y b) \} \end{aligned}$$



(a) Nearest-neighbour hopping

(b) Inter-orbital next-nearest-neighbour hopping

Figure 5.1: Schematics of the allowed electron hopping for a given site. The hopping amplitudes, $t_{\Delta_j}^{OO'}$, are shown for the allowed hopping from orbital O' to O , from the central site to a neighbouring site described by the hopping vector Δ_j . Figure 5.1a shows the case of nearest neighbour hopping only where both inter- and intra-orbital hopping takes place between nearest neighbour sites. Figure 5.1b shows the same nearest neighbour intra-orbital hopping but with next nearest neighbour inter-orbital hopping.

and repeating this for the other hopping energies gives the hopping energies as

$$\varepsilon_{\mathbf{k}\sigma}^{AA} = -2t \cos k_x a \quad (5.11a)$$

$$\varepsilon_{\mathbf{k}\sigma}^{BB} = -2t \cos k_y b \quad (5.11b)$$

$$\varepsilon_{\mathbf{k}\sigma}^{AB} = \varepsilon_{\mathbf{k}\sigma}^{BA} = -2t' [\cos k_x a + \cos k_y b]. \quad (5.11c)$$

Using these expression we can now calculate the energy dispersion of the two bands, $\varepsilon_{1\mathbf{k}}$ and $\varepsilon_{2\mathbf{k}}$.

Figure 5.2 shows the energy dispersion of the two bands as hybridisation is changed. However, the hybridisation does not lead to any Fermi surfaces that resemble those of LaNiGa_2 . Next we examine what the dispersion looks like when the inter-band hopping takes place between next-nearest-neighbours instead.

5.1.2 Anisotropic nearest-neighbour intraband hopping with next-nearest-neighbour interband hopping

We make a slight change to the allowed hopping with inter-orbit hopping this time being restricted to next-nearest-neighbours only while intra-orbit hopping is restricted to nearest-neighbours due to anisotropic orbitals as before, see figure 5.1b. The hopping is now given

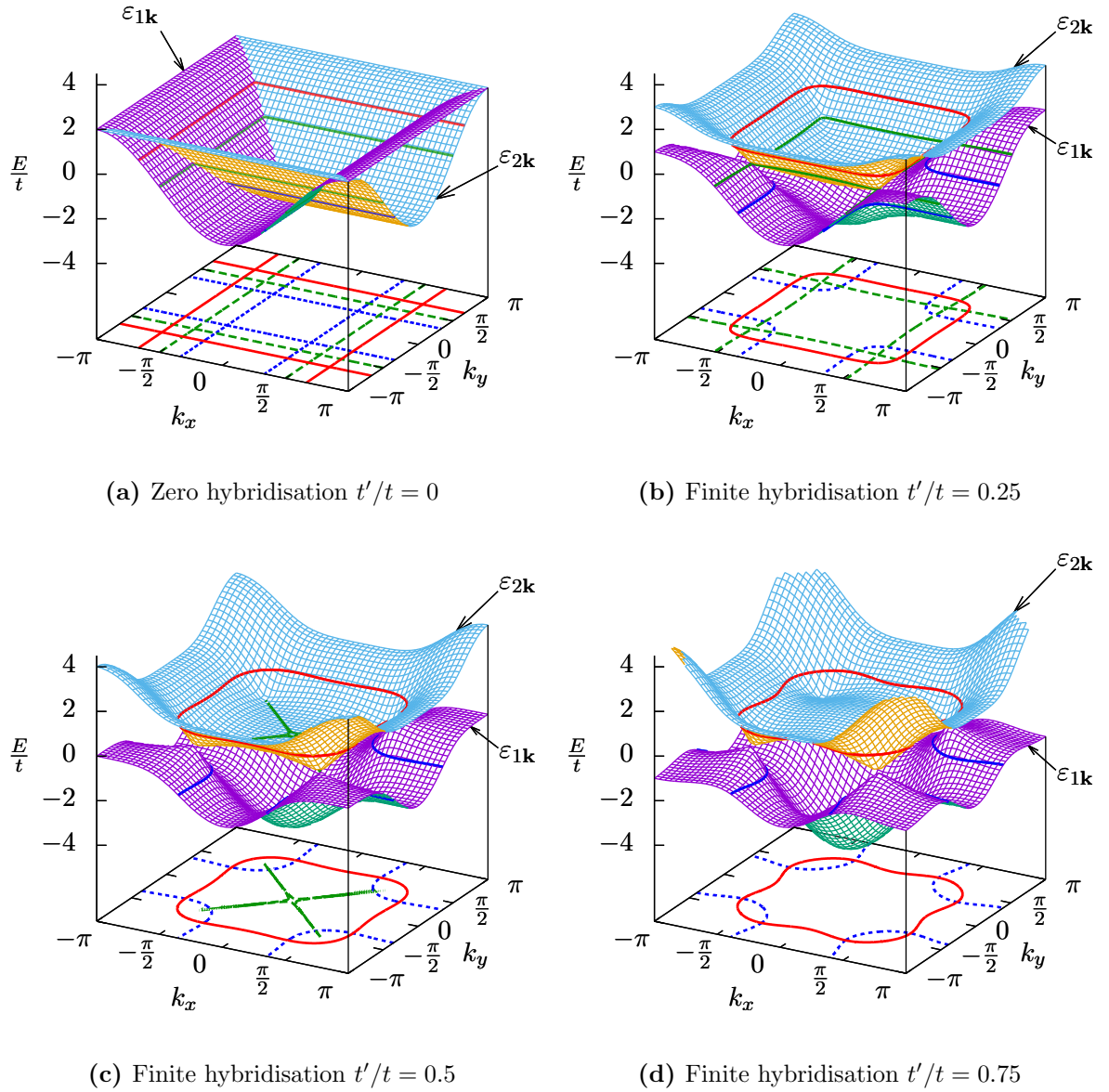


Figure 5.2: Non-interacting electron dispersion for a two-dimensional square lattice with nearest neighbour hopping and anisotropic orbitals. The two surfaces represent the non-interacting electron dispersion for each of the two bands. The contours on the surface and their projection on the $k_x k_y$ -plane correspond to different values of chemical potential μ . The red solid line corresponds to $\mu = 1$, the green dashed line to $\mu = 0$ and the blue dotted line to $\mu = -1$. The energy is in units of the intra-orbital particle hopping, t .

by:

$$\text{if } \mathbf{R}_{\Delta_j} = \begin{pmatrix} \pm a \\ 0 \end{pmatrix} \text{ then: } t_{\Delta_j}^{AA} = t \text{ and } t_{\Delta_j}^{AB} = t_{\Delta_j}^{BA} = t_{\Delta_j}^{BB} = 0$$

$$\text{if } \mathbf{R}_{\Delta_j} = \begin{pmatrix} 0 \\ \pm b \end{pmatrix} \text{ then: } t_{\Delta_j}^{AA} = t_{\Delta_j}^{AB} = t_{\Delta_j}^{BA} = 0 \text{ and } t_{\Delta_j}^{BB} = t$$

$$\text{if } \mathbf{R}_{\Delta_j} = \begin{pmatrix} \pm a \\ \pm b \end{pmatrix} \text{ then: } t_{\Delta_j}^{AA} = t_{\Delta_j}^{BB} = 0 \text{ and } t_{\Delta_j}^{AB} = t_{\Delta_j}^{BA} = t'$$

$$\text{for all other } \mathbf{R}_{\Delta_j}, t_{\Delta_j}^{AA} = t_{\Delta_j}^{BB} = t_{\Delta_j}^{AB} = t_{\Delta_j}^{BA} = 0.$$

With these allowed hoppings the intra-band hopping energies are unchanged but the inter-band hopping energies are slightly different:

$$\varepsilon_{\mathbf{k}\sigma}^{AA} = -2t \cos k_x a \quad (5.12a)$$

$$\varepsilon_{\mathbf{k}\sigma}^{BB} = -2t \cos k_y b \quad (5.12b)$$

$$\varepsilon_{\mathbf{k}\sigma}^{AB} = \varepsilon_{\mathbf{k}\sigma}^{BA} = -2t' [\cos(k_x a + k_y b) + \cos(k_x a - k_y b)]. \quad (5.12c)$$

The non-interacting dispersion is again plotted, figure 5.3, and once again none of the Fermi surfaces resemble any of those in LaNiGa₂, figure 5.4b. The $\mu = 0$ contour of figure 5.3d comes close in that it displays a central Fermi surface simultaneously with a circular one in the corners but it also has the crossed lines of the non-hybridised case, quite unlike any of the LaNiGa₂ Fermi surfaces. Next we will examine a simpler case with isotropic orbitals and nearest-neighbour only hopping.

5.1.3 Isotropic nearest-neighbour hopping

In the previous sections we saw that crossing 1D Fermi surfaces caused by anisotropic orbitals did not hybridise in a way which resembled the LaNiGa₂ Fermi surfaces. In this section we consider the simpler case of isotropic orbitals (still two orbitals per site) where the intraband hopping occurs in both a - and b -directions between nearest neighbour sites only. We neglect hybridisation effects i.e. $t' = 0$. Furthermore, we introduce a small splitting, s , between the two energy bands to create parallel Fermi surfaces.

The allowed hoppings are as follows:

$$\text{if } \mathbf{R}_{\Delta_j} = \begin{pmatrix} \pm a \\ 0 \end{pmatrix} \text{ then: } t_{\Delta_j}^{AA} = t_{\Delta_j}^{BB} = t \text{ and } t_{\Delta_j}^{AB} = t_{\Delta_j}^{BA} = 0$$

$$\text{if } \mathbf{R}_{\Delta_j} = \begin{pmatrix} 0 \\ \pm b \end{pmatrix} \text{ then: } t_{\Delta_j}^{AA} = t_{\Delta_j}^{BB} = t \text{ and } t_{\Delta_j}^{AB} = t_{\Delta_j}^{BA} = 0$$

$$\text{for all other } \mathbf{R}_{\Delta_j}, t_{\Delta_j}^{AA} = t_{\Delta_j}^{BB} = t_{\Delta_j}^{AB} = t_{\Delta_j}^{BA} = 0.$$

Such hoppings result in the following hopping energies:

$$\varepsilon_{\mathbf{k}\sigma}^{AA} = -2t [\cos k_x a + \cos k_y b - s] \quad (5.13a)$$

$$\varepsilon_{\mathbf{k}\sigma}^{BB} = -2t [\cos k_x a + \cos k_y b + s] \quad (5.13b)$$

$$\varepsilon_{\mathbf{k}\sigma}^{AB} = \varepsilon_{\mathbf{k}\sigma}^{BA} = 0 \quad (5.13c)$$

which also include the bare splitting between the bands, s .

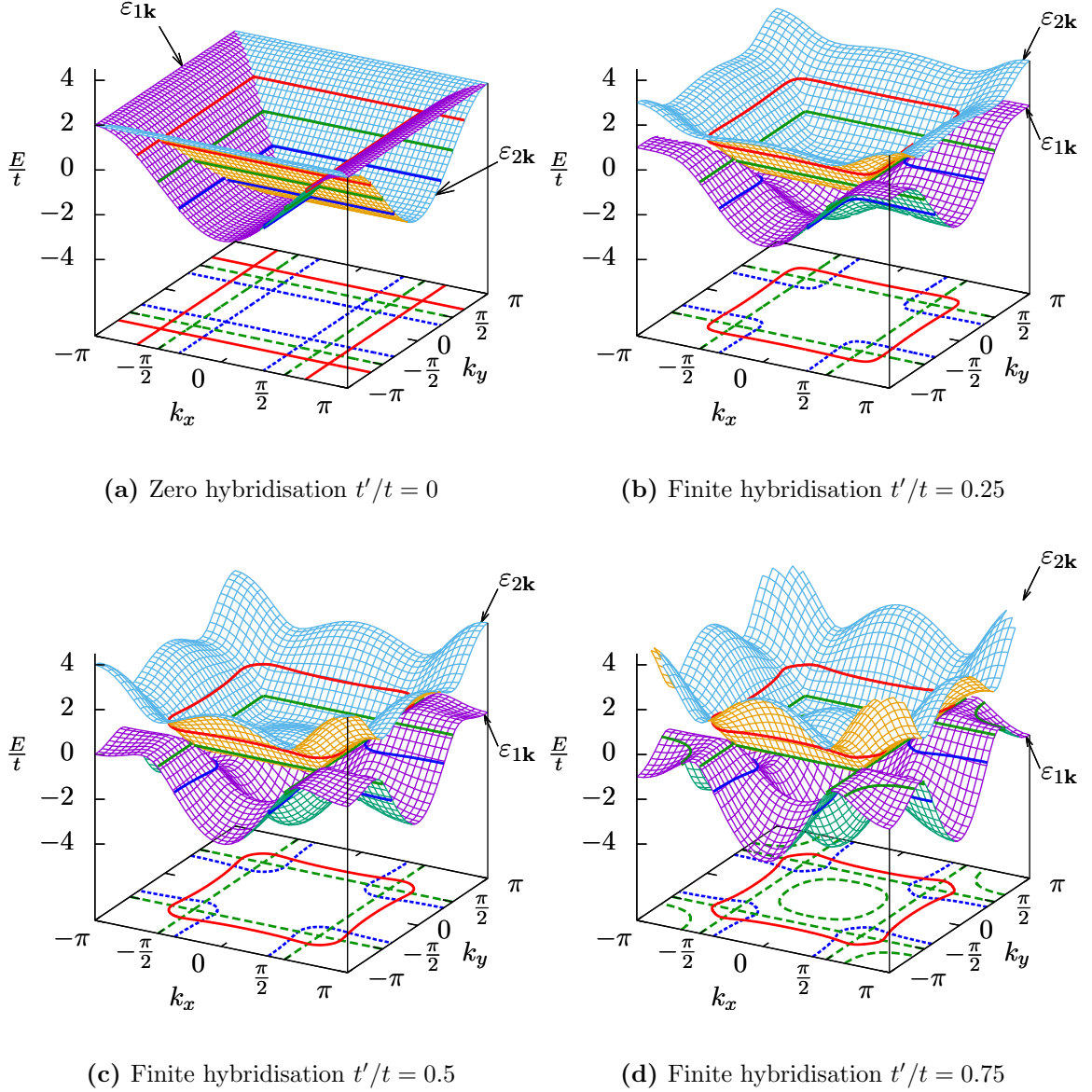
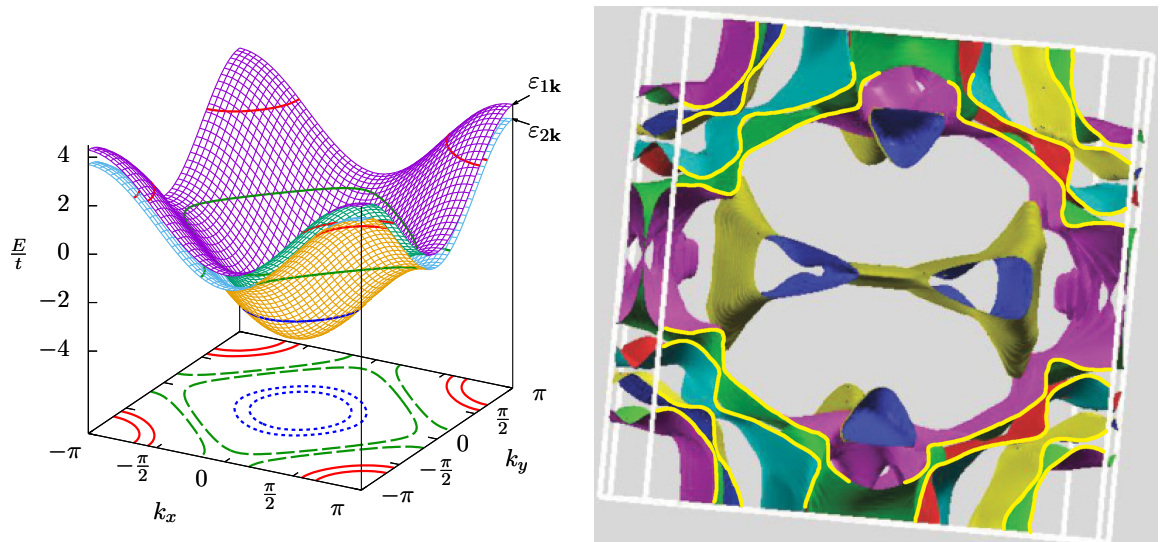


Figure 5.3: Non-interacting electron dispersion for a two-dimensional square lattice and anisotropic orbitals with nearest-neighbour intraband hopping and next-nearest-neighbour interband hopping. The intraband hopping is restricted to the nearest neighbours in the directions in which the anisotropic orbitals are nearest. The interband pairing occurs in all directions with the next nearest neighbours only. The two surfaces represent the non-interacting electron dispersion for each of the two bands. The contours on the surface and their projection on the $k_x k_y$ -plane correspond to different values of chemical potential μ . The red solid line corresponds to $\mu = 1$, the green dashed line to $\mu = 0$ and the blue dotted line to $\mu = -1$. The energy is in units of the intra-orbital particle hopping, t .

In figure 5.4 we compare the isotropic nearest-neighbour hopping model with the LaNiGa₂ Fermi surface obtained by Singh [123]. We can see in figure 5.4a that the isotropic nearest-neighbour hoppings give rise to Fermi surfaces which do share key features with LaNiGa₂. Both the $\mu = 2.5$ and $\mu = 0$ contours look qualitatively like the corner and central Fermi surfaces of LaNiGa₂ respectively, however both cannot be present simultaneously. More important is the presence of Fermi surfaces which look qualitatively like those of LaNiGa₂ and display regions which run parallel to each other, separated by some splitting. This is observed for all contours but crucially, the $\mu = 0$ contour displays the same behaviour of the central Fermi surface of LaNiGa₂ where the parallel Fermi surfaces diverge as they approach the Brillouin zone edges. Qualitatively speaking, of the three hopping models considered, this isotropic nearest-neighbour toy-model best represents the LaNiGa₂ Fermi surface.

The most important aspect of the Fermi surfaces is the splitting, rather than the shape, as the superconductivity being proposed is *interband*. The Cooper pairs are formed from electrons on different bands and, as can be clearly seen, the bands of LaNiGa₂ are separated. It is thought that the superconductivity will be weakened by splitting because there will be an additional energy barrier to the formation of Cooper pairs. If the energy of Cooper pair formation can not overcome the energy splitting then it will be unfavourable to create pairs. It is therefore important to be able to answer whether superconductivity can be obtained in such a model where there is a splitting between the bands. The isotropic nearest-neighbour hopping model without inter-orbital hopping provides the means to answer this question in addition to displaying Fermi surfaces that, at least qualitatively, look like those of LaNiGa₂. For simplicity we neglect inter-orbital hopping, since the key features we require are present without it, as well as spin-orbit coupling, which symmetry analysis tells us should be weak/negligible [110]. We will therefore use this model in our mean-field treatment of the equal-spin triplet-pairing theory.

In this section we examined a number of different hopping models in an attempt to obtain a toy-model which displays Fermi surfaces qualitatively similar to that of LaNiGa₂. We selected the isotropic nearest-neighbour hopping model with band splitting because, as discussed, it produced key features of the LaNiGa₂ Fermi surface. We shall now consider the full equal-spin triplet-pairing Hamiltonian with the interaction term included and solve it using a variational mean-field method.



(a) Non-interacting dispersion for a 2D square lattice with nearest neighbour hopping, $s = 0.15$

(b) Fermi surface of LaNiGa_2 . Adapted from Ref. [123]

Figure 5.4: Comparison between the nearest-neighbour 2D square lattice hopping model and the LaNiGa_2 Fermi surface. Figure 5.4a shows the non-interacting electron dispersion for the nearest-neighbour hopping toy-model with bare splitting, $s = 0.15$, between bands. The solid red, dashed green and dotted blue contours correspond to $\mu = 2.7$, $\mu = 0.0$ and $\mu = -2.7$ respectively. Figure 5.4b shows the Fermi surface of LaNiGa_2 obtained from density functional calculations. The yellow lines highlight the regions where the Fermi surfaces run parallel to each other and have a small splitting. It is these regions where the *interband* equal-spin pairing is proposed to occur. Adapted from Ref. [123].

5.2 Equal-spin triplet-pairing interaction

In this section we consider the full equal-spin triplet-pairing Hamiltonian with the interaction term included. We will make use of a variational mean-field method to obtain the energies of the Hamiltonian and to derive the free energy, as we did previously for the case of s-wave pairing, section 4.2. The interaction part of the Hamiltonian is given by:

$$\hat{V} = -U \sum_{\sigma=\uparrow,\downarrow} \sum_{j=1}^{\mathcal{N}} \hat{c}_{A_j\sigma}^\dagger \hat{c}_{B_j\sigma}^\dagger \hat{c}_{B_j\sigma} \hat{c}_{A_j\sigma}. \quad (5.14)$$

Here U is the interaction strength and is always positive so the interaction \hat{V} is attractive. The interaction is on-site between electrons on different orbitals but with the same spin. Ordinarily two electrons with the same spin cannot exist on the same site due to Pauli's exclusion principle however, in this theory, each site contains two orbitals, A and B , allowing the total wave function to remain anti-symmetric under the exchange of orbital labels.

5.2.1 Mean-field Hamiltonian

As was discussed in chapter 4, sections 4.2 and 4.3, because the Hamiltonian, $\hat{\mathbb{H}}$, is not diagonalisable, variational mean-field theory will be used to solve it. In mean-field theory it is assumed that a new, solvable Hamiltonian, $\hat{\mathbb{H}}_{\text{MF}}$, with variable parameters (mean-fields) can be a good approximation of the original Hamiltonian, $\hat{\mathbb{H}}$. If true then the free energy, F ,

can be approximated by:

$$F = \langle \hat{\mathbb{H}} \rangle - TS \approx \langle \hat{\mathbb{H}}_{\text{MF}} \rangle_{\text{MF}} - TS_{\text{MF}}.$$

The difference between the expectation values $\langle \dots \rangle$ and $\langle \dots \rangle_{\text{MF}}$ is as explained in section 4.3, equation (4.14).

We introduce the mean-field Hamiltonian:

$$\hat{\mathbb{H}}_{\text{MF}} = \hat{\mathbb{K}} - \mu \hat{\mathbb{N}} + \hat{\mathbb{V}}_{\text{MF}} \quad (5.15)$$

where the non-interacting part is identical to the non-interacting part of equation (5.1) and $\hat{\mathbb{V}}_{\text{MF}}$ is the mean field interaction term and is, by design, exactly solvable. We define $\hat{\mathbb{V}}$ as:

$$\begin{aligned} \hat{\mathbb{V}}_{\text{MF}} = & \sum_{j\sigma} (\Delta_{\sigma\sigma} \hat{c}_{Aj\sigma}^\dagger \hat{c}_{Bj\sigma}^\dagger + \Delta_{\sigma\sigma}^* \hat{c}_{Bj\sigma} \hat{c}_{Aj\sigma}) \\ & + \sum_{j\sigma} (\phi_{A\sigma} \hat{c}_{Aj\sigma}^\dagger \hat{c}_{Aj\sigma} + \phi_{B\sigma} \hat{c}_{Bj\sigma}^\dagger \hat{c}_{Bj\sigma}) \end{aligned} \quad (5.16)$$

where $\Delta_{\sigma\sigma}$ ($\Delta_{\sigma\sigma}^*$) is the mean-field pairing potential that pairs electrons (holes) of the same spin. There are no $\Delta_{\sigma\bar{\sigma}}$ terms as we consider only equal-spin triplet-pairing. The mean-field $\phi_{m\sigma}$ is the particle-density mean-field for electrons in the orbital m with spin σ . The σ -dependence of all these mean-fields in principle allows for an imbalance between both the spin-populations and/or pairing potentials, giving rise to magnetisation and/or two T_c 's respectively. Again, as discussed in section 4.3.1, we could include an additional mean-field that would couple with a Fock-like orbital swapping term from Wick's expansion of the interaction. Such a term could act to imbalance the orbital populations but not the spin populations and so we do not expect such a term to contribute to any magnetisation arising from the superconductivity. Since such terms do not arise naturally in the non-interacting part of the Hamiltonian, and because we are interested in superconductivity and the resulting magnetisation only, we exclude such terms in this mean-field theory.

By using the Fourier transform, equation (5.3), the interaction term of the mean-field Hamiltonian, $\hat{\mathbb{V}}_{\text{MF}}$, can be written in momentum space:

$$\hat{\mathbb{V}}_{\text{MF}} = \sum_{\mathbf{k}\sigma} \left\{ \Delta_{\sigma\sigma} \hat{c}_{A\mathbf{k}\sigma}^\dagger \hat{c}_{B\bar{\mathbf{k}}\sigma}^\dagger + \Delta_{\sigma\sigma}^* \hat{c}_{B\mathbf{k}\sigma} \hat{c}_{A\bar{\mathbf{k}}\sigma} + \phi_{A\sigma} \hat{c}_{A\mathbf{k}\sigma}^\dagger \hat{c}_{A\mathbf{k}\sigma} + \phi_{B\sigma} \hat{c}_{B\mathbf{k}\sigma}^\dagger \hat{c}_{B\mathbf{k}\sigma} \right\}. \quad (5.17)$$

In order to proceed we need to obtain the eigenvalues and eigenvectors of the mean-field Hamiltonian. Since this Hamiltonian is solvable (unlike the original, $\hat{\mathbb{H}}$) we can diagonalise it. We shall do so now by the Bogliobov transformation.

5.2.2 Diagonalising the mean-field Hamiltonian

The mean-field Hamiltonian, $\hat{\mathbb{H}}_{\text{MF}}$, is written in matrix form as:

$$\hat{\mathbb{H}}_{\text{MF}} = \frac{1}{2} \sum_{\mathbf{k}\sigma} \mathbf{C}_{\mathbf{k}\sigma}^* \mathbf{H}_{\mathbf{k}\sigma}^{\text{MF}} \mathbf{C}_{\mathbf{k}\sigma} + \sum_{\mathbf{k}\sigma} \frac{\epsilon_{A\mathbf{k}\sigma} + \epsilon_{B\mathbf{k}\sigma}}{2} \quad (5.18)$$

where $\epsilon_{m\mathbf{k}\sigma} = \epsilon_{\mathbf{k}\sigma}^{mm} - \mu + \phi_{m\sigma}$ is the renormalised dispersion and

$$\mathbf{H}_{\mathbf{k}\sigma}^{\text{MF}} = \begin{pmatrix} \epsilon_{A\mathbf{k}\sigma} & \Delta_{\sigma\sigma} & 0 & 0 \\ \Delta_{\sigma\sigma}^* & -\epsilon_{B\bar{\mathbf{k}}\sigma} & 0 & 0 \\ 0 & 0 & \epsilon_{B\mathbf{k}\sigma} & -\Delta_{\sigma\sigma} \\ 0 & 0 & -\Delta_{\sigma\sigma}^* & -\epsilon_{A\bar{\mathbf{k}}\sigma} \end{pmatrix} \quad \mathbf{C} = \begin{pmatrix} \hat{c}_{A\mathbf{k}\sigma} \\ \hat{c}_{B\bar{\mathbf{k}}\sigma}^\dagger \\ \hat{c}_{B\mathbf{k}\sigma} \\ \hat{c}_{A\bar{\mathbf{k}}\sigma}^\dagger \end{pmatrix}.$$

As per equation (5.13) we have assumed no orbital hybridisation in the normal state. The matrix $\mathbf{H}_{\mathbf{k}\sigma}^{\text{MF}}$ is diagonalised by the transformation matrix:

$$\mathbf{U} = \begin{pmatrix} a_{\mathbf{k}\sigma} & -c_{\mathbf{k}\sigma}^* & 0 & 0 \\ c_{\mathbf{k}\sigma} & a_{\mathbf{k}\sigma}^* & 0 & 0 \\ 0 & 0 & a_{\mathbf{k}\sigma} & c_{\mathbf{k}\sigma}^* \\ 0 & 0 & -c_{\mathbf{k}\sigma} & a_{\mathbf{k}\sigma}^* \end{pmatrix}, \quad (5.19)$$

more details of which can be found in appendix B. We define a new vector of fermionic operators $\boldsymbol{\gamma}^{\dagger*} = \left(\hat{\gamma}_{a\mathbf{k}\sigma}^{\dagger} \quad \hat{\gamma}_{b\mathbf{k}\sigma} \quad \hat{\gamma}_{c\mathbf{k}\sigma}^{\dagger} \quad \hat{\gamma}_{d\mathbf{k}\sigma} \right)$ which are defined by the diagonalisation of $\mathbf{H}_{\mathbf{k}\sigma}^{\text{MF}}$:

$$\mathbf{C}^* \mathbf{H}_{\mathbf{k}\sigma}^{\text{MF}} \mathbf{C} = \underbrace{\mathbf{C}^* \mathbf{U}}_{\boldsymbol{\gamma}^{\dagger*}} \mathbf{D} \underbrace{\mathbf{U}^* \mathbf{C}}_{\boldsymbol{\gamma}}$$

where \mathbf{D} is the diagonal matrix constructed with the eigenvalues of the mean-field Hamiltonian matrix $\mathbf{H}_{\mathbf{k}\sigma}^{\text{MF}}$. This transformation defines the Bogoliubon operators in terms of the electron operators as follows:

$$\hat{\gamma}_{a\mathbf{k}\sigma} = a_{\mathbf{k}\sigma}^* \hat{c}_{A\mathbf{k}\sigma} + c_{\mathbf{k}\sigma}^* \hat{c}_{B\bar{\mathbf{k}}\sigma}^{\dagger} \quad \hat{\gamma}_{a\mathbf{k}\sigma}^{\dagger} = a_{\mathbf{k}\sigma} \hat{c}_{A\mathbf{k}\sigma}^{\dagger} + c_{\mathbf{k}\sigma} \hat{c}_{B\bar{\mathbf{k}}\sigma} \quad (5.20a)$$

$$\hat{\gamma}_{d\mathbf{k}\sigma} = a_{\mathbf{k}\sigma}^* \hat{c}_{A\bar{\mathbf{k}}\sigma} + c_{\mathbf{k}\sigma}^* \hat{c}_{B\mathbf{k}\sigma}^{\dagger} \quad \hat{\gamma}_{d\mathbf{k}\sigma}^{\dagger} = a_{\mathbf{k}\sigma} \hat{c}_{A\bar{\mathbf{k}}\sigma}^{\dagger} + c_{\mathbf{k}\sigma} \hat{c}_{B\mathbf{k}\sigma} \quad (5.20b)$$

$$\hat{\gamma}_{b\mathbf{k}\sigma} = a_{\mathbf{k}\sigma}^* \hat{c}_{B\bar{\mathbf{k}}\sigma} - c_{\mathbf{k}\sigma}^* \hat{c}_{A\mathbf{k}\sigma}^{\dagger} \quad \hat{\gamma}_{b\mathbf{k}\sigma}^{\dagger} = a_{\mathbf{k}\sigma} \hat{c}_{B\bar{\mathbf{k}}\sigma}^{\dagger} - c_{\mathbf{k}\sigma} \hat{c}_{A\mathbf{k}\sigma} \quad (5.20c)$$

$$\hat{\gamma}_{c\mathbf{k}\sigma} = a_{\mathbf{k}\sigma}^* \hat{c}_{B\mathbf{k}\sigma} - c_{\mathbf{k}\sigma}^* \hat{c}_{A\bar{\mathbf{k}}\sigma}^{\dagger} \quad \hat{\gamma}_{c\mathbf{k}\sigma}^{\dagger} = a_{\mathbf{k}\sigma} \hat{c}_{B\mathbf{k}\sigma}^{\dagger} - c_{\mathbf{k}\sigma} \hat{c}_{A\bar{\mathbf{k}}\sigma} \quad (5.20d)$$

and the inverse is given by

$$\hat{c}_{A\mathbf{k}\sigma} = a_{\mathbf{k}\sigma} \hat{\gamma}_{a\mathbf{k}\sigma} - c_{\mathbf{k}\sigma}^* \hat{\gamma}_{b\mathbf{k}\sigma}^{\dagger} \quad \hat{c}_{A\mathbf{k}\sigma}^{\dagger} = a_{\mathbf{k}\sigma}^* \hat{\gamma}_{a\mathbf{k}\sigma}^{\dagger} - c_{\mathbf{k}\sigma} \hat{\gamma}_{b\mathbf{k}\sigma} \quad (5.21a)$$

$$\hat{c}_{A\bar{\mathbf{k}}\sigma} = a_{\mathbf{k}\sigma} \hat{\gamma}_{d\mathbf{k}\sigma} - c_{\mathbf{k}\sigma}^* \hat{\gamma}_{c\mathbf{k}\sigma}^{\dagger} \quad \hat{c}_{A\bar{\mathbf{k}}\sigma}^{\dagger} = a_{\mathbf{k}\sigma} \hat{\gamma}_{d\mathbf{k}\sigma}^{\dagger} - c_{\mathbf{k}\sigma} \hat{\gamma}_{c\mathbf{k}\sigma} \quad (5.21b)$$

$$\hat{c}_{B\bar{\mathbf{k}}\sigma} = c_{\mathbf{k}\sigma}^* \hat{\gamma}_{a\mathbf{k}\sigma}^{\dagger} + a_{\mathbf{k}\sigma} \hat{\gamma}_{b\mathbf{k}\sigma} \quad \hat{c}_{B\bar{\mathbf{k}}\sigma}^{\dagger} = c_{\mathbf{k}\sigma} \hat{\gamma}_{a\mathbf{k}\sigma} + a_{\mathbf{k}\sigma} \hat{\gamma}_{b\mathbf{k}\sigma}^{\dagger} \quad (5.21c)$$

$$\hat{c}_{B\mathbf{k}\sigma} = c_{\mathbf{k}\sigma}^* \hat{\gamma}_{d\mathbf{k}\sigma}^{\dagger} + a_{\mathbf{k}\sigma} \hat{\gamma}_{c\mathbf{k}\sigma} \quad \hat{c}_{B\mathbf{k}\sigma}^{\dagger} = c_{\mathbf{k}\sigma} \hat{\gamma}_{d\mathbf{k}\sigma} + a_{\mathbf{k}\sigma}^* \hat{\gamma}_{c\mathbf{k}\sigma}^{\dagger} \quad (5.21d)$$

As we shall see, the $a_{\mathbf{k}\sigma}$'s and $c_{\mathbf{k}\sigma}$'s are functions of $\epsilon_{o\mathbf{k}\sigma}$ and $\Delta_{\sigma\sigma}$, and are therefore functions of \mathbf{k} only through the energy dependence. Since the energy is symmetric under $\mathbf{k} \rightarrow -\mathbf{k}$ the $a_{\mathbf{k}\sigma}$'s and $c_{\mathbf{k}\sigma}$'s also have such symmetry i.e. $a_{\mathbf{k}\sigma} = a_{\bar{\mathbf{k}}\sigma}$ and $c_{\mathbf{k}\sigma} = c_{\bar{\mathbf{k}}\sigma}$. This makes some of the γ 's equivalent such that there are really only two independent flavours of quasi-particle:

$$\hat{\gamma}_{a\mathbf{k}\sigma}^{(\dagger)} = \hat{\gamma}_{d\bar{\mathbf{k}}\sigma}^{(\dagger)} \quad (5.22a)$$

$$\hat{\gamma}_{b\mathbf{k}\sigma}^{(\dagger)} = \hat{\gamma}_{c\bar{\mathbf{k}}\sigma}^{(\dagger)}. \quad (5.22b)$$

The eigenvalues are given by:

$$\lambda_{a\mathbf{k}\sigma} = -\sqrt{\xi_{\mathbf{k}\sigma}^2 + |\Delta_{\sigma\sigma}|^2} + s_{\sigma}^* = -\lambda_{d\mathbf{k}\sigma} \quad (5.23a)$$

$$\lambda_{b\mathbf{k}\sigma} = +\sqrt{\xi_{\mathbf{k}\sigma}^2 + |\Delta_{\sigma\sigma}|^2} + s_{\sigma}^* \quad (5.23b)$$

$$\lambda_{c\mathbf{k}\sigma} = -\sqrt{\xi_{\mathbf{k}\sigma}^2 + |\Delta_{\sigma\sigma}|^2} - s_{\sigma}^* = -\lambda_{b\mathbf{k}\sigma} \quad (5.23c)$$

$$\lambda_{d\mathbf{k}\sigma} = +\sqrt{\xi_{\mathbf{k}\sigma}^2 + |\Delta_{\sigma\sigma}|^2} - s_{\sigma}^* \quad (5.23d)$$

where

$$\xi_{\mathbf{k}\sigma} = \frac{1}{2}(\epsilon_{A\mathbf{k}\sigma} + \epsilon_{B\mathbf{k}\sigma}) = \frac{1}{2}(\epsilon_{\mathbf{k}\sigma}^{AA} + \epsilon_{\mathbf{k}\sigma}^{BB}) + \frac{1}{2}(\phi_{A\sigma} + \phi_{B\sigma}) - \mu \quad (5.24)$$

is the average energy of the two renormalised bands and

$$s_\sigma^* = \frac{1}{2}(\epsilon_{A\mathbf{k}\sigma} - \epsilon_{B\mathbf{k}\sigma}) = 2ts + \frac{1}{2}(\phi_{A\sigma} - \phi_{B\sigma}) \quad (5.25)$$

is the effective splitting between them.

When the bare splitting, s , between the different orbitals is zero, the equal-spin triplet-pairing model can be mapped to BCS theory, where the orbital labels map to spin labels. That is, when $A \mapsto \uparrow$ and $B \mapsto \downarrow$, the equal-spin pairing model looks like two copies of BCS theory (two because of the $\sum_{\sigma=\uparrow,\downarrow}$ in the equal-spin pairing model). For example, in this limit, equations (5.24) and (5.25) map to equations (4.28) and (4.29) respectively. Henceforth we refer to this $s = 0$ limit as the BCS-like case².

Written in terms of the Bogoliubon operators the Hamiltonian looks like:

$$\begin{aligned} \hat{\mathbb{H}}_{\text{MF}} - \sum_{\mathbf{k}\sigma} \frac{\epsilon_{A\mathbf{k}\sigma} + \epsilon_{B\mathbf{k}\sigma}}{2} &= \frac{1}{2} \sum_{\mathbf{k}\sigma} \gamma^* \mathbf{D} \gamma \\ &= \frac{1}{2} \sum_{\mathbf{k}\sigma} \left\{ \lambda_{a\mathbf{k}\sigma} \hat{\gamma}_{a\mathbf{k}\sigma}^\dagger \hat{\gamma}_{a\mathbf{k}\sigma} + \lambda_{b\mathbf{k}\sigma} \hat{\gamma}_{b\mathbf{k}\sigma}^\dagger \hat{\gamma}_{b\mathbf{k}\sigma} + \lambda_{c\mathbf{k}\sigma} \hat{\gamma}_{c\mathbf{k}\sigma}^\dagger \hat{\gamma}_{c\mathbf{k}\sigma} + \lambda_{d\mathbf{k}\sigma} \hat{\gamma}_{d\mathbf{k}\sigma}^\dagger \hat{\gamma}_{d\mathbf{k}\sigma} \right\} \end{aligned}$$

which written in normal order becomes

$$= \frac{1}{2} \sum_{\mathbf{k}\sigma} \left\{ \lambda_{a\mathbf{k}\sigma} \hat{\gamma}_{a\mathbf{k}\sigma}^\dagger \hat{\gamma}_{a\mathbf{k}\sigma} - \lambda_{b\mathbf{k}\sigma} \hat{\gamma}_{b\mathbf{k}\sigma}^\dagger \hat{\gamma}_{b\mathbf{k}\sigma} + \lambda_{c\mathbf{k}\sigma} \hat{\gamma}_{c\mathbf{k}\sigma}^\dagger \hat{\gamma}_{c\mathbf{k}\sigma} - \lambda_{d\mathbf{k}\sigma} \hat{\gamma}_{d\mathbf{k}\sigma}^\dagger \hat{\gamma}_{d\mathbf{k}\sigma} + \lambda_{b\mathbf{k}\sigma} - \lambda_{a\bar{\mathbf{k}}\sigma} \right\}$$

and writing in terms of the two non-equivalent flavours of quasi-particle gives

$$= \frac{1}{2} \sum_{\mathbf{k}\sigma} \left\{ \lambda_{a\mathbf{k}\sigma} \hat{\gamma}_{a\mathbf{k}\sigma}^\dagger \hat{\gamma}_{a\mathbf{k}\sigma} - \lambda_{b\mathbf{k}\sigma} \hat{\gamma}_{b\mathbf{k}\sigma}^\dagger \hat{\gamma}_{b\mathbf{k}\sigma} - \lambda_{b\mathbf{k}\sigma} \hat{\gamma}_{b\bar{\mathbf{k}}\sigma}^\dagger \hat{\gamma}_{b\bar{\mathbf{k}}\sigma} + \lambda_{a\mathbf{k}\sigma} \hat{\gamma}_{a\bar{\mathbf{k}}\sigma}^\dagger \hat{\gamma}_{a\bar{\mathbf{k}}\sigma} + \lambda_{b\mathbf{k}\sigma} - \lambda_{a\mathbf{k}\sigma} \right\}$$

because all \mathbf{k} 's are included in the sum we can write in terms of $+\mathbf{k}$ only

$$\begin{aligned} &= \frac{1}{2} \sum_{\mathbf{k}\sigma} \left\{ 2\lambda_{a\mathbf{k}\sigma} \hat{\gamma}_{a\mathbf{k}\sigma}^\dagger \hat{\gamma}_{a\mathbf{k}\sigma} - 2\lambda_{b\mathbf{k}\sigma} \hat{\gamma}_{b\mathbf{k}\sigma}^\dagger \hat{\gamma}_{b\mathbf{k}\sigma} + \lambda_{b\mathbf{k}\sigma} - \lambda_{a\mathbf{k}\sigma} \right\} \\ &= \sum_{\mathbf{k}\sigma} \left\{ E_{a\mathbf{k}\sigma} \hat{\gamma}_{a\mathbf{k}\sigma}^\dagger \hat{\gamma}_{a\mathbf{k}\sigma} + E_{b\mathbf{k}\sigma} \hat{\gamma}_{b\mathbf{k}\sigma}^\dagger \hat{\gamma}_{b\mathbf{k}\sigma} \right\} - \frac{1}{2} \sum_{\mathbf{k}\sigma} \{ E_{b\mathbf{k}\sigma} + E_{a\mathbf{k}\sigma} \} \end{aligned}$$

Collecting all the constants together gives the Hamiltonian as

$$\hat{\mathbb{H}}_{\text{MF}} = \sum_{m\mathbf{k}\sigma} E_{m\mathbf{k}\sigma} \hat{\gamma}_{m\mathbf{k}\sigma}^\dagger \hat{\gamma}_{m\mathbf{k}\sigma} + \underbrace{\frac{1}{2} \sum_{\mathbf{k}\sigma} \epsilon_{A\mathbf{k}\sigma} + \epsilon_{B\mathbf{k}\sigma} - E_{b\mathbf{k}\sigma} - E_{a\mathbf{k}\sigma}}_{E^{\text{GS}}} \quad (5.26)$$

where the constants form the ground state energy, E^{GS} , of the system. E^{GS} (and the whole Hamiltonian) can be decomposed into a sum of two identical parts, one for each spin: $E^{\text{GS}} = E_{\uparrow}^{\text{GS}} + E_{\downarrow}^{\text{GS}}$. As discussed in section 4.4 this Bogoliubov de Gennes transformation allows us to think of the system as a collection of non-interacting quasi-particle excitations (Bogoliubons), created/annihilated by the γ -operators, on top of some ground state, $|E^{\text{GS}}\rangle$, devoid of excitations.

As well as obtaining the mean-field Hamiltonian energies we also need the eigenvector amplitudes $a_{\mathbf{k}\sigma}$ and $c_{\mathbf{k}\sigma}$. We obtain these by solving the eigenvector equations for the common quantities $a_{\mathbf{k}\sigma} c_{\mathbf{k}\sigma}^*$, $a_{\mathbf{k}\sigma} a_{\mathbf{k}\sigma}^*$ and $c_{\mathbf{k}\sigma} c_{\mathbf{k}\sigma}^*$, as we did previously for the BCS case, section 4.4.1. We shall present these quantities explicitly in a moment, see equation (5.32), before that we shall derive the self-consistency equations.

²Furthermore, when $\phi_{A\sigma} = \phi_{B\sigma}$ in this BCS-like limit, each set of expressions for a given spin become exact copies of BCS theory, after the BCS-like mapping, since we recover the usual $\phi_{\uparrow} = \phi_{\downarrow}$ discussed in chapter 4

5.3 Self-consistency equations

In this section the self-consistency equations will be derived. As discussed in chapter 4 section 4.3.2, solving the self-consistency equations gives the values of the mean-fields corresponding to the stationary points of the free energy. Those mean-fields which correspond to the minimum points can be used to obtain information about the state of the system, e.g. whether there is superconductivity, an energy gap or magnetisation.

Often, as is the case for BCS theory, the solutions to the self-consistency equations *do* correspond to the free energy minima and as such serve as a quick method of minimising the free energy. However, as we shall see, in this case the self-consistency equations *do not* always find the free energy minimum and we will need to minimise the free energy directly to obtain information about the system.

Let us now derive the self-consistency equations. The method is the same as described in section 4.3.2; the stationary points of the free energy are obtained by varying the free energy with respect to the mean-fields and demanding it be zero, $\delta F = 0$. Doing so gives:

$$\delta \langle \hat{\mathbb{V}}_{\text{MF}} \rangle_{\text{MF}} = \delta \langle \hat{\mathbb{V}} \rangle_{\text{MF}}.$$

The variation of the mean-field interaction is given by

$$\begin{aligned} \delta \langle \hat{\mathbb{V}}_{\text{MF}} \rangle_{\text{MF}} = \sum_{j,\sigma} \left\{ \Delta_{\sigma\sigma} \delta \langle \hat{c}_{Aj\sigma}^\dagger \hat{c}_{Bj\sigma}^\dagger \rangle_{\text{MF}} + \Delta_{\sigma\sigma}^* \delta \langle \hat{c}_{Bj\sigma} \hat{c}_{Aj\sigma} \rangle_{\text{MF}} \right. \\ \left. + \Phi_{A\sigma} \delta \langle \hat{c}_{Aj\sigma}^\dagger \hat{c}_{Aj\sigma} \rangle_{\text{MF}} + \Phi_{B\sigma} \delta \langle \hat{c}_{Bj\sigma}^\dagger \hat{c}_{Bj\sigma} \rangle_{\text{MF}} \right\} \end{aligned} \quad (5.27)$$

and the variation of the original interaction is

$$\begin{aligned} \delta \langle \hat{\mathbb{V}} \rangle_{\text{MF}} = -U \sum_{j,\sigma} \left\{ \right. \\ \delta \langle \hat{c}_{Aj\sigma}^\dagger \hat{c}_{Bj\sigma}^\dagger \rangle_{\text{MF}} \langle \hat{c}_{Bj\sigma} \hat{c}_{Aj\sigma} \rangle_{\text{MF}} + \langle \hat{c}_{Aj\sigma}^\dagger \hat{c}_{Bj\sigma}^\dagger \rangle_{\text{MF}} \delta \langle \hat{c}_{Bj\sigma} \hat{c}_{Aj\sigma} \rangle_{\text{MF}} \\ - \delta \langle \hat{c}_{Aj\sigma}^\dagger \hat{c}_{Bj\sigma} \rangle_{\text{MF}} \langle \hat{c}_{Bj\sigma}^\dagger \hat{c}_{Aj\sigma} \rangle_{\text{MF}} - \langle \hat{c}_{Aj\sigma}^\dagger \hat{c}_{Bj\sigma} \rangle_{\text{MF}} \delta \langle \hat{c}_{Bj\sigma}^\dagger \hat{c}_{Aj\sigma} \rangle_{\text{MF}} \\ \left. + \delta \langle \hat{c}_{Aj\sigma}^\dagger \hat{c}_{Aj\sigma} \rangle_{\text{MF}} \langle \hat{c}_{Bj\sigma}^\dagger \hat{c}_{Bj\sigma} \rangle_{\text{MF}} + \langle \hat{c}_{Aj\sigma}^\dagger \hat{c}_{Aj\sigma} \rangle_{\text{MF}} \delta \langle \hat{c}_{Bj\sigma}^\dagger \hat{c}_{Bj\sigma} \rangle_{\text{MF}} \right\}. \end{aligned} \quad (5.28)$$

The self-consistency equations are obtained by comparing equations (5.27) and (5.28), treating variation terms $\delta \langle \dots \rangle_{\text{MF}}$ as independent and collecting their coefficients. Doing so gives the self-consistency equations as:

$$-U \langle \hat{c}_{Bj\sigma} \hat{c}_{Aj\sigma} \rangle_0 = \Delta_{\sigma\sigma} \quad (5.29a)$$

$$-U \langle \hat{c}_{Bj\sigma}^\dagger \hat{c}_{Aj\sigma}^\dagger \rangle_0 = \Delta_{\sigma\sigma}^* \quad (5.29b)$$

$$-U \langle \hat{c}_{Bj\sigma}^\dagger \hat{c}_{Bj\sigma} \rangle_0 = \phi_{A\sigma} \quad (5.29c)$$

$$-U \langle \hat{c}_{Aj\sigma}^\dagger \hat{c}_{Aj\sigma} \rangle_0 = \phi_{B\sigma}. \quad (5.29d)$$

To calculate the expectation values in the self-consistency equations, equation (5.29), the same process as in BCS section 4.5 is used. They are first written in momentum-space by use of the Fourier transformation, equation (5.3), then the electron creation/annihilation operators are written in terms of the Bogoliubon operators using the Bogoliubov transformation,

equation (5.21). The self-consistency equations then become:

$$\Delta_{\sigma\sigma} = + \frac{U}{\mathcal{N}} \chi_{\sigma} \quad (5.30a)$$

$$\phi_{A\sigma} = - \frac{U}{\mathcal{N}} N_{B\sigma} \quad (5.30b)$$

$$\phi_{B\sigma} = - \frac{U}{\mathcal{N}} N_{A\sigma} \quad (5.30c)$$

where

$$\chi_{\sigma} = \sum_{\mathbf{k}} \left\langle \hat{c}_{B\mathbf{k}\sigma} \hat{c}_{A\bar{\mathbf{k}}\sigma} \right\rangle_{\text{MF}} = \sum_{\mathbf{k}} \{ a_{\mathbf{k}\sigma} c_{\mathbf{k}\sigma}^* [1 - f(E_{a\mathbf{k}\sigma}) - f(E_{b\mathbf{k}\sigma})] \} \quad (5.31a)$$

$$N_{A\sigma} = \sum_{\mathbf{k}} \left\langle \hat{c}_{A\mathbf{k}\sigma}^{\dagger} \hat{c}_{A\mathbf{k}\sigma} \right\rangle_{\text{MF}} = \sum_{\mathbf{k}} \{ a_{\mathbf{k}\sigma}^* a_{\mathbf{k}\sigma} f(E_{a\mathbf{k}\sigma}) + c_{\mathbf{k}\sigma} c_{\mathbf{k}\sigma}^* [1 - f(E_{b\mathbf{k}\sigma})] \} \quad (5.31b)$$

$$N_{B\sigma} = \sum_{\mathbf{k}} \left\langle \hat{c}_{B\mathbf{k}\sigma}^{\dagger} \hat{c}_{B\mathbf{k}\sigma} \right\rangle_{\text{MF}} = \sum_{\mathbf{k}} \{ a_{\mathbf{k}\sigma}^* a_{\mathbf{k}\sigma} f(E_{b\mathbf{k}\sigma}) + c_{\mathbf{k}\sigma} c_{\mathbf{k}\sigma}^* [1 - f(E_{a\mathbf{k}\sigma})] \} \quad (5.31c)$$

and

$$a_{\mathbf{k}\sigma} c_{\mathbf{k}\sigma}^* = \frac{\Delta_{\sigma\sigma}}{2\sqrt{\xi_{\mathbf{k}\sigma}^2 + |\Delta_{\sigma\sigma}|^2}} \quad (5.32a)$$

$$a_{\mathbf{k}\sigma}^* a_{\mathbf{k}\sigma} = \frac{1}{2} \left(1 + \frac{\xi_{\mathbf{k}\sigma}}{\sqrt{\xi_{\mathbf{k}\sigma}^2 + |\Delta_{\sigma\sigma}|^2}} \right) \quad (5.32b)$$

$$c_{\mathbf{k}\sigma} c_{\mathbf{k}\sigma}^* = \frac{1}{2} \left(1 - \frac{\xi_{\mathbf{k}\sigma}}{\sqrt{\xi_{\mathbf{k}\sigma}^2 + |\Delta_{\sigma\sigma}|^2}} \right). \quad (5.32c)$$

Equations (5.32) were obtained by solving the eigenvector equations, as was done in section 4.4.1. Next we solve the self-consistency equations (5.30) numerically.

5.3.1 Self-consistency equations - numerical results

As was done in the BCS chapter, section 4.6, we start by examining the gap equation mathematically, using the contour method to obtain a first impression of how the gap equation could possibly behave. This is done without determining the ϕ -fields self-consistently, they are simply parameters to the gap equation. Afterwards all three self-consistent equations will be solved simultaneously using the iterative method discussed in section 4.6.

5.3.2 Solving the self-consistent gap equation via the contour method

Figure 5.5 was obtained by solving the self-consistent gap equation with the contouring method, described previously in section 4.6.1. It shows how Δ varies with temperature, T , for zero- and finite-splitting, s_{σ}^* (equation (5.25)), in figures 5.5a and 5.5b respectively. Both results are identical to those obtained for BCS theory, figure 4.5. This is not surprising since the self-consistency equations for the equal-spin triplet-pairing theory, equation (5.30), are mathematically identical to those of BCS theory, equation (4.39), if one changes the orbital labels to spin labels.

The difference here is that there is an underlying splitting in the non-interacting electron dispersion, which is absent in BCS theory. In BCS theory the effective splitting arises from an imbalance in the ϕ -fields, which at this level were chosen to give an effective splitting.

However, in BCS theory, as we saw in section 4.6.2, the effective splitting does not manifest in reality because it is a splitting between spin bands (rather than between orbitals as is the case here) and the free energy is minimised by $\phi_{\uparrow} = \phi_{\downarrow}$. In our equal-spin triplet-pairing theory however, the effective splitting, s_{σ}^* , can be finite even if $\phi_{A\sigma} = \phi_{B\sigma}$ due to the bare splitting, s , between the non-interacting electron bands (see equation (5.25)).

In the case of finite effective splitting, figure 5.5b, the Δ vs T contours exhibit three different types of behaviour, corresponding to the three different types of line. At relatively high interactions U there exists only one curve per interaction which behaves in the standard BCS way i.e. there is a critical temperature above which $\Delta = 0$ and below which $\Delta > 0$ (see $U \geq 2.96$, red solid lines). At relatively low interactions there again exists one contour per interaction but its behaviour is not BCS like. Instead there appears multiple non-trivial solutions to the gap equation with Δ suddenly becoming finite rather than evolving smoothly at T_c , (shown for interactions $U \leq 2.60$, green dashed lines in the figure). Finally there exists a third type of behaviour for intermediate interactions (see $U = 2.7, 2.8$; blue dot-dashed lines) whereby there exist two contours per interaction and two “ T_c ’s”, moreover the number of non-trivial solutions varies from one, if below the higher T_c but above the lower T_c , to two, if below the lower T_c .

Each contour, T_c is defined as the highest temperature at which Δ is finite. As we just discussed, in the case of some contours, this allows for two T_c ’s however, these are not necessarily actual transition temperatures where there is a change of state. As the self-consistency equations do not reveal which solution is the global minimum of the free energy, it is not possible to know which contour and which T_c actually corresponds to the onset of superconductivity. Instead we can use these T_c ’s to determine a preliminary phase diagram, as shown in figure 5.6.

Figure 5.6 shows the phase diagram for two different values of bare splitting, $s = 0$ and $s = 0.1$, represented by the crosses and triangle markers respectively. The BCS-like case ($s = 0$, red cross markers) shows the expected BCS like behaviour: $T_c \propto \exp(-1/\rho(0)U)$ [14] where for temperature $T > T_c$ the system is in the normal state while for $T < T_c$ the system is superconducting. At $U = 0$ it is known analytically that $\Delta = 0$, i.e. $T_c = 0$. Below $U \approx 0.9$ there is an absence of data points because the contours of figure 5.5a become too small compared with the density of calculated data points, making the interpolation a bad approximation to the actual contour, in fact data points below $U \approx 1.3$ already show linear behaviour, rather than exponential, due to this interpolation problem. Increasing the density of calculated data points would result in smoother contours at small U but significantly increases the computational time and the BCS-like exponential behaviour can already be seen.

In the case of finite splitting ($s = 0.1$, triangle markers) there are three different types of contour or critical temperature. The red triangles are high U and mark a BCS like transition, although the splitting has had the effect of suppressing T_c . Above the transition line the system is normal while it is superconducting beneath it. The blue markers correspond to interactions for which there exists two contours, hence there are two T_c ’s as we defined previously. Above the larger of the two T_c ’s the system is normal while below it there exists only one non-trivial solution to the self-consistent gap equation and the system is most likely BCS-like in nature, while below the lower of the two T_c ’s there exists two non-trivial solutions. The green marker corresponds to low U which has a single contour but also has two non-trivial

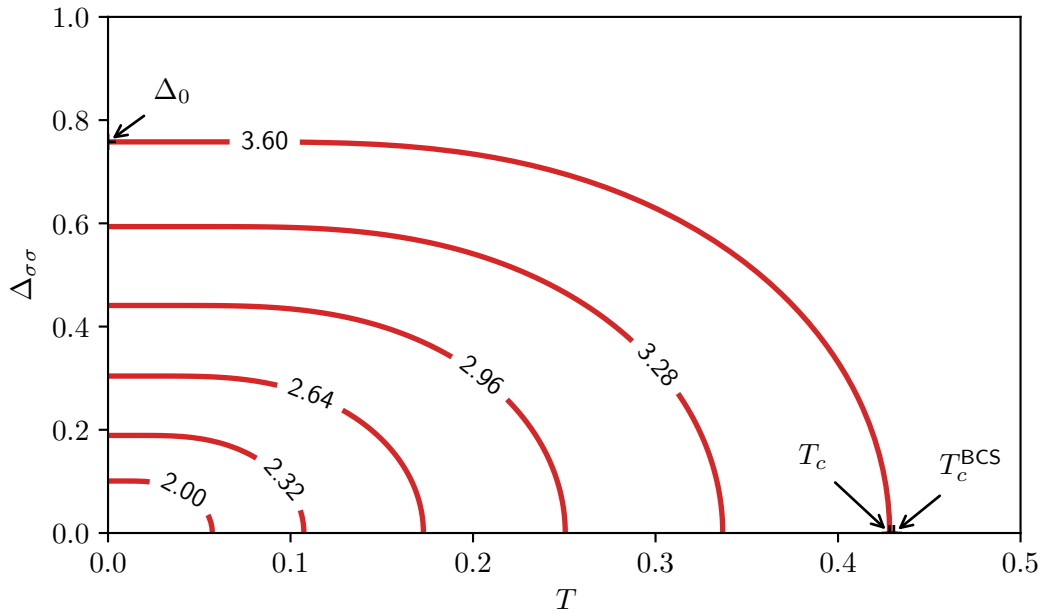
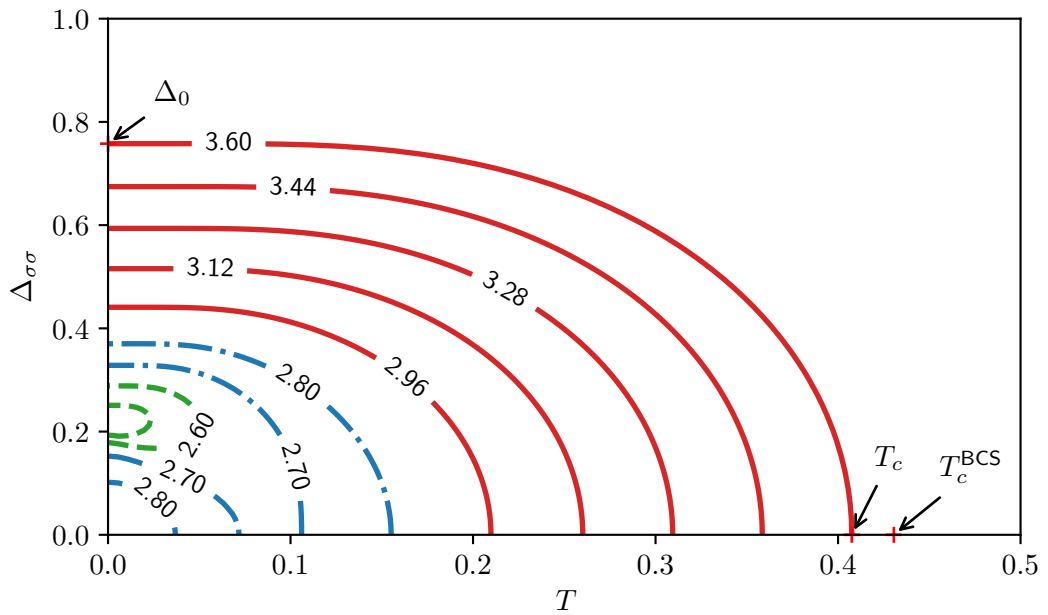
(a) Zero effective splitting - $s_{\sigma}^* = 0$ (b) Finite effective splitting - $s_{\sigma}^* = 0.2$

Figure 5.5: Solutions to the equal-spin triplet-pairing self-consistent gap equation. Each line shows $\Delta_{\sigma\sigma}$ vs T for different interactions U obtained by solving the self-consistent gap equation. Figures 5.5a and 5.5b correspond to zero and finite effective splitting respectively. Δ_0 , T_c and T_c^{BCS} are marked for the highest interaction $U = 3.6$ only. In the case of finite splitting there are regions with more than one trivial solution. Parameters: $\mu = -2$, $\phi_{A\sigma} = \phi_{B\sigma} = 0$

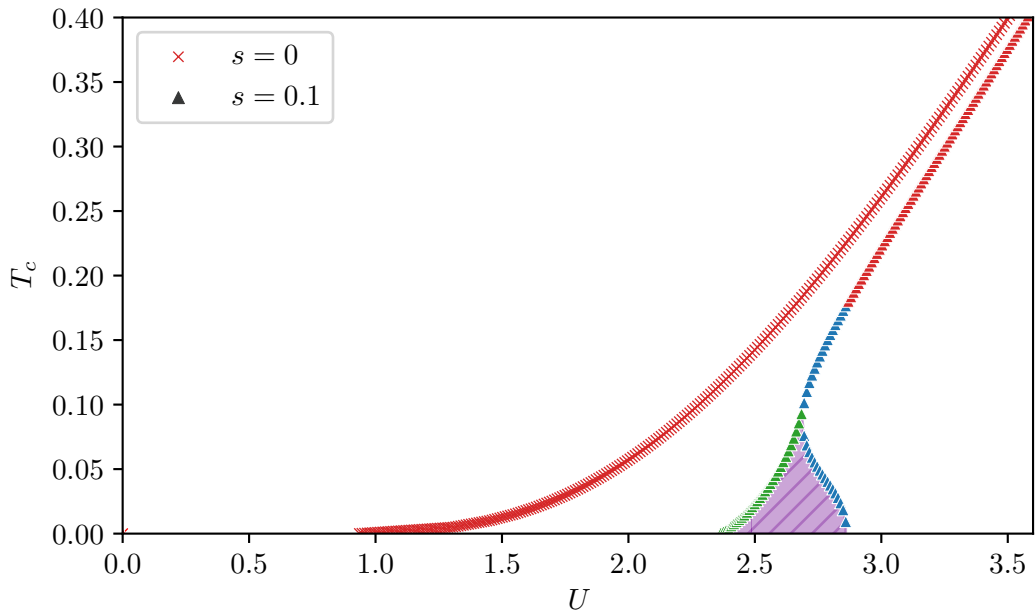


Figure 5.6: Phase diagram obtained from the solutions of the self-consistent gap equation only. T_c is determined by the Δ vs T contours of the self-consistent gap equation and is defined as the highest temperature at which $\Delta > 0$, by this definition some contours have multiple T_c 's. The red crosses correspond to the BCS-like case with zero splitting while the triangles correspond to finite effective splitting. The different coloured triangles match the three different groups of contour (single T_c BCS-like, multiple T_c or single T_c with first order jump). The purple highlighted region shows where two non-trivial solutions to gap equation are found, outside that region there is only one non-trivial solution.

solutions below T_c . The region where there exists two non-trivial solutions is highlighted in purple.

The self-consistency equations identify stationary points only. The free energy will need to be examined in order to know which of the multiple solutions present in the highlighted region (figure 5.6) minimises the free energy. The explicit form of the free energy will be discussed and minimised later in section 5.4 but before that we can infer the possible nature of these stationary points based on properties we know the free energy will have. For example, $F \rightarrow \infty$ as $\Delta \rightarrow \infty$ forbids the solution with largest Δ from being a maximum, which then affects which type of stationary point the remaining solutions can be. Additionally at high temperatures or high splitting the system will be in the normal state, hence $\Delta = 0$ will be the global minimum. Figure 5.7 shows some examples of the form the free energy could take.

Figure 5.7a shows the typical evolution of the free energy for a BCS superconductor, undergoing a second order phase transition between the normal and superconducting states as a function of temperature. At low temperature there exists two unique stationary points at $\Delta = 0$ and $|\Delta| \approx 0.2$, corresponding to a maximum and global minimum respectively. As temperature increases from $T = 0$ towards $T = T_c$, the global minimum occurs at finite Δ , the value of which tends to zero as $T \rightarrow T_c$. Eventually at T_c all stationary points have converged into one minimum at $\Delta = 0$ — the trivial solution to the self-consistency equations corresponding to the normal state. The free energy has evolved smoothly and continuously during the transition and the order parameter Δ has also evolved continuously.

Figure 5.7b on the other hand, shows how additional non-trivial solutions to the self-consistent gap equation may manifest in the free energy, giving rise to a first order phase transition. In this figure we are considering low T and so expect to be in the superconducting state i.e. there is a global minimum in the free energy at $|\Delta| > 0$. Indeed at $s = 0$ (BCS-like case) we observe the expected two stationary points with a minima at $\Delta \approx 0.2$. As s changes the free energy evolves smoothly and continuously but, unlike in a second order phase transition, the value of Δ does not. Instead Δ jumps from a finite value to $\Delta = 0$ as s is increased. The free energy can also have either one, two or three stationary points (ignoring the $\Delta = -\Delta$ mirror symmetry which would increase that count). This is consistent with the appearance of multiple solutions in the gap equation which also displays one (trivial), two (trivial + non-trivial) or three (trivial + 2 non-trivial) solutions.

In BCS theory there exists a correspondence between the number of solutions to the self-consistent gap equation and whether the system is superconducting or not, i.e. when there are two solutions, finite Δ minimises the free energy and hence the system is superconducting, while when there is only one trivial $\Delta = 0$ solution the system is normal – although it should be noted that this knowledge does not come from the self-consistency equations themselves but rather the study of the free energy. In the equal-spin triplet-pairing theory however, the number of solutions to the self-consistent gap equation does not reveal which solution minimises the free energy.

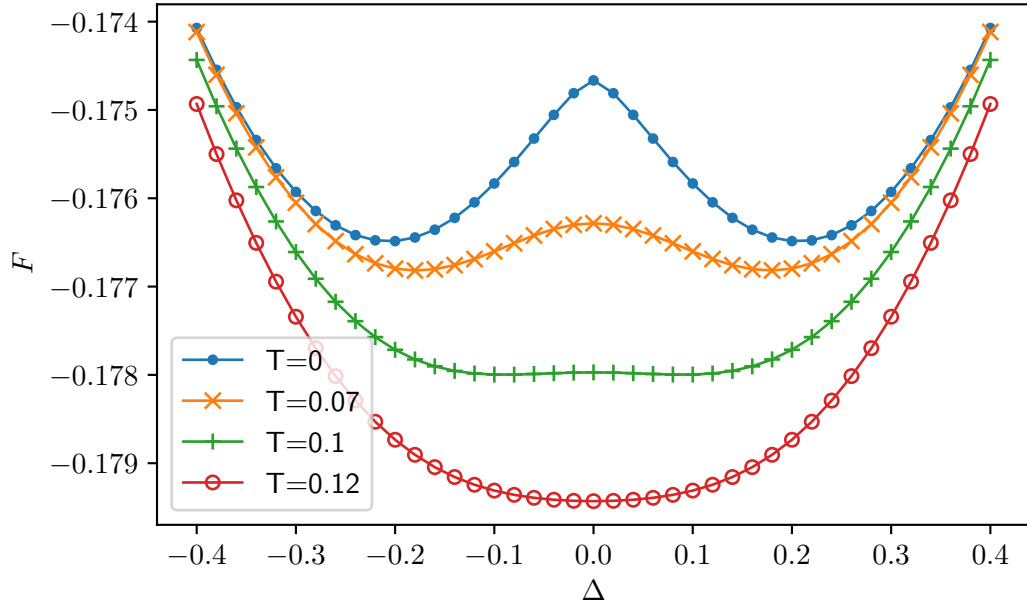
In analogy with BCS theory, it is probably safe to assume that the BCS-like case ($s = 0$, section 5.2.2) behaves like the BCS case and one can presume to know which state the system is in based on the number of solutions. Additionally, for very large U , where the contours of figure 5.5b are BCS-like, one can probably also assume that the effect of splitting is negligible and the number of solutions does determine the state of the system. Additionally, for intermediate U at temperatures above the lower of the two T_c 's, the free energy is also probably BCS-like due to the continuous nature of the free energy. However for small U and intermediate U below the lower T_c , where the contours of figure 5.5b correspond to three unique solutions, it is not possible to determine the state of the system from the number of solutions and hence the highlighted region in the phase diagram figure 5.6 cannot be assumed to be normal or superconducting.

The results discussed so far are all obtained from the gap equation only and as such may not be physically accurate. First we shall see if they persist after solving all self-consistency equations simultaneously.

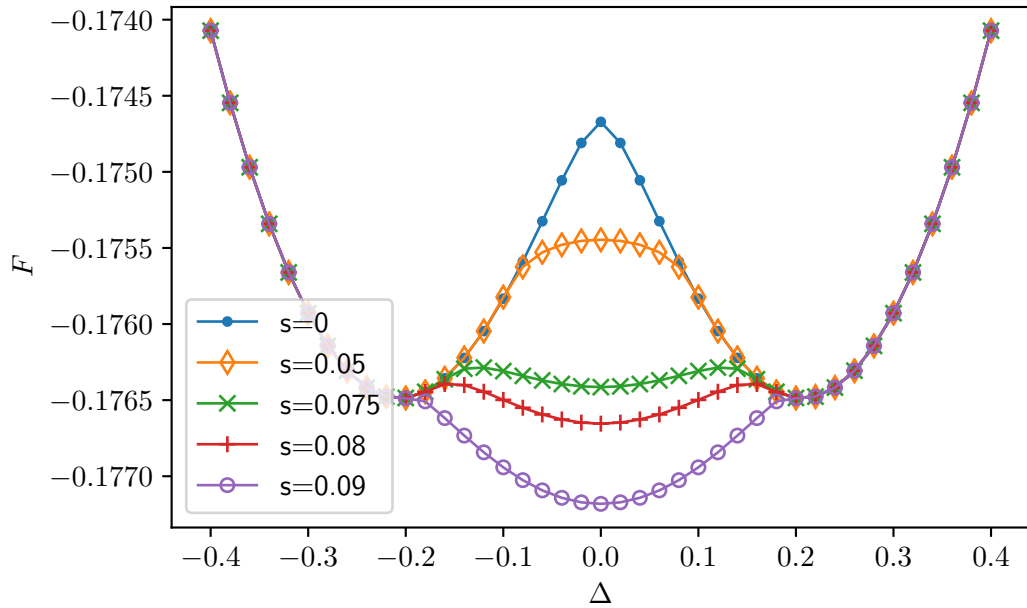
5.3.3 Solving the self-consistency equations iteratively

Recall that the results discussed so far were all obtained from the self-consistent gap equation only and the ϕ -fields were treated as arbitrary parameters rather than self-consistent mean-fields. Without self-consistently determining all mean-fields, the previous solutions to the self-consistent gap equation will not necessarily correspond to the global minimum of the free energy and hence may not be physically correct. To obtain the solutions to all the self-consistency equations simultaneously, and hence obtain the global minimum of the free energy, the same iterative procedure described in section 4.6.2 was used.

Figure 5.8 shows the solutions to the self-consistency equations obtained using the iterative method for two different values of splitting s . The dashed-lines and solid-lines correspond to zero splitting ($s = 0$) and finite splitting ($s \neq 0$) respectively, while the different colours



(a) Variation in the free energy w.r.t. Δ at different temperatures. Parameters (arbitrarily chosen): $U = 2.5$, $\mu = -2.7$, $s = 0$, $\phi_A = \phi_B = 0$.



(b) Variation in the free energy w.r.t. Δ at different splitting. Parameters (arbitrarily chosen): $U = 2.5$, $\mu = -2.7$, $T = 0.005$, $\phi_A = \phi_B = 0$.

Figure 5.7: Examples of stationary points of the free energy. Figure 5.7a shows typical evolution of the free energy with respect to temperature, showing two unique stationary points below T_c and one above it. The number of stationary points determines the state of the system and as temperature is changed the free energy evolves smoothly from one state to next. Figure 5.7b shows how finite splitting can give rise to an additional unique stationary point (totalling three) as predicted by the self-consistent gap equation. The red and green curves show that with three unique stationary points the system could be either superconducting or normal and hence the number of stationary points is not sufficient to determine what state the system is in.

correspond to different interactions U . When there is no splitting both $\Delta_{\sigma\sigma}$ (top panel) and effective splitting (bottom panel) behave as in the BCS case with $\Delta_0 = 1.76T_c$ and $s_\sigma^* = 0$ (i.e. $\phi_A = \phi_B$, see equation (5.25)). With finite splitting T_c is heavily suppressed and there exists a critical value of interaction, U , below which Δ is never finite, i.e. for a given interaction U , the bare splitting can completely kill the superconductivity if it is large enough because the energy gained by forming a pair is not enough to compensate the energy penalty incurred to overcome the bare splitting. Additionally the effective splitting is finite and its value depends on the interaction. Below the critical interaction the effective splitting is essentially independent of temperature but above it the effective splitting has a strong temperature dependence below T_c .

By solving the self-consistency equations as a function of temperature for different values of bare splitting, s , and interaction, U , it can be seen how T_c varies with these quantities, giving rise to the phase diagram in figure 5.9. Obtaining T_c accurately is difficult for a number of reasons: firstly the integrals become numerically difficult near T_c , resulting in a smoothing of Δ near T_c rather than a sudden onset; secondly it is desirable to have a large number of data points near T_c to improve the estimation, but T_c is not in general known before hand so it cannot be efficiently targeted programmatically; thirdly the integrals become even more difficult at small interaction U and small temperatures T .

Taking the difficulties of obtaining T_c into consideration, it was decided that it was best estimated by the temperature at which $|\frac{d\Delta}{dT}|$ was maximum. Testing this method on the BCS case, where T_c is known from Δ_0 , revealed that it tended to underestimate T_c slightly, with the accuracy improving with the number of points as expected. This method was more accurate than using a simple thresholding technique (which tended to overestimate T_c), whereby T_c is defined as the highest temperature at which Δ is greater than some small threshold value.

Each curve of the phase diagram, figure 5.9, corresponds to a different value of bare splitting s . The curve separates parameter space into two regions: a superconducting region below the curve and a normal region above it. For the case of zero splitting the behaviour is BCS-like with $T_c \propto \exp(-1/\rho(0)U)$ [14], note that due to the numerical difficulties discussed above, T_c goes to zero for some finite values of U even though it should be exponential.

With finite splitting there exists a critical finite value of U below which $T_c = 0$ and there is no superconductivity ($\Delta = 0$). Increasing the bare splitting has the effect of suppressing T_c and increasing the critical value of interaction U_c ; it acts to prevent superconductivity by requiring lower temperatures and larger interaction.

Solving only the self-consistent gap equation revealed that there should be multiple solutions of Δ for some values of U as long as the effective splitting, s_σ^* , was finite. However, after solving all the self-consistency equations iteratively we did not find any evidence for multiple solutions of Δ . In the BCS case, sections 4.6.2 and 4.7.3, we find that the effective splitting is self-consistently zero, that is $\phi_\uparrow = \phi_\downarrow$, and therefore the case of finite effective splitting, where multiple solutions are predicted, is not physically realised. However, in this case we see that the effective splitting is self-consistently finite when the bare splitting, s , is finite and, therefore, is physically realisable. It is curious then as to why we find no evidence of multiple solutions to the gap equation.

In order to understand why no evidence of multiple solutions is found we turn to the free energy. Using the free energy we can check that a particular solution of the self-consistency equations is a minimum or not by evaluating the free energy around that point. Furthermore

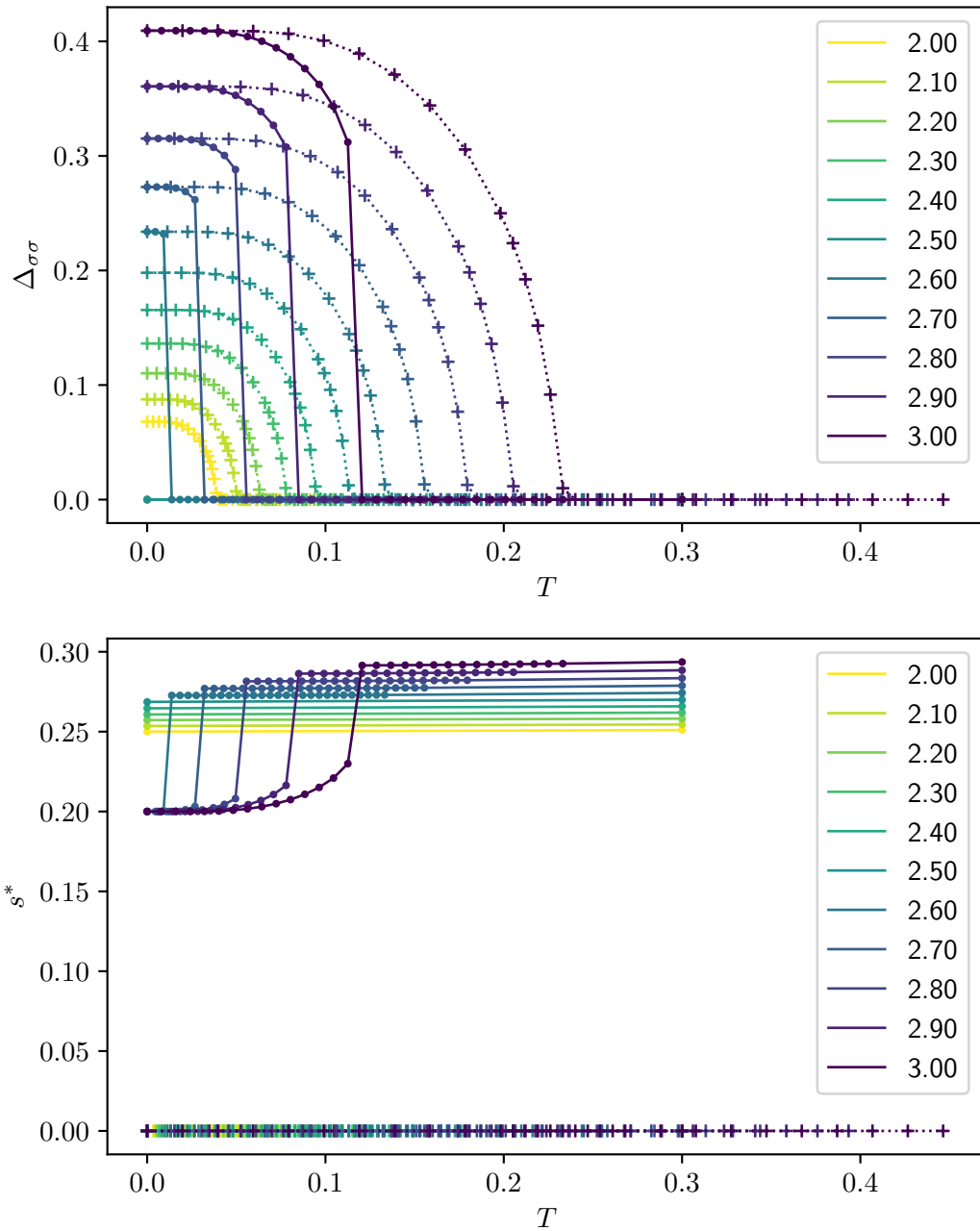


Figure 5.8: Solutions to the self-consistency equations when solved iteratively. The upper and lower panels show, respectively, how the $\Delta_{\sigma\sigma}$ - and $\phi_{m\sigma}$ -fields vary with temperature. In both panels the different colours represent different interactions U . The dashed-lines and solid-lines correspond to zero splitting, $s = 0$, and finite splitting, $s = 0.2$, respectively. As expected with zero splitting the behaviour is BCS-like however, with finite splitting the T_c is greatly suppressed and the effective splitting displays some significant temperature dependence below T_c . Here the chemical potential is $\mu = 0$.

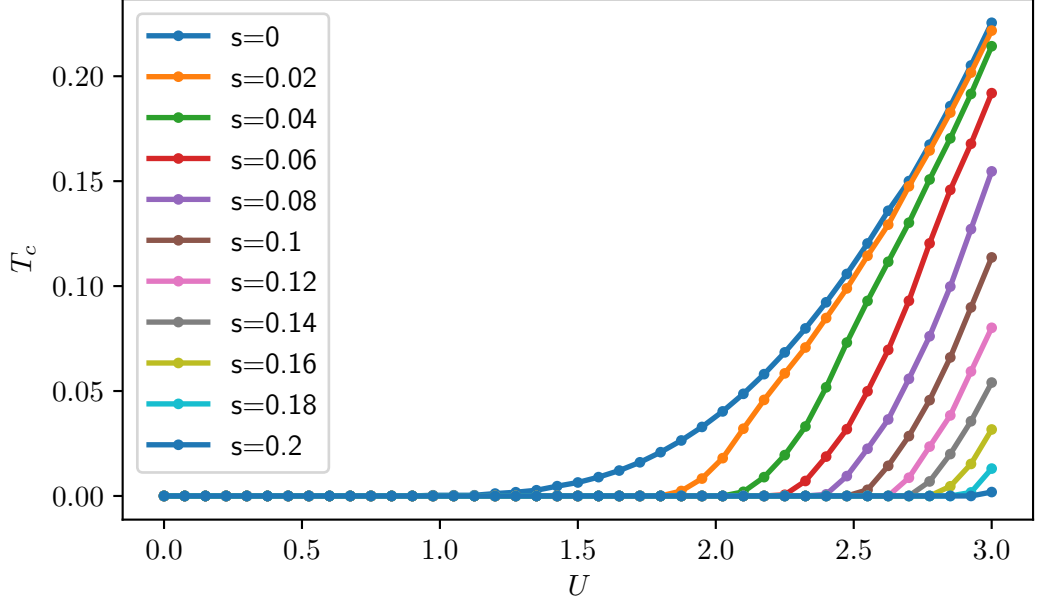


Figure 5.9: Phase diagram obtained from solving the self-consistent solutions iteratively. The different colour lines correspond to different values of bare splitting, s . For zero splitting the curve is BCS-like with $T_c \propto \exp(-1/\rho(0)U)$. With finite splitting there exists a critical value of interaction, U , below which superconductivity is fully suppressed. As splitting is increased the critical value of U also increases.

we can directly minimise the free energy itself to verify the results obtained by the self-consistency equations. We shall now investigate the free energy.

5.4 Free energy

The free energy is derived using the same method as discussed in section 4.7. At zero temperature the free energy corresponds to the ground state energy and is given by:

$$F_0 = \sum_{\sigma} \left\{ K_{A\sigma} + K_{B\sigma} - \mu(N_{A\sigma} + N_{B\sigma}) - \frac{U}{\mathcal{N}}(\chi_{\sigma}\chi_{\sigma}^* + N_{A\sigma}N_{B\sigma}) \right\} \quad (5.33)$$

where

$$K_{m\sigma} = \sum_{\mathbf{k}} \varepsilon_{\mathbf{k}\sigma}^{mm} \hat{n}_{\mathbf{k}\sigma} \quad (5.34)$$

and χ_{σ} and $N_{m\sigma}$ are as defined when discussing the self-consistency equations in section 4.5, equation (5.31). As with the BCS case, this expression is valid at zero temperature and can be solved with far fewer numerical issues than when solving the general expression at low temperatures.

The general expression for the free energy, valid at all temperatures, is again obtained by the same procedure as in section 4.7.2 and is given by:

$$F = \sum_{\sigma} \left\{ -\frac{U}{\mathcal{N}}(\chi_{\sigma}\chi_{\sigma}^* + N_{A\sigma}N_{B\sigma}) + \Delta_{\sigma\sigma}^* \chi_{\sigma} + \Delta_{\sigma\sigma} \chi_{\sigma}^* - \phi_{A\sigma} N_{A\sigma} - \phi_{B\sigma} N_{B\sigma} + F_{\sigma}^{\text{MF}} \right\} \quad (5.35)$$

where F_{σ}^{MF} is the mean-field free energy of the spin- σ part of the Hamiltonian and is given by:

$$F_{\sigma}^{\text{MF}} = E_{\sigma}^{\text{GS}} - k_B T \sum_{\mathbf{k}} \left\{ \ln(1 + e^{-\beta E_{a\mathbf{k}\sigma}}) + \ln(1 + e^{-\beta E_{b\mathbf{k}\sigma}}) \right\} \quad (5.36)$$

and E_σ^{GS} is as defined in equation (5.26). We can now use these expressions to verify the results from solving the self-consistency equations, both by evaluating the free energy around the solutions to check they are indeed minima and by direct minimisation of the free energy.

5.5 Phase diagram

The same hill descent algorithm as discussed previously in section 4.7.3 is used to directly minimise the free energy functions, equations (5.33) and (5.35), w.r.t. the mean-field parameters. In the BCS-like case ($s = 0$) the solutions to the self-consistency equations and the results of the hill climb agree, as they did in section 4.7.3, however, for finite splitting ($s = 0.1$, figure 5.10) there is a difference between the two methods.

Figure 5.10 shows that the stationary points obtained by iteratively solving the self-consistency equations significantly underestimate T_c or, equivalently, overestimate the suppression of T_c caused by the bare splitting. Both methods agree that finite bare splitting suppresses T_c and, moreover, introduces a critical interaction, U_c , below which superconductivity is fully suppressed. Additionally the bottom panel shows that the ϕ -fields (equivalently the effective splitting s_σ^*) change behaviour at T_c , with $(\phi_{A\sigma} - \phi_{B\sigma}) \rightarrow 0$, or equivalently $s_\sigma^* \rightarrow 2s$ (see equation (5.25)) as temperature decreases.

The difference between the two results occurs because in some cases the self-consistency equations find solutions which correspond to maxima of the free energy, rather than minima. Figure 5.11 demonstrates this. The top panel shows the results of the hill descent minimisation (blue dashed-line) and the solutions to the self-consistency equations (red solid-line). The four different symbols (purple and brown circles and orange and green diamonds) highlight the solutions that are tested in the lower panel to demonstrate the problem with the self-consistency equations.

In the lower panel of figure 5.11 the free energy has been calculated as a function of Δ four times, one for each solution highlighted in the upper panel. For each symbol the corresponding U , μ , s , T , ϕ_A and ϕ_B were used when calculating the free energy, giving rise to the four curves in the lower panel. The colour of each curve matches the colour of the corresponding symbol in the upper panel. The same symbol is used to highlight the corresponding value of Δ . The purple and brown dashed lines with ‘×’-markers show the free energy around the stationary point predicted by the self-consistency equations, while the orange and green dot-dashed lines with ‘+’-markers show the free energy around minimum points obtained by direct minimisation of the free energy via the hill descent algorithm.

The problem is highlighted by the free energy corresponding to the brown circle stationary point obtained by the self-consistency equations. This point actually corresponds to a local maxima in the free energy, whereas the solution returned by the hill descent algorithm (green diamond) really does correspond to a minimum in the free energy.

This is not surprising since the self-consistency equations were derived by requiring the derivative of the free energy w.r.t. the mean-fields be zero, a condition sufficient to find stationary points of the free energy but not sufficient to ensure those stationary points be minima. What is surprising is that solving the self-consistency equations iteratively does not seem to be able to converge on the solution, no matter what starting point, or friction term is used by the algorithm. Even using the result from the direct minimisation of the free energy

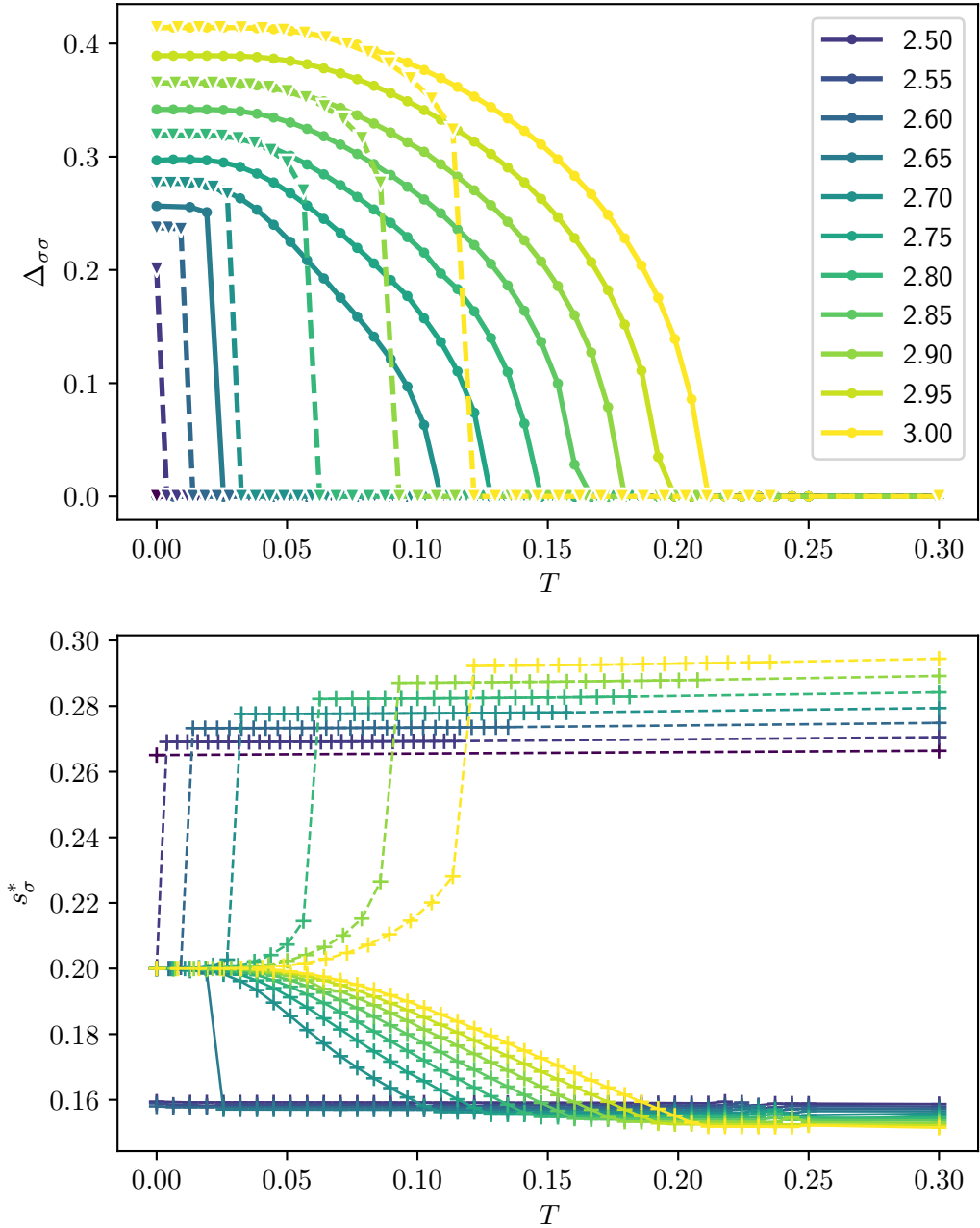


Figure 5.10: Comparison between the free energy minima obtained by direct hill descent minimisation and iteratively solving the self-consistency equations at finite bare splitting. The solid-lines and dashed-lines correspond to the hill descent minimisation and solutions to the self-consistency equations respectively. The different colours represent different interaction U . The top panel shows that the self-consistency equations significantly over estimate the suppression of T_c . The bottom panel also shows a difference between the effective splitting s_{σ}^* (directly related to the ϕ -fields). Both methods agree that finite bare splitting suppresses critical temperature and introduces a critical interaction U_c , below which superconductivity is fully suppressed. Additionally both methods agree that at T_c the effective splitting changes behaviour and tends towards $\phi_{A\sigma} - \phi_{B\sigma} = 0$ as temperature decreases. Parameters: $\mu = -2.7$, $s = 0.1$

as a seed when solving the self-consistency equations still sees them converge on the local maximum.

By direct minimisation of the free energy using the hill descent algorithm we can be much more confident that the result obtained is a minimum, compared to the stationary points identified by the self-consistency equations. However, due to problems in the integration of the free energy, which become more frequent close to U_c , the algorithm can become stuck before it reaches a minimum. To combat this the hill descent algorithm is run twice, once with fixed $\Delta = 0$ (as it is always a potential solution) and once more with a random starting point and all fields free to vary. The two results are compared and the one with the lower free energy is selected. It would be desirable to perform more repetitions but unfortunately the hill descent algorithm is much slower than solving the self-consistency equations iteratively. This problem is mitigated slightly by the fact that calculations are usually performed as a function of temperature or interaction so if the algorithm gets stuck away from the minima, it is often noticeable. Additionally, in such cases, the free energy can be evaluated around that point (as was done in figure 5.11) to verify whether it is a minimum or not - an advantage over only using the self-consistency equations.

Figure 5.12 shows how Δ and s_σ^* vary with temperature for different interaction, U , and splitting, s , using data obtained by direct minimisation of the free energy. The solid lines with ‘+’-markers and the solid lines with ‘dot’-markers correspond to $s = 0.0$ and $s = 0.1$ respectively. The different colours represent different interactions as shown in the legend. The top and centre panels show how Δ varies with temperature for zero and finite splitting respectively, while the bottom panel shows how the effective splitting (and therefore the ϕ -fields) vary with temperature for zero splitting (right axis) and finite splitting (left axis).

The centre panel shows that with finite splitting and relatively large interaction, $U >= 2.66$, T_c is suppressed compared to the case of zero splitting (top panel), but by less than the self-consistency equations predicted. As the interaction is reduced a shoulder/kink starts to appear between T_c and $T = 0$. For a small range of intermediate interactions $2.65 <= U < 2.66$ the shoulder turns into a sudden suppression of superconductivity with $\Delta = 0$, leaving two separate superconducting transitions, one second order the other first order. At $U = 2.64$ it appears that the superconductivity at higher temperatures becomes suppressed while a first order superconducting transition persists at low temperatures, although it could be the case that a small signature remains but at lower precision than our numerics. Finally, for interactions $U <= 2.6$ the superconductivity is suppressed completely for all T .

The small range of intermediate interaction $2.65 <= U < 2.66$ displays the fascinating phenomenon of re-entrant superconductivity: as the temperature is increased from zero, the superconductivity is weakened due to thermal fluctuations and cannot overcome the bare splitting. Yet as the temperature is further increased, the thermal fluctuations are now great enough to overcome the splitting and actually aid in the formation of superconducting pairs. This re-entrant superconductivity is a form of order by disorder: the increase in temperature increases thermal fluctuations but leads to the stabilisation of a more ordered state, rather than increasing disorder.

In the bottom panel of figure 5.12 we can see for the BCS-like case ($s = 0$, right axis, ‘+’-markers) the effective splitting is zero, $s_\sigma^* = 0$, i.e. $\phi_{A\sigma} = \phi_{B\sigma}$. There is again a very small difference in the ϕ -fields at low temperatures and again this is down to a numerical effect due to the line of constant free energy that appears at finite Δ , as discussed in section 4.7.3.

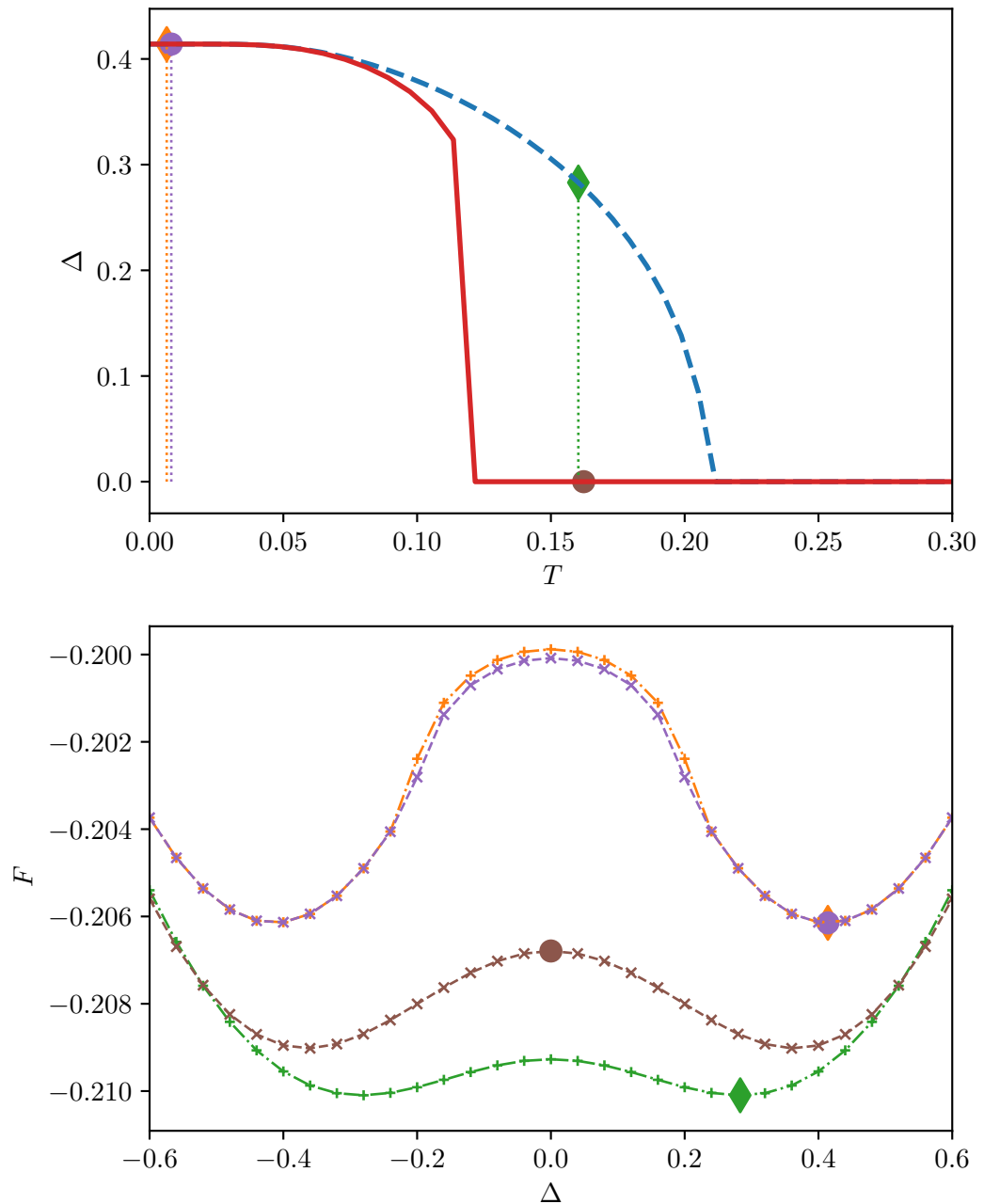


Figure 5.11: Stationary points and their corresponding free energies. The top panel compares the stationary points obtained from the solving the self-consistency equations iteratively (solid-line, circles) with the minima obtained from the free energy hill descent algorithm (dashed-line, diamonds). The diamonds and circles highlight the points about which the free energy is calculated and shown in the bottom panel. Purple circle and orange diamond correspond to the same stationary point obtained by both the hill descent algorithm and self-consistency equations. The brown circle and green diamond show the self-consistency equations and hill descent algorithm give different results and that the self-consistency equations have returned a maxima in the free energy.

With finite bare splitting ($s = 0.1$, left axis, ‘dot’-markers), the effective splitting, s_{σ}^* , takes some finite value above T_c due to a difference between the $\phi_{A\sigma}$ and $\phi_{B\sigma}$ fields. At T_c the ϕ -fields tend to equalise as temperature decreases and Δ increases, until $\phi_{A\sigma} = \phi_{B\sigma}$ as Δ reaches saturation. Let us now see how this difference impacts the phase diagram.

When minimising the free energy the hill descent algorithm tries both minimising the free energy w.r.t. all mean-fields as well as minimising while restricting $\Delta = 0$. This means T_c can be simply defined as the highest temperature at which $\Delta > 0$, unlike in section 5.3.1, where T_c is defined as the temperature at which $|\frac{d\Delta}{dT}|$ is maximum due to smoothing near the transition. Using the free energy hill descent algorithm, the corrected phase diagram, figure 5.13, can be obtained.

The corrected phase diagram shares the following common features with the incorrect phase diagram obtained by solving the self-consistency equations (figure 5.9): the BCS-like case ($s = 0$) shows the conventional exponential behaviour; at finite bare splitting, generally speaking, T_c is suppressed and, finally, there exists a critical interaction, U_c , below which superconductivity is completely suppressed. Both of these things are a sign that superconductivity is being weakened by the bare splitting. On the other hand however, the free energy minimisation shows a kink in the phase boundary (see figure 5.13 inset) corresponding to the Δ -vs- T curves that show two superconducting transitions (like those displayed in figure 5.12 centre panel). Such a kink was not detected by the self-consistency equations.

The kink in the phase diagram, figure 5.13 inset, corresponds to the re-entrant superconductivity we just mentioned. If the system has an interaction, U , between the two vertical dotted lines and is initially at $T = 0$ then it will be superconducting. As the temperature increases it will undergo a first order transition into the normal state. Further increase in T will then see another first order transition into a superconducting state, then followed by a further second order phase transition into the normal state. As we discussed, this is a form of order by disorder where the increase in temperature causes the stabilisation of the more ordered superconducting state. The empty purple circle in the inset of figure 5.13 marks the point where the phase boundary goes from a first order transition boundary (for temperatures below this point) to a second order transition boundary (for temperatures above this point). Although shown only for the $s = 0$ case, the same point is present in all phase boundaries for finite bare splitting and the same physics occurs however, the size of the re-entrant region decreases with bare splitting.

We end this discussion of re-entrant superconductivity by noting that the re-entrant behaviour is present in a *tiny* portion of the phase diagram, over a small range of interaction ($2.65 \lesssim U \lesssim 2.66$ for the $s = 0.1$ case) which is related to the size of the bare splitting. Bearing in mind the band width in this model is $8t$, the interaction range over which this can be observed is approximately $0.01t$, or 800 times smaller than the band width. This only gets smaller as the splitting is decreased and, realistically, the bare splitting must not be too large otherwise superconductivity becomes improbable. This fascinating phenomenon will therefore be difficult to observe.

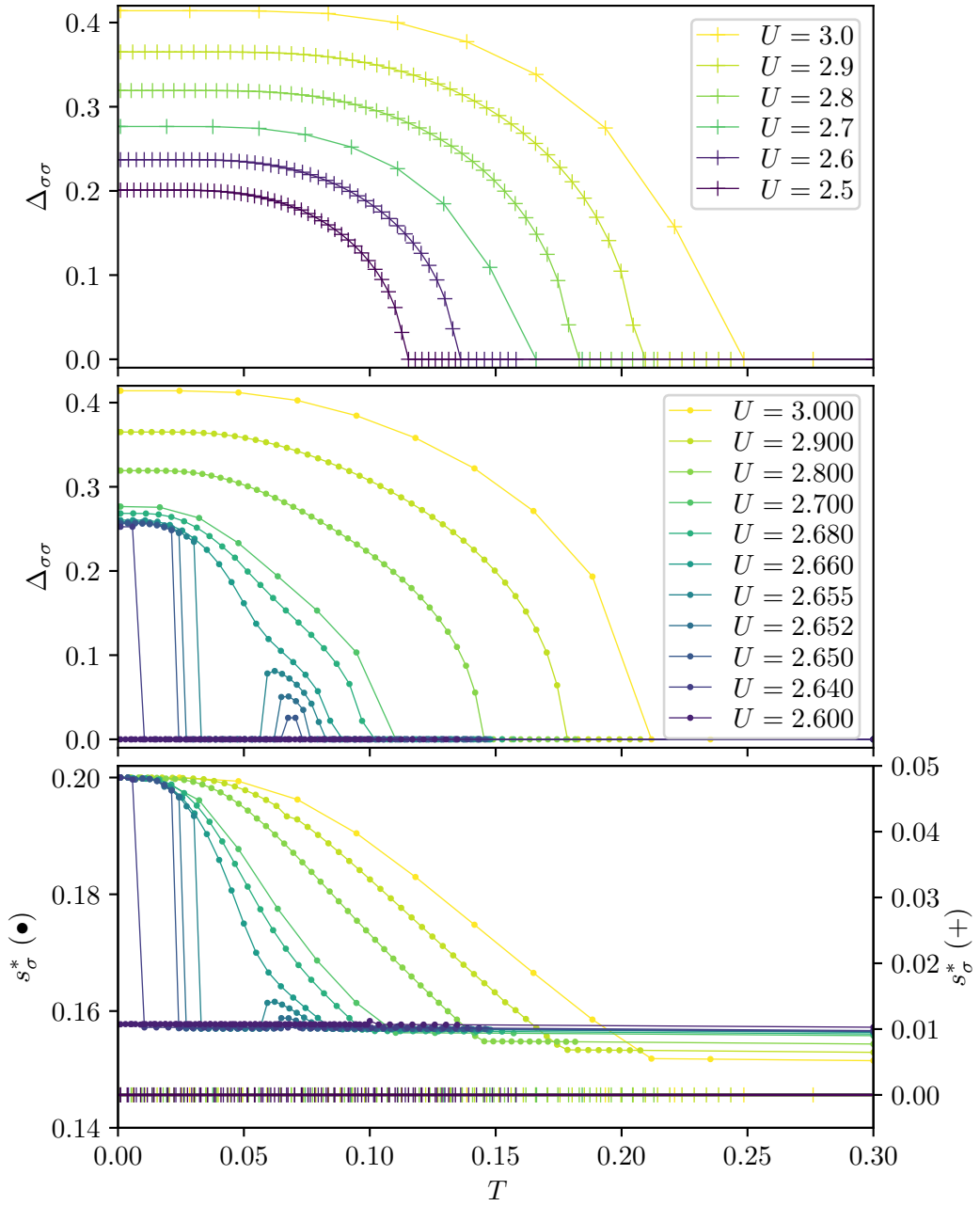


Figure 5.12: Minima of the free energy obtained by direct minimisation using the hill descent algorithm. In all panels the same set of colours correspond to the different values of interaction, U . The ‘+’-markers correspond to zero bare splitting, $s = 0$, while the dot-markers correspond to finite splitting, $s = 0.1$. The top and centre panels show how the $\Delta_{\sigma\sigma}$ -fields vary with temperature, for zero and finite bare splitting respectively. The bottom panel shows how the effective splitting, s_{σ}^* , (and hence the $\phi_{m\sigma}$ -fields) vary with temperature, with the left and right axes corresponding to finite and zero bare splitting respectively. Zero splitting exhibits the familiar BCS-like behaviour. At high U and finite splitting, Δ behaves in a BCS-like way albeit with a suppression of T_c . As the interaction is reduced, a suppression occurs somewhere between $T = 0$ and T_c , separating the phase space into two superconducting regions with two separate superconducting transitions; one second order, the other first order. At low enough interaction, all superconductivity is entirely suppressed.

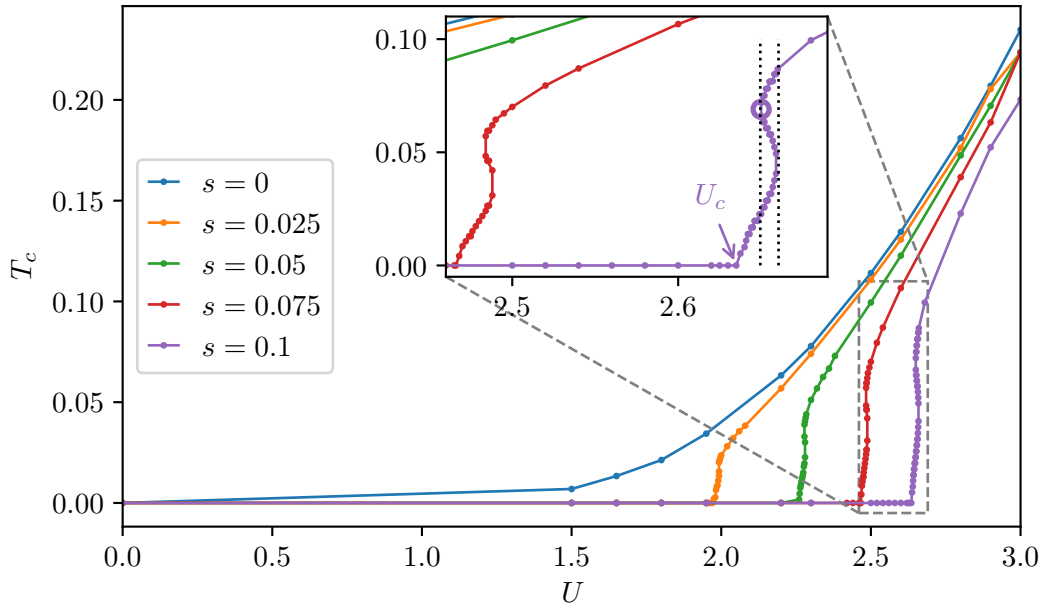


Figure 5.13: Phase diagram obtained by direct minimisation of the free energy using the hill descent algorithm. Each line marks the phase boundary between the normal state (higher T lower U side of line) and the superconducting state (lower T higher U side of line), with each colour corresponding to different bare splitting s . For finite splitting there exists a critical interaction U_c (labelled for $s = 0.1$) below which superconductivity is fully suppressed. With finite splitting, just above U_c there is a kink in the phase boundary caused by the bare splitting of the energy bands, leading to the possibility of re-entrant superconductivity. The circle marks (shown for the $s = 0.1$ case only) the point where the phase boundary changes between first order (temperatures below this point) and second order (temperatures above this point).

5.6 Quasi-particle spectrum

Another interesting phenomenon displayed by this model is that of gapless superconductivity; where Δ is finite, marking the presence of superconductivity, yet the energy spectrum has no energy gap. In this case the pairing potential Δ is isotropic but causes hybridisation of the bands away from the Fermi surface, which is quite different to nodal superconductors where the structure of the pairing potential Δ is anisotropic and has nodes as a result of sign changes or accidental cancellations. We demonstrate the difference between gapless and fully gapped superconductivity in figure 5.14.

Figure 5.14 shows the quasi-particle energy spectrum at two different temperatures, both below T_c and both superconducting ($\Delta > 0$). The mean-fields were determined by minimising the free energy for the given parameters. Figure 5.14a shows that the system is gapless. The pairing potential is finite and, just like in BCS, causes the hybridisation between the particle and hole bands (dashed lines). However, in this case the splitting has offset the hybridisation point away from the Fermi level such that when the BCS-like ‘gap’ opens, it does not create an actual energy gap. As the pairing potential increases, the hybridisation ‘gap’ also increases until it is big enough to create an actual energy gap, as shown in figure 5.14b.

One might wonder whether the gapless superconductivity is just a result of the special choice of non-interacting electron dispersion, where there is zero hybridisation and no spin

mixing terms so that this theory can be decomposed into two equivalent parts for each spin. However, the pairing interaction will always be exclusively between the A - and B -orbitals (because of the requirement of non-unitary triplet-pairing) and as such the quasiparticles will only hybridise particle and hole bands of the same spin. In order to hybridise the particle and hole bands (dashed lines of figure 5.14) at the point where they cross the Fermi surface would require hybridisation between opposite spins. The most direct way of obtaining such hybridisation is by analogy with the hybridisation already observed, i.e. a pairing potential between electrons of opposite spins, which as we just stated is forbidden because that would not be non-unitary triplet-pairing. It is not known whether equal-spin pairing with a fully general non-interacting dispersion (with all types of conceivable hopping terms), or with spin-orbit coupling, would allow for finite pairing potential to skip the gapless phase and go straight to fully gapped. Even so, it is likely that gapless superconductivity is a general feature of equal-spin triplet-pairing between two orbitals.

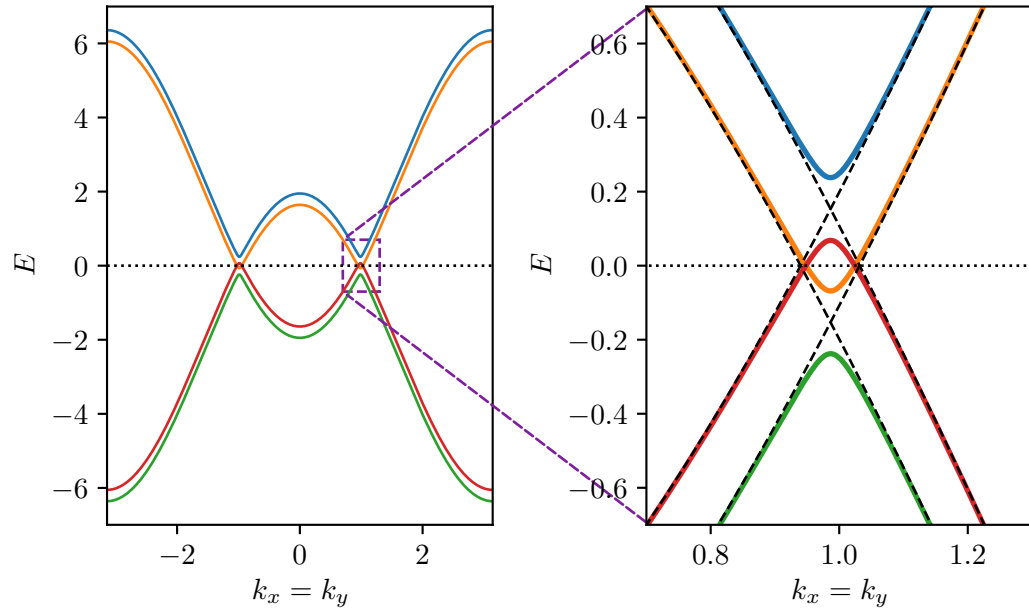
5.7 Spin imbalance

Throughout this chapter we have been discussing Δ without specifying whether we mean $\Delta_{\uparrow\uparrow}$ or $\Delta_{\downarrow\downarrow}$. That is because, for this theory, it turns out that $\Delta_{\uparrow\uparrow} = \Delta_{\downarrow\downarrow}$, always. This is first apparent in the self-consistency equations, equation (5.30), which have identical forms for \uparrow -spin and \downarrow -spin, and each is completely independent of the other spin-species' mean-fields. So solving the self-consistency equations gives the same result, independent of the spin label being considered. Secondly the total free energy can clearly be decomposed into the sum of two identical expressions, one for each spin, i.e. $F = F_{\uparrow} + F_{\downarrow}$. It was found that minimising the total free energy gave the same result as minimising the free energy for a single species. Indeed, one can see this should be the case from basic differentiation: $\delta F = \delta F_{\uparrow} + \delta F_{\downarrow}$. If F_{\uparrow} and F_{\downarrow} are identical expressions (except for a simple label) then they will be minimised by the same mean-field values, i.e. $\Delta_{\uparrow\uparrow} = \Delta_{\downarrow\downarrow}$.

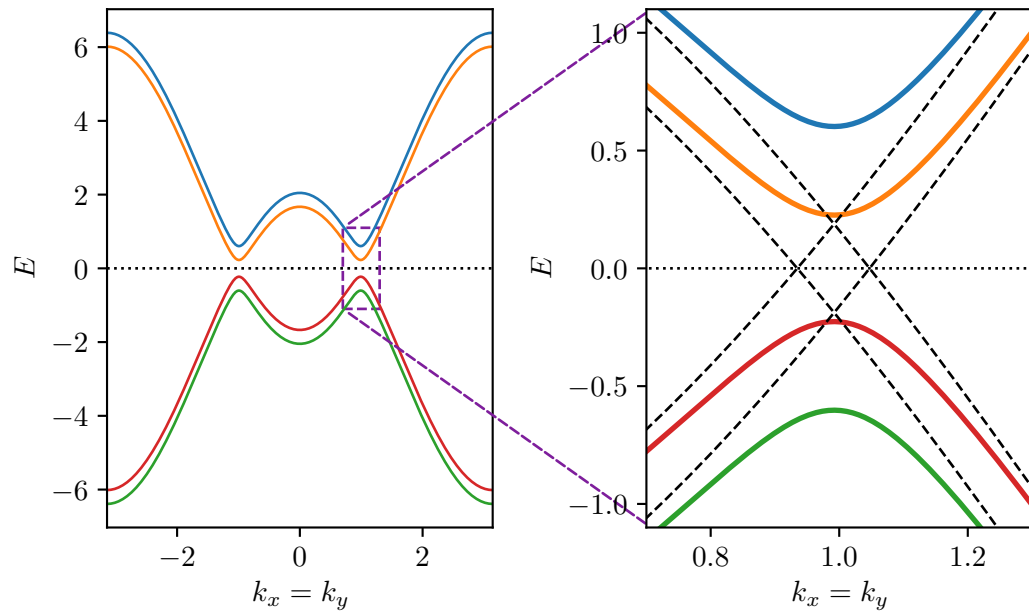
The consequences of equal \uparrow -spin and \downarrow -spin mean-fields are two fold. Firstly, as discussed in section 2.2, a triplet pairing potential with equal spin-up and spin-down components (as in this case) means $\hat{\Delta}(\mathbf{k})\hat{\Delta}(\mathbf{k})^{\dagger} \propto \mathbf{I}$, i.e. it is *unitary* triplet-pairing. It is for this reason that we have been referring to this theory as an equal-spin triplet-pairing theory, rather than a non-unitary triplet-pairing theory as it is described in [126]. While in principle the mean-fields $\Delta_{\uparrow\uparrow}$ and $\Delta_{\downarrow\downarrow}$ could have been different, it turns out that self-consistently they are not. Secondly, because all mean-fields are equivalent for different spin labels, there is no population imbalance between the different spins. This means that the magnetisation, $M = N_{\uparrow} - N_{\downarrow}$, is zero. Although we note here that our model does not include the effects of spin-orbit coupling and it is not known whether the free energy would retain this $\Delta_{\uparrow\uparrow} = \Delta_{\downarrow\downarrow}$ symmetry or give rise to a magnetisation with it included.

5.8 Summary

In this chapter we have used variational mean-field theory to study the physics of the equal-spin triplet-pairing theory proposed by Weng *et al.* [126]. We began by selecting a non-interacting dispersion, section 5.1, before applying the variational mean-field technique to solve the Hamiltonian. We derived the self-consistency equations and solved the gap equa-



(a) Gapless superconductivity. Parameters: $T = 0.205$, $\Delta = 0.085$, $\phi_A = -0.541$, $\phi_B = -0.447$, $s_\sigma^* = 0.153$. Here $\Delta < s_\sigma^*$



(b) Full gapped superconductivity. Parameters: $T = 0.013$, $\Delta = 0.414$, $\phi_A = -0.524$, $\phi_B = -0.500$, $s_\sigma^* = 0.188$. Here $\Delta > s_\sigma^*$

Figure 5.14: Energy spectrum of the Bogoliubov quasi-particles. The energy spectrum of the Bogoliubons was calculated using the values of the mean-fields obtained by the free energy minimisation, i.e. they are self-consistent and physically correct. Figure 5.14a shows gapless superconductivity, where Δ is finite but the energy spectrum is not gapped and figure 5.14b shows fully gapped superconductivity. The dashed lines on the right hand panels show the energy spectrum $\Delta = 0$ for comparison. In both cases $U = 3$, $\mu = -2.7$ and $s = 0.1$.

tion only while treating the ϕ -fields as free parameters, and also solved all self-consistency equations iteratively, section 5.3.

The self-consistent gap equation predicted multiple solutions when the effective splitting, s_σ^* , was finite, however, solving all equations iteratively found no evidence of this. In order to understand the contradiction between solving the self-consistent gap equation only and solving all equations iteratively, the free energy was derived and minimised, section 5.4. This revealed that iteratively solving the self-consistency equations, although fast, was not reliable for finding the global minima of the free energy. By minimising the free energy directly we confirmed that this *triplet*-pairing theory gave rise to two nodeless gaps of equal magnitude. Additionally and unexpectedly we found that this theory also contained re-entrant and gapless superconductivity. Although the re-entrant superconductivity occurred only in a very small region of the phase diagram, the gapless superconductivity is thought to be a generic feature of pairing between equal spin electrons on different bands and should persist for different non-interacting dispersions, although it only appears briefly near T_c before becoming fully gapped.

As we discussed in chapter 3, the non-unitary triplet-pairing theory [126] was proposed to try and explain the conflicting experimental results for LaNiGa₂. In order to do so it must achieve the following: it must be non-unitary triplet-pairing, in order to satisfy the symmetry requirements; it must have two nodeless gaps, consistent with experimental results; and it must break TRS by developing a net magnetisation in the superconducting state, as detected by μ SR results.

We have seen that such a theory does give rise to two nodeless gaps from triplet-pairing however, both gaps are of equal magnitude and as such do not constitute *non-unitary* triplet-pairing. Furthermore, the observation that the value of each mean-field is independent of spin means that no imbalance can occur between the population of each spin species, i.e. there can be no magnetisation. As we discussed in section 3.3, Ginzburg-Landau theory predicts non-unitary triplet-pairing should lower the free energy in these materials. From such a perspective the additional term coupling the \mathbf{d} -vector to the magnetisation, \mathbf{m} , must be included as it respects the symmetries of the problem, and it is this term that gives rise to magnetisation with non-unitary triplet-pairing. In order for our mean-field theory to be consistent with the very general Ginzburg-Landau picture, this term must be exactly zero (since no such term appears in our free energy). In order for that term to be exactly zero, there must be additional symmetries than were originally assumed in the Ginzburg-Landau framework. Indeed, in our mean-field theory, we obtain an additional symmetry between \uparrow - and \downarrow -spins such that the free energy can be decomposed into two identical copies for each spin, $F_\uparrow = F_\downarrow$. It was initially thought that, despite this symmetry, an imbalance between \uparrow - and \downarrow -spins would arise to balance the requirements of both the kinetic energy and equal-spin attraction terms however, this is not the case and this symmetry actually prevents magnetisation. This is not expected to be a symmetry of the real system in general, and shows that our mean-field description in its current state does not have all the necessary ingredients to describe LaNiGa₂.

In this chapter we have shown that it is possible to obtain two nodeless gaps from the equal-spin triplet-pairing theory but that this theory falls short of explaining the contradictory results for LaNiGa₂ due to an additional artificial symmetry. In the next chapter we shall investigate the lack of magnetisation in the theory and suggest an additional interaction term

as a way to eliminate the $F_{\uparrow} = F_{\downarrow}$ symmetry of our current mean-field theory and obtain magnetisation.

Chapter 6

Magnetism in the equal-spin triplet-pairing theory

In the previous chapter we saw how the equal-spin triplet-pairing theory gave rise to full gap superconductivity but did not exhibit either magnetisation or two *different* gaps, as is observed in experiments. In this chapter we will see how the addition of a repulsive Hubbard interaction to the equal-spin triplet-pairing theory gives rise to a spin-mixing term that can lead to magnetisation in the normal state. It is proposed that this spin-mixing term will lead to a spin-imbalance when superconductivity is included, leading to two *different* nodeless gaps and a net magnetisation.

We will first see why it was predicted that the equal-spin triplet-pairing theory would lead to a net magnetisation by considering the normal state limit ($\Delta_{\sigma\sigma} = 0$). We will see that this prediction is not correct and discuss the reasons for this. We will then briefly examine Stoner theory and show that the same reasoning, which lead to the prediction of net magnetisation in the normal state limit of the equal-spin triplet-pairing theory, this time leads to the correct prediction of magnetisation in Stoner theory. We will see that the key difference between the normal state limit and Stoner theory is a spin-mixing term. The absence of such a term in the equal-spin triplet-pairing theory is suspected to be the reason for the lack of magnetism. We will see that introducing a repulsive Hubbard interaction into the equal-spin pairing theory gives rise to magnetisation in the normal state.

6.1 Normal state theory of the equal-spin attraction

In this section we consider the same on-site equal-spin attraction as with our non-unitary triplet-pairing theory but restrict ourselves to the normal state by not including any $\Delta_{\sigma\sigma}$ pairing terms in the mean-field Hamiltonian. It turns out that this is equivalent to setting $\Delta_{\sigma\sigma} = 0$ in the full equal-spin triplet-pairing theory. It was expected that for the case of high interaction the system should develop some magnetisation by having more of one spin species than the other, allowing more interaction thus lowering the free energy. We will demonstrate how the expectation of magnetisation at high interaction arose, show that there is in fact no magnetic state and identify the problems that led to this incorrect expectation.

The mean-field Hamiltonian is given by

$$\hat{H}_{MF} = \sum_{m\mathbf{k}\sigma} \epsilon_{m\mathbf{k}\sigma} \hat{c}_{m\mathbf{k}\sigma}^\dagger \hat{c}_{m\mathbf{k}\sigma}$$

where $\epsilon_{m\mathbf{k}\sigma} = \epsilon_{\mathbf{k}\sigma}^{mm} - \mu + \phi_{m\sigma}$ is the dispersion of the interacting electrons in the m -orbital and $\epsilon_{\mathbf{k}\sigma}^{AA} = \epsilon_{\mathbf{k}} - 2ts$ and $\epsilon_{\mathbf{k}\sigma}^{BB} = \epsilon_{\mathbf{k}} + 2ts$ are the dispersions of the non-interacting electrons of the A - and B - orbitals respectively, here each orbital has been shifted by a small amount $\pm 2ts$ from the underlying 2D square lattice dispersion $\epsilon_{\mathbf{k}} = -2t[\cos k_x a + \cos k_y a]$ so that they are nearly degenerate.

The interaction term is the same as used in the equal-spin triplet-pairing theory and the derivation of the free energy is similar to that demonstrated in section 4.7, except this time we are interested only in the non-superconducting case and therefore exclude the $\Delta_{\sigma\sigma}$ terms in the mean-field Hamiltonian. Again, as discussed previously in sections 4.3.1 and 5.2.1, we do not include any mean-fields that couple to the Fock-like terms in the Wick expansion of the interaction and, because $\Delta_{\sigma\sigma}$ is also not included, there are no mean-fields that couple to the Gor'kov-like terms either. This means the only term from Wick's expansion of the interaction that are non-zero are the Hartree-like particle-density terms. Considering this, the ground state free energy for the normal state theory is:

$$\begin{aligned} F_0 &= \langle \hat{H} \rangle_{\text{MF}} \\ &= \sum_{m\mathbf{k}\sigma} (\epsilon_{\mathbf{k}\sigma}^{mm} - \mu) \langle \hat{c}_{m\mathbf{k}\sigma}^\dagger \hat{c}_{m\mathbf{k}\sigma} \rangle_{\text{MF}} - \frac{U}{\mathcal{N}} \sum_{\mathbf{k}_1\mathbf{k}_2\sigma} \langle \hat{c}_{A\mathbf{k}_1\sigma}^\dagger \hat{c}_{A\mathbf{k}_1\sigma} \rangle_{\text{MF}} \langle \hat{c}_{B\mathbf{k}_2\sigma}^\dagger \hat{c}_{B\mathbf{k}_2\sigma} \rangle_{\text{MF}}. \end{aligned}$$

The mean-field Hamiltonian is already diagonal so the expectation values are simply given by the Fermi-Dirac distribution evaluated at the corresponding energy $\langle \hat{c}_{m\mathbf{k}\sigma}^\dagger \hat{c}_{m\mathbf{k}\sigma} \rangle_{\text{MF}} = \hat{n}_F(\epsilon_{m\mathbf{k}\sigma})$. By making that substitution and expanding the summations the free energy can be written

$$\begin{aligned} F_0 &= K_{A\uparrow} + K_{B\uparrow} + K_{A\downarrow} + K_{B\downarrow} \\ &\quad - \mu(N_{A\uparrow} + N_{B\uparrow} + N_{A\downarrow} + N_{B\downarrow}) \\ &\quad - \frac{U}{\mathcal{N}}(N_{A\uparrow}N_{B\uparrow} + N_{A\downarrow}N_{B\downarrow}), \end{aligned} \tag{6.1}$$

where

$$\begin{aligned} K_{m\sigma} &= \sum_{\mathbf{k}} \epsilon_{\mathbf{k}\sigma}^{mm} \hat{n}_F(\epsilon_{m\mathbf{k}\sigma}) \\ N_{m\downarrow} &= \sum_{\mathbf{k}} \hat{n}_F(\epsilon_{m\mathbf{k}\sigma}). \end{aligned}$$

There are terms in the free energy for each orbital, m , and spin, σ , and each term is dependent on the corresponding mean-field, $\phi_{m\sigma}$, only. This is unlike the full theory where, in general, Δ is not zero and each term of the free energy depends on all three mean-fields for a given spin: $\Delta_{\sigma\sigma}$, $\phi_{A\sigma}$ and $\phi_{B\sigma}$. This simplification makes it possible to quickly calculate the free energy as a function of N_\uparrow and N_\downarrow . Furthermore we consider only the $s = 0$ case for two reasons; firstly because we expect the magnetisation to appear as a result of the non-unitary triplet-pairing, not the splitting and secondly we can assume the simplification: $\phi_{A\sigma} = \phi_{B\sigma}$ (supported by our results from BCS theory). A direct consequence of this assumption is that $N_{A\sigma} = N_{B\sigma} = N_\sigma/2$. The free energy then becomes:

$$F_0 = K_{A\uparrow} + K_{B\uparrow} + K_{A\downarrow} + K_{B\downarrow} - \mu(N_\uparrow + N_\downarrow) - \frac{U}{4\mathcal{N}}(N_\uparrow^2 + N_\downarrow^2). \tag{6.2}$$

The total number of particles is given by $N = N_\uparrow + N_\downarrow$ which means the free energy can be written as

$$F_0 = K_{A\uparrow} + K_{B\uparrow} + K_{A\downarrow} + K_{B\downarrow} - \mu N - \frac{U}{4\mathcal{N}}(N_\uparrow^2 + (N - N_\uparrow)^2). \tag{6.3}$$

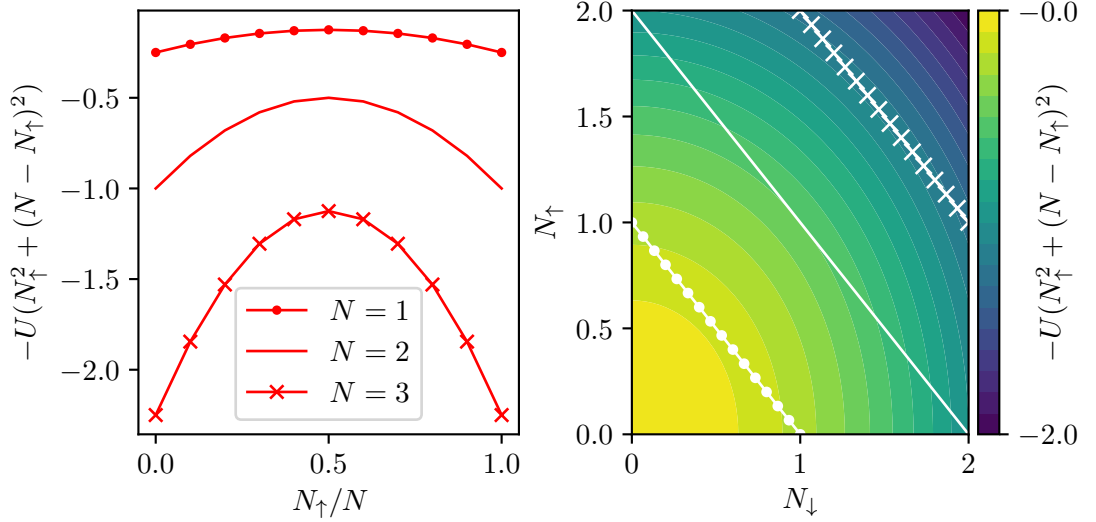


Figure 6.1: Comparison between the normal state free energy interaction term with and without fixed total particle number. The left hand panel shows how the interaction term varies with number of up particles N_{\uparrow} for different fixed total particle number N . Each curve is minimised at maximum particle imbalance. The right hand panel shows the interaction term as a function of N_{\uparrow} and N_{\downarrow} . The different lines correspond to different fixed particle number and the match the corresponding lines on the left hand panel. The global minimum appears at maximum filling: $N_{\uparrow} = N_{\downarrow} = 2$.

Since the free energy in this case is easy to calculate it is not necessary to consider the self-consistency equations and we progress immediately to discussions of the free energy.

If the interaction is large enough, it will dominate the free energy and the other terms can be considered negligible; we will call this the infinite U limit. Figure 6.1, left panel, shows how the interaction term of equation (6.3) behaves as the number of spin-up particles changes for different total particle number, N . It can be seen that in this limit the free energy is minimised by having maximally imbalanced spin populations, indicating that the normal state theory should have a magnetic phase at high U . However, the right hand panel of figure 6.1 shows how the same term varies as a function of both N_{\uparrow} and N_{\downarrow} , and it shows that in the infinite U limit the global minimum occurs at maximum filling: $N_{\uparrow} = N_{\downarrow} = 2$, i.e. magnetisation is zero.

The problem with using the free energy in the form of equation (6.3) is that it introduces the total number of particles, N , as a parameter when in fact its value should be determined by the mean-fields whose values minimise the free energy. Furthermore it does not take into account the allowed number of particles in each spin population. If at full filling $N_{A\uparrow} = N_{A\downarrow} = N_{B\uparrow} = N_{B\downarrow} = 1$, then the total population is $N = 4$ and equation (6.3) would find the free energy minimum corresponds to full spin imbalance: $N_{\uparrow} = 4$, $N_{\downarrow} = 0$ or vice versa. However, it is not possible to create such an imbalance because the individual bands are all full. Of course, if the correct value of N is used *and* it corresponds to half-filling or less, then equation (6.3) will give the correct minima, however, those quantities are not known before the free energy is minimised.

Having just seen how the simplest form of the free energy, equation (6.3), can lead to incorrect predictions of magnetisation we will now see how the free energy of the normal state, equation (6.2), varies with interaction. It can be seen in figure 6.2 that the minimum

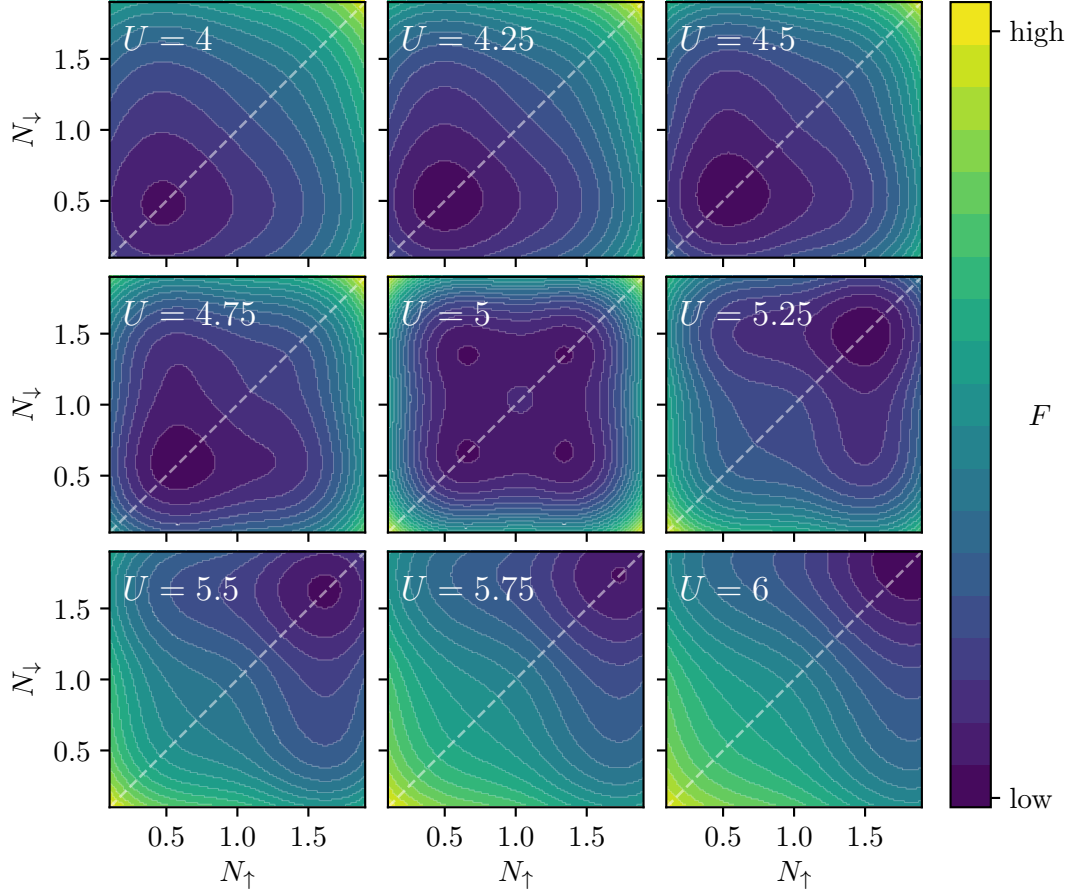


Figure 6.2: Normal state free energy. Each panel shows the free energy of the normal state limit of the equal-spin pairing theory corresponding to a different value of interaction with fixed chemical potential $\mu = -2.5$. The minimum of the free energy is always located on the dashed line, corresponding to zero magnetism, except for a single value of interaction U where there exists four degenerate minima, two of which correspond to magnetic states.

of the free energy always occurs on the $N_\uparrow = N_\downarrow$ line, i.e. $M = 0$. There is a phase transition from a low density phase to a high density phase as interaction is increased. At the transition point between the two phases there exists four degenerate minima in the free energy, two of which have a net magnetisation. These four minima appear to be degenerate at exactly the transition only, either side of it the global minimum corresponds to either the high or low density state.

Figure 6.3 shows the phase diagram for the normal state theory, obtained by minimising the free energy, equation (6.2), at different interaction, U , and chemical potential, μ . Generally speaking the chemical potential controls the particle number, this is seen clearly at $U = 0$. As the attractive interaction is increased the system transitions from a low- to high-density state as expected. There exists a first order phase transition, marked by the solid red line, which ends in a quantum critical end point, marked by the red circle.

From the right panel of figure 6.3, we see there is no magnetic phase in the normal state. Two of the four degenerate minima that occur exactly at the transition (see figure 6.2) are magnetic but occur simultaneously with two non-magnetic states. These are not the same magnetic states predicted by the naive minimisation of the fixed N free energy, equation (6.3), and as such do not help identify the missing magnetisation in the non-unitary triplet-pairing

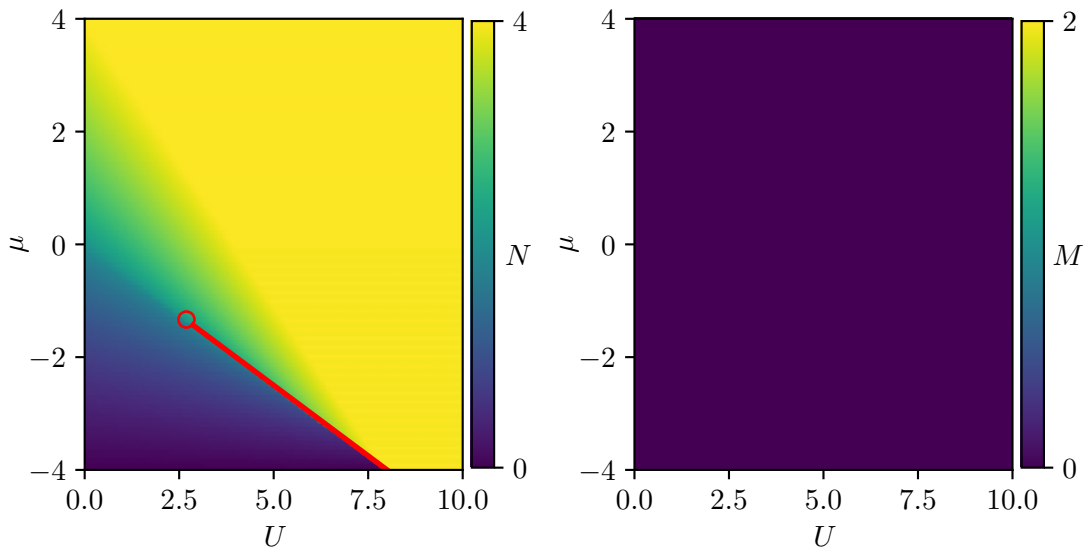


Figure 6.3: Normal state zero-temperature phase diagram, particle density and magnetisation. The left panel shows the normal state zero-temperature phase diagram (red lines) superimposed onto a particle density colour map. It shows a transition between a high- and low-density phase, separated by the red phase boundary, akin to a gas-liquid transition. The solid red line marks a first-order non-symmetry breaking phase transition. The red circle highlights a quantum critical end point that marks the end of the first order transition. The right panel shows the magnetisation of the normal state and no magnetisation is observed.

theory. Although interesting, it is beyond the scope of this work to investigate these four degenerate states, and any magnetism that results from them, any further.

In this section we have seen how a simplified form of the normal state free energy, equation (6.3), with fixed N gave rise to the expectation of magnetisation at large interaction, U . By comparing to an alternative form of the free energy, equation (6.2), we see that the prediction of magnetisation at high interaction comes from a naive minimisation of equation (6.3) and that in fact when minimised properly there is no magnetisation in the normal state. This is consistent with the findings from the general equal-spin triplet-pairing theory (where Δ can be finite), where the free energy is minimised by having equal mean-fields for spin-up and spin-down particles and, hence, equal spin populations and no magnetisation.

The above comparison of the two forms of the free energy, equations (6.2) and (6.3), was inspired by a similar analysis of Stoner theory. Again the free energy is written in terms of a fixed particle number, N , and the number of spins of a single species N_σ , just like equation (6.3). This time however, a magnetic state was found to minimise the free energy. We now briefly examine the Stoner theory to identify the difference that gives rise to the magnetisation.

6.2 Stoner theory

In this section we will briefly examine Stoner theory [131, 132] in the same way as we just did for the normal state limit of the equal-spin triplet-pairing theory. Unlike in the last section, we will see that the free energy is minimised by unbalancing the number of spin-up and spin-down particles, irrespective of which form the free energy is written in. We will see that a spin-mixing term in the Stoner theory free energy is responsible for a net magnetisation while

the absence of such a term in the equal-spin normal state theory gives rise to an additional $\uparrow=\downarrow$ symmetry that forbids magnetisation.

We take the Hubbard model [133] as our starting point:

$$\hat{\mathcal{H}} = \hat{\mathcal{K}} - \mu\hat{\mathcal{N}} + \hat{\mathcal{V}} \quad (6.4)$$

where the Hubbard interaction, $\hat{\mathcal{V}}$, is given by:

$$\hat{\mathcal{V}} = +U_S \sum_j \hat{c}_{j\uparrow}^\dagger \hat{c}_{j\downarrow}^\dagger \hat{c}_{j\downarrow} \hat{c}_{j\uparrow} \quad (6.5)$$

This is an on-site interaction between electrons of opposite spin. For our study of Stoner theory we take the interaction strength, U_S , to be a positive constant, making the interaction repulsive.

We define the mean-field Hamiltonian as:

$$\hat{\mathcal{H}}_{\text{MF}} = \sum_{\mathbf{k}\sigma} \epsilon_{\mathbf{k}\sigma} \hat{c}_{\mathbf{k}\sigma}^\dagger \hat{c}_{\mathbf{k}\sigma} \quad (6.6)$$

where $\epsilon_{\mathbf{k}\sigma} = \varepsilon_{\mathbf{k}\sigma} - \mu + \phi_\sigma$ and $\varepsilon_{\mathbf{k}\sigma}$ is the non-interacting electron dispersion. To obtain the most direct comparison between this Stoner theory (which gives rise to magnetism) and our normal state theory, section 6.1, (which does not) we include only the ϕ_σ mean-fields which couple to the Hartree-like term of Wick's expansion. As there are no mean-fields coupling to the Gor'kov- and Fock-like Wick terms, they do not appear in the free energy as their expectation values are zero (see section 4.7 for the derivation of the free energy and how Wick's theorem applies).

Again, following a similar process as used in section 4.7, the ground state free energy is obtained and is given by:

$$\begin{aligned} F_0 &= \langle \hat{\mathcal{H}} \rangle_{\text{MF}} \\ &= \sum_{\mathbf{k}\sigma} \varepsilon_{\mathbf{k}\sigma} \langle \hat{n}_{\mathbf{k}\sigma} \rangle_{\text{MF}} - \mu \sum_{\mathbf{k}\sigma} \langle \hat{n}_{\mathbf{k}\sigma} \rangle_{\text{MF}} + \frac{U_S}{\mathcal{N}} \sum_{\mathbf{k}_1} \langle \hat{n}_{\mathbf{k}_1\uparrow} \rangle_{\text{MF}} \sum_{\mathbf{k}_2} \langle \hat{n}_{\mathbf{k}_2\downarrow} \rangle_{\text{MF}}. \end{aligned}$$

As usual

$$\begin{aligned} \hat{\mathcal{N}} &= \sum_{\mathbf{k}\sigma} \hat{n}_{\mathbf{k}\sigma} = N_\uparrow + N_\downarrow \\ \hat{\mathcal{K}} &= \sum_{\mathbf{k}\sigma} \varepsilon_{\mathbf{k}\sigma} \hat{n}_{\mathbf{k}\sigma} \end{aligned}$$

In this case we take the common quadratic dispersion [132], $\varepsilon_{\mathbf{k}\uparrow} = \varepsilon_{\mathbf{k}\downarrow} = \frac{\hbar^2 \mathbf{k}^2}{2m}$, because the expectation value of kinetic energy term then takes a simple analytic form as we shall now see.

The kinetic energy written as an energy integral is:

$$\hat{\mathcal{K}} = \sum_\sigma \int_0^{E_{F\sigma}} \varepsilon g(\varepsilon) d\varepsilon \quad (6.7)$$

where the density of states for the quadratic dispersion is given by $g(\varepsilon) \propto \varepsilon^{\frac{1}{2}}$ [132] and $E_{F\sigma} = \varepsilon_{\mathbf{k}\sigma} - \mu + \phi_\sigma$ is the Fermi energy cut-off for the σ -band. In principle this cut-off can

be different for each band because of the mean-field ϕ_σ , allowing for different numbers of particles in each band. Performing the integral gives

$$\hat{\mathcal{K}} \propto \sum_{\sigma} E_{F\sigma}^{\frac{5}{2}}. \quad (6.8)$$

The particle number is given by [132]

$$N = \frac{V \mathbf{k}_F^3}{3\pi^2}. \quad (6.9)$$

Solving the electron dispersion relation for \mathbf{k}_F and substituting in to equation (6.9) gives

$$N = \frac{V}{3\pi^2} \left(\frac{2mE_{F\sigma}}{\hbar^2} \right)^{\frac{3}{2}} \quad (6.10)$$

and then solving for $E_{F\sigma}$ gives

$$E_{F\sigma} = \frac{\hbar^2}{2m} \left(\frac{3\pi^2}{V} \right)^{\frac{2}{3}} N^{\frac{2}{3}}. \quad (6.11)$$

Finally substituting equation (6.11) into equation (6.8) gives

$$\hat{\mathcal{K}} = \alpha (N_{\uparrow}^{\frac{5}{3}} + N_{\downarrow}^{\frac{5}{3}}) \quad (6.12)$$

where α is a constant consisting of quantities such as the volume, renormalised mass and Planck's constant. The kinetic energy written in this form is useful because it has a simple analytic dependence on the particle numbers.

The free energy can then also be written in terms of the two particle numbers

$$F = \alpha (N_{\uparrow}^{\frac{5}{3}} + N_{\downarrow}^{\frac{5}{3}}) - \mu (N_{\uparrow} + N_{\downarrow}) + U_S N_{\uparrow} N_{\downarrow}. \quad (6.13)$$

Just as we did for the equal-spin theory normal state, section 6.1, we can also write the free energy in terms of one of the spin populations N_{\uparrow} and the total number of particles N :

$$F = \alpha (N_{\uparrow}^{\frac{5}{3}} + (N - N_{\uparrow})^{\frac{5}{3}}) - \mu (N_{\uparrow} + (N - N_{\uparrow})) + U_S N_{\uparrow} (N - N_{\uparrow}) \quad (6.14)$$

As was done for the normal state limit of the equal-spin triplet-pairing theory, the interaction term of the free energy is calculated with fixed N (figure 6.4 left panel) and compared with the same term evaluated as a function of N_{\uparrow} and N_{\downarrow} with no restriction on N (figure 6.4 right panel). When U_S is large enough the non-interacting terms of the free energy are negligible and the free energy is described by the this interaction term. This is the infinite U_S limit of the free energy.

The left panel of figure 6.4 shows that the free energy in the infinite U_S limit is minimised by having maximally imbalanced spin populations, i.e. a magnetic state. The right panel shows the minima is formed of two lines: $N_{\uparrow} = 0$ or $N_{\downarrow} = 0$. Again the fixed N form of the free energy, equation (6.14), suffers from the same problems as with the non-unitary triplet-pairing normal state: N is not known before free energy minimisation and limitations on particle distribution due to particle filling is not taken into account. Coincidentally however, for any particle number less than half-filling these problems do not affect the minima and the two ways of calculating the free energy both predict magnetisation.

It is clear then that writing the free energy in terms of the particle number, equation (6.14), can be a helpful way to visualise and easily identify the minima however, as we saw in section 6.1, its validity is not guaranteed and the free energy should always be minimised without

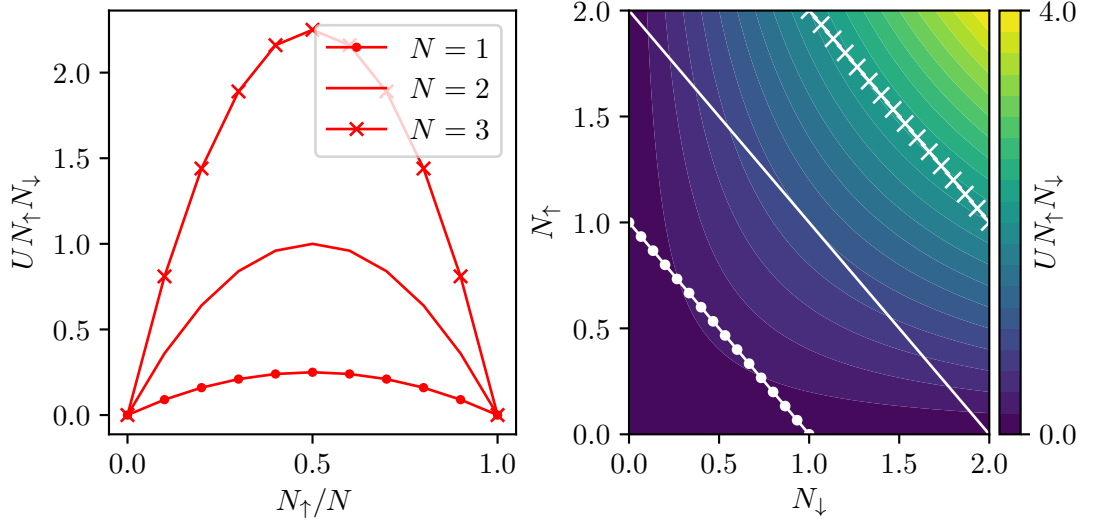


Figure 6.4: Comparison between the Stoner theory free energy interaction term with and without fixed total particle number. The left hand panel shows how the interaction term varies with number of up particles N_{\uparrow} for different fixed total particle number N . Each curve is minimised at maximum particle imbalance. The right hand panel shows the interaction term as a function of N_{\uparrow} and N_{\downarrow} . The different white lines correspond to different fixed particle number and the match the corresponding lines on the left hand panel. The global minimum is formed of two lines ($N_{\uparrow} = 0$ or $N_{\downarrow} = 0$) which correspond to maximally imbalanced spin populations (except the special point $N_{\uparrow} = N_{\downarrow} = 0$ where there are zero particles in the system).

restriction to be sure of the result. Let us investigate the general free energy, equation (6.13), further.

Figure 6.5 shows the free energy, equation (6.13), as a function of N_{\uparrow} and N_{\downarrow} at fixed μ for different interactions U_S . The white dashed-line is where $N_{\uparrow} = N_{\downarrow}$, i.e. magnetisation $M = 0$ and the red dots highlight the points where the free energy is minimum. At zero interaction (top left panel) the non-interacting terms of the free energy dominate and the system wants to fill both spin bands to the chemical potential. As the interaction increases the number of particles decreases due to the repulsion, until some critical value of interaction ($1.2 < U_S < 1.22$) is reached, at which point the system goes into a magnetic state by unbalancing the spin populations.

By repeatedly calculating the free energy and finding its minima as a function of N_{\uparrow} and N_{\downarrow} for different chemical potential, μ , and interaction, U_S , the phase diagrams shown in figure 6.6 were obtained. The left panels show the particle density and the right panels show the magnetisation. The bottom panels show specific cuts through the overall colour maps of the top panels. It can be seen that, for a given chemical potential, a magnetic phase exists above a critical value of interaction, U_c . At this critical interaction the system undergoes a second order phase transition, the phase boundary of which is shown in the upper panels by the red dots. The phase boundary was determined by the onset of the magnetisation (which corresponds to breaking of TRS) and the point at which the first order derivative was maximum.

The magnetic phase arises due to the repulsive interaction U_S . At zero interaction the system wants to fill both the spin-up and spin-down bands to the chemical potential however, at finite interaction filling both spin bands will lead to an energy penalty from the interaction

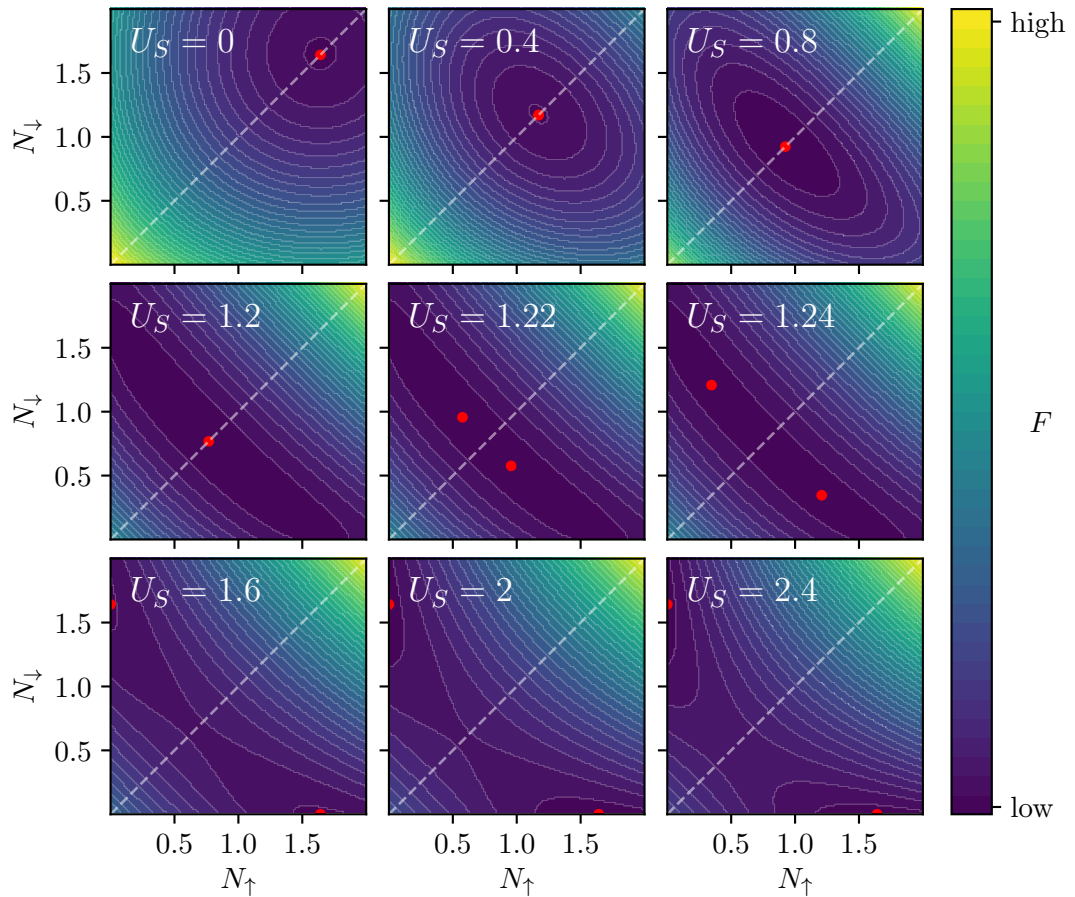


Figure 6.5: Stoner theory ground state free energy. Each panel corresponds to a different interaction, U_S , the red dots highlight the minimum of the free energy and the white dashed-line shows where the magnetisation is zero. At $U = 0$ there is a single minimum corresponding to a state with zero magnetisation. As interaction is increased, two degenerate minima emerge, each corresponding to the equal but opposite magnetisation.

term. For $U_S < U_c$ the system reduces its filling as U_S increases, thereby increasing the contribution to the free energy from the non-interacting terms but reducing the energy penalty from the interaction term. Just after the critical value of interaction, the system starts to magnetise. In doing so it reduces the energy penalty from the interacting term and is also able to increase the particle number nearer to chemical potential, also reducing the contribution from the non-interacting terms. Eventually the system becomes fully polarised with all electrons having the same spin giving rise to the maximum possible magnetisation and requiring that the system be at half-filling.

It was initially thought that non-unitary triplet-pairing would have a similar mechanism to unbalance the spin populations, giving rise to a net magnetisation. Since the pairing occurs between particles of the same spin, the free energy can be reduced by maximising the number of particles of a single spin — the more particles of a single spin species, the more pairing can be achieved. Of course, this would also increase the contribution to the free energy from the non-interacting terms. In principle a balance could be reached if the opposite were to occur in the other spin channel: reduce the number of particles (unfavourable because less pairing), but improve the free energy by bringing the particle number closer to the chemical potential again. Such an imbalance in spin species would lead to a net magnetisation $M = N_\uparrow - N_\downarrow$.

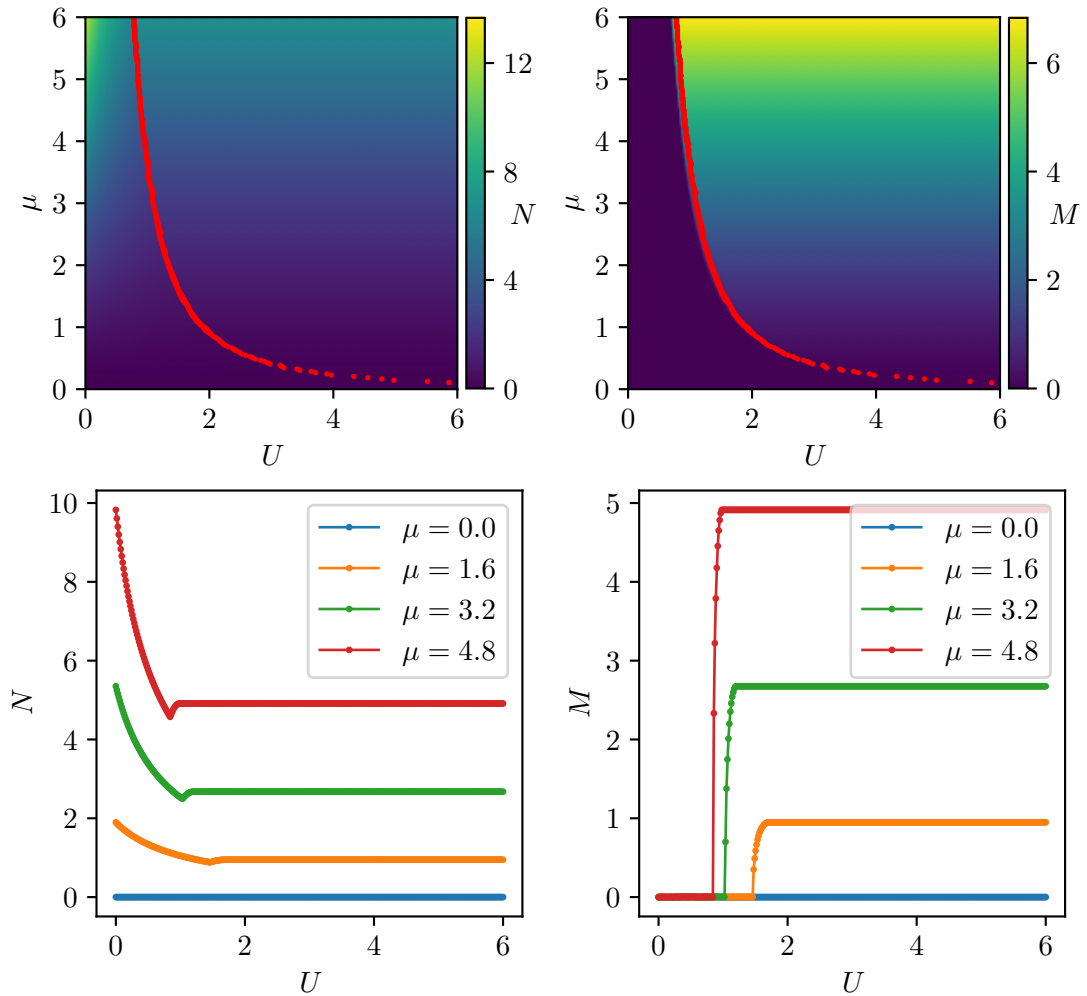


Figure 6.6: Stoner theory ground state phase diagram. The left and right panels correspond to particle density and magnetisation respectively. The upper panels show the phase boundary (marked by red dots) where there is a second order phase transition between a non-magnetic state and a magnetic state with half filling. The variation of the particle density and magnetisation with respect to the chemical potential and interaction are shown with the phase boundary. The lower panel shows cuts at constant μ through the particle density and magnetisation data shown in the upper panels. There is a critical value of interaction U_c above which the system becomes magnetic by undergoing a second order phase transition.

However, we have seen that with the equal-spin triplet-pairing theory this does not happen and no magnetic state is found in either the normal state limit, section 6.1, or the general theory, section 5.4.

As discussed in section 5.4, the free energy of the non-unitary triplet-pairing theory does not have any terms which mix spin labels, hence the free energy can always be written as the sum of two mathematically identical expressions: $F = F_{\uparrow} + F_{\downarrow}$, where the only difference between the two expressions is the spin-label. While in principle this allows for an imbalance between spin-up and spin-down mean-fields, in practice this is not observed. Indeed, as long as the free energy can be split into two mathematically identical terms like this then there can never be a net magnetisation. The Stoner theory free energy on the other hand does have a spin mixing term, and gives rise to magnetisation. Additionally the interaction is repulsive. We shall now see that adding a similar, repulsive interaction gives rise to magnetism in the normal state.

6.3 Hubbard extension

Previously, in section 5.4, we observed that the equal-spin triplet-pairing theory does not give rise to magnetism and that, moreover, magnetisation would not arise as long as it was possible to decompose the free energy into two mathematically identical components for each spin. In section 6.2 we identified that a repulsive, spin-mixing term would be required in the free energy (such as the one present in Stoner theory) to give rise to magnetisation. In this section we introduce an on-site Hubbard repulsion to the equal-spin triplet-pairing theory and show that it can lead to magnetisation in the normal state.

The Hamiltonian is now given by:

$$\begin{aligned} \hat{H} = & \sum_{m\mathbf{k}\sigma} (\varepsilon_{m\mathbf{k}\sigma}^{mm} - \mu) \hat{c}_{m\mathbf{k}\sigma}^\dagger \hat{c}_{m\mathbf{k}\sigma} - U \sum_{j\sigma} \hat{c}_{Aj\sigma}^\dagger \hat{c}_{Bj\sigma}^\dagger \hat{c}_{Bj\sigma} \hat{c}_{Aj\sigma} \\ & + U_H \sum_{mj} \hat{c}_{mj\uparrow}^\dagger \hat{c}_{mj\downarrow}^\dagger \hat{c}_{mj\downarrow} \hat{c}_{mj\uparrow} + U'_H \sum_{j\sigma\sigma'} \hat{c}_{Aj\sigma}^\dagger \hat{c}_{Bj\sigma'}^\dagger \hat{c}_{Bj\sigma'} \hat{c}_{Aj\sigma}. \end{aligned} \quad (6.15)$$

The first two terms are the same non-interacting and attractive on-site interaction terms previously introduced. U_H and U'_H are on-site, intra-orbital and inter-orbital repulsion terms respectively.

As per the usual steps we will minimise the free energy $F_0 \approx \langle \hat{H} - \hat{H}_{\text{MF}} \rangle_{\text{MF}} + F^{\text{MF}}$ with respect to the mean-fields. Before introducing the mean-field Hamiltonian we will use Wick's theorem to expand the interaction terms of our Hamiltonian. The Wick's expansion of each interaction term is as follows:

$$\begin{aligned} \langle \hat{c}_{Aj\sigma}^\dagger \hat{c}_{Bj\sigma}^\dagger \hat{c}_{Bj\sigma} \hat{c}_{Aj\sigma} \rangle_{\text{MF}} &= \langle \hat{c}_{Aj\sigma}^\dagger \hat{c}_{Bj\sigma}^\dagger \rangle_{\text{MF}} \langle \hat{c}_{Bj\sigma} \hat{c}_{Aj\sigma} \rangle_{\text{MF}} \\ &+ \langle \hat{c}_{Aj\sigma}^\dagger \hat{c}_{Aj\sigma} \rangle_{\text{MF}} \langle \hat{c}_{Bj\sigma}^\dagger \hat{c}_{Bj\sigma} \rangle_{\text{MF}} \\ &- \langle \hat{c}_{Aj\sigma}^\dagger \hat{c}_{Bj\sigma} \rangle_{\text{MF}} \langle \hat{c}_{Bj\sigma}^\dagger \hat{c}_{Aj\sigma} \rangle_{\text{MF}} \end{aligned} \quad (6.16)$$

$$\begin{aligned} \langle \hat{c}_{mj\uparrow}^\dagger \hat{c}_{mj\downarrow}^\dagger \hat{c}_{mj\downarrow} \hat{c}_{mj\uparrow} \rangle_{\text{MF}} &= \langle \hat{c}_{mj\uparrow}^\dagger \hat{c}_{mj\downarrow}^\dagger \rangle_{\text{MF}} \langle \hat{c}_{mj\downarrow} \hat{c}_{mj\uparrow} \rangle_{\text{MF}} \\ &+ \langle \hat{c}_{mj\uparrow}^\dagger \hat{c}_{mj\uparrow} \rangle_{\text{MF}} \langle \hat{c}_{mj\downarrow}^\dagger \hat{c}_{mj\downarrow} \rangle_{\text{MF}} \\ &- \langle \hat{c}_{mj\uparrow}^\dagger \hat{c}_{mj\downarrow} \rangle_{\text{MF}} \langle \hat{c}_{mj\downarrow}^\dagger \hat{c}_{mj\uparrow} \rangle_{\text{MF}} \end{aligned} \quad (6.17)$$

$$\begin{aligned} \langle \hat{c}_{Aj\sigma}^\dagger \hat{c}_{Bj\sigma'}^\dagger \hat{c}_{Bj\sigma'} \hat{c}_{Aj\sigma} \rangle_{\text{MF}} &= \langle \hat{c}_{Aj\sigma}^\dagger \hat{c}_{Bj\sigma'}^\dagger \rangle_{\text{MF}} \langle \hat{c}_{Bj\sigma'} \hat{c}_{Aj\sigma} \rangle_{\text{MF}} \\ &+ \langle \hat{c}_{Aj\sigma}^\dagger \hat{c}_{Aj\sigma} \rangle_{\text{MF}} \langle \hat{c}_{Bj\sigma'}^\dagger \hat{c}_{Bj\sigma'} \rangle_{\text{MF}} \\ &- \langle \hat{c}_{Aj\sigma}^\dagger \hat{c}_{Bj\sigma'} \rangle_{\text{MF}} \langle \hat{c}_{Bj\sigma'}^\dagger \hat{c}_{Aj\sigma} \rangle_{\text{MF}} \end{aligned} \quad (6.18)$$

The inter-orbital repulsion term, equation (6.18), is actually identical to the equal spin pairing attraction, equation (6.16), when $\sigma = \sigma'$. Since we are trying to identify the minimum model required to produce spontaneous magnetisation, we will examine the simpler case where the inter-orbital repulsion is negligible compared to the other energies i.e. when $U'_H = 0$.

With zero inter-orbital repulsion the only new term is the intra-orbital repulsion, equation (6.17), of which the first Gor'kov-like term will be zero as the equal-spin pairing-theory only allows pairing between electrons with the same spin. Again we do not include any mean-fields that couple with the Fock-like term, as such the expectation value of all Fock-like terms will be zero. This leaves only the Hartree-like term, which couples to the same $\phi_{m\sigma}$ mean-fields that appear in the non-unitary theory. As such the mean-field Hamiltonian takes

the same form as equation (6.6) if focusing on a normal state theory, or equation (5.17) if the non-unitary triplet-pairing $\Delta_{\sigma\sigma}$ is included. The same Bogoliubov de Gennes transformation will apply and the quasi-particle dispersion will remain the same.

The ground state free energy $F_0 = \langle \hat{H} \rangle_{\text{MF}}$ is given by

$$F_0 = \sum_{\sigma} \left\{ K_{A\sigma} + K_{B\sigma} - \mu(N_{A\sigma} + N_{B\sigma}) - \frac{U}{\mathcal{N}} N_{A\sigma} N_{B\sigma} - \frac{U}{\mathcal{N}} \chi_{\sigma} \chi_{\sigma}^* \right\} + \frac{U_H}{\mathcal{N}} (N_{A\uparrow} N_{A\downarrow} + N_{B\uparrow} N_{B\downarrow})$$

The only difference between this expression and the free energy for the non-unitary triplet-pairing theory, equation (5.33), is the additional Hubbard term, which contains the spin-mixing term necessary for magnetisation. This term lowers the free energy by unbalancing the spin populations.

As discussed in section 6.1 we obtain a theory of the normal state of this model by setting $\Delta_{\sigma\sigma} = 0$ and, for simplicity, we also set $s = 0$ allowing us to assume $\phi_{A\sigma} = \phi_{B\sigma}$ and $N_{A\sigma} = N_{B\sigma} = N_{\sigma}/2$. In this case the ground state free energy is given by:

$$F_0 = \sum_{\sigma} \left\{ K_{A\sigma} + K_{B\sigma} - \mu(N_{A\sigma} + N_{B\sigma}) - \frac{U}{\mathcal{N}} N_{A\sigma} N_{B\sigma} \right\} + \frac{U_H}{\mathcal{N}} (N_{A\uparrow} N_{A\downarrow} + N_{B\uparrow} N_{B\downarrow})$$

To obtain the phase diagram the usual procedure is followed: calculate the free energy as a function of N_{\uparrow} and N_{\downarrow} for different values of μ , U and U_H , then locate the minimum. At that minimum, calculate the total number of particles, N , and the magnetisation, M , to determine the difference between high/low density or magnetic phases. Figure 6.7 shows how the particle density varies as a function of U and U_H for different μ , while figure 6.8 shows the same for magnetisation.

From figure 6.7 we can see the familiar high density phase where the attractive interaction, U , is dominant and is matched by a zero-magnetisation phase in figure 6.8. This is consistent with the results from the normal state limit of the equal-spin triplet-pairing theory, figure 6.3. The density phase diagrams also exhibit a half-filling phase, matched by a magnetic phase in figure 6.8. This magnetism arises from the Hubbard repulsion interaction, U_H , which is absent in the equal-spin triplet-pairing theory, and gives rise to the spin-mixing term responsible for the magnetisation in Stoner theory. Finally, there is another low density zero magnetisation phase whose size depends on the chemical potential, μ . In this phase the non-interacting terms are dominant and the more negative the chemical potential the lower the Fermi energy and the less particles there will be in the system.

Using figures 6.7 and 6.8 we can determine the phase diagram, figure 6.9, of the equal-spin triplet-pairing theory with additional Hubbard repulsion. The phase diagram shows first order phase transitions (red lines) separating different phases of the system and in some cases there are also quantum critical end points (red circles). Phase I is non-magnetic and has a low particle density; phase II is highly magnetic and is at half filling; phase III is non-magnetic with a high particle density and phase IV has low magnetisation and low particle density. The first order transitions were determined by the points where there were clear jumps in the magnetisation and particle-density order parameters and where the first-order derivatives of those order parameters were divergent. Due to noise in the numerical derivatives, it was not

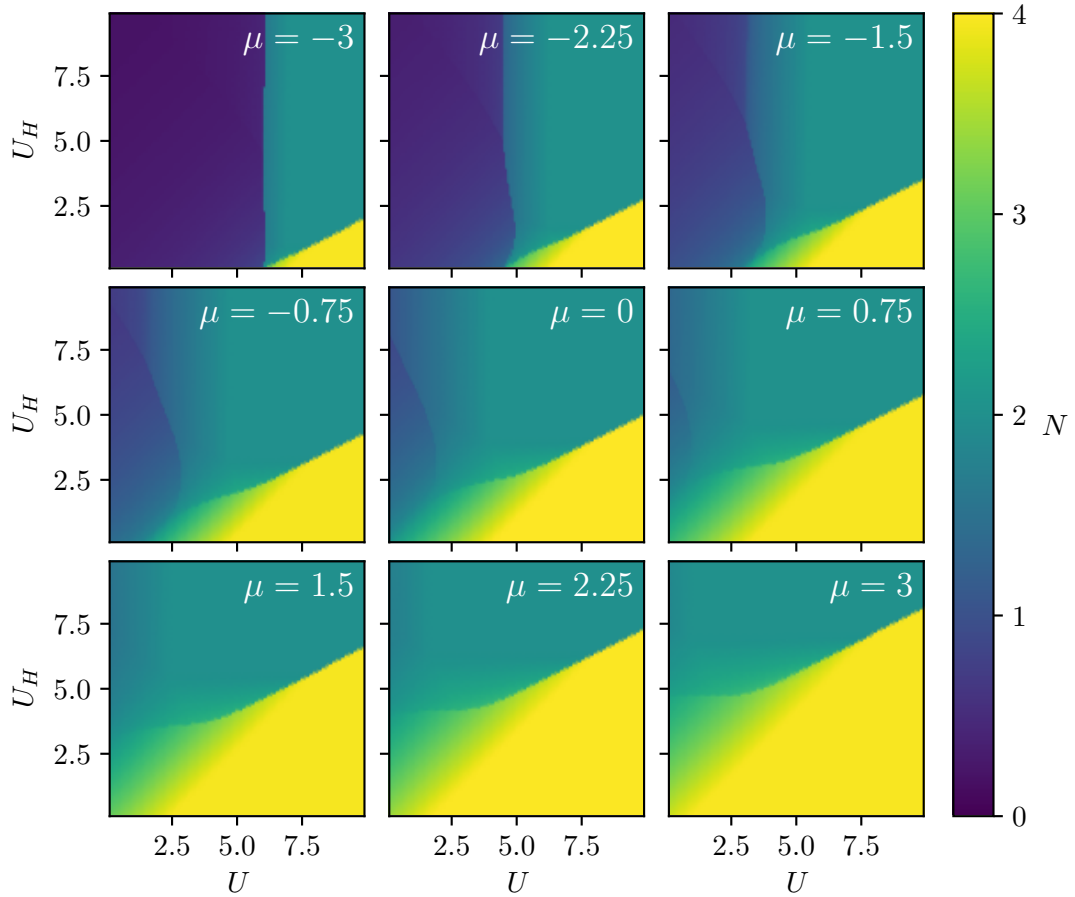


Figure 6.7: Normal state zero temperature particle density phase diagram of the equal-spin triplet-pairing theory with additional Hubbard repulsion term. Each panel corresponds to a different chemical potential, μ . There exists three different regions in the phase diagram: a high density region which arises when the attractive equal-spin triplet-pairing interaction, U_H , is dominant; a low density phase where the attraction is small and the repulsive Hubbard interaction is not strong enough to magnetise the system and finally a mid-density phase where the system is fully magnetised and at half-filling.

possible to conclusively obtain any second order phase transitions, although some may exist, perhaps after the quantum critical end point for example.

In this section we have shown that the addition of a Hubbard repulsive term can lead to magnetisation in the normal state phase diagram. Since this is a normal state theory, the magnetisation which arises is not caused by the superconductivity and as such does not explain the spontaneous magnetisation that occurs in LaNiGa_2 and LaNiC_2 . In this thesis we have only studied the zero-temperature normal-state limit of equal-spin attraction with Hubbard repulsion and leave the extension to finite temperature and finite Δ for further work.

6.4 Summary

In the previous chapter we applied a variational mean-field method to the equal-spin pairing theory proposed by Weng *et al.* [126]. Although the theory was predicted to display a net magnetisation in the superconducting state, we found in chapter 5 that this was not the case. In this chapter we continued our investigation of the equal-spin triplet-pairing theory to identify why no magnetisation was obtained.

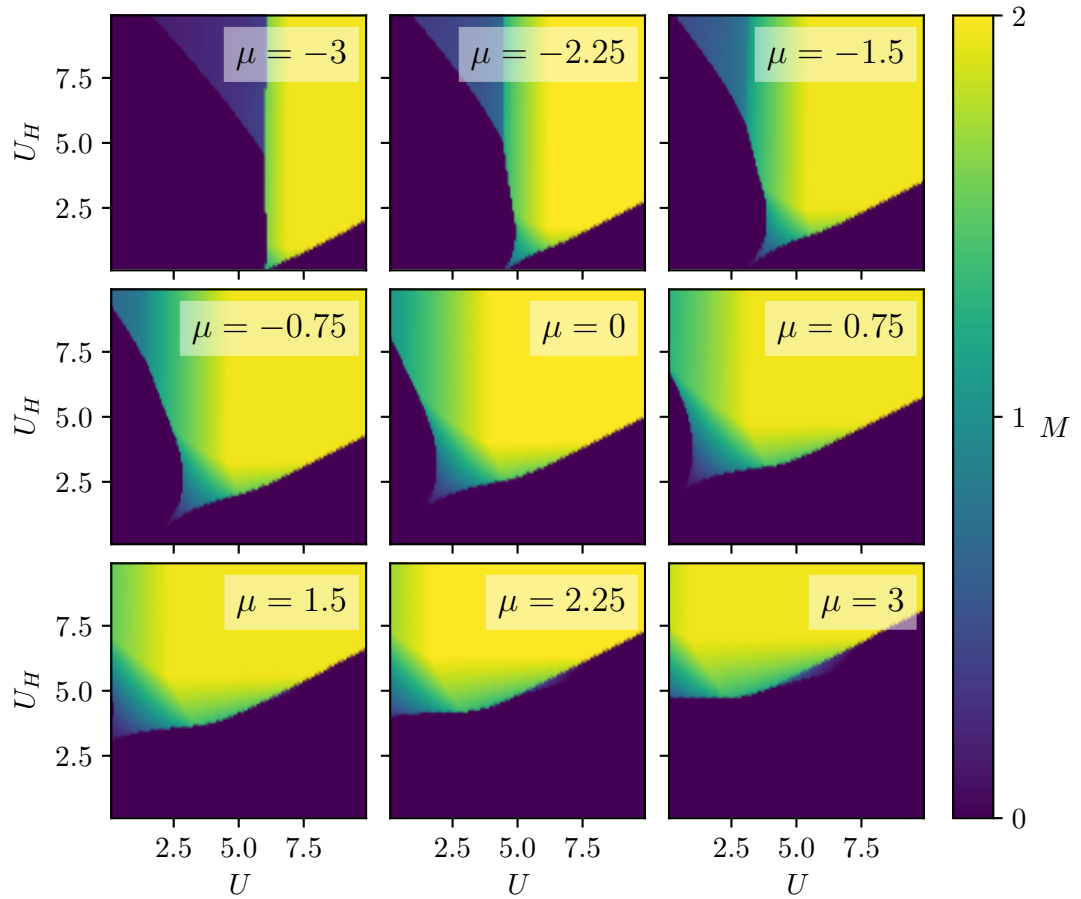


Figure 6.8: Normal state zero temperature magnetisation phase diagram of the equal-spin triplet-pairing theory with additional Hubbard repulsion term. Each panel corresponds to a different chemical potential, μ . The addition of the Hubbard repulsive interaction gives rise to a magnetic phase. There exists three different regions in the phase diagram: a non-magnetic region which arises when the attractive equal-spin triplet-pairing interaction, U , is dominant; a second non-magnetic phase where the attraction, U , is small and the repulsive Hubbard interaction, U_H , is not strong enough to magnetise the system; and finally a magnetic phase where U_H is dominant.

We started by considering the normal state theory of the equal-spin attraction, section 6.1, and found that the free energy could be written in two different, supposedly equivalent ways: one in which it depends explicitly on both the number of spin-up electrons, N_\uparrow , and spin-down electrons, N_\downarrow and another where it is written in terms of the total number of particles, N , and either of the other particle numbers, N_σ . We saw that by using the second form one must choose, and therefore restrict, the number of particles to N , and when one does this the resulting free energy is minimised by fully imbalancing the spin populations, hence the prediction that the theory would lead to magnetisation. However, the number of particles is not known until the free energy has been minimised and so the choice and restriction of N is arbitrary and unjustifiable. Moreover such a form only predicts the right minima for systems of half-filling or less. We saw that to identify the true minima of the free energy one had to use the first form of the free energy, equation (6.2).

Using a form of the free energy with an explicit dependence on the number of *both* spins, the free energy can be properly minimised. By doing just that we saw that the free energy for the normal state limit of the equal-spin pairing theory was minimised by maximising the

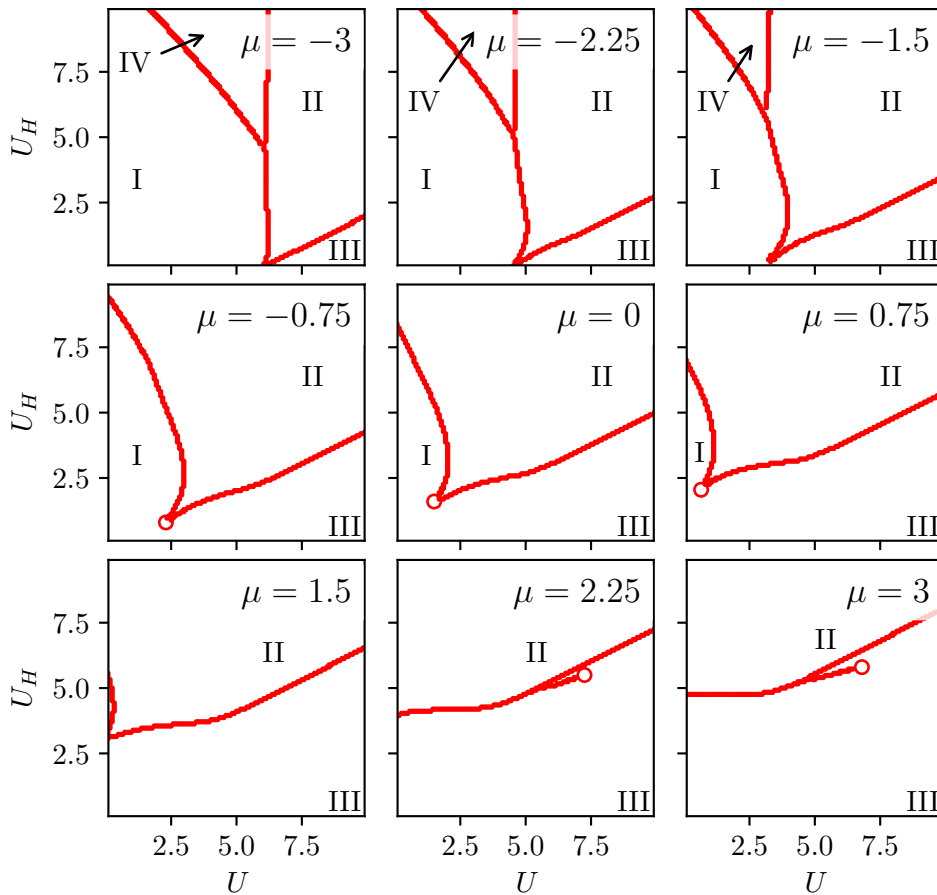


Figure 6.9: Normal state zero temperature phase diagram of the equal-spin triplet-pairing theory with additional Hubbard repulsion term. Each panel corresponds to a different chemical potential, μ . The different phases are separated by first order phase transitions (red lines) and in some cases there are quantum critical end points (red circles). Phase I is non-magnetic and has a low particle density; phase II is highly magnetic and is at half filling; phase III is non-magnetic with a high particle density and phase IV has low magnetisation and low particle density.

population of both spins, i.e. $N_{\uparrow} = N_{\downarrow}$. A consequence of which is the magnetisation must be zero; consistent with our results from chapter 5.

In section 6.2 we saw that writing the free energy of Stoner theory in terms of a fixed particle number this time correctly identified the minima of the free energy and was consistent with the minima obtained by the free energy written explicitly in terms of both spin populations. It seems then that writing the free energy in terms of a fixed total particle number, N , and one of the other particle numbers, N_{σ} , is a potentially useful simplification but is not necessarily reliable.

We identified that the critical aspect missing from the equal-spin triplet-pairing theory was a spin-mixing term in the free energy. Such a term is present in Stoner theory and it is this term which lowers the free energy by particle imbalance (magnetisation). In Stoner theory when a particle is added to one of the spin bands it suffers a kinetic energy penalty but, if the Stoner criterion is met [132], then the magnetisation associated with the particle imbalance lowers the free energy enough to compensate. It is easy to see then that removing as many particles as possible from one spin band and placing as many as possible in the other maximises the magnetisation and the lowering of the free energy.

A similar thing happens with the equal-spin pairing theory (either the full theory or the normal state theory presented here) where putting extra particles in one of the spin bands causes a kinetic energy penalty but the energy of forming pairs (if $\Delta > 0$) or simply satisfying the attractive term (if $\Delta = 0$) is enough to compensate. The crucial difference here is that without the spin-mixing term of Stoner theory there is no tendency or requirement to form an imbalance. If adding some more particles to the spin-up bands allows for the lowering of the free energy through the extra pairing or attraction, then the same is also true of simultaneously adding more to the spin-down bands. In this case balanced spin populations lower the free energy whereas in Stoner theory they destroy the magnetisation which is the free energy lowering mechanism.

After identifying the spin-mixing term in the Stoner theory free energy as the key feature missing from the equal-spin pairing theory, we included an additional Hubbard repulsive interaction, section 6.3. We saw that the zero temperature normal state phase diagram of such a theory gave rise to both a non-magnetic high particle density phase, caused by the equal-spin attraction; as well as a magnetic phase, thanks to the new Hubbard repulsion.

We note however that the magnetisation observed with the addition of the Hubbard repulsion is not the same spontaneous magnetisation detected by μ SR in the superconducting phase. The magnetisation observed here is a result of the Hubbard repulsive term being dominant. However we propose that with the inclusion of superconductivity this theory will demonstrate magnetisation in the superconducting state, without requiring excessive Hubbard repulsion, due to the following argument:

We know from our normal state theory of the model with equal-spin attraction that the attraction (without pairing) acts to fill both the spin bands simultaneously, and this is enhanced by including the pairing because more electrons of the same spin mean more (free energy lowering) pairs. When the Hubbard repulsive interaction is included, and dominant, the free energy is lowered by imbalancing the spin populations. Unlike with s-wave pairing, the equal-spin triplet-pairing is actually enhanced with the addition of such a repulsive term because adding more particles to one of the spin bands increases the amount of equal-spin pairing in that band (although the greater imbalance directly opposes the action desired by the equal-spin *attraction*). From this reasoning it seems that superconductivity can enhance *both* the attraction mediated spin balancing or the repulsive spin imbalancing.

It is probable that the system is not going to be in either of the attractive- or repulsive-dominant regimes but in some intermediate situation. We suspect that when the system leans slightly towards the repulsive-dominant case then the superconductivity will reinforce the magnetisation and vice versa, leading to the spontaneous magnetisation observed in μ SR experiments for LaNiGa₂.

Furthermore, with the addition of the Hubbard repulsion term, the free energy, section 6.3, can no longer be separated into the sum of two identical expressions for spin-up and spin-down. This and the imbalance between spins will give rise to two different values of $\Delta_{\uparrow\uparrow}$ and $\Delta_{\downarrow\downarrow}$. As such the equal-spin triplet-pairing theory with additional Hubbard repulsion would be a *non-unitary* triplet-pairing theory. Additionally, $\Delta_{\uparrow\uparrow}$ and $\Delta_{\downarrow\downarrow}$ are still both isotropic pairing potentials so the energy gap would still be nodeless. The possibility of gapless superconductivity is still present with the possibility of both spins being gapless, either one of them being gapless or none of them being gapless.

In conclusion we have seen in this chapter how the addition of a Hubbard repulsive

interaction to the equal-spin triplet-pairing theory can give rise to magnetisation in the normal state zero temperature phase diagram. Without such an additional term no magnetisation is detected. We propose that the addition of such a term will give rise to a net magnetisation in the superconducting state due to the pairing enhancing the magnetisation and vice versa. Furthermore two *nodeless* gaps of different magnitudes would manifest, making the triplet-pairing *non-unitary*. We propose therefore that a non-unitary triplet-pairing attraction with a Hubbard repulsion contains all the necessary ingredients to explain superconductivity in LaNiGa_2 .

Chapter 7

Using topological transitions to engineer quench-resilient wires

In chapter 2 we saw that unconventional superconductors can have unusual symmetry properties, namely they might lack a centre of inversion or break time reversal symmetry. In chapter 3 we saw that broken TRS can be a strong indicator of unconventional superconductivity and can lead to interesting constraints on the allowed-pairing of LaNiC_2 and LaNiGa_2 . We have spent chapters 5 and 6 discussing, from a theoretical point of view, a novel two-band equal-spin triplet-pairing theory, to try and explain and unify the conflicting experimental results in LaNiGa_2 .

In this chapter we turn our attention to those unconventional noncentrosymmetric superconductors that, as discussed in chapter 2, contain an admixture of singlet and triplet pairing and, more importantly, host different topological nodal states. We are interested in whether the different nodal states, particularly the nodal reconstruction state with the greatest enhancement of specific heat, can be potentially useful in the prevention of quenches in superconductors.

The question we wish to address in this chapter is: can topological transitions be used to engineer quench-resilient superconductors?

7.1 Introduction

In this chapter the idea of using topological transition states to engineer intrinsically quench-resilient superconducting wires is proposed and investigated. In order to understand this idea two concepts need to be introduced: the topological transition state and a superconductor quench.

Firstly, a superconductor quench is when a random localised fluctuation leads to the phase transition of the entire material. In short some small finite region of the superconductor transitions into the normal state with $T > T_c$ thus losing its superconducting properties. In this small region the resistivity is suddenly finite and will start generating heat due to the typically large current passing through it. The heat generated in this region spreads, increasing the temperature in the region surrounding it and causing more of the superconductor to transition into the normal state. This in turn generates more heat until eventually the entire superconductor has transitioned to the normal state, see figure 7.1. Another mechanism which can cause quenches is 'flux jumping/slipping'. With this mechanism the interactions

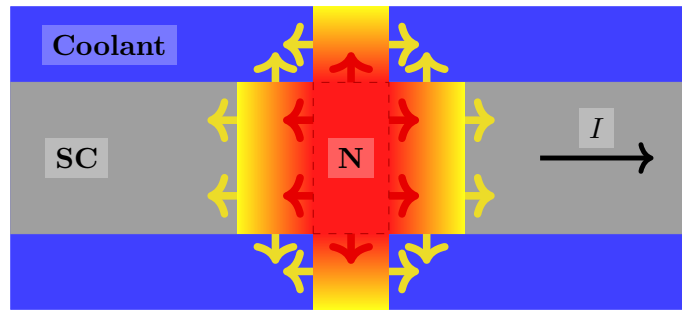


Figure 7.1: Schematic of a superconductor quench. A superconductor (SC) is surrounded by liquid helium (Coolant) that keeps it in its superconducting state. Typically there is a large current (I) flowing through it. A random thermal fluctuation causes a small region of the superconductor to transition into its normal (N) highly resistive state. Due to the large current and high resistance a lot of heat is suddenly generated. This heat spreads to the surrounding superconductor and coolant, causing further transition into the normal state, which then generates even more heat, causing a chain reaction of heating until the entire superconductor goes normal.

between the flux lines penetrating the normal state of the vortex cores cause random fluctuations in their position. Such fluctuations generate heat and can lead to quenches via a similar chain of events as with a thermal fluctuation. It is usual therefore to use materials with ‘strong pinning’ to minimise flux jumping. In this proof-of-concept work we do not consider the effect of flux pinning and assume it is just another mechanism that can initiate the quench. Engineering applications of superconductors already utilise a whole host of quench prevention and protection techniques, ranging from electronic detection methods to current-sharing fail-safe systems [134, 135, 136, 137, 138, 139]. In spite of this, quenches do occur regularly; the most well-known example being that which led to the shutdown of the LHC experiment at CERN for months in 2008 [140].

Secondly, the concept of topology in condensed matter, topological transitions in superconductors and their experimental detection via power law temperature dependence of thermodynamic properties has been discussed in chapter 2. Here the relevant point is that the topology of the superconducting state has an effect on the specific heat. Unconventional superconductors can have point- or line-nodes in the quasiparticle energy spectrum where the energy gap is zero [79], leading to an approximate power law temperature dependence of the specific heat, $C \propto T^n$, below T_c . In contrast, the specific heat of a conventional BCS superconductor has an exponential temperature dependence below T_c . Point- and line-nodes give rise to T^3 and T^2 specific heat dependence respectively [79, 90] but it is possible to obtain anomalously-low exponents at topological transitions where nodal lines cross ($n \approx 1.8$), form ($n \approx 1.5$) or even form and cross simultaneously ($n \approx 1.4$) [82]. At low temperatures, a lower exponent corresponds to a higher specific heat as well as a faster increase in specific heat as the temperature is increased.

It is the enhanced specific heat of these topological states that we propose to exploit. As already mentioned, the problem with quenches is the heat spreading from the normal region to the surrounding superconducting region. A superconductor with higher specific heat therefore would be able to absorb more of that heat before itself increasing in temperature. With any of the topological states, both the value of the specific heat at low temperatures and the rate at which the specific heat increases with increasing temperature are higher than the

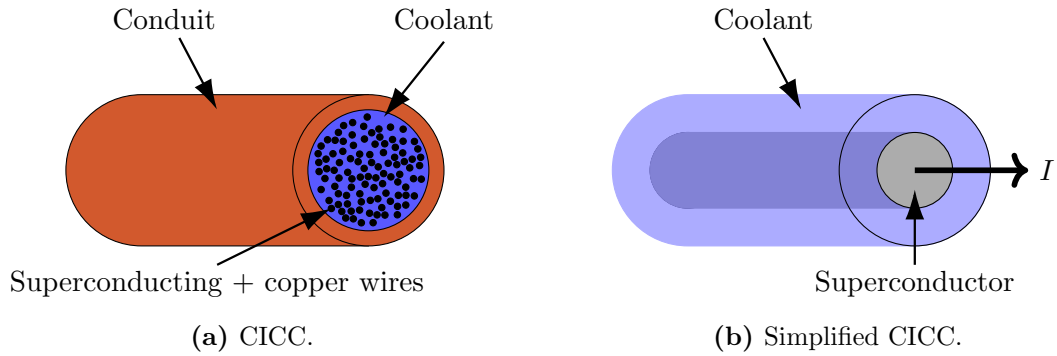


Figure 7.2: Schematic of a general CICC and the simplified CICC model. The left figure 7.2a is a schematic the CICC, of which a full simulation consists of heat equations for the wires and the insulating conduit as well as fluid dynamics equations for the coolant. The right figure 7.2b is a schematic of our simplified model. There is a single superconducting wire surrounded by a fixed temperature coolant bath, requiring a single heat equation to simulate.

conventional BCS case. Of those states, the topological node-reconstruction state offers the greatest specific heat increase at low temperatures ($n=1.4$).

Materials that can be tuned to node formation/reconstruction transitions include the non-centrosymmetric superconductors $\text{Li}_2(\text{Pt,Pd})_3\text{B}$ [84] and the high-temperature cobalt-doped pnictides $\text{Ba}(\text{Fe}_{1-x}\text{T}_x)_2\text{As}_2$ ($\text{T}=\text{Co, Ni, Pd}$) [89, 141, 142]. By tuning such superconductors to these topologically non-trivial states one could engineer a superconductor which is theoretically intrinsically quench-resilient. This “passive” approach to quench prevention is quite different to the existing approach of engineering solutions as mentioned previously. The two different approaches are entirely complementary.

The work presented in this chapter is a proof-of-concept investigation of this idea. An existing quench model is modified to simulate different topological states and the tendency of each state to quench is tested. The hypothesis we wish to verify is that the topological state with the highest low-temperature specific heat will be most resilient to quenching.

7.2 The simplest quench model

In order to test our hypothesis we need to be able to simulate a quench. A cable-in-conduit-conductor, CICC, has a core made of superconducting wires with a copper matrix throughout. It is surrounded by some liquid coolant and enclosed with cladding, see figure 7.2a. We use the general model for a CICC found in [139] as a starting point to simulate a quench. It consists of a collection of coupled partial differential equations: a heat equation with source terms for the wire itself; another heat equation for the cladding, both depending on the temperature of the coolant; and another set of equations describing the temperature change and fluid dynamics of the coolant itself. In order to test this idea the CICC model was simplified with a view to obtain the simplest possible model that captures the relevant physics of a quench.

The greatest simplification one can make to the CICC model is to consider only a heat equation describing a wire in contact with a bath of helium coolant at constant temperature, while neglecting all other terms (see figure 7.2b). Our simple model is:

$$\rho_c C_c \frac{\partial T(x, t)}{\partial t} = \kappa_c \frac{\partial^2 T(x, t)}{\partial x^2} - \frac{h P_c}{A_c} (T(x, t) - T_h) + \frac{\eta_c I^2}{A_c^2} \Theta(T(x, t) - T_c). \quad (7.1)$$

Here x is the distance along the superconducting wire and t is time; $T(x, t)$ is the temperature of the superconductor, T_c is its critical temperature and T_h is the temperature of the helium bath; ρ_c is the superconductor's density, C_c its specific heat, κ_c its thermal conductivity, P_c its wetted perimeter, η_c its resistivity, A_c its cross-sectional area and I is the current passing through it. h is the heat transfer coefficient between the helium and the conductor. Θ is a Heaviside step function that switches on when the temperature of the conductor is above the critical temperature T_c .

Equation (7.1) describes how the temperature of the wire changes with time: the first term on the right hand side describes the heat flow along the length of the wire; the second term describes heat transfer with the helium bath; and the third term simulates the Joule heating that occurs when the superconductor is in the normal state.

By introducing new dimensional scales, equation (7.1) takes a dimensionless form¹:

$$\frac{\partial \tilde{T}(\tilde{x}, \tilde{t})}{\partial \tilde{t}} = \frac{\partial^2 \tilde{T}(\tilde{x}, \tilde{t})}{\partial \tilde{x}^2} - \left(\tilde{T}(\tilde{x}, \tilde{t}) - \tilde{T}_h \right) + \Theta \left(\tilde{T}(\tilde{x}, \tilde{t}) - \tilde{T}_c \right). \quad (7.2)$$

Here “ \sim ” marks a quantity that has been made dimensionless by dividing by one of the following characteristic length, temperature and time scales respectively:

$$x_0 = \left(\frac{A_c \kappa_c}{h P_c} \right)^{\frac{1}{2}} \quad T_0 = \frac{\eta_c I^2}{A_c h P_c} \quad t_0 = \frac{\rho_c C_c A_c}{h P_c}. \quad (7.3)$$

The dimensionless form, equation (7.2), reveals that the specific heat can be rescaled into the time scale, t_0 . The implication of this is that a change in the specific heat will change the time it takes for the evolution of the temperature profile but won't change the outcome, i.e. if the initial conditions are such that a quench will occur, then the specific heat controls over what time scale it happens but a change in its value cannot stop it happening. This obviously prevents us from testing our hypothesis so in the next section we will introduce a new temperature dependent form for the specific heat.

7.3 Temperature dependent specific heat

The problem with the previous model is that the specific heat is assumed to be constant when in reality it is a function of temperature. In order to include this essential piece of physics a model for the specific heat of a nodal superconductor is introduced:

$$\tilde{C}_c \left(\tilde{T}(\tilde{x}, \tilde{t}), \tilde{T}_c \right) = \tilde{\alpha} \tilde{T}(\tilde{x}, \tilde{t})^n \Theta \left(\tilde{T}_c - \tilde{T}(\tilde{x}, \tilde{t}) \right) + \tilde{T}(\tilde{x}, \tilde{t}) \Theta \left(\tilde{T}(\tilde{x}, \tilde{t}) - \tilde{T}_c \right) \quad (7.4)$$

where

$$\tilde{\alpha} = \frac{\alpha}{\gamma} T_0^{n-1} \quad (7.5)$$

and α and γ are material-dependent constants. This model captures the following essential physics (see figure 7.3):

- The specific heat has a linear temperature-dependence above T_c with some fixed Sommerfeld coefficient γ . This is appropriate for any Fermi liquid at low temperature [90].

¹see appendix C for more information on rescaling equations.

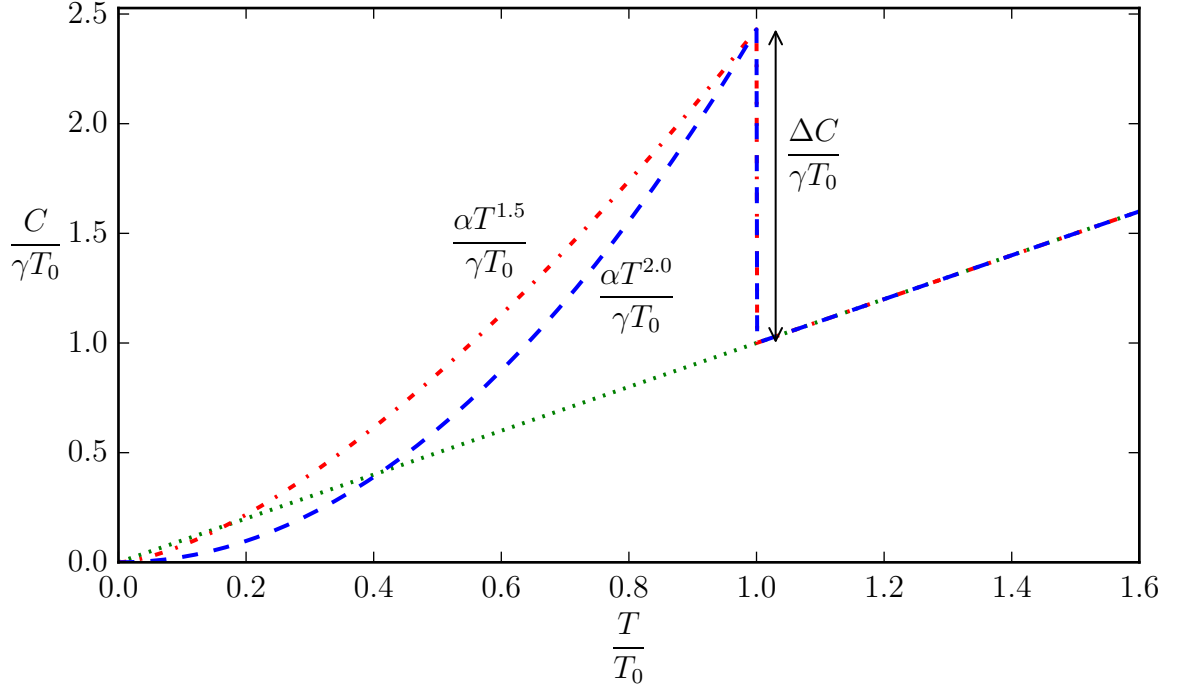


Figure 7.3: Specific heat of the superconductor. The green dotted line shows the linear Sommerfeld specific heat for normal metals. Our model for the nodal superconductors' specific heat is given by the blue dashed line (linear line nodes or shallow point nodes, exponent 2.0) and the red dot-dashed line (shallow line node, exponent 1.5). The specific heat is linear above T_c and a power law below. At low temperatures, a lower exponent gives a higher the specific heat. The jump in specific heat at T_c is fixed.

- At T_c the specific heat has a jump, ΔC , as predicted by Landau theory for any second-order phase transition [74]. For simplicity the size of the jump is fixed to the value predicted by BCS theory: $\Delta C = 1.43$ [14].
- Below T_c , the specific heat has a power law of temperature characterised by the exponent n which reflects the specific nodal state [90, 79, 82], as discussed above. The coefficient α is not a free parameter, but is instead fixed by the requirement that the specific heat has the right value at T_c^- . Its dimensionless form is $\tilde{\alpha} = 2.43\tilde{T}_c^{1-n}$.

Introducing this temperature dependent specific heat into equation (7.1) and rescaling makes the updated quench model:

$$\tilde{C}_c(\tilde{T}(\tilde{x}, \tilde{t}), \tilde{T}_c) \frac{\partial \tilde{T}(\tilde{x}, \tilde{t})}{\partial \tilde{t}} = \frac{\partial^2 \tilde{T}(\tilde{x}, \tilde{t})}{\partial \tilde{x}^2} - (\tilde{T}(\tilde{x}, \tilde{t}) - \tilde{T}_h) + \Theta(\tilde{T}(\tilde{x}, \tilde{t}) - \tilde{T}_c) \quad (7.6)$$

with the new characteristic scales

$$x_0 = \left(\frac{A_c \kappa_c}{h P_c} \right)^{\frac{1}{2}} \quad (7.7a)$$

$$T_0 = \frac{\eta_c I^2 x_0^2}{A_c^2 \kappa_c} \quad (7.7b)$$

$$t_0 = \frac{\rho_c C_0 x_0^2}{\kappa_c} \quad (7.7c)$$

$$C_0 = \gamma T_0. \quad (7.7d)$$

This model improves on equation (7.2) in that the specific heat is now more physically accurate with its temperature dependence. It is now possible to model different nodal superconductors which cannot be done when the specific heat is assumed constant. Furthermore, while the characteristic scale for the specific heat, C_0 , still appears in the time scale, t_0 , the dimensionless form of the specific heat, \tilde{C}_c , still appears in equation (7.6). Therefore the specific heat no longer simply controls the time scale of the quench, as it did when it was assumed constant, equation (7.2).

It is assumed that the system will be kept well below T_c as this is the safest regime to prevent a quench. In this regime a nodal superconductor is preferred as its specific heat rises faster at low temperatures than that of a fully gapped superconductor. More specifically, the nodal superconductor with the lowest exponent will be preferred as it will have the fastest rising specific heat. We can therefore study the effect different topological states can have on quench behaviour by altering the exponent, n , in the specific heat, equation (7.4).

7.4 Numerical method

The model was solved using a forward in time centred in space (FTCS) algorithm [128] using either zero-gradient or periodic boundary conditions, written in a combination of Python and Fortran 90. More details of which can be found in appendix D. The initial temperature profile of the wire has either a rectangular or Gaussian heat pulse centred at the middle of the wire with a temperature peak at T_q and a width W with $T > T_c$, called the hot-zone. At the edges of the hot-zone are the quench-fronts; positions x_q at which $T = T_c$. The quench-fronts mark a boundary between the superconducting and normal regions. The time evolution of the wire's temperature profile is computed using the FTCS algorithm. A quench is said to have occurred once the temperature of the entire wire (and the helium in section 7.6) is above T_c , if the full length of the wire goes below T_c then a quench has been prevented.

Using the FTCS quench solver some combination of T_c , T_h , T_q , W , L and n are chosen such that a quench does occur; then the exponent is lowered to simulate a different topological state to see if the quench can be prevented. The parameters T_c , T_h , T_q , W , and n are physical parameters which the result of the simulation will depend on, while L , dx and dt are numerical parameters which should *not* affect the result. Once a result is obtained it needs to be tested for convergence, this will reveal if the result is physically accurate or not.

Figure 7.4 shows that decreasing the exponent prevents a quench from occurring. The numerical parameters dx and dt were chosen such that the numerical stability condition for the simple heat equation, $\frac{dt}{dx^2} \leq \frac{1}{2}$, [128] was satisfied. Testing showed that meeting this stability condition was a good first approximation, and usually sufficient, to achieve convergence with these numerical parameters. However, as can be seen in figure 7.5, the quench is prevented by increasing length. This indicates that the quench occurring at small L , figure 7.4a, is a numerical artefact and not physically correct. Moreover this was observed for every set of initial conditions tested; including very high, wide initial heat pulses. A cold enough bath will always prevent a quench, given enough time (by increasing the length of the wire), no matter the size or intensity of the initial heat pulse. This can be understood further by considering the long term behaviour of the model.

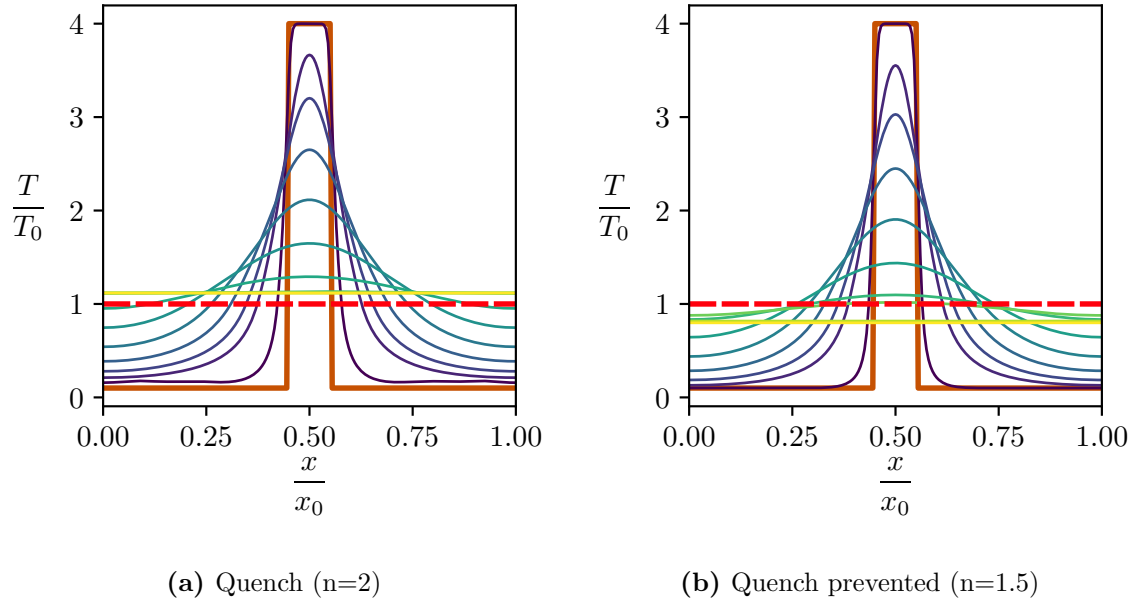


Figure 7.4: Comparison between the time evolution of the superconductor's temperature for different exponents. The initial temperature profile is the orange rectangular heat pulse. The different lines show how the heat pulse evolves over time, from dark blue to yellow as time increases. Figure 7.4a shows a quench occurring when the exponent is 2.0 while figure 7.4b shows that the quench is prevented when the exponent is changed to 1.5. Initial conditions $\tilde{T}_h = 0.1$, $\tilde{T}_q = 4.0$ and $\tilde{T}_c = 1.0$.

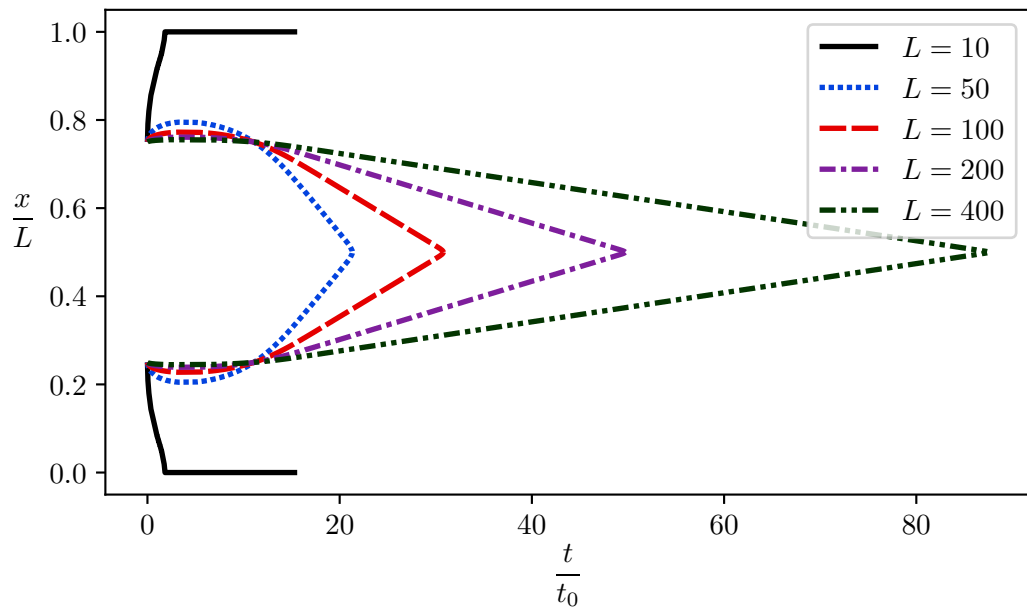


Figure 7.5: Convergence test of the quench-fronts position with time for different lengths. When \tilde{L} is small the quench-fronts move away from the centre and reach the ends of the wire, thus causing a quench. Increasing \tilde{L} changes this behaviour, the quench-fronts instead move towards the centre and eventually disappear, indicating that the quench has been prevented. The quench occurs because $\tilde{L} = 10$ is a poor approximation to an infinite wire; it is a numerical artefact.

7.5 Long term behaviour

Since the simulations cannot be run for infinite time, there is the question of when should the simulation stop, and whether the results would change drastically given more time. In general there is no singular answer, it depends on the particular system being evaluated e.g. in the case of some periodic feature, one would have to observe enough periods to infer that the behaviour being observed was indeed periodic. This could then be checked with what's understood about the model to see if such behaviour makes sense physically.

In this case the temperature profile of the wire was observed to flatten out then slowly converge on one of two temperatures: the temperature of the bath or some temperature above T_c . The first case makes sense, if a quench has been prevented and you have a constant heat bath, then all heat will be absorbed by the bath until the temperature of the wire is in equilibrium with the bath. The second case is not so obvious, why should there be some certain temperature above T_c which the wire seeks, rather than just increasing continuously? We will answer this by considering the long term behaviour of the model.

Using the fact that the temperature of the wire becomes essentially constant along its length, the heat conduction term in equation (7.6) can be set to zero, since there is no change in temperature wrt x , giving:

$$\frac{\partial \tilde{T}(\tilde{x}, \tilde{t})}{\partial \tilde{t}} = \frac{1}{\tilde{C}_c(\tilde{T}(\tilde{x}, \tilde{t}), \tilde{T}_c)} \left[\Theta \left(\tilde{T}(\tilde{x}, \tilde{t}) - \tilde{T}_c \right) - \left(\tilde{T}(\tilde{x}, \tilde{t}) - \tilde{T}_h(\tilde{x}, \tilde{t}) \right) \right] \quad (7.8)$$

which means the change in the conductors temperature with respect to time is just given by the balance between the Joule heating term and the heat transfer term. It is clear from equation (7.8) that if the temperature of the wire is constant in \tilde{x} and $\tilde{T} < \tilde{T}_c$ then the Joule heating term is zero (the entire wire is still superconducting). The only remaining term is a negative heat transfer term, which is proportional to the difference between the temperature of the wire and the bath; the wire will continue to transfer energy to the bath until the difference between the two is zero. i.e. the wire will decrease in temperature until $\tilde{T} = \tilde{T}_h$ as observed and expected.

If however, the temperature of the wire is constant in \tilde{x} and $\tilde{T}(\tilde{x}, \tilde{t}) > \tilde{T}_c$ then the joule heating term is equal to 1 (it is scaled by the specific heat but so is the heat transfer term so the scaling can be ignored) and the conductor will undergo a change in temperature of $\left(1 - \left(\tilde{T}(\tilde{x}, \tilde{t}) - \tilde{T}_h(\tilde{x}, \tilde{t}) \right) \right)$. By setting the change in temperature to zero, the condition for a stable temperature can be found:

$$1 - \left(\tilde{T}(\tilde{x}, \tilde{t}) - \tilde{T}_h(\tilde{x}, \tilde{t}) \right) = \frac{\partial \tilde{T}(\tilde{x}, \tilde{t})}{\partial \tilde{t}} = 0$$

$$\tilde{T}(\tilde{x}, \tilde{t}) = 1 + \tilde{T}_h(\tilde{x}, \tilde{t}).$$

So when the temperature is constant along the wire and above the critical temperature, it tends towards $\tilde{T}(\tilde{x}, \tilde{t}) = 1 + \tilde{T}_h(\tilde{x}, \tilde{t})$, while if $\left(1 + \tilde{T}_h(\tilde{x}, \tilde{t}) \right) < \tilde{T}_c$ then the temperature will decrease until it reaches equilibrium with the bath. Whether a quench occurs or not therefore depends on the temperature of the bath, T_h , relative to T_c .

The above argument relies on having a constant temperature along the length of the wire. In order for a quench to occur the quench-fronts must reach the end of the wire and the temperature must equalise, all before the wire cools below T_c . Increasing the length increases the time it takes the quench-fronts to reach the end of the wire and so the hot-zone loses more

heat to the bath and to the wire through conduction. In this model it is therefore always possible to prevent a quench by increasing the length of the wire, i.e. a (convergent) quench can never occur. We will now make a final alteration to this model to obtain the minimum quench model.

7.6 Minimum quench model

Although the introduction of a temperature dependent specific heat improved the quench model; convergence tests, figure 7.5, and the long-term limit, section 7.5, show it still does not contain all the relevant physics to simulate a quench. The problem is that the temperature of the heat bath is assumed constant (and well below T_c). When this is the case, given enough time (equivalently length), the system will always equalise with the bath. A variable temperature heat bath is required to allow the temperature of the overall system to increase and ultimately quench. The requirement of this addition is not entirely surprising since it is stated in [139] that the convection of helium is the dominant mechanism of quench-front propagation. As already mentioned, in [139] this mechanism is included by multiple coupled hydrodynamics equations and is too complicated and computationally intensive for our purposes, so we consider a simpler way of describing our heat bath.

The simplest way of describing a heat bath that can vary in temperature is

$$\frac{\partial \tilde{T}_h(\tilde{x}, \tilde{t})}{\partial \tilde{t}} = \beta \left(\tilde{T}(\tilde{x}, \tilde{t}) - \tilde{T}_h(\tilde{x}, \tilde{t}) \right) \quad (7.9)$$

where $T_h(x, t)$ is the temperature of the helium bath which now depends on position, x , and time, t . β is a dimensionless constant that depends on the design of the CICC:

$$\beta = \frac{\rho_c C_0 A_c}{\rho_h C_h A_h}, \quad (7.10a)$$

which in addition to the other characteristic scales, equations (7.7a) to (7.7c), is used to make equation (7.9) dimensionless. The material properties are the same as before but this time the subscripts c and h differentiate between the conductor and helium respectively.

Equation (7.9) describes the change in the temperature of the helium bath with respect to time. It is given by a single heat transfer term which acts between the helium and the conductor — there are no terms describing the fluid dynamics of the liquid coolant. This simplification decreases computational complexity but maintains the effect of the helium increasing in temperature and helping to propagate the quench.

Together equation (7.6) and equation (7.9) form the ‘quench model’ — a system of coupled partial differential equations that describe the minimum physics necessary to simulate a quench: a description of how the temperature in the superconductor changes with time; a heat bath that can change in temperature and a specific heat that changes with temperature and nodal state being modelled.

7.7 Results

The quench model was solved numerically for different initial conditions to see if a quench occurred or not. Figure 7.6 shows an example of the wire’s temperature profile evolution during a quench. In this case the initial Gaussian heat pulse expands until the full length

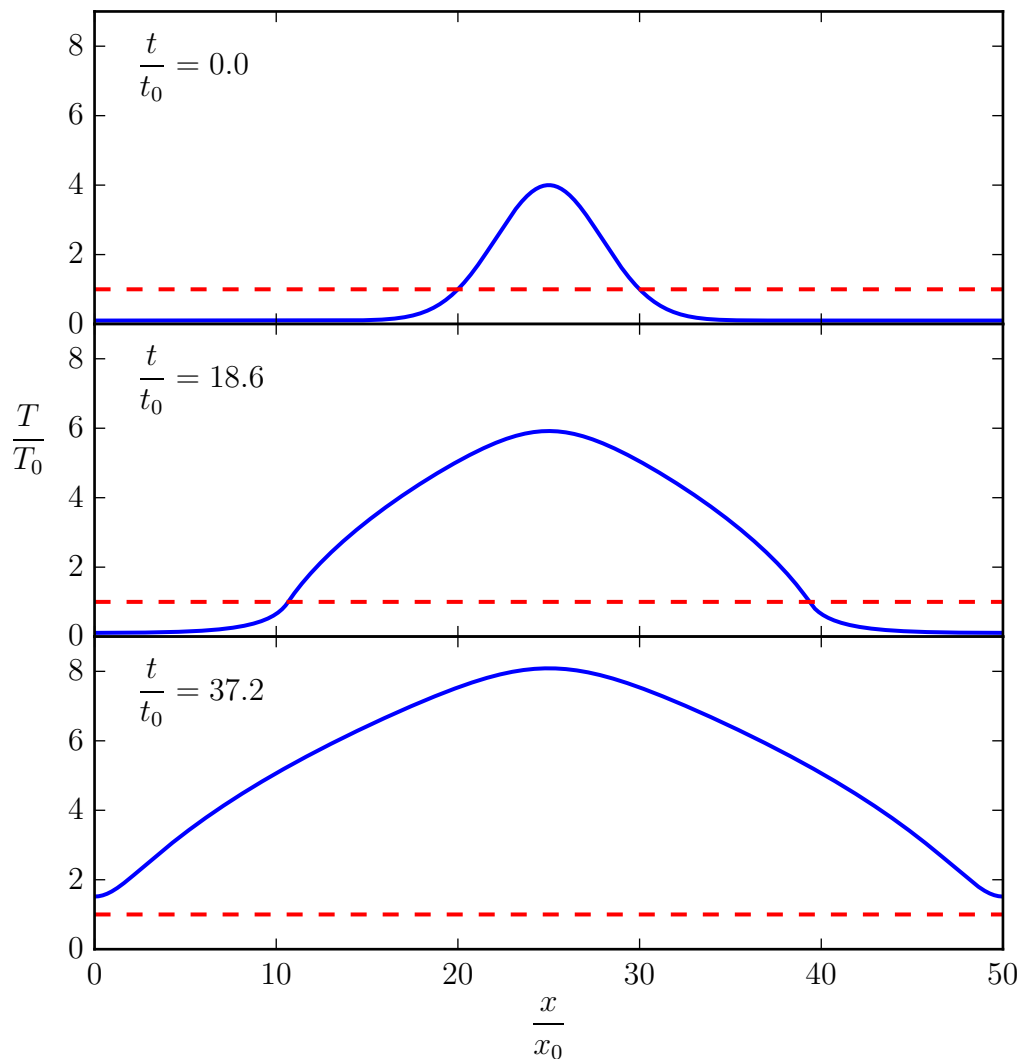


Figure 7.6: Time evolution of a quench. The red dashed line is the critical temperature, the blue solid line is the temperature profile of the superconductor. Each panel shows the temperature profile at a different time, with time increasing from top to bottom. The final panel shows the characteristic feature of a quench: the entire length of the superconductor is above T_c .

of the wire is above T_c , at which point it has quenched. The simulation continues until the helium bath is above T_c to ensure that there is no possibility that the wire could cool down again given enough time. In the non-quenching case, the width and height of the initial Gaussian heat pulse decrease until the pulse disappears and the entire wire is below T_c . Note how with this model the hot-zone is able to increase and expand indefinitely, and is not restricted to some specific temperature as was the case with the constant-temperature helium bath.

Time evolution of the quench-fronts shows the expansion or contraction of the length of the hot-zone, see figure 7.7. If the initial conditions were correct for a quench to occur then the hot-zone will increase in temperature and expand; the quench-fronts will move outwards until they reach the ends of the wire. If however, the initial conditions were not sufficient for a quench, the quench-fronts will move towards the centre of the wire; reducing the length of

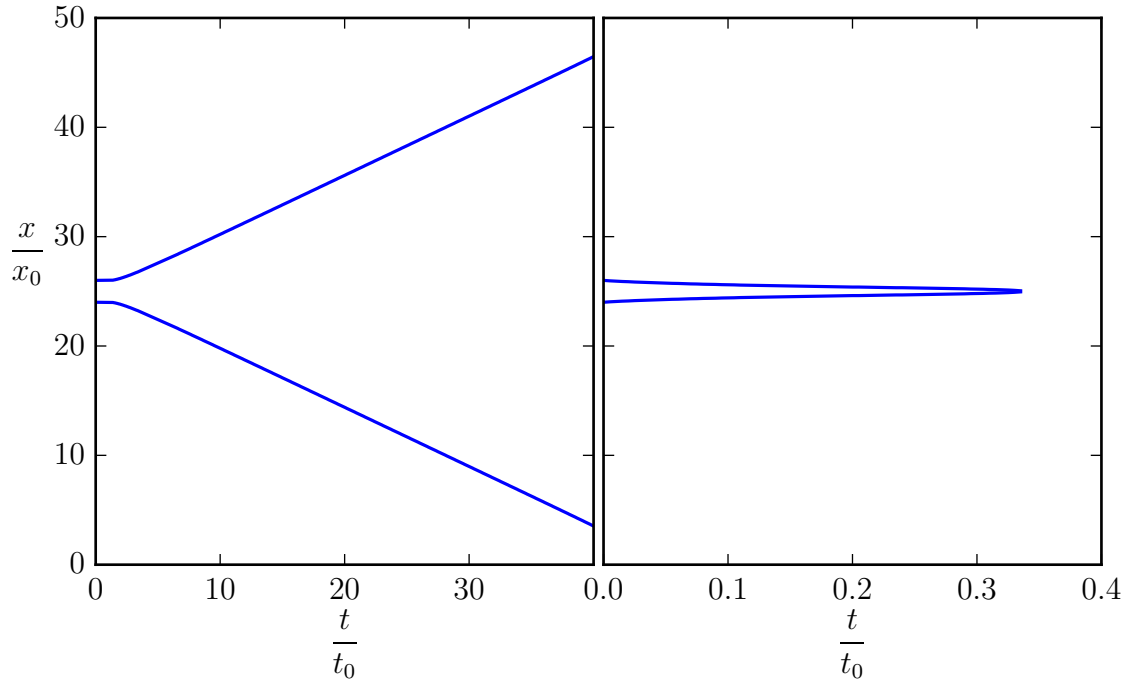


Figure 7.7: Time evolution of the quench-front. The solid blue line shows the position of the quench-front as a function of time. The length of wire between the quench-fronts is above T_c . The left panel shows a quench and the right shows a quench being prevented.

the hot-zone while it decreases in temperature until the entire wire is below T_c . Additionally the quench-fronts are used in determining convergence of the simulations with respect to the numerical parameters: the number of spatial divisions of the system, dx , the time step, dt and length used to simulate an infinite wire, L .

Figure 7.8 shows how the time evolution of the quench-fronts vary with increasing L and that the quench model produces quenches that are not just numerical artefacts. Before, with a fixed temperature heat bath, increasing L would see the quench behaviour disappear, whereas now the increase in L produces the same behaviour. In convergence tests, all parts of the plot which stay the same as the numerical parameter, L , is improved (increased) are convergent, physical results. Anything that changes is a numerical artefact. The inset of figure 7.8 shows such a numerical artefact, where there is a kink in the quench-front as it approaches the end of the wire, that disappears when L is increased.

Different topological states are modelled by changing the exponent, n , in the specific heat equation (7.6). For each topological state a ‘phase boundary’ is constructed as a function of W , T_h and T_q ; see figure 7.9. The parameter space is split into two regions, one which causes a quench and another which does not. All phase boundaries converge to some critical width W_c which is T_h -dependent. For $W < W_c$ the phase boundaries separate and the area of parameter space that causes quenches changes with exponent. The highest exponent has the largest quench-causing area of parameter space whereas the lowest exponent ($n = 1.4$ shallow line node crossing state) has the lowest quench-causing area. This smaller area in parameter space means there are fewer combinations of parameters that cause quenches, thus making the lower exponent state more resilient.

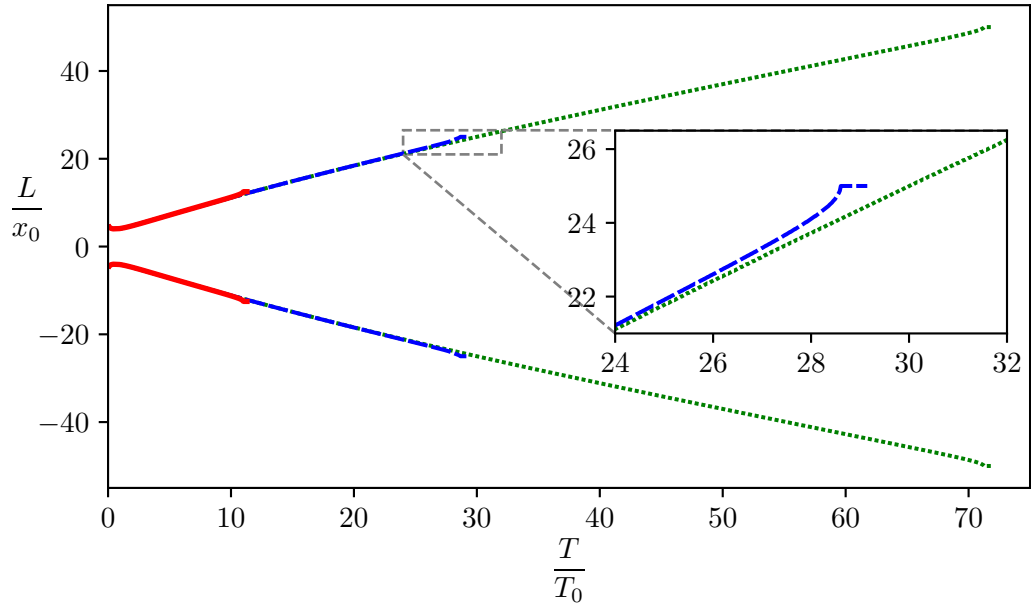


Figure 7.8: Convergence of the quench front with varying wire length. The quench persists after increasing L , with the evolution of the quench-front for smaller L being reproduced by the quench-front for the larger L . There are numerical artefacts near the ends of the wires where there is a kink in the quench-front, see inset.

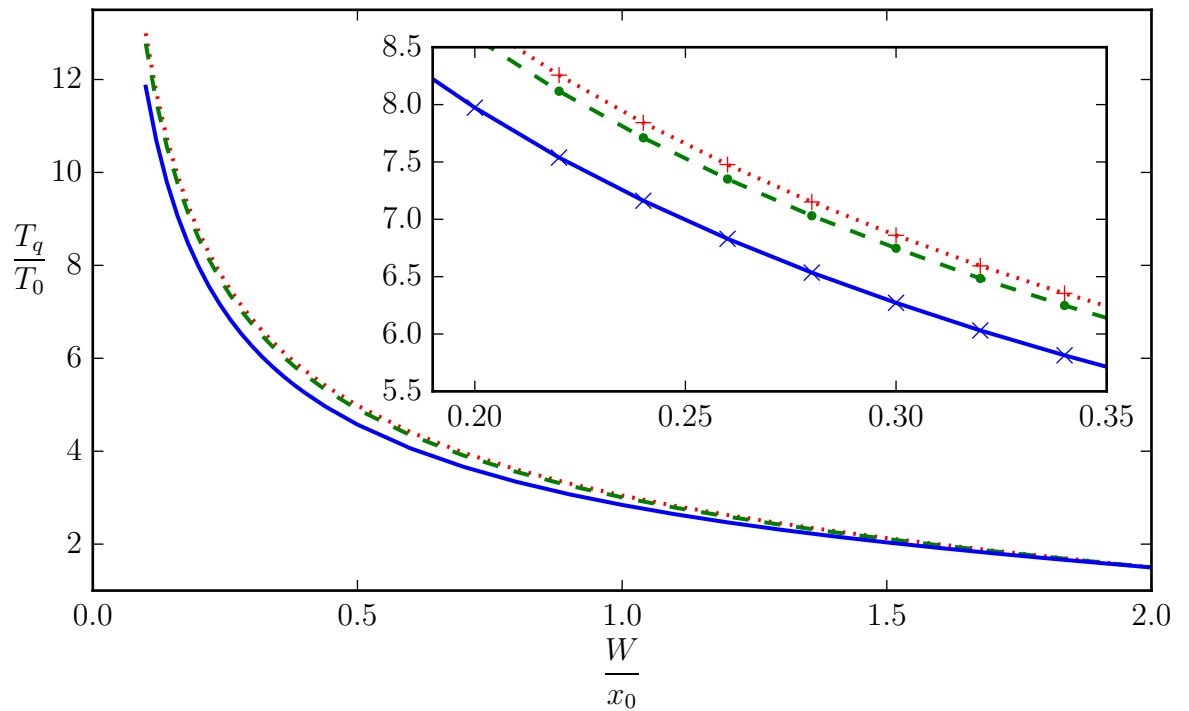


Figure 7.9: Quench parameter space phase-diagram. The phase diagram separates the parameter space into two quench and non quench regions. Each line corresponds to a different nodal state with the solid blue line characterised by $n = 2.0$, the dashed green line by $n = 1.5$ and the dotted red line by $n = 1.4$. Above the line is the quench region, below it quenches are prevented. Here $\tilde{T}_h = 0.1\tilde{T}_c$ but the plot stays qualitatively the same for different \tilde{T}_h , except the width at which the lines join is \tilde{T}_h dependent. The lower the exponent, the smaller the area of the quench-causing region and the more resilient the system is to quenching.

7.8 Conclusion

In this chapter we have investigated the effect specific heat has on the occurrence of quenches. Specifically, we have concentrated on the difference between specific heat power laws, corresponding to different nodal states with $n=2$ corresponding to ordinary line nodes and $n=1.5$, 1.4 corresponding to topological transition states [82, 89]. It is shown that the lower the power law exponent, the higher the specific heat and the greater the quench resilience. It is assumed that the temperature is low so that the power law approximation is valid. In this regime the power law specific heat is higher than the exponential BCS specific heat, so even the worst of the test cases would offer an improvement over BCS should the optimum topological state not be achievable.

In summary, we have asked whether a nodal superconductor could be made more resistant to quenches by tuning its parameters to a node-reconstruction topological transition point. Our calculations, using a minimum model, show that this is indeed the case although the effect is small. This concept has the potential to enhance the quench resilience of superconductors, especially if used in conjunction with current quench detection and mitigation techniques, however, detailed materials modelling will be required to ascertain whether the effect could be useful for applications. Possible candidates include the non-centrosymmetric superconductors $\text{Li}_2(\text{Pt,Pd})_3\text{B}$ [84] and the high-temperature cobalt-doped pnictides $\text{Ba}(\text{Fe}_{1-x}\text{T}_x)_2\text{As}_2$ ($\text{T}=\text{Co, Ni, Pd}$) [89, 141, 142]. This could lead to the first applications of topological transitions in the fields of energy distribution, storage and magnetic field generation.

Chapter 8

Summary

In this thesis we have discussed two main topics: a two-band equal-spin triplet-pairing theory that was proposed to explain the experimental results of LaNiGa_2 and the possibility of using the topological transition state to engineer quench-resilient wires. We started our discussion of superconductivity in chapter 1, where a brief historical summary of the key discoveries and concepts was provided.

In chapter 2 we focused on the fundamental microscopic aspects of superconductivity. We saw how in the framework of BCS theory superconductivity is enabled by the effective attraction between electrons due to the exchange of virtual phonons, and that such attraction causes pairs of electrons to form bound states. The superconducting state is described as a coherent state formed by a macroscopic, yet ill-defined, number of these bound pairs all with the same global phase, θ . We discussed the idea of symmetry breaking, the prime example of which is the adoption of a well defined phase, θ , by all the electron pairs upon entering the superconducting state.

We saw that superconductors can be divided into two classes: conventional and unconventional, where conventional superconductors can be described by BCS theory and unconventional ones cannot. We learned that unconventional superconductors can have additional interesting properties such as: the breaking of additional symmetries, particularly breaking of time reversal symmetry; topological properties, specifically different nodal gap topologies and transitions between them; and the possibility of singlet triplet mixing in the absence of centre of inversion symmetry.

We finished our discussion of the fundamental microscopic aspects of superconductivity by introducing some of the experimental techniques of particular relevance to this thesis. We saw that measurements of a superconductor's thermodynamic properties can be used to determine the superconducting gap structure and that μSR experiments, as well as measurements of the Kerr effect and the samples magnetisation, can be used to determine if TRS is broken.

In chapter 3 we looked in detail at two nickel-based superconductors: LaNiC_2 and LaNiGa_2 . We began by reviewing the literature and found that there are conflicting experimental and theoretical results for both materials. Both break TRS upon entering the superconducting state, as detected by μSR , and both have low symmetry. A result of the low symmetry is that there are only a small number (12) of possible symmetry-allowed pairing states and only four of those twelve break TRS. All 4 TRS breaking states are non-unitary triplet-pairing states.

During our review we saw multiple experimental and theoretical reports that found ev-

idence for both conventional and unconventional superconductivity, details of which can be found in chapter 3, but we concluded our review as follows. The current situation seems to be that LaNiC_2 and LaNiGa_2 are both TRS-breaking unconventional superconductors. Older thermodynamic measurements that find conventional full gap superconductivity seem to be better explained by the more recent observation of two-gap behaviour in both materials. Although most recent results suggest that LaNiC_2 is nodal with a coexistent antiferromagnetic phase emerging with increased pressure, no such result has yet been reported for LaNiGa_2 . Therefore in order to explain the superconductivity in LaNiGa_2 a theory would need to be able to produce two full-gaps *and* be non-unitary triplet-pairing. A two-orbital non-unitary triplet-pairing theory was proposed in [126] that gave rise to two full gaps. This theory was the motivation and starting point for chapters 5 and 6 of this thesis.

We introduced the variational mean-field method in chapter 4 by applying it to the well known case of conventional singlet pairing. We demonstrated the main steps and mathematical techniques of the theory, starting with the Fourier transformation of the non-interaction part of the Hamiltonian and the introduction of the non-interacting electron dispersion. As the interacting term of the Hamiltonian was quartic in creation/annihilation operators, we could not solve it via simple diagonalisation. Instead we introduced the concept of the variational mean-field Hamiltonian, an exactly solvable Hamiltonian whose eigenvalues and eigenvectors approximate those of the original Hamiltonian. We introduced variational mean-field Hamiltonian along with its mean-fields and solved it using a Bogoliubov de Gennes transformation.

We demonstrated how to derive the self-consistency equations and that these equations yield the stationary points of the free energy when solved. Additionally we saw that the expressions for the self-consistent gap equation, quasi-particle energy spectrum and quasi-particle amplitudes were the same expressions as obtained in BCS theory, as expected.

We discussed two methods of solving the self-consistency equations: a contour method which solved only the gap equation and an iterative method that was able to solve all self-consistency equations simultaneously. We saw that solving the self-consistent gap equation by the contour method gave a good first approximation to the possible values the pairing potential, Δ , could take, however without self-consistently determining the particle-density mean-fields, ϕ , the results were not necessarily correspondent with the true stationary point of the free energy. We found by solving all self-consistency equations simultaneously via the iterative method the same qualitative results were obtained, but this time they should correspond to the actual stationary points of the free energy.

We then demonstrated how to derive the free energy and described the hill descent algorithm that we used to minimise it. By minimising the free energy directly we did indeed find the same results as obtained by iteratively solving the self-consistency equations. Furthermore we were able to obtain the familiar results from BCS theory regarding the fixed ratio of Δ to T_c and the equivalence of the spin-dependent mean-fields, i.e. $\Delta_0 = 1.76k_B T_c$ and $\phi_\uparrow = \phi_\downarrow$.

By applying the variational mean-field method to the well known case of BCS superconductivity we were able to demonstrate and focus on the technical steps and mathematical techniques. Obtaining the well known results of BCS theory suggests that the technique works and that we applied it correctly.

In chapter 5 we applied variational mean-field theory to the two-band equal-spin triplet-

pairing theory of [126]. We began by selecting a non-interacting electron dispersion for a two-dimensional square lattice with nearest neighbour hopping. We imposed a small bare splitting, s , between the dispersions for each orbital so that the Fermi surface of this toy model contained features that were qualitatively similar to that of LaNiGa₂. We then introduced the mean-field Hamiltonian, \hat{H}_{MF} , and its mean-fields and again solved it using the Bogoliubov de Gennes transformation.

We derived the self-consistency equations and found that, just like with the BCS case, solving the gap-equation with the contour method found multiple solutions when the effective splitting, s^* , was finite. Unlike with the BCS case where the effective splitting was always zero, in this theory it was expected, and indeed observed, that the effective splitting would be finite in some cases. The possibility of multiple non-trivial solutions to the gap equation therefore was of physical significance.

However, by solving all the self-consistency equations simultaneously using the iterative method, multiple solutions were not obtained. Instead the value of T_c was greatly suppressed with finite bare splitting, s , and the superconducting transition appeared first order, with Δ suddenly jumping to a finite value at T_c .

To understand the inconsistency between the two methods of solving the self-consistency equations, the free energy was derived and investigated. First, the expressions for the free energy were used to evaluate the free energy surrounding the stationary points obtained by the self-consistency equations. It was found that in some cases, when solving iteratively, the self-consistency equations were unable to find the free energy minima and were instead converging on a maximum stationary point. From this we learned that one cannot always rely on the self-consistency equations to obtain physically correct results. This seems to be the case particularly when there may be multiple solutions to the gap-equation and the free energy necessarily has an extra (compared to the simple BCS case) maximum point.

By directly minimising the free energy using a hill descent algorithm we could be sure that the results obtained were minimum points only. Doing so revealed that, with finite splitting, this two-band equal-spin triplet-pairing theory contained both first order and second order superconducting transitions, as predicted by solving the self-consistent gap-equation with the contour method.

At zero splitting (the BCS-like limit) the theory behaved just like BCS theory, as expected. There is a single, second order superconducting phase transition at a critical temperature, T_c , given by the familiar BCS ratio $\Delta = 1.76k_B T_c$. With finite splitting there is an energy difference between the two orbitals, as such there is an extra energy barrier to overcome in order to form Cooper pairs. This manifests in a general suppression of T_c , as expected. In addition, there exists a critical interaction strength, U_c , below which superconductivity is fully suppressed because the energy barrier caused by the splitting is too large.

Just above the critical interaction strength, U_c , we observed a kink in the phase boundary, see figure 5.13. This kink shows the possibility of *re-entrant* superconductivity, whereby the normal state emerges as the temperature is increased but then gives way once again to the superconducting state as the temperature is increased further. This is an instance of order-by-disorder. The phase boundary exhibits both second order phase transitions, where Δ increases continuously, and first order phase transitions, where there is a discontinuous jump in Δ .

In addition to the fascinating phenomenon of re-entrant superconductivity, the two-band

equal-spin triplet-pairing theory displays gapless superconductivity just below the second order phase transition. Here Δ is finite but not yet large enough to open a full gap in the energy spectrum of the quasi-particles. Indeed, the observation of a full gap arising from a *triplet*-pairing theory is another key result, since a common argument against non-unitary triplet-pairing in LaNiGa_2 is that it must be nodal (and therefore incompatible with a two-gap model). We thus confirm, at a self-consistent level, the findings of Weng *et al.* [126] who proposed such a theory would give rise to two full gaps.

However, while Weng *et al.* [126] proposed that the equal-spin triplet-pairing theory would give rise to two full-gaps of *different* magnitudes, our results indicate that the two gaps are always the same, i.e. $\Delta_{\uparrow\uparrow} = \Delta_{\downarrow\downarrow}$. Two consequences of which are: this equal-spin pairing theory is a *unitary*-triplet pairing theory, rather than a non-unitary one; and this theory contains no net magnetisation in the superconducting state (or anywhere else in the phase diagram).

In order to successfully explain the results of LaNiGa_2 a theory must: be a non-unitary triplet-pairing theory, have two different nodeless gaps and display a magnetisation in the superconducting state. Again we note that our theory did not include any effects due to spin-orbit coupling, as such it is not known whether its inclusion would give rise to the net magnetisation and non-unitary triplet-pairing that we are looking for. Our results show therefore that the two-band equal-spin triplet-pairing theory cannot, in its current form, explain LaNiGa_2 .

Having identified that the equal-spin triplet-pairing theory is unitary and non-magnetic, we investigated further the lack of magnetisation in chapter 6. We started by considering the normal state limit ($\Delta = 0$) of the two-band equal-spin triplet-pairing theory. We showed how the free energy could be written in two, supposedly equivalent, ways: either explicitly in terms of both the number of up- and down-spins, N_{\uparrow} and N_{\downarrow} , or in terms of the total number of particles, N , and one of the the other particle numbers, N_{σ} . We showed that the minimum of the free energy depended on which form it was expressed in, with one form predicting a magnetic ground state and the other predicting a non-magnetic one. This is because when the free energy was written in terms of both spin populations, the full parameter space was explored. However, when written in terms of the total particle number and one of the other spin populations, the free energy being considered was restricted to some arbitrary choice of total particle number. On the other hand, we showed how when one does the same thing for Stoner theory, both forms of the free energy predict the same minimum.

We identified the key difference between Stoner theory and the equal-spin pairing theory was that in Stoner theory there is a particle spin-mixing term in the free energy due to the repulsive interaction term. Such a term lowers the free energy by creating a particle imbalance (net magnetisation). This imbalance of course causes a penalty in the kinetic energy but, if the Stoner criterion is met, then the interaction term is most significant and it is more favourable to create the imbalance at the cost of the kinetic energy.

We saw how a similar interplay between the kinetic energy and interaction terms existed in the normal state of the equal-spin pairing theory, but in this case the effect of the interaction term was to fill up the spin bands. Because the free energy has no spin mixing terms and can be split into two identical expressions for each spin, there is no tendency or requirement that the system create a spin imbalance. The equivalent of the Stoner criterion in this theory marks a gas-liquid transition, where the system goes from a low-density to high-density

(always non-magnetic) phase as interaction is increased.

Motivated by the spin-mixing term in Stoner theory, we added an intra-orbital Hubbard repulsion term to the two-band equal-spin triplet-pairing theory. We showed that the addition of such a term resulted in a theory whose zero temperature ground state contained both a non-magnetic high density phase, caused by the equal-spin attraction, as well as a magnetic phase, due to the Hubbard repulsion. We noted how the observed magnetisation was not the same as that detected by μ SR, instead arguing that if the system leaned slightly towards the repulsive-dominant regime, then the onset of the pairing at the superconducting transition would enhance the tendency to form an imbalance, causing a net magnetisation.

Additionally we saw that with the inclusion of the Hubbard repulsive term, the free energy could no longer be separated into the sum of two identical expressions for spin-up and spin-down. This and the imbalance between spins will give rise to two different values of $\Delta_{\uparrow\uparrow}$ and $\Delta_{\downarrow\downarrow}$, making this a *non-unitary* triplet-pairing theory. In addition, the pairing potentials, $\Delta_{\sigma\sigma}$, will still both be isotropic and nodeless. Therefore, with the addition of a Hubbard repulsion term, the two-band equal-spin triplet-pairing theory is expected to contain everything necessary to explain superconductivity in LaNiGa_2 . In future work it would be desirable to minimise the free energy of the full theory (rather than just the zero temperature normal state) to see if two different gaps arise alongside a net magnetisation.

In chapter 7 we investigated the effect specific heat has on preventing quenches. Specifically, we concentrated on the effect of different specific heat power laws corresponding to different topological nodal states, with exponents $n = 2$ for ordinary line nodes and $n = 1.5, 1.4$ for topological transition states [82, 89]. We saw how the enhancement of both the value of the specific heat and the rate at which it increased with temperature are greater in nodal states with lowest exponents.

To test our hypothesis we performed numerical simulations of a quench using a minimum model that captured the necessary physics. We assumed the temperatures would be kept well below T_c where the power law approximation of the specific heat is valid. Our results show that the lower the exponent, the more resilient the superconducting wire is to quenches, although the effect is small.

The topological transition state has the lowest exponent, $n = 1.4$, and as such is the most quench-resistant. Even so, any of the specific heat power laws at low temperature are an improvement over the exponential specific heat so even the worst test case would offer an improvement. This concept has the potential to enhance the quench resilience of superconductors, especially if used in conjunction with existing quench detection and prevention techniques. In this proof-of-concept work a simplified quench model was used. As such, more detailed materials modelling will be required to determine exactly how useful this effect would be for applications.

In this thesis we have discussed two topics related to unconventional superconductivity. We first looked at the interesting case of unconventional superconductivity in LaNiGa_2 and saw that in order to explain it, a theory would require the following properties: it must be non-unitary triplet-pairing, possess two full gaps and display net magnetisation in the superconducting state. We found that with the addition of a Hubbard repulsive term, the two-orbital equal-spin triplet-pairing theory proposed by Weng *et al.* [126] should possess the properties required to describe the superconductivity in LaNiGa_2 .

Secondly we answered the question of whether the nodal topological-transition state could

be potentially useful in engineering quench-resilient superconducting wires. Using numerical simulations of a minimum quench model we found that the power law specific heat associated with the topological transition state provided an enhanced specific heat that made the superconducting wire more resilient to quenching, although the effect was small.

Appendix A

Diagonalising a Hamiltonian

In this section we will demonstrate the procedure of diagonalising a Hamiltonian written in matrix form. We start by showing how to diagonalise a matrix, using a 2×2 matrix as an example, and show that the transformation matrix is constructed by the eigenvectors of the Hamiltonian. We then demonstrate how to obtain the eigenvalues of the Hamiltonian matrix and how those are used to construct the diagonal matrix. We then show how the BCS transformation matrix gets its well known form as a direct consequence of the requirement that it be unitary. We finish by bringing all these things together and show how they lead to the diagonal form of the BCS mean-field Hamiltonian, and how this gives rise to Bogoliubov de Gennes transformation.

A.1 Diagonalising a matrix

In this thesis our Hamiltonians are Hermitian, they have real eigenvalues and are a type of normal matrix [143]. A matrix \mathbf{A} is normal if $\mathbf{A}\mathbf{A}^* = \mathbf{A}^*\mathbf{A}$ and normal matrices can be diagonalised by *unitary* transformations. If a matrix \mathbf{A} can be diagonalised it can be written in the form

$$\mathbf{A} = \mathbf{M}\mathbf{D}\mathbf{M}^* \quad (\text{A.1})$$

where \mathbf{D} is a diagonal matrix and in this case, because \mathbf{A} is normal, \mathbf{M} is unitary. A matrix \mathbf{M} is unitary if $\mathbf{M}\mathbf{M}^* = \mathbf{I}$ where \mathbf{M}^* is the complex transpose of \mathbf{M} and is obtained by taking the transpose and complex conjugate of \mathbf{M} . \mathbf{I} is the identity matrix. The process of diagonalising a matrix requires finding the unitary matrix \mathbf{M} , its inverse \mathbf{M}^* and the diagonal matrix \mathbf{D} .

By multiplying both sides of equation (A.1) by \mathbf{M} we obtain:

$$\mathbf{A}\mathbf{M} = \mathbf{M}\mathbf{D}$$

which written more verbosely may look like:

$$\begin{pmatrix} W_{11} & W_{12} \\ W_{21} & W_{22} \end{pmatrix} \begin{pmatrix} M_{11} & M_{12} \\ M_{21} & M_{22} \end{pmatrix} = \begin{pmatrix} M_{11} & M_{12} \\ M_{21} & M_{22} \end{pmatrix} \begin{pmatrix} D_{11} & 0 \\ 0 & D_{22} \end{pmatrix}.$$

which is equivalent to (verify by performing the above matrix multiplication):

$$\begin{pmatrix} \mathbf{A} \begin{pmatrix} M_{11} \\ M_{21} \end{pmatrix} & \mathbf{A} \begin{pmatrix} M_{12} \\ M_{22} \end{pmatrix} \end{pmatrix} = \begin{pmatrix} D_{11} \begin{pmatrix} M_{11} \\ M_{21} \end{pmatrix} & D_{22} \begin{pmatrix} M_{12} \\ M_{22} \end{pmatrix} \end{pmatrix}.$$

Comparing the elements of each matrix gives two eigenvalue equations:

$$\begin{aligned}\mathbf{A} \begin{pmatrix} M_{11} \\ M_{21} \end{pmatrix} &= D_{11} \begin{pmatrix} M_{11} \\ M_{21} \end{pmatrix} \\ \mathbf{A} \begin{pmatrix} M_{12} \\ M_{22} \end{pmatrix} &= D_{22} \begin{pmatrix} M_{12} \\ M_{22} \end{pmatrix}.\end{aligned}$$

These two eigenvalue equations tell us that the columns of the transformation matrix \mathbf{M} are the eigenvectors of the matrix \mathbf{A} and that D_{11} and D_{22} are the eigenvalues of the first and second columns of \mathbf{M} respectively.

A.2 Obtaining the eigenvalues

To obtain the eigenvalues of \mathbf{A} we use the characteristic equation:

$$\det(\mathbf{A} - \lambda \mathbf{I}) = 0 \tag{A.2}$$

which forms an n -order polynomial in λ , the roots of which are the eigenvalues of \mathbf{A} . Let us take our BCS mean field Hamiltonian, equation (4.23), as an example. We define $\mathbf{A} = \begin{pmatrix} \epsilon_{\mathbf{k}\sigma} & -\Delta \\ -\Delta^* & -\epsilon_{\mathbf{k}\sigma} \end{pmatrix}$ and seek to diagonalise \mathbf{A} . First we use the characteristic equation, equation (A.2), to find the eigenvalues:

$$\begin{aligned}\left| \begin{pmatrix} \epsilon_{\mathbf{k}\sigma} & -\Delta \\ -\Delta^* & -\epsilon_{\mathbf{k}\sigma} \end{pmatrix} - \begin{pmatrix} \lambda & 0 \\ 0 & \lambda \end{pmatrix} \right| &= 0 \\ \left| \begin{pmatrix} \epsilon_{\mathbf{k}\sigma} - \lambda & -\Delta \\ -\Delta^* & -\epsilon_{\mathbf{k}\sigma} - \lambda \end{pmatrix} \right| &= 0 \\ (\epsilon_{\mathbf{k}\sigma} - \lambda)(-\epsilon_{\mathbf{k}\sigma} - \lambda) - |\Delta|^2 &= 0 \\ \lambda^2 - \epsilon_{\mathbf{k}\sigma}^2 - |\Delta|^2 &= 0 \\ \lambda_{\pm} &= \pm \sqrt{\epsilon_{\mathbf{k}\sigma}^2 + |\Delta|^2}.\end{aligned}$$

Having obtained the eigenvalues the diagonal matrix \mathbf{D} can now be defined:

$$\mathbf{D} = \begin{pmatrix} \lambda_+ & 0 \\ 0 & \lambda_- \end{pmatrix}. \tag{A.3}$$

Next we need to define the transformation matrix \mathbf{M} that will diagonalise \mathbf{A} .

A.3 Unitary Transformation Matrix

In section 4.4 the transformation matrix is simply defined as

$$\mathbf{M} = \begin{pmatrix} u_{\mathbf{k}} & -v_{\mathbf{k}}^* \\ v_{\mathbf{k}} & u_{\mathbf{k}}^* \end{pmatrix}. \tag{A.4}$$

This matrix, or the resulting relations between the $\hat{\gamma}$ -operators and the \hat{c} -operators, are typically just given in a presentation of BCS theory without any derivation. This can lead to confusion to those new to the subject and does not explain how one would obtain \mathbf{M} for

other theories. Here we will go through the derivation of such a matrix and show that its structure comes simply as a result of using a unitary transformation.

In general a transformation matrix simply looks like a 2×2 matrix with no other structure between the elements i.e.

$$\mathbf{M} = \begin{pmatrix} a & b \\ c & d \end{pmatrix} \quad \mathbf{M}^* = \begin{pmatrix} a^* & c^* \\ b^* & d^* \end{pmatrix}$$

Since \mathbf{M} is a *unitary* matrix, the definition of which is $\mathbf{M}\mathbf{M}^* = \mathbf{I}$, we obtain

$$\begin{pmatrix} aa^* + bb^* & ac^* + bd^* \\ ca^* + db^* & cc^* + dd^* \end{pmatrix} = \begin{pmatrix} 1 & 0 \\ 0 & 1 \end{pmatrix}.$$

This gives us four equations:

$$aa^* + bb^* = 1 \quad (\text{A.5a})$$

$$cc^* + dd^* = 1 \quad (\text{A.5b})$$

$$ac^* + bd^* = 0 \quad (\text{A.5c})$$

$$ca^* + db^* = 0 \quad (\text{A.5d})$$

From equations (A.5c) and (A.5d) we get $b = -\frac{ac^*}{d^*}$ and $b^* = -\frac{ca^*}{d}$ which, when substituted into equation (A.5a), gives

$$\begin{aligned} aa^* + \frac{aa^*cc^*}{dd^*} &= 1 \\ aa^*(dd^* + cc^*) &= dd^* \\ aa^* &= dd^*. \end{aligned}$$

We have used equation (A.5b) to reach the last stage. By writing equations (A.5c) and (A.5d) in terms of d rather than b , substituting into equation (A.5b) and following a similar line of reasoning one obtains $cc^* = bb^*$.

By requiring this general 2×2 matrix \mathbf{M} be unitary we obtain the conditions:

$$\begin{aligned} aa^* &= dd^* \\ cc^* &= bb^* \\ bd^* &= -ac^* \\ db^* &= -ca^* \end{aligned}$$

which, when substituted into our product matrix gives

$$\mathbf{M}\mathbf{M}^* = \begin{pmatrix} aa^* + cc^* & ac^* - ac^* \\ ca^* - ca^* & cc^* + aa^* \end{pmatrix} = \begin{pmatrix} aa^* + cc^* & 0 \\ 0 & cc^* + aa^* \end{pmatrix} = \begin{pmatrix} 1 & 0 \\ 0 & 1 \end{pmatrix}.$$

One possible way of decomposing this product matrix is by

$$\mathbf{M} = \begin{pmatrix} a & -c^* \\ c & a^* \end{pmatrix} \quad \mathbf{M}^* = \begin{pmatrix} a^* & c^* \\ -c & a \end{pmatrix} \quad (\text{A.7})$$

which has the same structure as the u 's and v 's in equation (A.4). There are of course other ways to decompose the product $\mathbf{M}\mathbf{M}^*$ which is how and why the transformation may vary between different demonstrations of BCS theory. The point here is that \mathbf{M} can be obtained for any $n \times n$ Hamiltonian, not just BCS theory, by parametrising a general $n \times n$ unitary matrix.

A.4 The diagonalised Hamiltonian

Now that we have obtained \mathbf{D} and \mathbf{M} we can replace $\mathbf{A} = \mathbf{M}\mathbf{D}\mathbf{M}^*$ in the mean field Hamiltonian, equation (4.23), and write as:

$$\hat{\mathcal{H}}_{\text{BCS}}^{\text{MF}} - \sum_{\mathbf{k}} \epsilon_{\mathbf{k}\sigma} = \sum_{\mathbf{k}} \mathbf{C}^* \mathbf{M} \mathbf{D} \mathbf{M}^* \mathbf{C}$$

where we have defined $\mathbf{C} = \begin{pmatrix} \hat{c}_{\mathbf{k}\uparrow} \\ \hat{c}_{\mathbf{k}\downarrow}^\dagger \end{pmatrix}$ as the vector of creation/annihilation operators and \mathbf{C}^*

is its conjugate transpose. Defining new fermionic operators $\boldsymbol{\gamma} = \begin{pmatrix} \hat{\gamma}_a \\ \hat{\gamma}_b^\dagger \end{pmatrix}$ we can obtain the relations between the two operator types using $\boldsymbol{\gamma} = \mathbf{M}^* \mathbf{C}$ and $\boldsymbol{\gamma}^* = \mathbf{C}^* \mathbf{M}$. These relations are known as the Bogoliobov transformations and give rise to equation (4.25). The inverse relations $\mathbf{M}\boldsymbol{\gamma} = \mathbf{C}$ and $\boldsymbol{\gamma}^* \mathbf{M}^* = \mathbf{C}^*$ give equation (4.26).

Appendix B

Non-unitary triplet-pairing diagonalisation transition matrix

In this section we shall describe how the transition matrix for the equal-spin triplet-pairing theory, U , equation (5.19), was obtained.

In appendix A.3 we showed how the particular form of the transition matrix for BCS theory arose from the requirement that it be a unitary transition matrix. This time however, because the transformation matrix is a 4×4 matrix, the requirement that it be unitary is not enough to be able to usefully parametrise it.

We used the computer algebra system ‘Maxima’ (with GUI wxMaxima) [144, 145] to diagonalise the mean-field Hamiltonian matrix, $\mathbf{H}_{\mathbf{k}\sigma}^{\text{MF}}$, and obtain the eigenvalues and eigenvectors. The problem with this method is that each eigenvector is determined independently of the others so there is an arbitrary complex phase factor between them, making the expressions unnecessarily cumbersome. However, we note that some elements have the same expression and there are some zeros in the eigenvectors simplifying the the transition matrix to:

$$U = \begin{pmatrix} a_{\mathbf{k}\sigma} & b_{\mathbf{k}\sigma} & 0 & 0 \\ c_{\mathbf{k}\sigma} & -d_{\mathbf{k}\sigma} & 0 & 0 \\ 0 & 0 & a_{\mathbf{k}\sigma} & b_{\mathbf{k}\sigma} \\ 0 & 0 & -c_{\mathbf{k}\sigma} & d_{\mathbf{k}\sigma} \end{pmatrix} \quad (\text{B.1})$$

where we have used the notation $a_{\mathbf{k}\sigma}$, $b_{\mathbf{k}\sigma}$, $c_{\mathbf{k}\sigma}$ and $d_{\mathbf{k}\sigma}$ in place of the cumbersome expressions produced by Maxima.

The four eigenvalues of $\mathbf{H}_{\mathbf{k}\sigma}^{\text{MF}}$ are given by equation (5.23). An important property is that some of them are negatives of each other:

$$\lambda_{a\mathbf{k}\sigma} = -\lambda_{d\mathbf{k}\sigma} \quad (\text{B.2a})$$

$$\lambda_{b\mathbf{k}\sigma} = -\lambda_{c\mathbf{k}\sigma}. \quad (\text{B.2b})$$

This property allows us to link certain eigenvectors as follows: if an eigenvector $\mathbf{V}_{a\sigma}$ has an eigenvalue $\lambda_{a\mathbf{k}\sigma}$ then the negative eigenvalue $\lambda_{d\mathbf{k}\sigma}$ has the same eigenvector but with the elements reversed and conjugated. Let us prove this now.

We consider the Hamiltonian in matrix form, $\mathbf{H}_{\mathbf{k}\sigma}^{\text{MF}}$, one of its eigenvector/eigenvalue pairs and the eigenvector equation:

$$\mathbf{H}_{\mathbf{k}\sigma}^{\text{MF}} \mathbf{W}_{a\mathbf{k}\sigma} = \lambda_{a\mathbf{k}\sigma} \mathbf{W}_{a\mathbf{k}\sigma} \quad (\text{B.3})$$

The Hamiltonian, $\mathbf{H}_{\mathbf{k}\sigma}^{\text{MF}}$, and eigenvector, $\mathbf{W}_{a\mathbf{k}\sigma}$ can be written in general as

$$\mathbf{H}_{\mathbf{k}\sigma}^{\text{MF}} = \begin{pmatrix} H_{11} & H_{12} & H_{13} & H_{14} \\ H_{21} & H_{22} & H_{23} & H_{24} \\ H_{31} & H_{32} & H_{33} & H_{34} \\ H_{41} & H_{42} & H_{43} & H_{44} \end{pmatrix} \quad \mathbf{W}_{a\mathbf{k}\sigma} = \begin{pmatrix} W_1 \\ W_2 \\ W_3 \\ W_4 \end{pmatrix}. \quad (\text{B.4})$$

Multiplying out equation (B.3) and leaving blank the terms that are zero gives

$$\begin{aligned} H_{11}W_1 + H_{12}W_2 + & & + & & = \lambda_{a\mathbf{k}\sigma}W_1 \\ H_{21}W_1 + H_{22}W_2 + & & + & & = \lambda_{a\mathbf{k}\sigma}W_2 \\ & + & & + H_{33}W_3 + H_{34}W_4 = \lambda_{a\mathbf{k}\sigma}W_3 \\ & + & & + H_{43}W_3 + H_{44}W_4 = \lambda_{a\mathbf{k}\sigma}W_4 \end{aligned}$$

One symmetry of $\mathbf{H}_{\mathbf{k}\sigma}^{\text{MF}}$ is that the secondary diagonal divides the matrix into a top left block and bottom right block whose elements are negatives of each other, e.g. $H_{11} = -H_{44}$. Using this symmetry we can write $\mathbf{H}_{\mathbf{k}\sigma}^{\text{MF}}$ equivalently as:

$$\begin{aligned} -H_{44}W_1 - H_{34}W_2 - & & - & & = \lambda_{a\mathbf{k}\sigma}W_1 \\ -H_{43}W_1 - H_{33}W_2 - & & - & & = \lambda_{a\mathbf{k}\sigma}W_2 \\ - & & - & - H_{22}W_3 - H_{12}W_4 = \lambda_{a\mathbf{k}\sigma}W_3 \\ - & & - & - H_{21}W_3 - H_{11}W_4 = \lambda_{a\mathbf{k}\sigma}W_4 \end{aligned}$$

Another property of $\mathbf{H}_{\mathbf{k}\sigma}^{\text{MF}}$ is Hermiticity, $\mathbf{H}_{\mathbf{k}\sigma}^{\text{MF}} = (\mathbf{H}_{\mathbf{k}\sigma}^{\text{MF}})^{\text{T}*}$. This means we can take the complex conjugate and transpose, giving:

$$\begin{aligned} -H_{44}^*W_1 - H_{43}^*W_2 - & & - & & = \lambda_{a\mathbf{k}\sigma}W_1 \\ -H_{34}^*W_1 - H_{33}^*W_2 - & & - & & = \lambda_{a\mathbf{k}\sigma}W_2 \\ - & & - & - H_{22}^*W_3 - H_{21}^*W_4 = \lambda_{a\mathbf{k}\sigma}W_3 \\ - & & - & - H_{12}^*W_3 - H_{11}^*W_4 = \lambda_{a\mathbf{k}\sigma}W_4. \end{aligned}$$

Multiplying this system of equations by -1 and taking the complex conjugate gives

$$\begin{aligned} H_{44}W_1^* + H_{43}W_2^* + & & + & & = -\lambda_{a\mathbf{k}\sigma}W_1^* \\ H_{34}W_1^* + H_{33}W_2^* + & & + & & = -\lambda_{a\mathbf{k}\sigma}W_2^* \\ & + & & + H_{22}W_3^* + H_{21}W_4^* = -\lambda_{a\mathbf{k}\sigma}W_3^* \\ & + & & + H_{12}W_3^* + H_{11}W_4^* = -\lambda_{a\mathbf{k}\sigma}W_4^* \end{aligned}$$

and simply swapping the order of the equations gives

$$\begin{aligned} & + & & + H_{12}W_3^* + H_{11}W_4^* = -\lambda_{a\mathbf{k}\sigma}W_4^* \\ & + & & + H_{22}W_3^* + H_{21}W_4^* = -\lambda_{a\mathbf{k}\sigma}W_3^* \\ H_{34}W_1^* + H_{33}W_2^* + & & + & & = -\lambda_{a\mathbf{k}\sigma}W_2^* \\ H_{44}W_1^* + H_{43}W_2^* + & & + & & = -\lambda_{a\mathbf{k}\sigma}W_1^* \end{aligned}$$

This system of equations can then be written in matrix form giving:

$$\begin{pmatrix} H_{11} & H_{12} & 0 & 0 \\ H_{21} & H_{22} & 0 & 0 \\ 0 & 0 & H_{33} & H_{34} \\ 0 & 0 & H_{43} & H_{44} \end{pmatrix} \begin{pmatrix} W_4^* \\ W_3^* \\ W_2^* \\ W_1^* \end{pmatrix} = -\lambda_{ak\sigma} \begin{pmatrix} W_4^* \\ W_3^* \\ W_2^* \\ W_1^* \end{pmatrix}$$

which is itself another eigenvector equation:

$$\mathbf{H}_{k\sigma}^{\text{MF}} \mathbf{W}_{ak\sigma}^{R*} = -\lambda_{ak\sigma} \mathbf{W}_{ak\sigma}^{R*}. \quad (\text{B.5})$$

Here we have defined the eigenvector element reversal operation, R , such that $\mathbf{W}_{ak\sigma}^R$ is obtained by reversing the elements of the eigenvector $\mathbf{W}_{ak\sigma}$. This procedure shows that if there exists an eigenvector $\mathbf{W}_{ak\sigma}$ with eigenvalue $\lambda_{ak\sigma}$, then there also must exist another eigenvalue with opposite sign, $-\lambda_{ak\sigma}$, and eigenvector, $\mathbf{W}_{ak\sigma}^{R*}$, given by reversing the elements and taking the complex conjugate of the original eigenvector.

As mentioned above, we can use this link between positive and negative eigenvalues to help simplify our transition matrix, \mathbf{U} . The diagonal matrix, \mathbf{D} , is defined as:

$$\mathbf{D} = \begin{pmatrix} \lambda_{ak\sigma} & 0 & 0 & 0 \\ 0 & \lambda_{ck\sigma} & 0 & 0 \\ 0 & 0 & \lambda_{bk\sigma} & 0 \\ 0 & 0 & 0 & \lambda_{dk\sigma} \end{pmatrix} \quad (\text{B.6})$$

where there is a correspondence between the eigenvalues and eigenvectors in the same column of \mathbf{D} and \mathbf{U} . Using the fact that some of these eigenvalues are the negative of the other, see equation (B.2), we can write the transition matrix in terms of only two eigenvectors and their reversed-conjugated counterparts:

$$\mathbf{U} = \begin{pmatrix} \mathbf{W}_{ak\sigma} & \mathbf{W}_{ck\sigma} & \mathbf{W}_{bk\sigma} & \mathbf{W}_{dk\sigma} \\ a_{k\sigma} & b_{k\sigma} & 0 & 0 \\ c_{k\sigma} & -d_{k\sigma} & 0 & 0 \\ 0 & 0 & a_{k\sigma} & b_{k\sigma} \\ 0 & 0 & -c_{k\sigma} & d_{k\sigma} \end{pmatrix} = \begin{pmatrix} \mathbf{W}_{ak\sigma} & \mathbf{W}_{bk\sigma}^{R*} & \mathbf{W}_{bk\sigma} & \mathbf{W}_{ak\sigma}^{R*} \\ a_{k\sigma} & -c_{k\sigma}^* & 0 & 0 \\ c_{k\sigma} & a_{k\sigma}^* & 0 & 0 \\ 0 & 0 & a_{k\sigma} & c_{k\sigma}^* \\ 0 & 0 & -c_{k\sigma} & a_{k\sigma}^* \end{pmatrix}. \quad (\text{B.7})$$

The row vector above the transition matrix identifies which column corresponds to which eigenvector and eigenvalue. The final matrix on the right has been constructed by reverse-conjugating the corresponding vectors as shown.

By using the link between positive and negative eigenvalues to identify which eigenvectors are simply reverse-conjugated forms of the other independent ones, we have obtained a simple parametrised transition matrix, \mathbf{U} , which is also unitary as required. It is this transition matrix that we use when solving the mean-field Hamiltonian of the two-orbital equal-spin triplet-pairing theory of chapter 5.

Appendix C

Dimensionless equations

In this section we will demonstrate how equations can be made dimensionless by rescaling through new characteristic length, time and temperature scales. As an example we will use the simplest quench model, equation (7.1), from section 7.2. The procedure works as follows: we write all of the characteristic quantities, e.g. length, temperature and time, as dimensionless quantities and then absorb the various constants into the characteristic scales.

A dimensionless quantity \tilde{Q} is obtained by rescaling the dimension-full quantity, Q , by some characteristic scale, Q_0 , like so: $\tilde{Q} = Q/Q_0$. If we write the length, L , temperature, T , and time, t , in terms of the dimensionless quantity and its characteristic scale we get $L = \tilde{L}L_0$, $T = \tilde{T}T_0$ and $t = \tilde{t}t_0$ respectively, and equation (7.1) becomes:

$$\rho_c C_c \frac{T_0}{t_0} \frac{\partial \tilde{T}}{\partial \tilde{t}} = \kappa_c \frac{T_0}{x_0^2} \frac{\partial^2 \tilde{T}}{\partial \tilde{x}^2} - \frac{hP_c}{A_c} T_0 (\tilde{T} - \tilde{T}_h) + \frac{\eta_c I^2}{A_c^2} \Theta (\tilde{T} - \tilde{T}_c). \quad (\text{C.1})$$

Note that for convenience we have not written explicitly that the temperature of the superconductor, T , depends on the time, t , and the position, x , along the conductor.

The second term on the RHS that describes the heat transfer with the bath can be made dimensionless by multiplying the equation by $\frac{A_c}{hP_c} \frac{1}{T_0}$, giving:

$$\frac{\rho_c C_c A_c}{hP_c} \frac{1}{t_0} \frac{\partial \tilde{T}}{\partial \tilde{t}} = \frac{A_c \kappa_c}{hP_c} \frac{1}{x_0^2} \frac{\partial^2 \tilde{T}}{\partial \tilde{x}^2} - (\tilde{T} - \tilde{T}_h) + \frac{\eta_c I^2}{A_c h P_c T_0} \Theta (\tilde{T} - \tilde{T}_c). \quad (\text{C.2})$$

By defining the characteristic scales as in equation (7.3):

$$x_0 \equiv \left(\frac{W_c \kappa_c}{hP_c} \right)^{\frac{1}{2}} \quad T_0 \equiv \frac{\eta_c I^2}{W_c h P_c} \quad t_0 \equiv \frac{\rho_c C_c W_c}{hP_c}, \quad (\text{C.3})$$

the simplest quench model takes the dimensionless form:

$$\frac{\partial \tilde{T}}{\partial \tilde{t}} = \frac{\partial^2 \tilde{T}}{\partial \tilde{x}^2} - (\tilde{T} - \tilde{T}_h) + \Theta (\tilde{T} - \tilde{T}_c). \quad (\text{C.4})$$

A similar procedure is applied for all dimensionless equations presented in chapter 7.

Appendix D

Forward in time centred in space algorithm

D.1 Technical details of the forward in time centred in space algorithm

In this section we shall describe the forward-in-time centred-in-space (FTCS) algorithm for solving partial differential equations, using the simple heat diffusion equation as an example. For a more detailed look at this and many other numerical algorithms, see the book Numerical Recipes [128].

Our starting point is a simple heat diffusion equation of the form:

$$\frac{\partial T(x, t)}{\partial t} = D \frac{\partial^2 T(x, t)}{\partial x^2}. \quad (\text{D.1})$$

In order to model the system numerically, the continuous variables x and t are discretised and mapped onto a finite two-dimensional array of size $N_x \times N_t$. N_x is the number of discretised spatial divisions being used to represent the total length, L , of the system and N_t is the number of time steps over which the calculation will be performed. The spatial and temporal difference between adjacent elements of the array are given by $\Delta x = L/N_x$ and $\Delta t = t_{\text{tot}}/N_t$ respectively. t_{tot} is the total time being simulated.

Working in discrete spatial and time steps, the heat equation can be written in the form of a finite difference equation as follows:

$$\left[\frac{T(x_i, t_{j+1}) - T(x_i, t_j)}{\Delta t} \right] = D \left[\frac{T(x_{i+1}, t_j) - 2T(x_i, t_j) + T(x_{i-1}, t_j)}{\Delta x^2} \right], \quad (\text{D.2})$$

where the partial derivatives have been expressed in terms of finite differences. Here $T(x_i, t_j)$ is the temperature at the i 'th spatial position and the j 'th time step. This expression can be rearranged for the temperature at the $(j + 1)$ 'th time step as follows:

$$T(x_i, t_{j+1}) = D \frac{\Delta t}{\Delta x^2} [T(x_{i+1}, t_j) - 2T(x_i, t_j) + T(x_{i-1}, t_j)] + T(x_i, t_j). \quad (\text{D.3})$$

The temperature of the i 'th spatial position at the next time step, $T_{x_i, t_{j+1}}$, depends exclusively on its current temperature and the temperatures of the neighbouring spatial divisions at the current time step. The FTCS algorithm is said to be centred-in-space because it uses the information of its immediate neighbours in both directions to calculate the next temperature, and is said to be forward-in-time because it uses the information at the current

time step to calculate the temperature at the next time. By providing an initial temperature profile (the initial condition of the simulation) the algorithm can calculate the temperature of each spatial division at the next time step, which it can then in turn use to calculate the time step after that. The algorithm iterates, using the information at the current time step to calculate the temperature of the system at the next, repeatedly stepping forward in time. In this way it builds up the time evolution of the temperature of the system.

D.2 Stability of the forward in time centred in space algorithm

As mentioned in chapter 7 section 7.4, there is a stability condition for the simple heat equation, that determines if the FTCS algorithm will be stable or not. Stability is very closely related to numerical convergence, one has to obtain stability before the results are potentially physically correct, then one can ensure numerical convergence.

When replacing the partial derivatives with the finite differences, we introduced the quantities Δx and Δt . In a differential these quantities are infinitesimally small and therefore, in order for our numerics to be a correct approximation to a differential, these quantities need to be as small as possible, i.e. $\Delta x \ll L$ and $\Delta t \ll t_{\text{tot}}$. If these relations are obeyed then one might expect the results to be numerically convergent, since our numerical finite difference derivative should be a good approximation to the actual mathematical derivative.

However, the problem of stability may also arise. Consider equation (D.3), specifically the $\frac{\Delta t}{\Delta x^2}$ term. This term scales the amount of temperature being transferred with neighbouring segments of the system. If $\Delta x^2 \ll \Delta t$ then this scaling term will be very large, the effect of which will be that the temperature will change drastically at the next time step. This drastic change can lead to further, more drastic changes in neighbouring positions and further time steps, often with oscillatory features. Sometimes the algorithm can recover, with the oscillations averaging out and dying away, other times they are too large and no convergent behaviour is obtained.

It is possible to investigate the stability of the finite difference scheme by von Neumann stability analysis, a full explanation of which can be found in [128]. Using this stability analysis it is sometimes possible (although not always) to derive a stability condition that ensures the method is stable, however, we will not do so in this work. Here we simply state that the stability condition for the heat equation is given by [128]:

$$\frac{D\Delta t}{\Delta x^2} \leq \frac{1}{2}. \quad (\text{D.4})$$

By ensuring this condition is met, the FTCS algorithm is stable when solving the simple heat equation. As mentioned above, this does not ensure numerical convergence, as such this still needs to be tested.

The equations we use in our quench model are not simple heat equations. It was beyond the scope of this work to perform the von Neumann stability analysis for our model as we found that ensuring the stability condition of the simple heat equation was well met was enough to ensure stability in our simulations.

Bibliography

- [1] P. Whittlesea *et al.* “Can Topological Transitions be Exploited to Engineer Intrinsically Quench-Resistant Wires?” In: *IEEE Transactions on Applied Superconductivity* 28.4 (June 2018), pp. 1–5. ISSN: 1051-8223. DOI: [10.1109/TASC.2018.2791515](https://doi.org/10.1109/TASC.2018.2791515).
- [2] G. van Rossum. *Python tutorial*. Tech. rep. CS-R9526. Amsterdam: Centrum voor Wiskunde en Informatica (CWI), May 1995.
- [3] *Python Software Foundation*. Version Version 2.7.15. URL: <http://www.python.org>.
- [4] *GNU Fortran Web page*. URL: <https://gcc.gnu.org/fortran/>.
- [5] Travis E. Oliphant. *Guide to NumPy*. 2nd. USA: CreateSpace Independent Publishing Platform, 2015. ISBN: 151730007X, 9781517300074.
- [6] Eric Jones, Travis Oliphant, Pearu Peterson, *et al.* *SciPy: Open source scientific tools for Python*. 2001. URL: <http://www.scipy.org/>.
- [7] Wes McKinney. “Data Structures for Statistical Computing in Python”. In: *Proceedings of the 9th Python in Science Conference*. Ed. by Stéfan van der Walt and Jarrod Millman. 2010, pp. 51–56.
- [8] Fernando Pérez and Brian E. Granger. “IPython: A System for Interactive Scientific Computing”. In: *Computing in Science & Engineering* 9.3 (2007), pp. 21–29. DOI: [10.1109/MCSE.2007.53](https://doi.org/10.1109/MCSE.2007.53).
- [9] Thomas Kluyver *et al.* “Jupyter Notebooks – a publishing format for reproducible computational workflows”. In: *Positioning and Power in Academic Publishing: Players, Agents and Agendas*. Ed. by F. Loizides and B. Schmidt. IOS Press. 2016, pp. 87–90.
- [10] Pearu Peterson. “F2PY: a tool for connecting Fortran and Python programs”. In: *International Journal of Computational Science and Engineering* 4.4 (2009), p. 296. DOI: [10.1504/ijcse.2009.029165](https://doi.org/10.1504/ijcse.2009.029165).
- [11] J. D. Hunter. “Matplotlib: A 2D graphics environment”. In: *Computing In Science & Engineering* 9.3 (2007), pp. 90–95.
- [12] *Gnuplot: an interactive plotting program*. <https://sourceforge.net/projects/gnuplot/files/gnuplot/>.
- [13] James Annett. *Superconductivity, superfluids, and condensates*. Oxford New York: Oxford University Press, 2004. ISBN: 9780198507567.
- [14] P. G. de Gennes. *Superconductivity of Metals and Alloys*. WESTVIEW PR, Mar. 11, 1999. 292 pp. ISBN: 0738201014.

- [15] H. Kamerlingh Onnes. In: *Commun. Phys. Lab. Univ. Leiden. Suppl.* 29 (1911). Cited in Dirk van Delft and Peter Kes. “The discovery of superconductivity”. In: *Physics Today* 63.9 (Sept. 2010), pp. 38–43. DOI: [10.1063/1.3490499](https://doi.org/10.1063/1.3490499).
- [16] J. File and R. G. Mills. “Observation of Persistent Current in a Superconducting Solenoid”. In: *Phys. Rev. Lett.* 10 (3 Feb. 1963), pp. 93–96. DOI: [10.1103/PhysRevLett.10.93](https://doi.org/10.1103/PhysRevLett.10.93).
- [17] W. Meissner and R. Ochsenfeld. In: *Naturwissenschaften* 21.787 (1933). Cited in Jörg Schmalian. “FAILED THEORIES OF SUPERCONDUCTIVITY”. In: *BCS: 50 Years*, pp. 41–55. DOI: [10.1142/9789814304665_0004](https://doi.org/10.1142/9789814304665_0004).
- [18] F. London and H. London. “The electromagnetic equations of the supraconductor”. In: *Proceedings of the Royal Society of London A: Mathematical, Physical and Engineering Sciences* 149.866 (1935), pp. 71–88. ISSN: 0080-4630. DOI: [10.1098/rspa.1935.0048](https://doi.org/10.1098/rspa.1935.0048).
- [19] A. A. Abrikosov. “On the Magnetic Properties of Superconductors of the Second Group”. In: *JETP* 5.6 (1957), p. 1174.
- [20] Lev P. Gor’kov. “DEVELOPING BCS IDEAS IN THE FORMER SOVIET UNION”. In: *BCS: 50 Years*, pp. 107–126. DOI: [10.1142/9789814304665_0007](https://doi.org/10.1142/9789814304665_0007).
- [21] Emanuel Maxwell. “Isotope Effect in the Superconductivity of Mercury”. In: *Phys. Rev.* 78 (4 May 1950), pp. 477–477. DOI: [10.1103/PhysRev.78.477](https://doi.org/10.1103/PhysRev.78.477).
- [22] C. A. Reynolds *et al.* “Superconductivity of Isotopes of Mercury”. In: *Phys. Rev.* 78 (4 May 1950), pp. 487–487. DOI: [10.1103/PhysRev.78.487](https://doi.org/10.1103/PhysRev.78.487).
- [23] B. Serin, C. A. Reynolds, and L. B. Nesbitt. “Superconductivity of Isotopes of Mercury”. In: *Phys. Rev.* 78 (6 June 1950), pp. 813–814. DOI: [10.1103/PhysRev.78.813](https://doi.org/10.1103/PhysRev.78.813).
- [24] C. A. Reynolds, B. Serin, and L. B. Nesbitt. “The Isotope Effect in Superconductivity. I. Mercury”. In: *Phys. Rev.* 84 (4 Nov. 1951), pp. 691–694. DOI: [10.1103/PhysRev.84.691](https://doi.org/10.1103/PhysRev.84.691).
- [25] Jules de Launay. “The Isotope Effect in Superconductivity”. In: *Phys. Rev.* 93 (4 Feb. 1954), pp. 661–665. DOI: [10.1103/PhysRev.93.661](https://doi.org/10.1103/PhysRev.93.661).
- [26] J. Bardeen, L. N. Cooper, and J. R. Schrieffer. “Theory of Superconductivity”. In: *Phys. Rev.* 108 (5 Dec. 1957), pp. 1175–1204. DOI: [10.1103/PhysRev.108.1175](https://doi.org/10.1103/PhysRev.108.1175).
- [27] J. Bardeen, L. N. Cooper, and J. R. Schrieffer. “Microscopic Theory of Superconductivity”. In: *Phys. Rev.* 106 (1 Apr. 1957), pp. 162–164. DOI: [10.1103/PhysRev.106.162](https://doi.org/10.1103/PhysRev.106.162).
- [28] N. N. Bogoliubov. “A new method in the theory of superconductivity”. In: *JETP* 34 (1958), pp. 58–65.
- [29] J. G. Valatin. “Comments on the theory of superconductivity”. In: *Il Nuovo Cimento (1955-1965)* 7.6 (Mar. 1958), pp. 843–857. ISSN: 1827-6121. DOI: [10.1007/BF02745589](https://doi.org/10.1007/BF02745589).
- [30] Leon N Cooper. “REMEMBRANCE OF SUPERCONDUCTIVITY PAST”. In: *BCS: 50 Years*, pp. 3–19. DOI: [10.1142/9789814304665_0001](https://doi.org/10.1142/9789814304665_0001).
- [31] L. P. Gor’kov. “On the Energy Spectrum of Superconductors”. In: *JETP* 7.3 (1958), p. 505.

- [32] L. P. Gor'kov. "Microscopic Derivation of the Ginzburg-Landau Equations in the Theory of Superconductivity". In: *JETP* 9.6 (1959). (Russian original - ZhETF, Vol. 36, No. 6, p. 1918, December 1959), p. 1364.
- [33] B. T. Matthias. "Superconductivity in the Cobalt-Silicon System". In: *Phys. Rev.* 87 (2 July 1952), pp. 380–380. DOI: [10.1103/PhysRev.87.380](https://doi.org/10.1103/PhysRev.87.380).
- [34] B. T. Matthias and J. K. Hulm. "Superconducting Properties of Cobalt Disilicide". In: *Phys. Rev.* 89 (2 Jan. 1953), pp. 439–441. DOI: [10.1103/PhysRev.89.439](https://doi.org/10.1103/PhysRev.89.439).
- [35] George F. Hardy and John K. Hulm. "Superconducting Silicides and Germanides". In: *Phys. Rev.* 89 (4 Feb. 1953), pp. 884–884. DOI: [10.1103/PhysRev.89.884](https://doi.org/10.1103/PhysRev.89.884).
- [36] J. R. Gavaler. "Superconductivity in Nb-Ge films above 22 K". In: *Applied Physics Letters* 23.8 (1973), pp. 480–482. DOI: [10.1063/1.1654966](https://doi.org/10.1063/1.1654966).
- [37] S. Foner *et al.* "Upper critical fields of Nb₃Ge thin film superconductors". In: *Physics Letters A* 47.6 (1974), pp. 485–486. ISSN: 0375-9601. DOI: [https://doi.org/10.1016/0375-9601\(74\)90588-X](https://doi.org/10.1016/0375-9601(74)90588-X).
- [38] F. Steglich *et al.* "Superconductivity in the Presence of Strong Pauli Paramagnetism: CeCu₂Si₂". In: *Phys. Rev. Lett.* 43 (25 Dec. 1979), pp. 1892–1896. DOI: [10.1103/PhysRevLett.43.1892](https://doi.org/10.1103/PhysRevLett.43.1892).
- [39] C Petrovic *et al.* "Heavy-fermion superconductivity in CeCoIn₅ at 2.3 K". In: *Journal of Physics: Condensed Matter* 13.17 (2001), p. L337.
- [40] E. Bauer *et al.* "Heavy Fermion Superconductivity and Magnetic Order in Noncentrosymmetric CePt₃Si". In: *Phys. Rev. Lett.* 92 (2 Jan. 2004), p. 027003. DOI: [10.1103/PhysRevLett.92.027003](https://doi.org/10.1103/PhysRevLett.92.027003).
- [41] H. Hegger *et al.* "Pressure-Induced Superconductivity in Quasi-2D CeRhIn₅". In: *Phys. Rev. Lett.* 84 (21 May 2000), pp. 4986–4989. DOI: [10.1103/PhysRevLett.84.4986](https://doi.org/10.1103/PhysRevLett.84.4986).
- [42] N. D. Mathur *et al.* "Magnetically mediated superconductivity in heavy fermion compounds". In: *Nature* 394 (July 1998), p. 39.
- [43] Hilbert v. Löhneysen *et al.* "Fermi-liquid instabilities at magnetic quantum phase transitions". In: *Rev. Mod. Phys.* 79 (3 Aug. 2007), pp. 1015–1075. DOI: [10.1103/RevModPhys.79.1015](https://doi.org/10.1103/RevModPhys.79.1015).
- [44] J. G. Bednorz and K. A. Müller. "Possible highT_c superconductivity in the Ba-La-Cu-O system". In: *Zeitschrift für Physik B Condensed Matter* 64.2 (June 1986), pp. 189–193. ISSN: 1431-584X. DOI: [10.1007/BF01303701](https://doi.org/10.1007/BF01303701).
- [45] M. K. Wu *et al.* "Superconductivity at 93 K in a new mixed-phase Y-Ba-Cu-O compound system at ambient pressure". In: *Phys. Rev. Lett.* 58 (9 Mar. 1987), pp. 908–910. DOI: [10.1103/PhysRevLett.58.908](https://doi.org/10.1103/PhysRevLett.58.908).
- [46] A. Schilling *et al.* "Superconductivity above 130 K in the Hg-Ba-Ca-Cu-O system". In: *Nature* 363 (May 1993), p. 56.
- [47] L. Gao *et al.* "Superconductivity up to 164 K in HgBa₂Ca_{m-1}Cu_mO_{2m+2+δ} (m=1, 2, and 3) under quasihydrostatic pressures". In: *Phys. Rev. B* 50 (6 Aug. 1994), pp. 4260–4263. DOI: [10.1103/PhysRevB.50.4260](https://doi.org/10.1103/PhysRevB.50.4260).

- [48] G. R. Stewart. “Unconventional superconductivity”. In: *Advances in Physics* 66.2 (2017), pp. 75–196. DOI: [10.1080/00018732.2017.1331615](https://doi.org/10.1080/00018732.2017.1331615).
- [49] N. P. Armitage, P. Fournier, and R. L. Greene. “Progress and perspectives on electron-doped cuprates”. In: *Rev. Mod. Phys.* 82 (3 Sept. 2010), pp. 2421–2487. DOI: [10.1103/RevModPhys.82.2421](https://doi.org/10.1103/RevModPhys.82.2421).
- [50] Jin Mo Bok *et al.* “Quantitative determination of pairing interactions for high-temperature superconductivity in cuprates”. In: *Science Advances* 2.3 (2016). DOI: [10.1126/sciadv.1501329](https://doi.org/10.1126/sciadv.1501329).
- [51] G. M. Luke *et al.* “Muon spin relaxation in UPt₃”. In: *Phys. Rev. Lett.* 71 (9 Aug. 1993), pp. 1466–1469. DOI: [10.1103/PhysRevLett.71.1466](https://doi.org/10.1103/PhysRevLett.71.1466).
- [52] G. M. Luke *et al.* “Time-reversal symmetry-breaking superconductivity in Sr₂RuO₄”. In: *Nature* 394 (Aug. 1998), p. 558.
- [53] E. R. Schemm *et al.* “Observation of broken time-reversal symmetry in the heavy-fermion superconductor UPt₃”. In: *Science* 345.6193 (2014), pp. 190–193. ISSN: 0036-8075. DOI: [10.1126/science.1248552](https://doi.org/10.1126/science.1248552).
- [54] Jing Xia *et al.* “High Resolution Polar Kerr Effect Measurements of Sr₂RuO₄: Evidence for Broken Time-Reversal Symmetry in the Superconducting State”. In: *Phys. Rev. Lett.* 97 (16 Oct. 2006), p. 167002. DOI: [10.1103/PhysRevLett.97.167002](https://doi.org/10.1103/PhysRevLett.97.167002).
- [55] A. D. Hillier, J. Quintanilla, and R. Cywinski. “Evidence for Time-Reversal Symmetry Breaking in the Noncentrosymmetric Superconductor LaNiC₂”. In: *Phys. Rev. Lett.* 102 (11 Mar. 2009), p. 117007. DOI: [10.1103/PhysRevLett.102.117007](https://doi.org/10.1103/PhysRevLett.102.117007).
- [56] A. D. Hillier *et al.* “Nonunitary Triplet Pairing in the Centrosymmetric Superconductor LaNiGa₂”. In: *Phys. Rev. Lett.* 109 (9 Aug. 2012), p. 097001. DOI: [10.1103/PhysRevLett.109.097001](https://doi.org/10.1103/PhysRevLett.109.097001).
- [57] Yoichi Kamihara *et al.* “Iron-Based Layered Superconductor La[O_{1-x}F_x]FeAs (x = 0.05–0.12) with T_c = 26 K”. In: *Journal of the American Chemical Society* 130.11 (2008). PMID: 18293989, pp. 3296–3297. DOI: [10.1021/ja800073m](https://doi.org/10.1021/ja800073m).
- [58] A. A. Kordyuk. “Iron-based superconductors: Magnetism, superconductivity, and electronic structure (Review Article)”. In: *Low Temperature Physics* 38.9 (2012), pp. 888–899. DOI: [10.1063/1.4752092](https://doi.org/10.1063/1.4752092).
- [59] Masatoshi Sato and Yoichi Ando. “Topological superconductors: a review”. In: *Reports on Progress in Physics* 80.7 (2017), p. 076501.
- [60] C. L. Kane and E. J. Mele. “Quantum Spin Hall Effect in Graphene”. In: *Phys. Rev. Lett.* 95 (22 Nov. 2005), p. 226801. DOI: [10.1103/PhysRevLett.95.226801](https://doi.org/10.1103/PhysRevLett.95.226801).
- [61] C. L. Kane and E. J. Mele. “Z₂ Topological Order and the Quantum Spin Hall Effect”. In: *Phys. Rev. Lett.* 95 (14 Sept. 2005), p. 146802. DOI: [10.1103/PhysRevLett.95.146802](https://doi.org/10.1103/PhysRevLett.95.146802).
- [62] G. E. Volovik. “Quantum Phase Transitions from Topology in Momentum Space”. In: *Quantum Analogues: From Phase Transitions to Black Holes and Cosmology*. Ed. by William G. Unruh and Ralf Schützhold. Berlin, Heidelberg: Springer Berlin Heidelberg, 2007, pp. 31–73. ISBN: 978-3-540-70859-9. DOI: [10.1007/3-540-70859-6_3](https://doi.org/10.1007/3-540-70859-6_3).

- [63] N. Read and Dmitry Green. “Paired states of fermions in two dimensions with breaking of parity and time-reversal symmetries and the fractional quantum Hall effect”. In: *Phys. Rev. B* 61 (15 Apr. 2000), pp. 10267–10297. DOI: [10.1103/PhysRevB.61.10267](https://doi.org/10.1103/PhysRevB.61.10267).
- [64] A Yu Kitaev. “Unpaired Majorana fermions in quantum wires”. In: *Physics-Uspekhi* 44.10S (2001), p. 131.
- [65] A. P. Drozdov *et al.* “Conventional superconductivity at 203 kelvin at high pressures in the sulfur hydride system”. In: *Nature* 525 (Aug. 2015), p. 73.
- [66] G. M. Eliashberg. “Interactions between electrons and lattice vibrations in a superconductor”. In: *Soviet Phys. JETP* 11.3 (1960).
- [67] G.W. Webb, F. Marsiglio, and J.E. Hirsch. “Superconductivity in the elements, alloys and simple compounds”. In: *Physica C: Superconductivity and its Applications* 514 (2015). Superconducting Materials: Conventional, Unconventional and Undetermined, pp. 17–27. ISSN: 0921-4534. DOI: <https://doi.org/10.1016/j.physc.2015.02.037>.
- [68] B. T. Matthias, T. H. Geballe, and V. B. Compton. “Superconductivity”. In: *Rev. Mod. Phys.* 35 (1 Jan. 1963), pp. 1–22. DOI: [10.1103/RevModPhys.35.1](https://doi.org/10.1103/RevModPhys.35.1).
- [69] H. Fröhlich. “Theory of the Superconducting State. I. The Ground State at the Absolute Zero of Temperature”. In: *Phys. Rev.* 79 (5 Sept. 1950), pp. 845–856. DOI: [10.1103/PhysRev.79.845](https://doi.org/10.1103/PhysRev.79.845).
- [70] John Bardeen and David Pines. “Electron-Phonon Interaction in Metals”. In: *Phys. Rev.* 99 (4 Aug. 1955), pp. 1140–1150. DOI: [10.1103/PhysRev.99.1140](https://doi.org/10.1103/PhysRev.99.1140).
- [71] Leon N. Cooper. “Bound Electron Pairs in a Degenerate Fermi Gas”. In: *Phys. Rev.* 104 (4 Nov. 1956), pp. 1189–1190. DOI: [10.1103/PhysRev.104.1189](https://doi.org/10.1103/PhysRev.104.1189).
- [72] Manfred Sgrist and Kazuo Ueda. “Phenomenological theory of unconventional superconductivity”. In: *Rev. Mod. Phys.* 63 (2 Apr. 1991), pp. 239–311. DOI: [10.1103/RevModPhys.63.239](https://doi.org/10.1103/RevModPhys.63.239).
- [73] V. L. Ginsburg and L. D. Landau. Russian. In: *Zh. Eksp. Teor. Fiz.* 20 (1950). Cited in Lev P. Gor’kov. “DEVELOPING BCS IDEAS IN THE FORMER SOVIET UNION”. In: *BCS: 50 Years*, pp. 107–126. DOI: [10.1142/9789814304665_0007](https://doi.org/10.1142/9789814304665_0007), p. 1064.
- [74] J. C. Tolédano. *LANDAU THEORY OF PHASE TRANSITIONS, THE*. World Scientific Publishing Company, Aug. 1, 1987. 470 pp. ISBN: 9971500264.
- [75] B.D. Josephson. “Possible new effects in superconductive tunnelling”. In: *Physics Letters* 1.7 (1962), pp. 251–253. ISSN: 0031-9163. DOI: [https://doi.org/10.1016/0031-9163\(62\)91369-0](https://doi.org/10.1016/0031-9163(62)91369-0).
- [76] A. Barone and G. Paternò. *Physics and Applications of the Josephson Effect*. 1989.
- [77] P. W. Anderson and J. M. Rowell. “Probable Observation of the Josephson Superconducting Tunneling Effect”. In: *Phys. Rev. Lett.* 10 (6 Mar. 1963), pp. 230–232. DOI: [10.1103/PhysRevLett.10.230](https://doi.org/10.1103/PhysRevLett.10.230).
- [78] “Mise en pratique for the definition of the ampere and other electric units in the SI”. In: *SI Brochure – 9th edition (2019) – Appendix 2 20 May*. 2019.
- [79] James F. Annett. “Symmetry of the order parameter for high-temperature superconductivity”. In: *Advances in Physics* 39.2 (1990), pp. 83–126. DOI: [10.1080/00018739000101481](https://doi.org/10.1080/00018739000101481).

- [80] Geoff Brumfiel. “Topological insulators: Star material”. In: *Nature* 466.7304 (July 2010), pp. 310–311. DOI: [10.1038/466310a](https://doi.org/10.1038/466310a).
- [81] Andreas P. Schnyder *et al.* “Classification of topological insulators and superconductors in three spatial dimensions”. In: *Phys. Rev. B* 78 (19 Nov. 2008), p. 195125. DOI: [10.1103/PhysRevB.78.195125](https://doi.org/10.1103/PhysRevB.78.195125).
- [82] B. Mazidian *et al.* “Anomalous thermodynamic power laws near topological transitions in nodal superconductors”. In: *Phys. Rev. B* 88 (22 Dec. 2013), p. 224504. DOI: [10.1103/PhysRevB.88.224504](https://doi.org/10.1103/PhysRevB.88.224504).
- [83] Andreas P. Schnyder, P. M. R. Brydon, and Carsten Timm. “Types of topological surface states in nodal noncentrosymmetric superconductors”. In: *Phys. Rev. B* 85 (2 Jan. 2012), p. 024522. DOI: [10.1103/PhysRevB.85.024522](https://doi.org/10.1103/PhysRevB.85.024522).
- [84] H. Q. Yuan *et al.* “*S*-Wave Spin-Triplet Order in Superconductors without Inversion Symmetry: $\text{Li}_2\text{Pd}_3\text{B}$ and $\text{Li}_2\text{Pt}_3\text{B}$ ”. In: *Phys. Rev. Lett.* 97 (1 July 2006), p. 017006. DOI: [10.1103/PhysRevLett.97.017006](https://doi.org/10.1103/PhysRevLett.97.017006).
- [85] M. Nishiyama, Y. Inada, and Guo-qing Zheng. “Spin Triplet Superconducting State due to Broken Inversion Symmetry in $\text{Li}_2\text{Pt}_3\text{B}$ ”. In: *Phys. Rev. Lett.* 98 (4 Jan. 2007), p. 047002. DOI: [10.1103/PhysRevLett.98.047002](https://doi.org/10.1103/PhysRevLett.98.047002).
- [86] H. Takeya *et al.* “Specific-heat studies of the spin-orbit interaction in noncentrosymmetric $\text{Li}_2(\text{Pd}_{1-x}\text{Pt}_x)_3\text{B}$ ($x = 0, 0.5, 1$) superconductors”. In: *Phys. Rev. B* 76 (10 Sept. 2007), p. 104506. DOI: [10.1103/PhysRevB.76.104506](https://doi.org/10.1103/PhysRevB.76.104506).
- [87] S. Harada *et al.* “Abrupt enhancement of noncentrosymmetry and appearance of a spin-triplet superconducting state in $\text{Li}_2(\text{Pd}_{1-x}\text{Pt}_x)_3\text{B}$ beyond $x = 0.8$ ”. In: *Phys. Rev. B* 86 (22 Dec. 2012), p. 220502. DOI: [10.1103/PhysRevB.86.220502](https://doi.org/10.1103/PhysRevB.86.220502).
- [88] B. Béri. “Topologically stable gapless phases of time-reversal-invariant superconductors”. In: *Phys. Rev. B* 81 (13 Apr. 2010), p. 134515. DOI: [10.1103/PhysRevB.81.134515](https://doi.org/10.1103/PhysRevB.81.134515).
- [89] Rafael M. Fernandes and Jörg Schmalian. “Scaling of nascent nodes in extended-*s*-wave superconductors”. In: *Phys. Rev. B* 84 (1 July 2011), p. 012505. DOI: [10.1103/PhysRevB.84.012505](https://doi.org/10.1103/PhysRevB.84.012505).
- [90] Anthony J. Leggett. “A theoretical description of the new phases of liquid ^3He ”. In: *Rev. Mod. Phys.* 47 (2 Apr. 1975), pp. 331–414. DOI: [10.1103/RevModPhys.47.331](https://doi.org/10.1103/RevModPhys.47.331).
- [91] Andrew Peter Mackenzie and Yoshiteru Maeno. “The superconductivity of Sr_2RuO_4 and the physics of spin-triplet pairing”. In: *Rev. Mod. Phys.* 75 (2 May 2003), pp. 657–712. DOI: [10.1103/RevModPhys.75.657](https://doi.org/10.1103/RevModPhys.75.657).
- [92] P. W. Anderson and P. Morel. “Generalized Bardeen-Cooper-Schrieffer States and the Proposed Low-Temperature Phase of Liquid He^3 ”. In: *Phys. Rev.* 123 (6 Sept. 1961), pp. 1911–1934. DOI: [10.1103/PhysRev.123.1911](https://doi.org/10.1103/PhysRev.123.1911).
- [93] N. E. Hussey. “Low-energy quasiparticles in high- T_c cuprates”. In: *Advances in Physics* 51.8 (2002), pp. 1685–1771. DOI: [10.1080/00018730210164638](https://doi.org/10.1080/00018730210164638).
- [94] S. L. Lee, S.H. Kilcoyne, and R. Cywinski. *Muon science: muons in physics, chemistry, and materials*. CRC Press, 1999. ISBN: 9780750306300.

- [95] A. Yaouanc and P. Dalmas de Reotier. *Muon spin rotation, relaxation, and resonance: applications to condensed matter*. Oxford England New York: Oxford University Press, 2011. ISBN: 9780199596478.
- [96] R. S. Hayano *et al.* “Zero- and low-field spin relaxation studied by positive muons”. In: *Phys. Rev. B* 20 (3 Aug. 1979), pp. 850–859. DOI: [10.1103/PhysRevB.20.850](https://doi.org/10.1103/PhysRevB.20.850).
- [97] R. P. Singh *et al.* “Detection of Time-Reversal Symmetry Breaking in the Noncentrosymmetric Superconductor Re_6Zr Using Muon-Spin Spectroscopy”. In: *Phys. Rev. Lett.* 112 (10 Mar. 2014), p. 107002. DOI: [10.1103/PhysRevLett.112.107002](https://doi.org/10.1103/PhysRevLett.112.107002).
- [98] S. J. Ray *et al.* “Muon-spin rotation measurements of the vortex state in Sr_2RuO_4 : Type-1.5 superconductivity, vortex clustering, and a crossover from a triangular to a square vortex lattice”. In: *Phys. Rev. B* 89 (9 Mar. 2014), p. 094504. DOI: [10.1103/PhysRevB.89.094504](https://doi.org/10.1103/PhysRevB.89.094504).
- [99] E.R. Schemm, E.M. Levenson-Falk, and A. Kapitulnik. “Polar Kerr effect studies of time reversal symmetry breaking states in heavy fermion superconductors”. In: *Physica C: Superconductivity and its Applications* 535 (2017), pp. 13–19. ISSN: 0921-4534. DOI: <https://doi.org/10.1016/j.physc.2016.11.012>.
- [100] Akihiko Sumiyama *et al.* “Spontaneous Magnetization of Non-centrosymmetric Superconductor LaNiC_2 ”. In: *Journal of the Physical Society of Japan* 84.1 (2015), p. 013702. DOI: [10.7566/JPSJ.84.013702](https://doi.org/10.7566/JPSJ.84.013702).
- [101] W.H. Lee *et al.* “Superconductivity in the Ni based ternary carbide LaNiC_2 ”. In: *Physica C: Superconductivity* 266.1 (1996), pp. 138–142. ISSN: 0921-4534. DOI: [https://doi.org/10.1016/0921-4534\(96\)00309-7](https://doi.org/10.1016/0921-4534(96)00309-7).
- [102] W.H. Lee and H.K. Zeng. “Superconductivity in the series $(\text{La}_{1-x}\text{Th}_x)\text{NiC}_2$ ($0 \leq x \leq 0.8$)”. In: *Solid State Communications* 101.5 (1997), pp. 323–326. ISSN: 0038-1098. DOI: [https://doi.org/10.1016/S0038-1098\(96\)00589-3](https://doi.org/10.1016/S0038-1098(96)00589-3).
- [103] K.J. Syu *et al.* “Superconductivity in $\text{LaNiC}_2-\delta\text{N}_x$ ”. In: *Physica C: Superconductivity and its Applications* 470 (2010). Proceedings of the 9th International Conference on Materials and Mechanisms of Superconductivity, S662–S663. ISSN: 0921-4534. DOI: <https://doi.org/10.1016/j.physc.2009.11.063>.
- [104] V. K. Pecharsky, L. L. Miller, and K. A. Gschneidner. “Low-temperature behavior of two ternary lanthanide nickel carbides: Superconducting LaNiC_2 and magnetic CeNiC_2 ”. In: *Phys. Rev. B* 58 (1 July 1998), pp. 497–502. DOI: [10.1103/PhysRevB.58.497](https://doi.org/10.1103/PhysRevB.58.497).
- [105] Y. Iwamoto *et al.* “Microscopic measurements in ^{139}La -NQR of the ternary carbide superconductor LaNiC_2 ”. In: *Physics Letters A* 250.4 (1998), pp. 439–442. ISSN: 0375-9601. DOI: [https://doi.org/10.1016/S0375-9601\(98\)00839-1](https://doi.org/10.1016/S0375-9601(98)00839-1).
- [106] B. J. C. van der Hoeven and P. H. Keesom. “Specific Heat of Lead and Lead Alloys Between 0.4 and 4.2°K”. In: *Phys. Rev.* 137 (1A Jan. 1965), A103–A107. DOI: [10.1103/PhysRev.137.A103](https://doi.org/10.1103/PhysRev.137.A103).
- [107] Izumi Hase and Takashi Yanagisawa. “Electronic Structure of RNiC_2 (R=La, Y, and Th)”. In: *Journal of the Physical Society of Japan* 78.8 (2009), p. 084724. DOI: [10.1143/JPSJ.78.084724](https://doi.org/10.1143/JPSJ.78.084724).

- [108] J. Laverock *et al.* “Electronic structure of $R\text{NiC}_2$ ($R = \text{Sm}, \text{Gd}, \text{and Nd}$) intermetallic compounds”. In: *Phys. Rev. B* 80 (12 Sept. 2009), p. 125111. DOI: [10.1103/PhysRevB.80.125111](https://doi.org/10.1103/PhysRevB.80.125111).
- [109] Alaska Subedi and David J. Singh. “Electron-phonon superconductivity in noncentrosymmetric LaNiC_2 : First-principles calculations”. In: *Phys. Rev. B* 80 (9 Sept. 2009), p. 092506. DOI: [10.1103/PhysRevB.80.092506](https://doi.org/10.1103/PhysRevB.80.092506).
- [110] Jorge Quintanilla *et al.* “Relativistic analysis of the pairing symmetry of the noncentrosymmetric superconductor LaNiC_2 ”. In: *Phys. Rev. B* 82 (17 Nov. 2010), p. 174511. DOI: [10.1103/PhysRevB.82.174511](https://doi.org/10.1103/PhysRevB.82.174511).
- [111] Soumya P. Mukherjee and Stephanie H. Curnoe. “Superconductivity in non-centrosymmetric LaNiC_2 ”. In: *Physica C: Superconductivity* 499 (2014), pp. 6–8. ISSN: 0921-4534. DOI: <https://doi.org/10.1016/j.physc.2014.01.008>.
- [112] I Bonalde *et al.* “Nodal gap structure in the noncentrosymmetric superconductor LaNiC_2 from magnetic-penetration-depth measurements”. In: *New Journal of Physics* 13.12 (2011), p. 123022.
- [113] Takashi Yanagisawa and Izumi Hase. “Nonunitary Triplet Superconductivity in the Noncentrosymmetric Rare-Earth Compound LaNiC_2 ”. In: *Journal of the Physical Society of Japan* 81.Suppl.B (2012), SB039. DOI: [10.1143/JPSJS.81SB.SB039](https://doi.org/10.1143/JPSJS.81SB.SB039).
- [114] Yusuke Hirose *et al.* “Fermi Surface and Superconducting Properties of Non-centrosymmetric LaNiC_2 ”. In: *Journal of the Physical Society of Japan* 81.11 (2012), p. 113703. DOI: [10.1143/JPSJ.81.113703](https://doi.org/10.1143/JPSJ.81.113703).
- [115] J Chen *et al.* “Evidence for two-gap superconductivity in the non-centrosymmetric compound LaNiC_2 ”. In: *New Journal of Physics* 15.5 (2013), p. 053005.
- [116] Susumu Katano *et al.* “Magnetic impurity effects on the superconductivity of noncentrosymmetric LaNiC_2 : Ce substitution for La”. In: *Phys. Rev. B* 95 (14 Apr. 2017), p. 144502. DOI: [10.1103/PhysRevB.95.144502](https://doi.org/10.1103/PhysRevB.95.144502).
- [117] Akihiko Sumiyama *et al.* “Search for Spontaneous Magnetization of Superconductors with Broken Time-Reversal Symmetry”. In: *Proceedings of the International Conference on Strongly Correlated Electron Systems (SCES2013)*. DOI: [10.7566/JPSCP.3.015017](https://doi.org/10.7566/JPSCP.3.015017).
- [118] Susumu Katano *et al.* “Anomalous pressure dependence of the superconductivity in noncentrosymmetric LaNiC_2 : Evidence of strong electronic correlations”. In: *Phys. Rev. B* 90 (22 Dec. 2014), p. 220508. DOI: [10.1103/PhysRevB.90.220508](https://doi.org/10.1103/PhysRevB.90.220508).
- [119] B. Wiendlocha *et al.* “Pressure effects on the unconventional superconductivity of noncentrosymmetric LaNiC_2 ”. In: *Phys. Rev. B* 94 (13 Oct. 2016), p. 134517. DOI: [10.1103/PhysRevB.94.134517](https://doi.org/10.1103/PhysRevB.94.134517).
- [120] J. F. Landaeta *et al.* “Unconventional superconductivity and an ambient-pressure magnetic quantum critical point in single-crystal LaNiC_2 ”. In: *Phys. Rev. B* 96 (17 Nov. 2017), p. 174515. DOI: [10.1103/PhysRevB.96.174515](https://doi.org/10.1103/PhysRevB.96.174515).
- [121] Yuji Aoki, Ko Terayama, and Hideyuki Sato. “Magnetic, Thermal and Transport Properties of CeNiGa_2 ”. In: *Journal of the Physical Society of Japan* 64.10 (1995), pp. 3986–3992. DOI: [10.1143/JPSJ.64.3986](https://doi.org/10.1143/JPSJ.64.3986).

- [122] N. L. Zeng and W. H. Lee. “Superconductivity in the Ni-based ternary compound LaNiGa_2 ”. In: *Phys. Rev. B* 66 (9 Sept. 2002), p. 092503. DOI: [10.1103/PhysRevB.66.092503](https://doi.org/10.1103/PhysRevB.66.092503).
- [123] David J. Singh. “Electronic structure and fermiology of superconducting LaNiGa_2 ”. In: *Phys. Rev. B* 86 (17 Nov. 2012), p. 174507. DOI: [10.1103/PhysRevB.86.174507](https://doi.org/10.1103/PhysRevB.86.174507).
- [124] Izumi Hase and Takashi Yanagisawa. “Electronic Structure of LaNiGa_2 ”. In: *Journal of the Physical Society of Japan* 81.10 (2012), p. 103704. DOI: [10.1143/JPSJ.81.103704](https://doi.org/10.1143/JPSJ.81.103704).
- [125] Bayan Mazidian. “Symmetry and Topology in Triplet Superconductors”. PhD thesis. University of Bristol, 2013.
- [126] Z. F. Weng *et al.* “Two-Gap Superconductivity in LaNiGa_2 with Nonunitary Triplet Pairing and Even Parity Gap Symmetry”. In: *Phys. Rev. Lett.* 117 (2 July 2016), p. 027001. DOI: [10.1103/PhysRevLett.117.027001](https://doi.org/10.1103/PhysRevLett.117.027001).
- [127] A. de Visser. “Superconducting Ferromagnets”. In: *Encyclopedia of Materials: Science and Technology*. Ed. by K.H. Jürgen Buschow *et al.* Oxford: Elsevier, 2010, pp. 1–6. ISBN: 978-0-08-043152-9. DOI: <https://doi.org/10.1016/B978-0-08043152-9.02222-3>.
- [128] William H. Press *et al.* *Numerical Recipes*. Cambridge University Pr., Sept. 6, 2007. 1248 pp. ISBN: 0521880688.
- [129] J. Quintanilla and A. J. Schofield. “Pomeranchuk and topological Fermi surface instabilities from central interactions”. In: *Phys. Rev. B* 74 (11 Sept. 2006), p. 115126. DOI: [10.1103/PhysRevB.74.115126](https://doi.org/10.1103/PhysRevB.74.115126).
- [130] Kazumasa Miyake. “Theory of Pairing Assisted Spin Polarization in Spin-Triplet Equal Spin Pairing: Origin of Extra Magnetization in Sr_2RuO_4 in Superconducting State”. In: *Journal of the Physical Society of Japan* 83.5 (2014), p. 053701. DOI: [10.7566/JPSJ.83.053701](https://doi.org/10.7566/JPSJ.83.053701).
- [131] Edmund C. Stoner. “Collective electron ferromagnetism II. Energy and specific heat”. In: *Proceedings of the Royal Society of London A: Mathematical, Physical and Engineering Sciences* 169.938 (1939), pp. 339–371. ISSN: 0080-4630. DOI: [10.1098/rspa.1939.0003](https://doi.org/10.1098/rspa.1939.0003).
- [132] S. Blundell. *Magnetism in Condensed Matter*. Oxford Master Series in Condensed Matter Physics. OUP Oxford, 2001. ISBN: 9780198505914.
- [133] J. Hubbard. “Electron correlations in narrow energy bands”. In: *Proceedings of the Royal Society of London A: Mathematical, Physical and Engineering Sciences* 276.1365 (1963), pp. 238–257. ISSN: 0080-4630. DOI: [10.1098/rspa.1963.0204](https://doi.org/10.1098/rspa.1963.0204).
- [134] R. Denz. “Electronic Systems for the Protection of Superconducting Elements in the LHC”. In: *IEEE Transactions on Applied Superconductivity* 16.2 (June 2006), pp. 1725–1728. DOI: [10.1109/tasc.2005.864258](https://doi.org/10.1109/tasc.2005.864258).
- [135] R. Denz *et al.* “Detection of Resistive Transitions in Lhc Superconducting Components”. In: *Proceedings of the 2001 Particle Accelerator Conference, Chicago*. IEEE, 2001.

- [136] A Vergara Fernández and F Rodríguez-Mateos. “Reliability of the quench protection system for the LHC superconducting elements”. In: *Nuclear Instruments and Methods in Physics Research Section A: Accelerators, Spectrometers, Detectors and Associated Equipment* 525.3 (2004), pp. 439–446. ISSN: 0168-9002. DOI: <https://doi.org/10.1016/j.nima.2004.01.081>.
- [137] Y. Khristi *et al.* “Quench Detection System for TF Coil-Test Campaigns of SST-1”. In: *IEEE Transactions on Applied Superconductivity* 22.2 (Apr. 2012), pp. 4200108–4200108. DOI: [10.1109/tasc.2012.2184757](https://doi.org/10.1109/tasc.2012.2184757).
- [138] Peter J. Lee. “Applications and Related Technology”. In: *Engineering Superconductivity*. Wiley-IEEE Press, 2001, pp. 672–. ISBN: 9780470547175. DOI: [10.1109/9780470547175.ch3](https://doi.org/10.1109/9780470547175.ch3).
- [139] A. Shajii and J. P. Freidberg. “Quench in superconducting magnets. I. Model and numerical implementation”. In: *Journal of Applied Physics* 76.5 (1994), pp. 3149–3158. DOI: [10.1063/1.357498](https://doi.org/10.1063/1.357498).
- [140] Dennis Overbye. *Collider Operations on Hold Until Next Year - The New York Times*. 2008.
- [141] Valentin Stanev *et al.* “Robust accidental nodes and zeros and critical quasiparticle scaling in iron-based multiband superconductors”. In: *Phys. Rev. B* 84 (1 July 2011), p. 014505. DOI: [10.1103/PhysRevB.84.014505](https://doi.org/10.1103/PhysRevB.84.014505).
- [142] V. Mishra *et al.* “Lifting of nodes by disorder in extended-*s*-state superconductors: Application to ferropnictides”. In: *Phys. Rev. B* 79 (9 Mar. 2009), p. 094512. DOI: [10.1103/PhysRevB.79.094512](https://doi.org/10.1103/PhysRevB.79.094512).
- [143] Eric W. Weisstein. *Normal Matrix. From MathWorld—A Wolfram Web Resource*. URL: <http://mathworld.wolfram.com/NormalMatrix.html> (visited on 10/07/2018).
- [144] Maxima. *Maxima, a Computer Algebra System. Version 5.34.1*. 2014. URL: <http://maxima.sourceforge.net/>.
- [145] *wxMaxima*. Version 13.04.2. URL: <https://wxmaxima-developers.github.io/wxmaxima/index.html> (visited on 10/08/2018).
- [146] Dirk van Delft and Peter Kes. “The discovery of superconductivity”. In: *Physics Today* 63.9 (Sept. 2010), pp. 38–43. DOI: [10.1063/1.3490499](https://doi.org/10.1063/1.3490499).
- [147] Jörg Schmalian. “FAILED THEORIES OF SUPERCONDUCTIVITY”. In: *BCS: 50 Years*, pp. 41–55. DOI: [10.1142/9789814304665_0004](https://doi.org/10.1142/9789814304665_0004).